



Virginia Commonwealth University
VCU Scholars Compass

Theses and Dissertations

Graduate School

2016

Interactions of the Naphthalene Radical Cation with Polar and Unsaturated Molecules in the Gas Phase

Sean P. Platt
Virginia Commonwealth University

Follow this and additional works at: <https://scholarscompass.vcu.edu/etd>

 Part of the [Physical Chemistry Commons](#)

© The Author

Downloaded from

<https://scholarscompass.vcu.edu/etd/4210>

This Dissertation is brought to you for free and open access by the Graduate School at VCU Scholars Compass. It has been accepted for inclusion in Theses and Dissertations by an authorized administrator of VCU Scholars Compass. For more information, please contact libcompass@vcu.edu.

College of Humanities and Sciences

Virginia Commonwealth University

This is to verify that the dissertation prepared by Sean Patrick Platt entitled Interactions of the Naphthalene Radical Cation with Polar and Unsaturated Molecules in the Gas Phase has been approved by his committee as satisfactory completion of the thesis or dissertation requirement for the degree of Doctor of Philosophy

M. Samy El-Shall, Ph. D., Professor, Department of Chemistry, Research Advisor

James Turner, Ph. D., Professor, Department of Chemistry

Scott Gronert, Ph. D., Professor, Department of Chemistry

Shiv Khanna, Ph. D., Commonwealth Professor, Department of Physics

Alison A. Baski, Ph. D., Dean, College of Humanities and Sciences

F. Douglas Boudinot, Ph. D., Dean of the School of Graduate Studies

April 20, 2016

© Sean Patrick Platt, 2016

All Rights Reserved

INTERACTIONS OF THE NAPHTHALENE RADICAL CATION WITH
UNSATURATED MOLECULES IN THE GAS PHASE

A dissertation in partial fulfillment of the requirement for the degree of doctor of
philosophy at Virginia Commonwealth University

by

SEAN PATRICK PLATT

B.S., Hampden-Sydney College, Virginia, 2009

Director: M. SAMY EL-SHALL

Professor, Department of Chemistry

Virginia Commonwealth University

Richmond, Virginia

April 2016

Acknowledgements

There are many people I want to acknowledge for getting me to the point of writing this dissertation. I want to first thank my advisor Dr. M. Samy El-Shall for allowing me join his research group and for his guidance in my research. When I first joined the group, I did bench top graphene research, but after a few months I was offered the chance to switch to gas phase research and it has been a very rewarding experience. Thank you to all of my group members for all the interactions we had over the years. In particular, I want to single out Dr. Isaac Kwame Attah and thank him for training me when I joined the gas phase division of the group. When I started I only had a basic understanding of mass spectrometry, but even today I am still learning subtle nuances of the systems we use. Kwame is also responsible for many of the theoretical calculations found throughout this dissertation. In addition, I need to thank him along with Dr. M. Head-Gordon for their work on the theoretical calculations found in this dissertation. I want to say thank you for everything. I also want to thank Dr. Michael Meot-Ner (Mautner) who was here at the beginning of my time in the gas phase and help build the knowledge foundation that I still use today.

Outside of the lab, there are many people who have helped through the years. My roommate and friend through all of this, Andrea Moreau, deserves a lot of credit for accepting that there are times where I would just be in my own tunnel and really could not help with much. Thanks to two of my oldest friends, Christopher Arnatt and Matt Huff, who were going through their own grad school experiences and always willing to share stories or insight into background information.

Most importantly I want to thank my family for their patience and support over this journey. First and foremost, I want to thank my parents, Ina Blackburn and Bill Platt, instilling in me the belief to work hard and set my sights as high as possible. I also need to acknowledge my sisters, Lauren Warren and Rhiannon Platt, for their encouragement in this endeavor even when they were not paying attention to what I was describing. Of course during my time at VCU, my family has grown so I need to thank Richard Blackburn and my brother-in-law Lee Warren. Finally, I want to acknowledge my nephew Harry, who will make me laugh when I was having a rough day.

Table of Contents

Acknowledgements.....	ii
Table of Contents.....	iii
List of Figures.....	vii
List of Tables.....	xvii
Abstract.....	xix
Chapter 1: Introduction and Overview.....	1
Chapter 2: Experimental Setup.....	7
2.1. Experimental System Overview.....	7
2.2. Vacuum System.....	9
2.3. Cluster Formation.....	10
2.4. Quadrupole Mass Selector – Ion Mobility – Quadrupole Mass Selector.....	13
2.4.1. Ion Generation – Electron Impact Ionization.....	13
2.4.2. Quadrupole Mass-Filter.....	14
2.4.3. Drift Cell and Focusing Ion Optics.....	15
2.4.4. Detection of Ions - Electron Multiplier Detector.....	20
2.4.5. Ion Energy and Injection Energy.....	21
Chapter 3: Experimental Measurements.....	24
3.1. Thermochemistry Measurements.....	24
3.2. Mobility Measurements and Structure Determination.....	25
3.2.1. Mobility Measurements.....	26
3.2.2. Experimental Structure Determination.....	32
3.2.3. Theoretical Methods of Calculating Mobilities and Collision Integrals.....	32
3.2.3.1. Exact Hard Sphere Approximation.....	33
3.2.3.2. Projection Approximation.....	34
3.2.3.3. Trajectory Calculation.....	35
3.3. Theoretical Calculations.....	35
Chapter 4: Stepwise Solvation of the Naphthalene Radical Cation by Small Polar Molecules.....	37
4.1. Introduction.....	37

4.2. Experimental Section	39
4.3. Theoretical Calculations	41
4.4. Results and Discussion	42
4.4.1. Study of the Energies and Structures of the Stepwise Hydration of the Naphthalene Radical Cation	43
4.4.1.1. Mass Spectra and Thermochemical Results for the Hydration of Naphthalene ^{•+}	43
4.4.1.2. Calculated Structures and Binding Energies for Naphthalene ^{•+} (H ₂ O) _n Clusters	46
4.4.2. Study of the Energies and Structures of the Stepwise Solvation of Naphthalene ^{•+} with Methanol	53
4.4.2.1. Mass Spectra and Thermochemical Results for Naphthalene ^{•+} (CH ₃ OH) _n Clusters	53
4.4.2.2. Calculated Structures and Binding Energies for Naphthalene ^{•+} (CH ₃ OH) _n Clusters	56
4.4.2.3. Deprotonation of Naphthalene ^{•+} by Methanol Clusters	59
4.4.3. Study of the Energies and Structures of the Stepwise Solvation of Naphthalene ^{•+} with Primary and Secondary Alcohols of 2, 3, and 4 Carbons	62
4.4.3.1. Mass Spectra and Thermochemical Results for Naphthalene ^{•+} (ROH) Clusters	63
4.4.3.2. Calculated Structures and Binding Energies of Naphthalene ^{•+} (ROH) Clusters	75
4.4.4. Study of the Energies and Structures of the Stepwise Solvation of Naphthalene ^{•+} by HCN	86
4.4.4.1. Mass Spectra and Thermochemical Results for Naphthalene ^{•+} (HCN) _n clusters	86
4.4.4.2. Calculated Structures and Binding Energies of Naphthalene ^{•+} (HCN) _n Clusters	90
4.4.5. Study of the Energies and Structures of the Stepwise Solvation of Association of Naphthalene ^{•+} by Acetonitrile	97
4.4.5.1. Mass Spectra and Thermochemical Results for Naphthalene ^{•+} (CH ₃ CN) _n clusters	97
4.4.5.2. Calculated Structures Binding Energies of Naphthalene ^{•+} (CH ₃ CN) _n Clusters	102
4.5. Summary and Conclusions	107

Chapter 5: Interactions of the Naphthalene Radical Cation with Acetylene and Olefin Molecules.....	110
5.1. Introduction.....	110
5.2. Experimental Section.....	111
5.3. Results and Discussion	113
5.3.1. Mass Spectra and Thermochemistry Results for Naphthalene ^{•+} (C ₂ H ₂) _n clusters	113
5.3.2. Association of Neutral Olefin Molecules with the Naphthalene Radical Cation	117
5.4. Summary and Conclusions	128
Chapter 6: Structures and Binding Energies of the Naphthalene ₂ ^{•+} Homodimer and (Naphthalene•Benzene) ^{•+} and (Naphthalene•Pyridine) ^{•+} Heterodimers	129
6.1. Introduction.....	129
6.2. Experimental Section.....	132
6.3. Theoretical Calculations	134
6.4. Results and Discussion	135
6.4.1. Ion Mobility Measurements and Structures of the (Naphthalene) ₂ ^{•+} Dimer.	135
6.4.2. Structures and Binding of the Solvation of the Naphthalene ^{•+} by Benzene..	138
6.4.2.1. Thermochemical Results and Structures for Naphthalene ^{•+} (Benzene) _n Clusters	138
6.4.2.2. Ion Mobility Measurements for the (Naphthalene•Benzene) ^{•+} Heterodimer	146
6.4.3. Structure and Binding of the Solvation of Naphthalene ^{•+} by Pyridine	149
6.4.3.1. Mass Spectra and Thermochemical Results for Naphthalene ^{•+} (Pyridine) _n Clusters	149
6.4.3.2. Ion Mobility Measurements for the (Naphthalene•Pyridine) ^{•+} Heterodimer	156
6.4.3.3. Calculated Structures of Naphthalene ^{•+} (Pyridine) _n Clusters for <i>n</i> = 1 and 2	159
6.5. Summary and Conclusions	164
Chapter 7: Stepwise Solvation of the Phenyl Cation by Small Polar Molecules with Comparisons to Naphthalene ^{•+}	166
7.1. Introduction.....	166
7.2. Experimental Section.....	168

7.3. Theoretical Calculations	170
7.4. Results and Discussion	171
7.4.1. Stepwise Hydration of the Phenyl Cation	171
7.4.1.1. Mass Spectra and Thermochemical Results for Phenyl ⁺ (H ₂ O) _n Clusters	171
7.4.1.2. Calculated Structures of the Hydrated Phenyl Cation with 1-5 Water Molecules	178
7.4.2. Thermochemistry Results for the Association of CH ₃ OH with the Phenyl Cation	183
7.4.3. Thermochemistry Results for the Association of HCN with the Phenyl Cation	187
7.4.4. Thermochemistry Results for the Association of CH ₃ CN with the Phenyl Cation	192
7.4.5. Comparisons Between Interactions of Small Polar Molecules with the Phenyl Cation and Naphthalene Radical Cation	197
7.5. Summary and Conclusions	198
Chapter 8: Summary of Results and Future Outlooks	200
List of References	205
Vita	213

List of Figures

- Figure 1. Schematic diagram of the VCU QMS-IM-QMS system. The labels above are: (1) pulsed nozzle, (2) 3 mm skimmer cone, (3) electron-impact ionizer, (4) quadrupole mass filter, (5) ion transport lens stack 1 (Einzel lenses 1, 2, and 3), (6) steering lenses (also act as the ion gate), (7) drift cell, (8) baratron line, (9) ion transport lens stack 2 (Einzel lenses 4, 5, and 6), (10) quadrupole mass filter, (11) detector housing (contains electron multiplier)..... 7
- Figure 2. General diagram for the experimental setup of the VCU QMS-IM-QMS system.⁸⁷ 8
- Figure 3. Schematic drawing of the ion region basket surrounded by the tungsten filament illustrating the region where ionization occurs. 14
- Figure 4. Side view cross section of the drift cell used in the VCU QMS-IM-QMS system with the following components (all units in inches): (1) Endcap, (2) Reaction Cell Body, (3) Entrance Lens (Lens B), Tapered Entrance Lens (Lens A), (5) Entrance Orifice (0.25 mm), (6) Drift Rings (inside of drift cell body), (7) Exit Orifice (0.25 mm), (8) Tapered Exit Lens (Lens C), (9) Cell Body Liquid Nitrogen Inlet, (10) Baratron Connection, (11) Drift Cell, (12) Endcap Liquid Nitrogen Inlet. 17
- Figure 5. Breakdown of the drift cell endcap and components mounted on each side including: tapered exit lens (Lens C), copper drift rings, ceramic spacers, and liquid nitrogen inlet and outlet. 18
- Figure 6. Mass spectra obtained resulting from the injection of the mass-selected naphthalene radical cation ($C_{10}H_8^{*+}$, $Naph^+$) into He gas (a) or He/water (H_2O , W) vapor mixture (b-d) at different pressures (Torr) and temperatures (K) as indicated. 44
- Figure 7. van't Hoff plots for the temperature dependence of the equilibrium constants of the association reaction of naphthalene radical cation with water where H_2O is shown in (a) and D_2O shown in (b). The resulting $-\Delta H^\circ$ and $-\Delta S^\circ$ are in ($kcal\ mol^{-1}$) and ($cal\ mol^{-1}\ K^{-1}$) respectively. The error for the measurements are $\pm 1\ kcal\ mol^{-1}$ for $-\Delta H^\circ$ and $\pm 2\ cal\ mol^{-1}\ K^{-1}$ for $-\Delta S^\circ$ 46
- Figure 8. DFT structures and binding energies (ΔE , $kcal\ mol^{-1}$, calculated using Equation 4.3) of: (a) the four lowest energy isomers of the $C_{10}H_8^{*+}(H_2O)$ cluster obtained at the B3LYP/6-311++G** level and (b) the lowest energy structures of the $C_{10}H_8^{*+}(H_2O)_n$ clusters for $n = 1-6$ obtained at B3LYP/6-311++G** level..... 48
- Figure 9. DFT structures and binding energies (ΔE , $kcal\ mol^{-1}$, calculated using Equation 4.3) for (a) the lowest energy “*externally solvated*” isomer of the $C_{10}H_8^{*+}(H_2O)_2$ cluster and (b-d) higher energy “*internally solvated*” isomers with corresponding binding energies. 49

Figure 10. DFT structures and binding energies (ΔE , kcal mol ⁻¹ , calculated using Equation 4.3) for (a) the lowest energy “ <i>externally solvated</i> ” isomer of the C ₁₀ H ₈ ^{•+} (H ₂ O) ₃ cluster and (b-d) higher energy isomers with corresponding binding energies.	50
Figure 11. DFT structures and binding energies (ΔE , kcal mol ⁻¹ , calculated using Equation 4.3) for (a) the lowest energy isomer of the C ₁₀ H ₈ ^{•+} (H ₂ O) ₅ cluster and (b-d) higher energy isomers with corresponding binding energies.	51
Figure 12. DFT structures and binding energies (ΔE , kcal mol ⁻¹ , calculated using Equation 4.3) for (a) the lowest energy isomer of the C ₁₀ H ₈ ^{•+} (H ₂ O) ₅ cluster and (b-d) higher energy isomers with corresponding binding energies.	52
Figure 13. DFT structures and binding energies (ΔE , kcal mol ⁻¹ , calculated using Equation 4.3) for (a) the lowest energy isomer of the C ₁₀ H ₈ ^{•+} (H ₂ O) ₆ cluster and (b-d) higher energy isomers with corresponding binding energies.	52
Figure 14. Mass spectra obtained resulting from the injection of the mass-selected naphthalene radical cation (C ₁₀ H ₈ ^{•+} , Naph ⁺) into He gas (a) or He/methanol (M) vapor mixture (b-f) at different pressures (Torr) and temperatures (K) as indicated.	54
Figure 15. van't Hoff plots of the temperature dependence of the equilibrium constants for the association reaction of the naphthalene radical cation with methanol for the first and second solvation steps. The resulting $-\Delta H^\circ$ and $-\Delta S^\circ$ are in (kcal mol ⁻¹) and (cal mol ⁻¹ K ⁻¹) respectively. The error for the measurements are ± 1 kcal mol ⁻¹ for $-\Delta H^\circ$ and ± 2 cal mol ⁻¹ K ⁻¹ for $-\Delta S^\circ$	56
Figure 16. DFT structures and binding energies (ΔE , kcal mol ⁻¹ , calculated using Equation 4.3) of the lowest energy isomers of the lowest energy isomers of the C ₁₀ H ₈ ^{•+} (CH ₃ OH) _{<i>n</i>} clusters (N ^{•+} M _{<i>n</i>}) for <i>n</i> = 1-6 obtained at the B3LYP/6-311++G** level.	57
Figure 17. DFT Structures and binding energies (ΔE , kcal mol ⁻¹ , calculated using Equation 4.3) for higher energy isomers of the C ₁₀ H ₈ ^{•+} (CH ₃ OH) _{<i>n</i>} clusters for <i>n</i> = 2-6 obtained at the B3LYP/6-311++G** level.	59
Figure 18. DFT structures and binding energies of the lowest energy structures of the C ₁₀ H ₇ ^{•+} H ⁺ (CH ₃ OH) _{<i>n</i>} clusters for <i>n</i> = 4-6 as obtained at the B3LYP/6-311++G** level.	62
Figure 19. Mass spectra resulting from the injection of the mass-selected naphthalene radical cations (C ₁₀ H ₈ ^{•+} , Naph ⁺) into He gas (a) or He/ethanol (EtOH) vapor mixture (b-e) at different pressures (Torr) and temperatures (K) as indicated.	64
Figure 20. Mass spectra resulting from the injection of the mass-selected naphthalene radical cations (C ₁₀ H ₈ ^{•+} , Naph ⁺) into He gas (a) or He/1-propanol (1-PrOH) vapor mixture (b-f) at different pressures (Torr) and temperatures (K) as indicated.	66

- Figure 21. Mass spectra resulting from the injection of the mass-selected naphthalene radical cations ($C_{10}H_8^{+\bullet}$, $Naph^+$) into He gas (a) or He/2-propanol (2-PrOH) vapor mixture (b-e) at different pressures (Torr) and temperatures (K) as indicated. 67
- Figure 22. Mass spectra resulting from the injection of the mass-selected naphthalene radical cations ($C_{10}H_8^{+\bullet}$, $Naph^+$) into He gas (a) or He/1-butanol (1-BuOH) vapor mixture (b-e) at different pressures (Torr) and temperatures (K) as indicated. 69
- Figure 23. Mass spectra resulting from the injection of the mass-selected naphthalene radical cations ($C_{10}H_8^{+\bullet}$, $Naph^+$) into He gas (a) or He/2-BuOH (2-BuOH) vapor mixture (b-e) at different pressures (Torr) and temperatures (K) as indicated. 70
- Figure 24.** van't Hoff plots for the temperature dependence of the equilibrium constants of the association reaction of naphthalene radical cation with ethanol (b), 1-propanol (c), 2-propanol (d), 1-butanol (e), and 2-butanol (e) for the first solvation step. The resulting ΔH° and ΔS° are in ($kcal\ mol^{-1}$) and ($cal\ mol^{-1}\ K^{-1}$) respectively. The experimental error for these measurements are $\pm 1\ kcal\ mol^{-1}$ and $\pm 2\ cal\ mol^{-1}\ K^{-1}$. A composite of all plots is shown in (a). 72
- Figure 25. Arrival time distributions (ATDs) of the naphthalene radical cation ($Naph^+$) and the first association product with ethanol, $C_{10}H_8^{+\bullet}(EtOH)$ ($Naph^+(EtOH)$), obtained following the injection of the mass-selected naphthalene radical cation into a He/EtOH vapor mixture at: (a) 243 K, (b) 238 K, and (c) 233 K. Similar ATD overlap suggests the reaction is in equilibrium. 73
- Figure 26. Arrival time distributions (ATDs) of the naphthalene radical cation ($Naph^+$) and the first association product with 1-propanol, $C_{10}H_8^{+\bullet}(1-PrOH)$ ($Naph^+(1-PrOH)$), obtained following the injection of the mass-selected naphthalene radical cation into He/1-PrOH vapor mixture at: (a) 258 K and (b) 263 K. Similar ATD overlap suggests the reaction is in equilibrium. 74
- Figure 27. Arrival time distributions (ATDs) of the naphthalene radical cation ($Naph^+$) and the first association product with 2-propanol, $C_{10}H_8^{+\bullet}(2-PrOH)$ ($Naph^+(2-PrOH)$), obtained following the injection of the mass-selected naphthalene radical cation into He/2-PrOH vapor mixture at: (a) 263 K and (b) 258 K. Similar ATD overlap suggests the reaction is in equilibrium. 75
- Figure 28. DFT structures and binding energies ($\Delta E\ kcal\ mol^{-1}$, calculated according to Equation 4.3) of the lowest energy isomers of the $C_{10}H_8^{+\bullet}(EtOH)_n$ clusters for $n = 1-3$ obtained at the B3LYP/6-311++G** level. 76
- Figure 29. DFT Structures and binding energies (ΔE , $kcal\ mol^{-1}$, calculated according to Equation 4.3) for higher energy isomers of the $C_{10}H_8^{+\bullet}(EtOH)_n$ clusters for $n = 1-3$ obtained at the B3LYP/6-311++G** level. 77
- Figure 30. DFT structures and binding energies ($\Delta E\ kcal\ mol^{-1}$, calculated according to Equation 4.3) of the lowest energy isomers of the $C_{10}H_8^{+\bullet}(1-PrOH)_n$ clusters for $n = 1-3$ obtained at the B3LYP/6-311++G** level. 79

Figure 31. DFT Structures and binding energies (ΔE , kcal mol ⁻¹ , calculated according to Equation 4.3) for higher energy isomers of the C ₁₀ H ₈ ^{•+} (1-PrOH) _n clusters for n = 1-3 obtained at the B3LYP/6-311++G** level.	80
Figure 32. DFT structures and binding energies (ΔE kcal mol ⁻¹ , calculated according to Equation 4.3) of the lowest energy isomers of the C ₁₀ H ₈ ^{•+} (2-PrOH) _n clusters for n = 1-3 obtained at the B3LYP/6-311++G** level.	81
Figure 33. DFT Structures and binding energies (ΔE , kcal mol ⁻¹ , calculated according to Equation 4.3) for higher energy isomers of the C ₁₀ H ₈ ^{•+} (2-PrOH) _n clusters for n = 1-3 obtained at the B3LYP/6-311++G** level.	82
Figure 34. DFT structures and binding energies (ΔE kcal mol ⁻¹ , calculated according to Equation 4.3) of the lowest energy isomers of the C ₁₀ H ₈ ^{•+} (1-BuOH) _n clusters for n = 1-3 obtained at the B3LYP/6-311++G** level.	83
Figure 35. DFT Structures and binding energies (ΔE , kcal mol ⁻¹ , calculated according to Equation 4.3) for higher energy isomers of the C ₁₀ H ₈ ^{•+} (1-BuOH) _n clusters for n = 1-3 obtained at the B3LYP/6-311++G** level.	84
Figure 36. DFT structures and binding energies (ΔE kcal mol ⁻¹ , calculated according to Equation 4.3) of the lowest energy isomers of the C ₁₀ H ₈ ^{•+} (2-BuOH) _n clusters for n = 1-3 obtained at the B3LYP/6-311++G** level.	85
Figure 37. DFT Structures and binding energies (ΔE , kcal mol ⁻¹ , calculated according to Equation 4.3) for higher energy isomers of the C ₁₀ H ₈ ^{•+} (1-BuOH) _n clusters for n = 1-3 obtained at the B3LYP/6-311++G** level.	86
Figure 38. Mass spectra resulting from the injection of the mass-selected naphthalene radical cation (C ₁₀ H ₈ ^{•+} , Naph ⁺) into He gas (a) or He/HCN vapor mixture (b-e) at different pressures (Torr) and decreasing temperatures (K) as indicated.	87
Figure 39. van't Hoff plots for the temperature dependence of the equilibrium constants of the association reaction of naphthalene radical cation with HCN for the first, second, and third solvation steps. The resulting ΔH° and ΔS° are in (kcal mol ⁻¹) and (cal mol ⁻¹ K ⁻¹) respectively. The experimental error for the $-\Delta H^\circ$ and $-\Delta S^\circ$ values are ± 1 kcal mol ⁻¹ and ± 2 cal mol ⁻¹ K ⁻¹ respectively.	89
Figure 40. Arrival time distributions (ATDs) of the naphthalene radical cation (Naph ⁺) and the the first three association products with HCN, C ₁₀ H ₈ ^{•+} (HCN) _n for n = 1-3 (Naph ⁺ (HCN) _n for n = 1-3), obtained following the injection of the mass-selected naphthalene radical cation into the drift cell containing a He/HCN gas mixture at: (a) 263 K, (b) 223 K, and 183. Similar ATD overlap suggests the reaction is in equilibrium.	90
Figure 41. Structures of the four lowest energy isomers of the C ₁₀ H ₈ ^{•+} (HCN) complex obtained used two functionals: M06-2X and ω 97X-D, within the 6-311+G** basis set. The calculated energies ΔE in kcal mol ⁻¹ are given using M06-2X and ω 97X-D (in parenthesis) methods.	92

- Figure 42. Structures of the six lowest energy isomers of the $C_{10}H_8^{++}(HCN)_2$ complex obtained used two functionals: M06-2X and ω 97X-D, within the 6-311+G** basis set. The calculated energies ΔE in kcal mol⁻¹ are given using M06-2X and ω 97X-D (in parenthesis) methods..... 94
- Figure 43. Structures of the two lowest energy isomers of the $C_{10}H_8^{++}(HCN)_n$ clusters for $n = 1-4$ obtained using the B3LYP method within the 6-311++G** basis set. The calculated energies ΔE are given in kcal mol⁻¹. 96
- Figure 44. Mass spectra resulting from the injection of the naphthalene radical cation ($C_{10}H_8^{++}$, Naph⁺) into He gas (a) or He/CH₃CN vapor mixture (b-d) at different pressures (Torr) and decreasing temperatures (K) as indicated. 98
- Figure 45. van't Hoff plots for the temperature dependence of the equilibrium constants of the association reaction of naphthalene radical cation with acetonitrile for the first five solvation steps. The resulting $-\Delta H^\circ$ and $-\Delta S^\circ$ are in (kcal mol⁻¹) and (cal mol⁻¹ K⁻¹) respectively. The experimental error for the $-\Delta H^\circ$ and $-\Delta S^\circ$ values are ± 1 kcal mol⁻¹ and ± 2 cal mol⁻¹ respectively. 100
- Figure 46. Arrival time distributions (ATDs) of the fourth and fifth association products of the naphthalene radical cation with acetonitrile (A), $C_{10}H_8^{++}(CH_3CN)_n$ for $n = 4$ and 5 (Naph⁺(A)_{*n*}, $n = 4, 5$), obtained following the injection of the mass-selected naphthalene radical cation into the drift cell containing He/CH₃CN vapor mixture at: (a) 223 K and (b) 208 K. Similar ATD overlap suggests the reaction is in equilibrium. 101
- Figure 47. Structures of the four lowest energy isomers of the $C_{10}H_8^{++}(CH_3CN)$ complex obtained used two functionals: M06-2X and ω 97X-D, within the 6-311+G** basis set. The calculated energies ΔE in kcal mol⁻¹ are given using M06-2X and ω 97X-D (in parenthesis) methods..... 103
- Figure 48. Structures of the six lowest energy isomers of the $C_{10}H_8^{++}(CH_3CN)_2$ complex obtained used two functionals: M06-2X and ω 97X-D, within the 6-311+G** basis set. The calculated energies ΔE in kcal mol⁻¹ are given using M06-2X and ω 97X-D (in parenthesis) methods..... 104
- Figure 49. Structures of the lowest energy isomers of the $C_{10}H_8^{++}(CH_3CN)_n$ clusters for $n = 1-4$ and the two lowest energy isomers for $n = 5$ and 6 obtained using the B3LYP method within the 6-311++G** basis set. The calculated energies ΔE are given in kcal mol⁻¹ 106
- Figure 50. Mass spectra resulting from the injection of the mass-selected naphthalene radical cation ($C_{10}H_8^{++}$, Naph⁺) into He gas (a) or acetylene (C₂H₂) gas (b-f) at different pressures (Torr) and temperatures (K) as indicated. 114
- Figure 51. van't Hoff plots for the temperature dependence of the equilibrium constants of the association reaction of naphthalene radical cation with acetylene for the first three solvation steps. The resulting ΔH° and ΔS° are in (kcal mol⁻¹) and (cal mol⁻¹ K⁻¹)

respectively. The error for the measurements are $\pm 1 \text{ kcal mol}^{-1}$ for $-\Delta H^\circ$ and $\pm 2 \text{ cal mol}^{-1} \text{ K}^{-1}$ for $-\Delta S^\circ$ 116

Figure 52. Arrival time distributions (ATDs) of the naphthalene radical cation (Naph^+) and the first two association products with acetylene, $\text{C}_{10}\text{H}_8^{*+}(\text{C}_2\text{H}_2)_n$ for $n = 1$ and 2 ($\text{Naph}^+(\text{C}_2\text{H}_2)_n$ for $n = 1$ and 2), obtained following the injection of the mass-selected naphthalene radical cation into C_2H_2 at: (a) 168 K and (b) 138 K. Similar ATD overlap suggests the reaction is in equilibrium. 117

Figure 53. Mass spectra resulting from the injection of the mass-selected naphthalene radical cation ($\text{C}_{10}\text{H}_8^{*+}$, Naph^+) into He gas (a) or ethylene (C_2H_4) gas (b-f) at different pressures (Torr) and temperatures (K) as indicated. 119

Figure 54. Mass spectra resulting from the injection of the mass-selected naphthalene radical cation ($\text{C}_{10}\text{H}_8^{*+}$, Naph^+) into He gas (a) or He/propylene (C_3H_6) gas mixture (b-f) at different pressures (Torr) and temperatures (K) as indicated. 120

Figure 55. Mass spectra resulting from the injection of the mass-selected naphthalene radical cation ($\text{C}_{10}\text{H}_8^{*+}$, Naph^+) into He gas (a) or He/isobutene (C_4H_8) gas mixture (b-f) at different pressures (Torr) and temperatures (K) as indicated. 122

Figure 56. van't Hoff plots for the temperature dependence of the equilibrium constants of the association reaction of naphthalene radical cation with ethylene for the first three solvation steps. The resulting ΔH° and ΔS° are in (kcal mol^{-1}) and ($\text{cal mol}^{-1} \text{ K}^{-1}$) respectively. The error for the measurements are $\pm 1 \text{ kcal mol}^{-1}$ for $-\Delta H^\circ$ and $\pm 2 \text{ cal mol}^{-1} \text{ K}^{-1}$ for $-\Delta S^\circ$ 123

Figure 57. Time profile based on the arrival time distributions (ATDs) of the naphthalene radical cation (Naph^+) and the first three association products with ethylene, $\text{C}_{10}\text{H}_8^{*+}(\text{C}_2\text{H}_4)_n$ for $n = 1-3$ ($\text{Naph}^+(\text{C}_2\text{H}_4)_n$ for $n = 1-3$), obtained following the injection of the mass-selected naphthalene radical cation into He/ C_2H_4 gas mixtures at 113 K. 124

Figure 58. van't Hoff plots for the temperature dependence of the equilibrium constants of the association reaction of naphthalene radical cation with propylene for the first three solvation steps. The resulting ΔH° and ΔS° are in (kcal mol^{-1}) and ($\text{cal mol}^{-1} \text{ K}^{-1}$) respectively. The error for the measurements are $\pm 1 \text{ kcal mol}^{-1}$ for $-\Delta H^\circ$ and $\pm 2 \text{ cal mol}^{-1} \text{ K}^{-1}$ for $-\Delta S^\circ$ 125

Figure 59. Time profile based on the arrival time distributions (ATDs) of the naphthalene radical cation (Naph^+) and the first two association products with propylene, $\text{C}_{10}\text{H}_8^{*+}(\text{C}_3\text{H}_6)_n$ for $n = 1-2$ ($\text{Naph}^+(\text{C}_3\text{H}_6)_n$ for $n = 1-2$), obtained following the injection of the mass-selected naphthalene radical cation into He/ C_3H_6 gas mixtures at 143 K. 126

Figure 60. van't Hoff plot for the temperature dependence of the equilibrium constants of the association reaction of naphthalene radical cation with isobutene for the first step. The resulting ΔH° and ΔS° are in (kcal mol^{-1}) and ($\text{cal mol}^{-1} \text{ K}^{-1}$) respectively. The

error for the measurements are ± 1 kcal mol⁻¹ for $-\Delta H^\circ$ and ± 2 cal mol⁻¹ K⁻¹ for $-\Delta S^\circ$.
..... 127

Figure 61. Time profiles based on the arrival time distributions (ATDs) of the naphthalene radical cation (Naph⁺) and the first association product with isobutene, C₁₀H₈⁺⁺(C₄H₈) (Naph⁺(C₄H₈)), obtained following the injection of the mass-selected naphthalene radical cation into He/C₄H₈ gas mixtures at: (a) 193 K and (b) 173 K..... 127

Figure 62. Mass-spectrum of the ions injected into the drift cell containing 1.0 Torr helium at a temperature of 302 K. The ions are formed by 70 eV EI ionization of the neutral clusters generated by a supersonic beam coexpansion of the binary mixture containing naphthalene (Naph) and benzene (Bz) using helium as a carrier gas. 136

Figure 63. (a) ATDs and (b) t_d versus P/V plot for the naphthalene radical cation homodimer (Naph)₂⁺. All the data are obtained in 4.5 Torr helium at a temperature of 302 K..... 136

Figure 64. Two classes of isomers for the naphthalene radical cation homodimers: (a) stacked parallel and (b) T-shaped. The structures are optimized at the B3LYP/6-311++G** level of theory..... 137

Figure 65. Mass spectra resulting from the injection of the mass-selected naphthalene radical cation (C₁₀H₈⁺⁺, Naph⁺) into the drift cell containing He gas (a) or He/benzene (C₆D₆) vapor mixture (b-e) at different temperatures and pressures as indicated. . 139

Figure 66. Mass spectra resulting from the injection of the mass-selected naphthalene radical cation (C₁₀H₈⁺⁺, Naph⁺) into the drift cell containing He gas (a) or He/benzene (C₆H₆) vapor mixture (b-f) at different temperatures and pressures as indicated... 141

Figure 67. van't Hoff plots for the formation of C₁₀H₈⁺⁺(C₆H₆) (a) and C₁₀H₈⁺⁺(C₆D₆) (b) heterodimer cations. Error estimates are ± 1 kcal mol⁻¹ and ± 2 cal mol⁻¹ K⁻¹ for ΔH° and ΔS° respectively..... 142

Figure 68. Arrival time distributions (ATDs) of the naphthalene radical cation (Naph⁺) and the naphthalene⁺(benzene) heterodimer, C₁₀H₈⁺⁺(C₆D₆) (Naph⁺(C₆D₆)), obtained following the injection of the mass-selected naphthalene radical cation into a He/C₆D₆ vapor mixture at: (a) 253 K and (b) 228 K. Similar ATD overlap suggests the reaction is in equilibrium. 143

Figure 69. DFT structures and binding energies (ΔE , kcal mol⁻¹) of the three classes of isomers for the naphthalene⁺(benzene) heterodimer: (a) stacked parallel, (b) V-shaped, (c) T-shaped calculated using the M11/cc-pVTZ where the lowest energy isomer is depicted. 144

Figure 70. DFT structures for the three classes of isomers for the naphthalene⁺⁺(benzene)₂ heterotrimer: (a) sandwich, (b) slanted U-shaped, (c) stacked parallel calculated using the M11/cc-pVTZ where the lowest energy isomer is depicted. 145

- Figure 71. (a) ATDs and (b) t_d versus P/V plot for the naphthalene^{•+}(benzene) heterodimer (Naph•Bz)⁺. All the data are obtained in 4.5 Torr helium at a temperature of 302 K. 147
- Figure 72. Mass spectra resulting from the injection of the mass-selected naphthalene radical cation (C₁₀H₈^{•+}, Naph^{•+}) into the drift cell containing He gas (a) or He/pyridine (Pyr) vapor mixture (b-f) at increasing temperatures and pressures as indicated. ... 151
- Figure 73. Mass spectra resulting from the injection of the mass-selected naphthalene radical cation (C₁₀H₈^{•+}, Naph^{•+}) into the drift cell containing He gas (a) or He/pyridine (Pyr) vapor mixture (b-f) at decreasing temperatures and pressures as indicated. . 152
- Figure 74. van't Hoff plots for the temperature dependence of the equilibrium constants of the association reaction of naphthalene radical cation with pyridine for the first four solvation steps. The resulting ΔH° and ΔS° are in (kcal mol⁻¹) and (cal mol⁻¹ K⁻¹) respectively. The error for the measurements are ± 1 kcal mol⁻¹ for $-\Delta H^\circ$ and ± 2 cal mol⁻¹ K⁻¹ for $-\Delta S^\circ$ 154
- Figure 75. Time profile based on the arrival time distributions (ATDs) of the naphthalene radical cation (Naph^{•+}); the naphthalene^{•+}(pyridine) heterodimer, C₁₀H₈^{•+}(C₅H₅N) (Naph^{•+}(Pyr)); and the protonated pyridine dimer, H⁺(C₅H₅N) (written as (Pyr)⁺₂) obtained following the injection of the mass-selected naphthalene radical cation into He/C₅H₅N vapor mixtures at 400 K. 155
- Figure 76. Arrival time distributions (ATDs) of the naphthalene^{•+}(pyridine) heterodimer, C₁₀H₈^{•+}(C₅H₅N) (Naph^{•+}(Pyr)), and the second association product, C₁₀H₈^{•+}(C₅H₅N)₂ (Naph^{•+}(Pyr)₂), obtained following the injection of the mass-selected naphthalene radical cation into He/C₅H₅N vapor mixture at: (a) 273 K, (b) 258 K, and 243 K. Similar ATD overlap suggests the reaction is in equilibrium. 156
- Figure 77. Mass spectra of the products of the coexpansion of a mixture of naphthalene and pyridine into the drift cell containing helium at the temperatures and pressures indicated. The ions are formed by 70 eV EI ionization and He was used as as carrier gas. 157
- Figure 78. (a) ATDs and (b) t_d versus P/V plot for the naphthalene^{•+}(pyridine) heterodimer. All data are obtained in 2.2 Torr He at a temperature of 302 K. 158
- Figure 79. DFT structures and binding energies (ΔE , kcal mol⁻¹) of four isomers for the naphthalene^{•+}(pyridine) heterodimer: (a) covalent structure 1 (C1), (b) covalent structure 2 (C2), (c) stacked parallel, and (d) T-shaped calculated at the M06-2X/cc-pVTZ level of theory. 160
- Figure 80. AIMD structures and binding energies (ΔE , kcal mol⁻¹) of four low energy isomers for the naphthalene^{•+}(pyridine)₂ heterotrimer using the two low energy covalent structures of the naphthalene^{•+}(pyridine) heterodimer (C1 or C2) as a starting point with the second pyridine molecule binding to the same side (SS) or opposite side (OS): (a) C1/OS, (b) C1/SS, (c) C2/OS, and (d) C2/SS 163

- Figure 81. Mass spectra resulting from the injection of the mass-selected phenyl cation ($C_6H_5^+$, Ph^+) into He gas at different pressures and temperatures as indicated. 172
- Figure 82. Mass spectra resulting from the injection of the mass-selected phenyl cation ($C_6H_5^+$, Ph^+) into He gas (a) or He/water (W) vapor mixture (b-e) at different pressures (Torr) and increasing temperatures (K) as indicated. 174
- Figure 83. Mass spectra resulting from the injection of the mass-selected phenyl cation ($C_6H_5^+$, Ph^+) into He gas (a) or He/water (W) vapor mixture (b-e) at different pressures (Torr) and decreasing temperatures (K) as indicated. 175
- Figure 84 van't Hoff plots for the temperature dependence of the equilibrium constants of the association reaction of phenyl cation with water where (a) shows the first hydration product and the presence of two separate species and (b) shows the second and third hydration products. The resulting $-\Delta H^\circ$ and $-\Delta S^\circ$ are in ($kcal\ mol^{-1}$) and ($cal\ mol^{-1}\ K^{-1}$) respectively. The experimental error for these measurements are $\pm 1\ kcal\ mol^{-1}$ and $\pm 2\ cal\ mol^{-1}\ K^{-1}$ 178
- Figure 85. DFT Structures and binding energies (ΔE , $kcal\ mol^{-1}$) for (a) the formation of the covalent protonated phenol cation ($C_6H_5OH_2^+$) and (b) the addition of a water to the phenyl cation at the (i) *ortho* and (ii) *para* positions, represented as $C_6H_5^+(H_2O)$. Both sets are obtained at the B3LYP/6-311++G** level. 179
- Figure 86. DFT Structures and binding energies (ΔE , $kcal\ mol^{-1}$) for (a) addition of a water molecule to the covalent protonated phenol and (b) the addition of a water to the hydrated phenyl cation. Both sets are obtained at the B3LYP/6-311++G** level. 180
- Figure 87. DFT Structures and binding energies (ΔE , $kcal\ mol^{-1}$) for (a) addition of a second water molecule to the covalent protonated phenol and (b) the addition of a third water to phenyl cation. Both sets are obtained at the B3LYP/6-311++G** level. 182
- Figure 88. DFT Structures and binding energies (ΔE , $kcal\ mol^{-1}$) for (a) addition of a third water molecule to the covalent protonated phenol and (b) the addition of a fourth water to phenyl cation. Both sets are obtained at the B3LYP/6-311++G** level. 183
- Figure 89. Mass spectra resulting from the injection of the mass-selected phenyl cation ($C_6H_5^+$, Ph^+) into He gas (a) or He/methanol (M) vapor mixture (b-e) at different pressures (Torr) and increasing temperatures (K) as indicated. 185
- Figure 90. Mass spectra resulting from the injection of the mass-selected phenyl cation ($C_6H_5^+$, Ph^+) into He gas (a) or He/methanol (M) vapor mixture (b-e) at different pressures (Torr) and decreasing temperatures (K) as indicated. 186
- Figure 91. Mass spectra resulting from the injection of the mass-selected phenyl cations ($C_6H_5^+$, Ph^+) into He gas (a) or He/HCN gas mixture (b-f) at different pressures (Torr) and increasing temperatures (K) as indicated. 188

- Figure 92. Mass spectra resulting from the injection of the mass-selected phenyl cations ($C_6H_5^+$, Ph^+) into He gas (a) or He/HCN gas mixture (b-f) at different pressures (Torr) and decreasing temperatures (K) as indicated..... 189
- Figure 93. van't Hoff plot for the temperature dependence of the equilibrium constants of the association reaction of phenyl cation with HCN for the second, third, and fourth solvation products. The resulting $-\Delta H^\circ$ and $-\Delta S^\circ$ are in ($kcal\ mol^{-1}$) and ($cal\ mol^{-1}\ K^{-1}$) respectively. The experimental error for these measurements are $\pm 1\ kcal\ mol^{-1}$ and $\pm 2\ cal\ mol^{-1}\ K^{-1}$ 191
- Figure 94. Mass spectra resulting from the injection of the mass-selected phenyl cation ($C_6H_5^+$, Ph^+) into He gas (a) or He/acetonitrile (CH_3CN , A) gas mixture (b-f) at different pressures (Torr) and increasing temperatures (K) as indicated..... 193
- Figure 95. Mass spectra resulting from the injection of the mass-selected phenyl cation ($C_6H_5^+$, Ph^+) into He gas (a) or He/acetonitrile (CH_3CN , A) gas mixture (b-e) at different pressures (Torr) and decreasing temperatures (K) as indicated. 194
- Figure 96. van't Hoff plot for the temperature dependence of the equilibrium constants of the association reaction of phenyl cation with acetonitrile for the second, third, and fourth solvation products. The resulting $-\Delta H^\circ$ and $-\Delta S^\circ$ are in ($kcal\ mol^{-1}$) and ($cal\ mol^{-1}\ K^{-1}$) respectively. The experimental error for these measurements are $\pm 1\ kcal\ mol^{-1}$ and $\pm 2\ cal\ mol^{-1}\ K^{-1}$ 196
- Figure 97. Arrival time distributions (ATDs) of the first four association products of the phenyl cation with acetonitrile (A), $C_6H_5^+(CH_3CN)_n$ for $n = 1-4$ ($Ph^+(A)_n$ $n = 1-4$), obtained following the injection of the mass-selected phenyl cation into He/ CH_3CN vapor mixtures at: (a) 290 K, (b) 273 K, and (c) 233 K. Similar ATD overlap suggests the reaction is in equilibrium. 197
- Figure 98. Summary of structures and binding energy (measured using $-\Delta H^\circ$ with an experimental error of $\pm 1\ kcal\ mol^{-1}$) for the first association product of the solvation of the naphthalene radical cation by various neutral molecules. Three classes are studied: (1) polar molecules (H_2O , CH_3OH , HCN , and CH_3CN are shown), (2) unsaturated organic molecules (an estimate for C_2H_2 is shown), and (3) aromatic molecules (C_6H_6 and C_5H_5N are shown). The structures were calculated at B3LYP/6-311++G** level for the polar molecules, M11/cc-pVTZ level for C_6H_6 , and M06-2X/cc-pVTZ level for C_5H_5N 203

List of Tables

- Table 1. Experimental thermochemistry (ΔH° and ΔS°)^a for the formation of $C_{10}H_8^{++}(H_2O)$ and $C_{10}H_8^{++}(D_2O)$ clusters and the calculated binding energies (ΔE , corrected ZPVE) and enthalpies ($-\Delta H$ calc) at the B3LYP/6-311++G** (ΔE and $-\Delta H$ calc) and M06-2X/6-311++G** (ΔE only) levels of $C_{10}H_8^{++}(H_2O)_n$ for $n = 1-6$ 47
- Table 2. Experimental thermochemistry (ΔH° and ΔS°)^a of the formation of $C_{10}H_8^{++}(CH_3OH)_n$ clusters for $n = 1-2$ and the calculated binding energies (ΔE , corrected ZPVE) at the B3LYP/6-311++G** (ΔE and ΔH) and M06-2X/6-311++G** levels (ΔE only) for $C_{10}H_8^{++}(CH_3OH)_n$ cluster for $n = 1-6$ 58
- Table 3. Measured thermochemistry ($-\Delta H^\circ$ and $-\Delta S^\circ$)^a of the formation of $C_{10}H_8^{++}(ROH)$ clusters for R = Et, 1-Pr, 2-Pr, 1-Bu, and 2-Bu and the calculated binding energies (ΔE), enthalpies ($-\Delta H$), and Gibbs Free Energies (ΔG) at the B3LYP/6-311++G** level for the lowest energy isomers of $C_{10}H_8^{++}(ROH)_n$ cluster for R = Et, 1-Pr, 2-Pr, 1-Bu, and 2-Bu and $n = 1-3$ 73
- Table 4.** Measured thermochemistry ($-\Delta H^\circ$ and $-\Delta S^\circ$)^a of the formation of $C_{10}H_8^{++}(HCN)_n$ clusters for $n = 1-3$ and the calculated binding energies (ΔE , corrected ZPVE) and enthalpies ($-\Delta H$ calc) at the B3LYP/6-311++G** (ΔE and $-\Delta H$ calc), M06-2X/6-311+G**, and ω 97X-D/6-311+G** levels for $C_{10}H_8^{++}(H_2O)_n$ cluster for $n= 1-4$. .. 89
- Table 5. Measured thermochemistry ($-\Delta H^\circ$ and $-\Delta S^\circ$)^a of the formation of $C_{10}H_8^{++}(CH_3CN)_n$ clusters for $n = 1-5$ and the calculated binding energies (ΔE , corrected ZPVE), enthalpies ($-\Delta H$ calc), and Gibbs free energies (ΔG calc) at the B3LYP/6-311++G**, M06-2X/6-311+G**, and ω 97X-D/6-311+G** levels for $C_{10}H_8^{++}(CH_3CN)_n$ cluster for $n = 1-6$ 99
- Table 6. Summary of measured $-\Delta H^\circ$ (kcal mol⁻¹) of the association of small polar molecules with naphthalene radical cation to form $C_{10}H_8^{++}(B)_n$ clusters where B is the small polar molecule indicated. Estimated error for $-\Delta H^\circ$ is ± 1 kcal mol⁻¹. The enthalpy of vaporization (ΔH_{vap} , kcal mol⁻¹) and dipole moments (in Debye) for these molecules are also shown.² 109
- Table 7.** Measured thermochemistry ($-\Delta H^\circ$ and $-\Delta S^\circ$)^a of the formation of $C_{10}H_8^{++}(C_2H_2)_n$ clusters for $n = 1-3$ as well as reference values for $C_6H_6^{++}(C_2H_2)_n$ ¹⁰⁸ clusters for $n = 1-4$ 115
- Table 8. Measured thermochemistry ($-\Delta H^\circ$ and $-\Delta S^\circ$)^a of the formation of $C_{10}H_8^{++}(C_mH_{2m})_n$ clusters for ethylene ($m = 2, n = 1-3$), propylene ($m = 3, n = 1-3$), and isobutene ($m = 4, n = 1$). 128
- Table 9. Experimental-based collision cross sections of naphthalene radical cation homodimers in helium at different temperatures and pressures as indicated. The calculated cross sections obtained from the trajectory method¹²⁵ for the stacked

parallel and T-shaped structures optimized at the B3LYP/6-311++G** level of theory. ¹³⁰ The boldface values represent the best agreement between experimental and calculated cross sections.	138
Table 10. Experimental-based collision cross sections of naphthalene ⁺ (benzene) heterodimer in helium at different temperatures and pressures as indicated. The calculated cross sections obtained from the trajectory method ¹²⁵ for the stacked parallel and T-shaped structures optimized at the B3LYP/6-311++G** level of theory. ¹³⁰ The boldface values represent the best agreement between experimental and calculated cross sections. Structures shown are calculated using M11/cc-pVTZ...	148
Table 11. Measured thermochemistry ($-\Delta H^\circ$ and $-\Delta S^\circ$) ^a of the formation of $C_{10}H_8^{*+}(C_5H_5N)_n$ clusters for $n = 1-4$	153
Table 12. Experimental-based collision cross sections of the naphthalene ⁺ (pyridine) heterodimer in helium at different temperatures as indicated. The calculated cross sections obtained from the trajectory method ¹²⁵ for two covalent (C1 and C2), stacked parallel, and T-shaped structures optimized at M06-2X/cc-pVTZ level of theory. The bold face values represent the best agreement between the experimental and calculated cross sections.	159
Table 13. Measured thermochemistry ($-\Delta H^\circ$ and $-\Delta S^\circ$) ^a for the stepwise hydration of $C_6H_5^+(H_2O)_n$ clusters for $n = 2-4$	177
Table 14. Summary of the measured thermochemistry ($-\Delta H^\circ$ and $-\Delta S^\circ$) for the formation of the first association product of the solvation of naphthalene radical cation ($C_{10}H_8^{*+}$) with neutral molecules (B) as indicated the calculated binding energies (ΔE , corrected ZPVE) and calulather enthalpies at either the B3LYP/6-311++G** ^a , M11/cc-pVTZ ^b , or M06-2X/cc-pVTZ ^c levels of theory for $C_{10}H_8^{*+}(B)$ clusters. The experimental error for these measurements are ± 1 kcal mol ⁻¹ and ± 2 cal mol ⁻¹ K ⁻¹ for $-\Delta H^\circ$ and $-\Delta S^\circ$ respectively.	201

Abstract

INTERACTIONS OF THE NAPHTHALENE RADICAL CATION WITH UNSATURATED MOLECULES IN THE GAS PHASE

Sean Patrick Platt

A dissertation in partial fulfillment of the requirements for the degree of Doctor of Philosophy at
Virginia Commonwealth University

Virginia Commonwealth University, 2016

Director: M. SAMY EL-SHALL

Professor, Department of Chemistry

Characterizing the interactions of solvent molecules with ions is fundamental in understanding the thermodynamics of solution chemistry. These interactions are difficult to observe directly in solution because the number of solvent molecules far exceed that of ions. This lend the gas phase to be the ideal medium in the study ion-solvent interactions on a molecular level. Ionized polycyclic aromatic hydrocarbon (PAH) molecules can readily form hydrogen bonds with neutral solvent molecules in aqueous and interstellar medium. Previous research has been done for stepwise solvation of small molecules such as benzene⁺, pyridine, and phenylacetylene. The similarity in these results show that these organic ions can be considered prototypical model

systems for aromatic ion-neutral solvent interactions. The goal of this dissertation is to demonstrate that naphthalene can act as a prototypical model of PAH ions for ion-solvent interactions.

Two types of experiments are considered throughout this dissertation using ion mobility mass spectrometry: (1) ion-neutral equilibrium thermochemistry and (2) mobility measurements. For thermochemistry experiments, the naphthalene radical cation was injected into the drift cell containing helium and/or neutral solvent vapor and the enthalpy and entropy changes were measured by varying the drift cell temperature and measuring the equilibrium constants. The results of these studies showed that small polar molecules bind to naphthalene with similar energy based on the measured by the enthalpy changes. Unsaturated aliphatic molecules behave similarly, but with much lower binding energy. Aromatic ions tend to bind to the naphthalene with lower binding energy than that observed with the benzene ion. The results for small polar molecules were compared to similar studies using the phenyl cation. The second series of experiments required the coexpansion of the naphthalene and benzene or pyridine. Injecting these dimers into the drift cell allowed the measurement of reduced mobility on the dimers at a series of temperatures. These were used to calculate the average collision cross section and thus give insight in to the structure of these aromatic dimers. Structures were determined by comparing these results to those predicted by DFT calculations.

Chapter 1: Introduction and Overview

The characterization of the interactions between ions and solvent molecules is key to understanding the thermodynamics of solution chemistry. The results of ion-equilibria measurements in solution are in the form of acid-base dissociation constants, stability constants of ion-ligand complexes, and other variables that are key information to chemists.^{1,2} Direct observation of the interactions between an individual ion and a solvent molecule is difficult or impossible since the number of solvent molecules far outnumber that of ions in solution. Therefore, the gas phase lends itself to be the ideal medium to study these systems on a molecular level through the direct observation of the interactions between a central ion and the first and second solvation layers.³⁻⁵ Gas phase ion equilibrium measurements were first introduced in the 1960s by P. Kebarle and his associates and have expanded rapidly becoming critical sources of thermochemical information for ions.^{3,4,6-13} When investigating an ion's structure, energetics, or reactivity with a solvent or third body molecule in the gas phase, mass spectrometry has been shown to be one of the most useful and accurate techniques available.¹⁴ These methods are aided by studying the properties of the clusters that are formed with neutral molecules around a central ion.

Clusters are assemblies of atoms and molecules that are sometimes attached to ions and have properties that lie between gas and bulk condensed phases.^{15,16} This would mean that the study of cluster ions offers a way to bridge the gap between the gas phase and condensed phase through the understanding and quantifying solvent effects within a cluster.^{14,17} The solvation factors of ion clusters have been analyzed using gas phase data.^{3,4,18} Since the amount of solvent molecules present can be readily controlled in the gas phase, the dependence of the solvent on the physical and chemical of an ion can be easily followed through the stepwise solvation of the ion.

To aid in the study of clusters formed from van der Waals interactions, metals, or fullerenes, supersonic molecular beams are used.^{1,19-23} In the gas phase, these beams are formed via supersonic adiabatic expansion and allow molecular level studies that are used to model macroscopic interactions.^{6,23-25} Cold clusters formed in the gas phase help to identify various low energy configurations of solute/ion-(solvent)_n systems including hydrogen bonding complexes where the lowest energy isomer maximizes the hydrogen bonding interactions.^{23,26,27}

Early methods for measuring the thermochemical data of ion-molecule clustering reactions involved the use of pulsed high-pressure mass spectrometry (PHPMS).³ An ion mobility drift cell setup, commonly called “ion mobility mass spectrometry” (IMMS), is more desirable than these high pressure techniques because the ions are generated outside of the drift cell and are completely thermalized before entering the drift cell.^{3,4,28,29} Determination of different structural isomers is also possible when using drift time ion mobility spectroscopy because the collision cross sections are different despite having the same mass-to-charge ratio (*m/z* ratio).²¹ The resolution of such techniques has allowed for separation of isomers where the arrival times and collision cross sections have a difference of less than 1%.³⁰ Ion mobility is also used to analyze a variety of chemical species including explosives, drugs, and chemical warfare agents in ambient conditions.^{31,32} Ion mobility instruments have become widespread, portable, and fully automated for commercial use in public spaces like security gates in airports.³³

The collisions that occur with a third body or buffer gas also allow IMMS to probe the molecular interactions and energy transfer reactions that occur within the drift cell.^{29,34} One of the most popular studies using this technique involves investigating ion-molecule interactions since the solvent effect would not be present in the gas phase.^{3,4,7,35} This is achieved by mass-selecting the ion of interest based on its *m/z* ratio using a mass filter and injecting the selected ion into a

neutral gas within the drift cell. After exiting the cell, the resulting products are determined with a second mass filter. This makes it possible to measure the thermochemistry of ion-molecule reactions through the observation of successive equilibrium steps. In addition to the thermodynamics of these ion-molecule reactions, the kinetics can be determined if the reactions are irreversible or fast enough to occur within the time the ions spend in the drift cell (also called the “drift time”) through the determination of rate constants.^{7,17}

Polycyclic aromatic hydrocarbon (PAH) molecules are of interest because they are considered the most abundant free interstellar organic molecules.^{36,37} PAHs and PANHs (polycyclic aromatic nitrogen containing hydrocarbons) have been detected in interstellar medium and are believed to be the reason for unidentified IR bands and are intermediated in soot formation processes.³⁸⁻⁴⁰ Solar nebulae are diverse in nature and are thus suitable for rich organic chemistry that can result in the formation of PAH molecules.⁴¹⁻⁴³ Protoplanetary disks (PPDs) are a diverse environment where variations in temperature, density, ionization rate, and UV/X-ray intensities allow the formation of simple molecules to occur in the gas phase and complex organic materials to form on the surface of dust grains.⁴²⁻⁴⁵ In space environments such as interstellar media and solar nebulae, PAH molecules are assumed to typically be in ionized states because of their low ionization energies and high proton affinities.^{44,46-51} The ionized PAH molecules are in turn reactive in condensation and cluster formation processes where increasingly more complex organic molecules and aggregates are formed. This occurs when interstellar molecules such as water, methanol, hydrogen cyanide, and acetonitrile cluster with PAH ions to form of large hydrogen-bonded networks around or on the surface of the PAH. This makes the PAH ion act as a nucleation center for the formation of organic-doped icy grains. These doped icy grains when exposed to

interstellar UV radiation can go on to form complex organics such as the components necessary for membrane formation.⁵²⁻⁵⁷

Naphthalene ($C_{10}H_8$) is the simplest polycyclic aromatic hydrocarbon (PAH) and the solvation and thermochemistry with interstellar molecules are of interest. Understanding these interactions allow for extrapolation to larger PAH molecules. The electronic transitions of naphthalene radical cation have been assigned to new diffuse interstellar band (DIBs) based on complementary experimental measurements. This discovery has been the impetus for several experimental and theoretical studies of structures, spectroscopy and reactions of the ion.⁵⁸⁻⁶³

The understanding of hydrogen bonding interactions with ionized aromatic molecules is vital in both aqueous solvents and astrochemical environments.^{35,64} These interactions are seen in many biological, chemical, and astrochemical processes including the conformation and folding of proteins, base pair stacking in DNA, drug design, macromolecular assemblies, molecular recognition, clathrate hydrate formation, and the formation of complex organics and ices in interstellar space.^{53,64-68} A special type of hydrogen bonding interactions called “ionic hydrogen bonds” (IHBs) involves hydrogen bonding between radical ions or protonated molecules with neutral polar molecules such as water, methanol, hydrogen cyanide, and acetonitrile.^{5,67} IHBs are typically stronger than conventional hydrogen bonds in neutral systems with bond strengths up to 35 kcal mol^{-1} , which is about a third the strength of typical covalent bonds.⁶⁴ Unconventional carbon-based IHBs are formed when the hydrogen donors are ionized hydrocarbons containing CH groups and the hydrogen acceptors are electron lone pairs on heteroatoms such as O and N or π electrons in olefin double bonds and aromatic systems.⁶⁴ Carbon based $CH^{\delta+} \cdots O$ IHBs are seen in the hydration of benzene ($C_6H_6^{*+}$), cyclic $C_3H_3^+$, cyclobutadiene ($C_4H_4^{*+}$), phenylacetylene ($C_8H_6^{*+}$), and naphthalene ($C_{10}H_8^{*+}$).^{9,10,28,35,56,69} Organic ions can also interact with water to form

stronger conventional hydrogen bonds, where an example of this is found in the protonated $C_5H_5N^+(H_2O)$ complex where the $NH^{\delta+}\cdots O$ hydrogen bond that is formed stabilizes the resulting distonic structure.⁸ The results of these studies act as prototypical models for hydrophobic hydration in the condensed phase.⁷⁰ When discussing the formation of simple alcohols in space, the hydration of $C_2H_2^+$ can serve as the prototypical model.⁷¹

In addition to water, other polar molecules containing lone pairs of electrons including methanol, hydrogen cyanide, and acetonitrile can participate in hydrogen bonding interactions with the $CH^{\delta+}$ hydrogen atoms of the ring of ionized aromatics. Hydrogen cyanide (HCN) is useful for the observations of non-covalent interactions because it is highly polar with a dipole moment of 2.98 D and can serve as a hydrogen bond donor and as a lone-pair hydrogen acceptor in hydrogen bonds.^{2,64} Terrestrially, HCN is of particular interest because of its role in atmospheric chemistry due to biomass burning, but it is also a major molecule present in interstellar medium and solar nebulae.⁷²⁻⁷⁴ In space, HCN can be produced from reactions of ammonia and methane and polymers of this molecule are observed in comets, planets, moons, and circumstellar envelopes.^{75,76} HCN is believed to be the source of nitrogen in the formation of nitrogen-containing PANHs. These PANH molecules are the starting points for biologically significant molecules like DNA, RNA, and proteins in space. By studying reactions involving HCN, insights to the origins of life can be better understood.⁷⁵⁻⁷⁸

To supplement the experimental data, molecular computational techniques aid in understanding the structures of the resulting products of ion-neutral interactions.⁷⁹⁻⁸² Advances in computational techniques and advanced *ab-initio* and DFT electronic calculations have become essential tools in explaining experimental results.^{83,84} These calculations are time-independent and in addition to structures, reaction enthalpies and binding energies can be calculated for the

hydrogen bonded complexes.^{23,85} Solvent-solvent interactions and the impact of the solvent on the activation energy barriers can also be calculated.^{7,11,86}

This dissertation is divided into three major sections: (1) introduction and overview, (2) studies of the association of various unsaturated molecules with the naphthalene radical cation, and (3) comparison of the observed naphthalene radical cation/neutral molecule interactions to interactions of similar neutral molecules with the phenyl cation. The first section includes Chapters 1-3 which includes general overview (Chapter 1) and introduces the experimental setup used (Chapter 2) and measurements obtained (Chapter 3) throughout the remainder of this dissertation. The second section includes the experimental and theoretical work of the association of various unsaturated molecules with the naphthalene radical cation. Chapter 4 covers interactions of a variety of polar molecules including: water, methanol, ethanol, 1-propanol, 2-propanol, 1-butanol, 2-butanol, HCN, and acetonitrile. The experimental thermochemical data for unsaturated aliphatic molecules (acetylene, ethylene, propylene, and isobutene) are discussed in Chapter 5. The final chapter involving the naphthalene radical cation (Chapter 6) shows the structures and binding energies of the naphthalene radical cation with the monocyclic aromatic compounds benzene and pyridine. The third and final section of this dissertation uses the results discussed in Chapter 4 and compares the interactions of other aromatic ions with small polar molecules. The interactions of water, methanol, HCN, and acetonitrile with the phenyl cation are discussed in Chapter 7 these results are compared to similar systems with the naphthalene radical cation discussed in Chapter 4.

Chapter 2: Experimental Setup

2.1. Experimental System Overview

All experiments were conducted using the Virginia Commonwealth University quadrupole mass-selected ion mobility quadrupole mass spectrometer (QMS-IM-QMS). This system consists of four stainless steel chambers with breakdowns of components shown in Figure 1 and a simplified diagram is shown in Figure 2.⁸⁷ The breakdown of these chambers are: expansion, ionization, reaction, and detection chambers respectively.

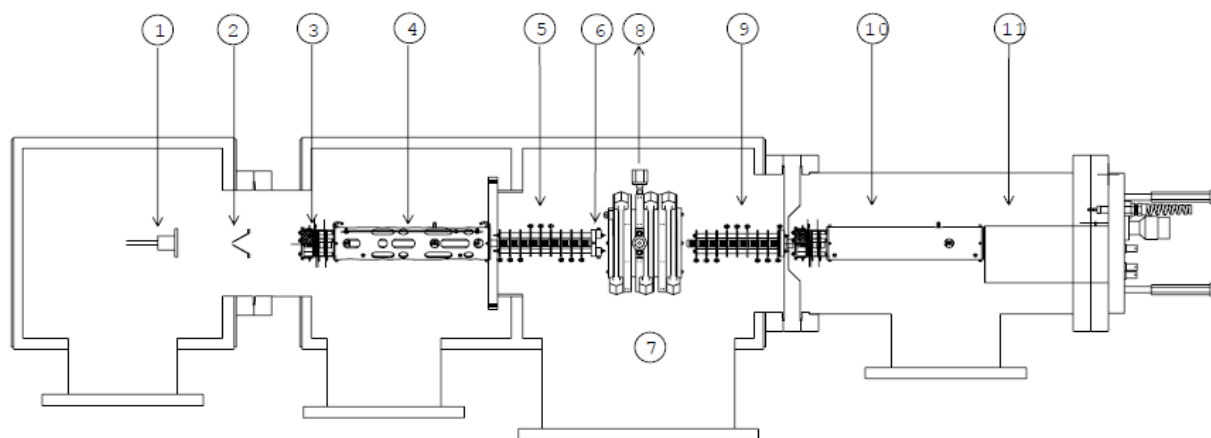


Figure 1. Schematic diagram of the VCU QMS-IM-QMS system. The labels above are: (1) pulsed nozzle, (2) 3 mm skimmer cone, (3) electron-impact ionizer, (4) quadrupole mass filter, (5) ion transport lens stack 1 (Einzel lenses 1, 2, and 3), (6) steering lenses (also act as the ion gate), (7) drift cell, (8) baratron line, (9) ion transport lens stack 2 (Einzel lenses 4, 5, and 6), (10) quadrupole mass filter, (11) detector housing (contains electron multiplier).

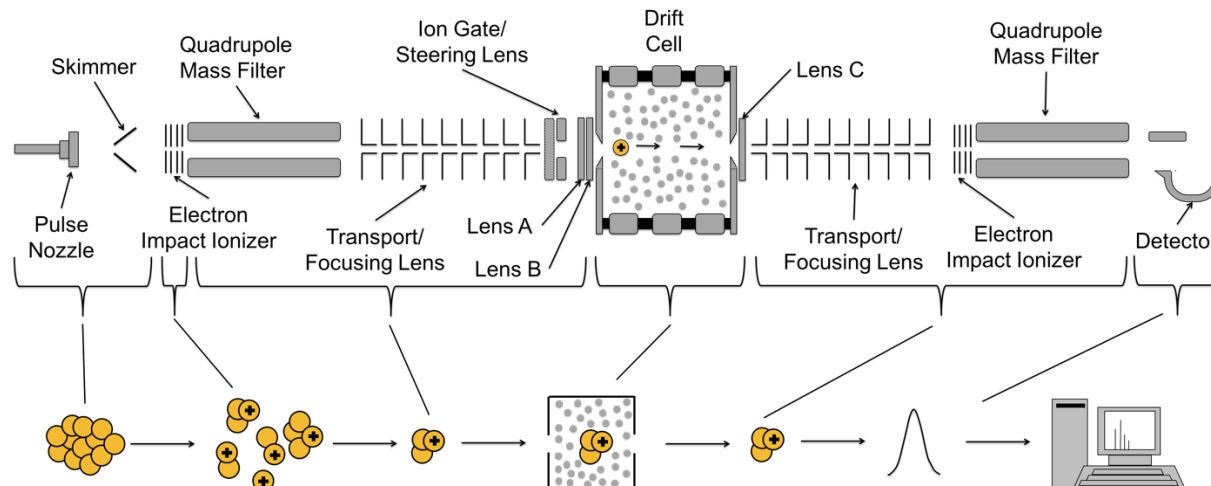


Figure 2. General diagram for the experimental setup of the VCU QMS-IM-QMS system.⁸⁷

The first chamber is the expansion chamber where neutral clusters are formed via supersonic adiabatic expansion. The contents of the chamber include a Parker Series 9 pulse valve (28 VDC) containing a VESPEL poppet and mounted on a stainless steel tube. The pulse valve is fitted with a No. 20 driver body which has a 0.5 mm orifice. In addition, the chamber contains a 3 mm aluminum canonical skimmer cone which allows differential pumping and vacuum isolation from the second chamber.

The second chamber is the ionization chamber and contains an Extrel electron impact ionizer assembly (1 in stainless steel, part No. 812447) and co-axial quadrupole mass filter (Extrel, part No. 813685). The chamber is isolated from the third chamber through differential pumping using a mass filter isolation kit (part No. 814338).

The third chamber is the reaction chamber and contains the drift cell (Extrel, part No. 814336) with two lenses attached to the drift cell body (Lenses A and B) and one on the drift cell end cap (Lens C). The ion beam is focused into the drift cell using a series of transport and focusing lenses (Einzel Lenses 1-3, Extrel, part No. 814312) with a set of steering lenses that guide the

beam into the drift cell. A second stack of transport and focusing lenses (Einzel Lenses 4-6, Extrel, part No. 814312) is found after the drift cell guiding the beam into the forth chamber.

The forth chamber is the detection chamber and houses a second electron impact ionizer assembly (Extrel, part No. 812447) and quadrupole (Extrel 400 with mass filter). These components are attached to a multiplier isolation kit (Extrel, part No. 814275) containing an off-axis collision dynode and electron multiplier (DeTech Inc., part No. J208-AB).

Further details of the VCU QMS-IM-QMS system will be explained in detail in subsequent sections.

2.2. Vacuum System

Vacuum for each chamber of the system is obtained via a diffusion pump that is backed by a mechanical pump. The pressure of each chamber is measured individually by separate Bayard-Alpert Pyrex iridium ion gauges (Scientific Instrument Services, G75P) with each connected to a vacuum gauge controller (Granville-Phillips, Model 307).

The first chamber is the expansion chamber where neutral clusters are formed via supersonic adiabatic expansion. Vacuum for the chamber is achieved using a Varian VHS-6 diffusion pump filled with 250 mL of Dow Corning 705 oil and has a pumping speed of 2400 L sec⁻¹ (in air and He). This pump is backed by an Edwards E2M28 mechanical pump filled with mechanical pump fluid 19. This mechanical pump has a pumping speed of 9.2 L sec⁻¹. When the nozzle is not pulsing, the pressure in the chamber is typically 10⁻⁷ to 10⁻⁶ Torr. Under typical operation, the chamber pressure is roughly 10⁻⁵ to 10⁻⁴ Torr.

The second chamber is the ionization and selection chamber where neutral clusters are ionized and selected based on its m/z ratio. An Edwards DiffStak 160/700M diffusion pump filled with 250 mL of Santovac 7 oil with a pumping speed of 700 L sec⁻¹ (using N₂ as a standard) is

used for vacuum. Backing is achieved by an Edwards E2M40 two-stage mechanical pump filled with roughly 4 L of Edwards Ultragrade 70 oil with a pumping speed of 10.2 L sec^{-1} . Typical background pressure is 10^{-8} to 10^{-7} Torr while during the experiment, the pressures are typically 10^{-6} to 10^{-5} Torr.

The third chamber is the reaction chamber with vacuum achieved using an Edwards DiffStak 250/2000M diffusion pumped filled with 500 mL of Santovac 7 oil. The pumping speed of the diffusion pump is 200 L sec^{-1} (using N_2 as a standard). This pump is subsequently backed by and Edwards E1M40 one-stage mechanical pump filled with 4 L of Edwards Ultragrade 70 oil with a pumping speed of 10.2 L sec^{-1} (or 9.17 L sec^{-1}). The background pressure is typically 10^{-7} to 10^{-6} Torr while the pressure during experiments is typically 10^{-5} Torr.

The fourth chamber, also called the detection chamber, uses an Edwards DiffStak 160/700M diffusion pump filled with 250 mL of Santovac 7 oil with a pumping speed of 700 L sec^{-1} (using N_2 as a standard) for vacuum. The diffusion pump is backed by the same Edwards E2M40 two-stage mechanical pump that is used for the second chamber. The typical background pressure is 10^{-8} to 10^{-7} Torr and 10^{-7} Torr during an experiment.

2.3. Cluster Formation

Clusters are composed of assemblies of atoms, molecules, and sometimes ions that range in size from two or three component units to several thousand. These units are held together by weak forces compared to a chemical bond and are considered van der Waals-like. These forces are largely dispersion forces, but can also include electrostatic forces, hydrogen bonding, and metal-metal bonding. Clusters therefore have properties that are somewhere between bulk gas and condensed phases.¹⁵ With these unique properties, clusters have come to be categorized as a fifth state of matter.⁸⁸

In general, intermolecular forces within a cluster are a combination of cohesive forces that order the units of the cluster and repulsive forces (also called thermal forces) that cause disorder within the cluster. Under normal experimental parameters, clusters are formed via supersonic adiabatic expansion where the expanding gas condenses due to the low temperatures of the vacuum chamber. Here the thermal forces are very small and the cohesive forces are dominant, making these conditions ideal for cluster formation.¹⁵

Experimentally, the neutral clusters of interest are seeded in an inert carrier gas (usually helium or argon) and pulsed into a low pressure chamber. This seeding is achieved by mixing the neutral sample gas with the inert gas or by passing the inert gas over the vapor of the solid or liquid sample. The pressure of the carrier gas during experiments is set between 1-8 atm creating a high pressure region prior to expansion. A Parker series 9 pulse valve operated at 10 to 100 Hz pulses of 200-400 μ s duration fitted with a 0.5 mm orifice is used to expand the gas mixture into the chamber maintained between 10^{-7} to 10^{-4} Torr (note 760 Torr \approx 1 atm \approx 15 PSI).

Once the mixture undergoes expansion at the nozzle, the thermal energy of the high pressure source is converted into directed velocity (u) of the cluster beam. This process can be shown in a thermodynamic expression (Equation 2.1):

$$C_p T_0 = C_p T_1 + \frac{mu^2}{2} \quad (2.1)$$

where C_p is the heat capacity of the expanding gas, T_0 is the source temperature, T_1 is the temperature of the beam, m is the molecular weight of the expanding gas, and u is the velocity of the this gas.⁸⁹

The temperature of the beam, T_1 , must be lower than the source temperature, T_0 , because the kinetic energy term (mu^2) is positive. This temperature change can be quantified using Equation 2.2:

$$T_1 - T_0 = T_1 \left[\left(\frac{P_1}{P_0} \right)^{\frac{\gamma-1}{\gamma}} - 1 \right] \quad (2.2)$$

$$\gamma = \frac{C_p}{C_v} \quad (2.3)$$

where P_1 is the cluster beam pressure, P_0 is the source pressure, and γ is the heat capacity ratio (Equation 2.3). This cooling allows clustering via condensation of the sample molecule where the beam temperature (T_1) can get as low as 30 K.⁹⁰

The size of the clusters that are formed via supersonic adiabatic expansion can be predicted using the Hagen parameter (Γ^*) which is defined using Equation 2.4:

$$\Gamma^* = k \frac{\left(\frac{d}{\tan \alpha} \right)^{0.85}}{T_0^{2.3}} P_0 \quad (2.4)$$

where k is a bond formation parameter that measures the intermolecular bond strength, d is the nozzle diameter (0.5 mm in the discussed experiments), and α is half of the expansion angle (note that in supersonic expansion $\alpha < 45^\circ$ and $\alpha = 45^\circ$ for sonic expansion).^{91,92} P_0 and T_0 are defined previously, but the P_0 is in mbar. When $\Gamma^* > 100-300$, clustering will begin and the overall size of the cluster is proportional to $\Gamma^{*2.0-2.5}$.⁹²

The molecular beam produced via supersonic adiabatic expansion consists of clusters of various sizes with larger clusters in the centerline due to the migration of lighter atoms radially away from the middle of the beam axis.⁹³ This beam is collimated into a unidirectional molecular cluster beam using a 3 mm skimmer cone. This skimmer cone also acts as a conductance limiter allowing differential pumping in the source and ionization chambers.

If only a monomer ion is desired, a second method of introducing the sample into the drift cell is used. Here the seeded gas is not pulsed into the source chamber, but instead allowed to flow continuously using a process called “continuous flow.” Here the sample flows through a 0.1 mm

nozzle body with no driver or poppet inside the coil. The pressure of the chamber can not be controlled by pulse duration and therefore is controlled using a needle valve to ensure that the pressure in the source chamber does not exceed 10^{-4} . This beam still employs the 3 mm skimmer cone to allow differential pumping between the source and ionization chambers.

2.4. Quadrupole Mass Selector – Ion Mobility – Quadrupole Mass Selector

2.4.1. Ion Generation – Electron Impact Ionization

The neutral ion beam generated in the first chamber is ionized in the second chamber by an axial electron-impact ionizer (Extrel, part No. 812447). The tungsten filament of the ionizer assembly is heated to 1870-2970 K using an emission current of 0.05 to 5.0 mA which allows for the thermionic emission of electrons that are accelerated into the ion region using an electrostatic field.^{94,95} Ionization occurs in this ion region basket (also known as the ionizing volume shown Figure 3) when the ions collide with the neutral clusters. The electron energy of the filament is set to 50-80 eV, which is enough to ionize the organic clusters studied by abstracting an electron from an atomic or molecular orbital of the neutral cluster as shown in Equation 2.5.^{94,96,97}



At high electron energies, fragmentation of the parent ion can occur. If a fragment ion is of interest, then higher electron energies are used to mass-select the fragment ion. Once the ions are generated, they are accelerated into the quadrupole by a series of ion optics.

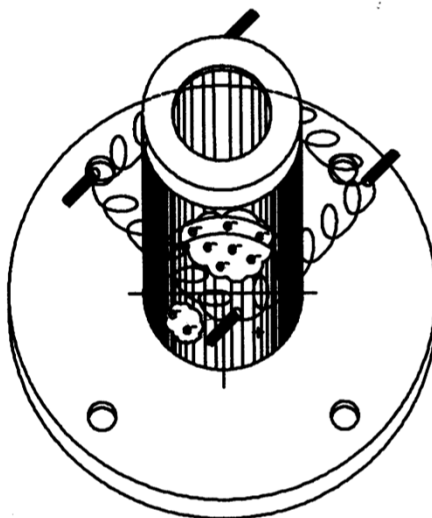


Figure 3. Schematic drawing of the ion region basket surrounded by the tungsten filament illustrating the region where ionization occurs.

2.4.2. Quadrupole Mass-Filter

The ions of interest that are generated by the electron impact ionizer are mass selected using a quadrupole mass filter (Extrel, part No. 813685) based on their mass-to-charge ratio (m/z). The quadrupole used consists of four stainless steel rods ($3/8$ " diameter and 7.88" length) with circular cross sections where opposite pairs are connected electrically. The effective mass range of the quadrupole used is 10-4000 amu. The quadrupole has pre- and post-filters attached to the beginning and end of each main rod. The pre- and post-filters are used to increase the abundance of the detectable ions by collimating the beam.^{98,99}

The quadrupole can be set to two specific modes during operation, mass-selecting (RF-DC or resolved) mode, and RF-only (integral) mode. In mass-selecting mode only an ion of a specific m/z will be transmitted through the quadrupole while ions of other m/z are deflected and is the preferred mode to use.¹⁰⁰ Whereas in RF-only mode, the mass-selection function is "looser" than in mass-selection mode; a preference for ions of a selected m/z ratio exists, but ions of a similar m/z ratio or fragments also leave the quadrupole. RF-only mode is used when there is a low signal

or when the only ion transmitted through the quadrupole is the desired parent ion with no fragmentation. To effect an ion's path, the electric field of the rods fluctuates in strength and frequency (880 kHz is the average frequency used) of the uniform RF and DC applied voltages.^{98,99,101} The fluctuating electric fields cause the ions to oscillate in a stable trajectory along the z -axis of the quadrupole thus allowing for discrimination based on m/z .¹⁰⁰

The resolution of a quadrupole is determined by the number of oscillations (n) ions traveling through the mass filter undergo. The two main factors for changing n are the length of the quadrupole and the time that the ions spend in the quadrupole. Since the length of the quadrupole is fixed, time is the variable changed by adjusting the velocity of the ions as they enter the mass filter. This velocity is dependent on the energy of the ion.¹⁰² If the ions enter the quadrupole at high energies, then low resolution leading to poor peak shape are observed. A moderate ion energy level of 10-30 eV is used during experimentation to allow for sufficient resolution.

The ionizer, ionizer ion optics, and quadrupole voltages are supplied by ABB Extrel power supply setup. This setup includes a QMS DC Power supply (Model 813370), Merlin QMS Controller (3500 series), and a 150-QC quadrupole power supply (model J304). The Merlin QMS Controller and Merlin Software (version 2.4.0) allow remote control of the applied voltages.

2.4.3. Drift Cell and Focusing Ion Optics

As ions exit the quadrupole, they enter the third chamber and travel through a set of three Einzel lenses and are guided into the pinhole orifice of the drift cell by horizontal and vertical steering lenses. Each set of steering lenses are composed of two half circle nickel plates. For each set, one plate is connected to an individual high-voltage power supply (Agilent, E3612A) and is considered the "steering plate." The second plate for each set is biased with Einzel lens 3 and

connected to a high-voltage power supply set to 240 V (Bertan Associates, Model 205A-05R). These plates guide the ions into the drift cell by changing the voltage of unbiased steering lens relative to the biased lens. This allows the ion path to be adjusted in both the vertical and horizontal directions.

A second function of the steering lenses is to act as an ion gate. Here the steering lenses “chop” the ion beam into 10-100 μs packets for time-dependent studies. The gating pulse is triggered by a pulse generator (DEI, PVX-4140) connected to the power supply of the unbiased vertical steering lens providing +240 V. Since the biased lens is kept at -240 V, the gate is effectively closed when the +240 V is applied to the unbiased lens and is opened again when the voltage is no longer applied.

The drift cell in the VCU QMS-IM-QMS system was designed by Paul Kemper with the schematic shown in Figure 4.^{90,103} The drift cell is composed of two main units: the cell body and the endcap. Both units are made of oxygen free high conductivity copper alloy (Alloy 10100 PFHC, melting point 1360 K). The outside dimensions of the cell body are 3.5” \times 3.5” \times 2.14” and the endcap outside dimensions are: 3.5” \times 3.5” \times 0.40”. The inside of the drift cell is a cylindrical tube (1.84” length and 2.0” diameter). The diameter of the last 0.28” of this tube increases in diameter to 2.35” where a ceramic ring (2.34” outer diameter, 1.97” inner diameter, 0.40” thickness) is placed to electrically isolate the cell body and endcap units.

The entrance plate of the drift cell is made of stainless steel and is attached inside the drift cell body and kept in position by a copper retainer that has an orifice of 0.254 mm. Just before the drift cell entrance are two entrance lenses that are separated by ceramic spacers (Lenses A and B). Both lenses help to focus the ion beam into the drift cell. Lens A is a tapered lens that collimates

ions into the entrance orifice of the drift cell entrance plate. Each lens is isolated and connected to a separate high voltage power supply.

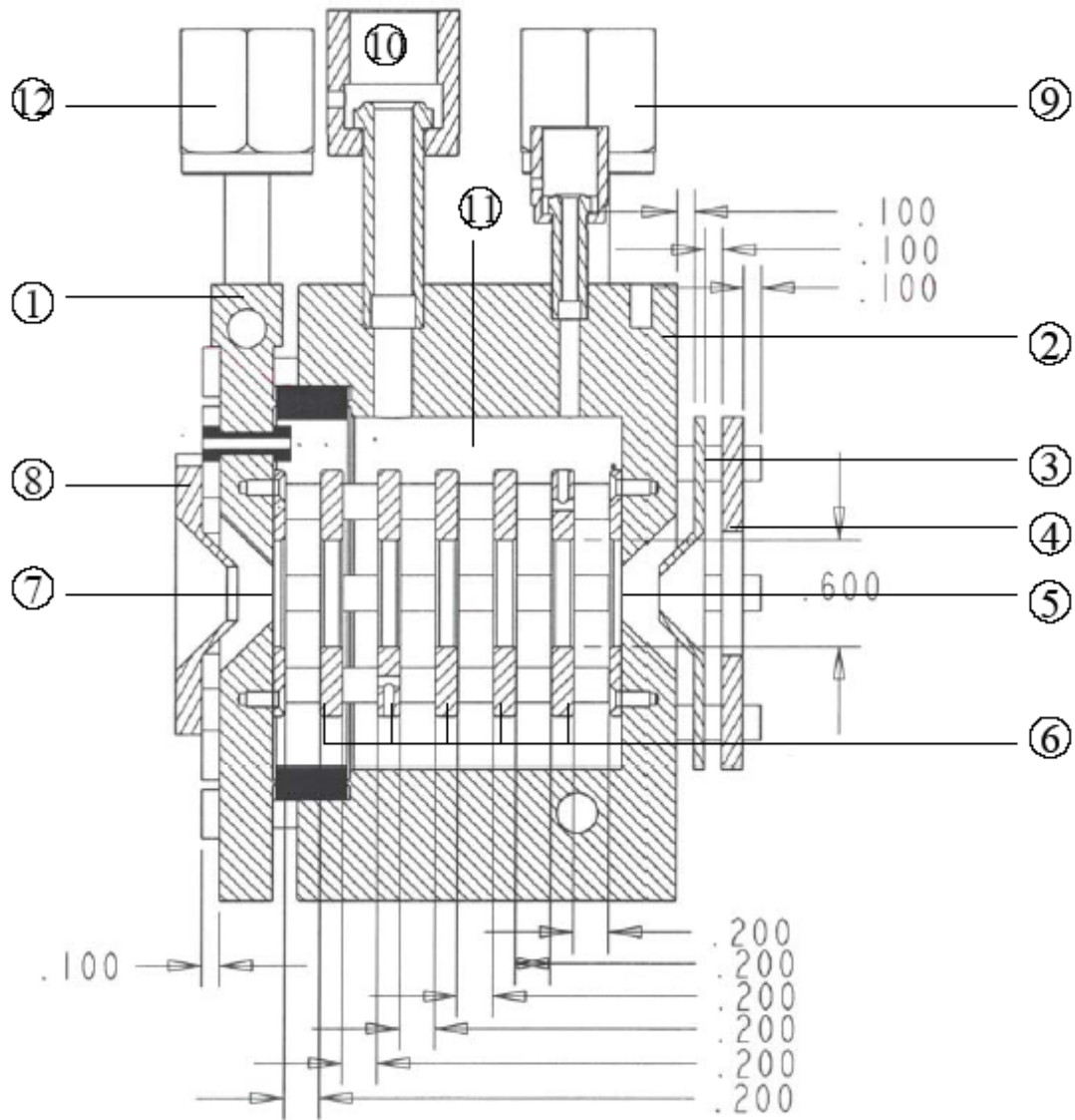


Figure 4. Side view cross section of the drift cell used in the VCU QMS-IM-QMS system with the following components (all units in inches): (1) Endcap, (2) Reaction Cell Body, (3) Entrance Lens (Lens B), Tapered Entrance Lens (Lens A), (5) Entrance Orifice (0.25 mm), (6) Drift Rings (inside of drift cell body), (7) Exit Orifice (0.25 mm), (8) Tapered Exit Lens (Lens C), (9) Cell Body Liquid Nitrogen Inlet, (10) Baratron Connection, (11) Drift Cell, (12) Endcap Liquid Nitrogen Inlet.

The endcap consists of a stainless steel exit plate held in position by a copper retainer with a 0.254 mm orifice (the same as the entrance plate). After the drift cell exit plate, ions travel through a tapered exit lens (Lens C) that is powered by an independent high voltage power supply (Agilent E3612A). On the interior side of the endcap (the side that attaches to the drift cell body) five stainless steel drift rings are mounted using six ceramic rods. These rings when mounted are found inside the cylindrical chamber of the drift cell body and have the dimensions: 1.40" outer diameter, 0.60" inner diameter, and 0.128" thickness. A schematic of this setup is shown in Figure 5.

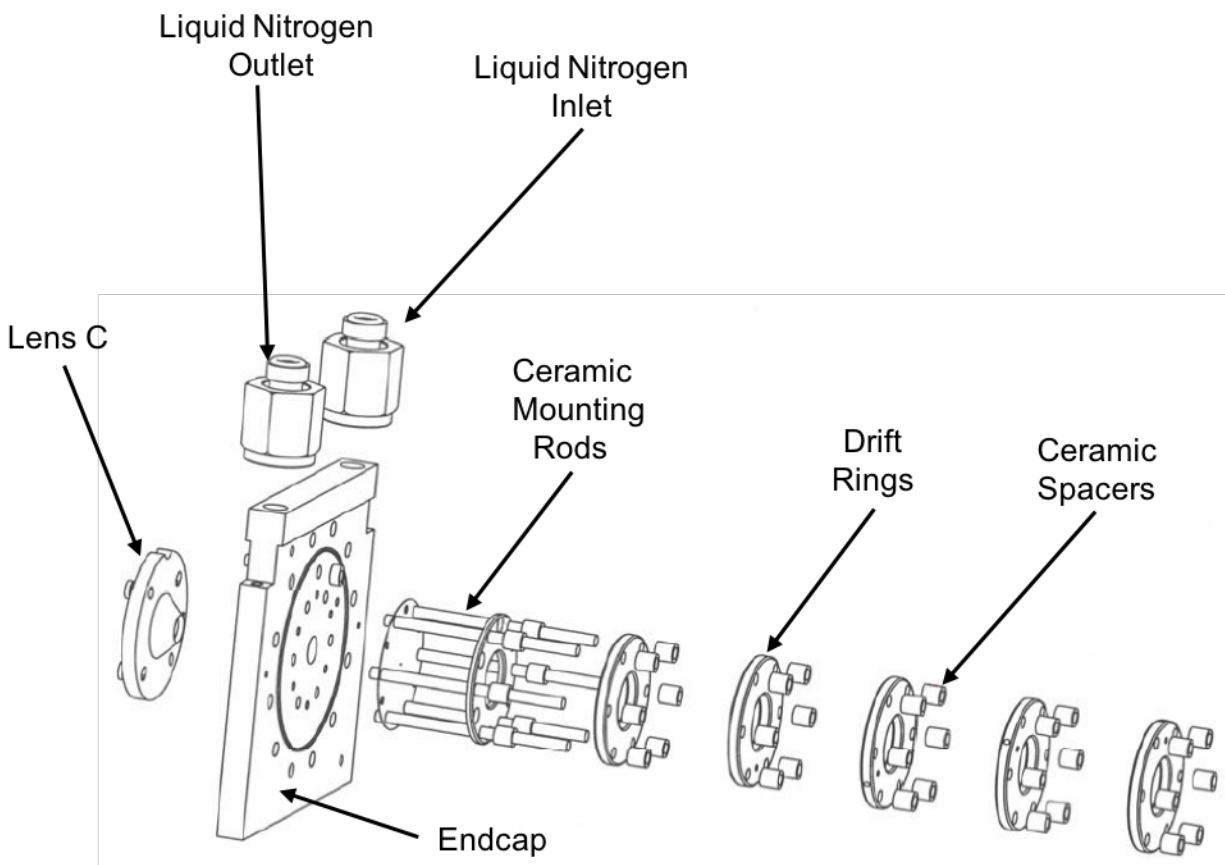


Figure 5. Breakdown of the drift cell endcap and components mounted on each side including: tapered exit lens (Lens C), copper drift rings, ceramic spacers, and liquid nitrogen inlet and outlet.

The drift cell can be temperature controlled by either heating or cooling mechanisms depending on desired study with a temperature range of -196 to 500 °C (77-773 K). Liquid nitrogen is used to cool the cell to its minimum of -196 °C (77 K), the temperature of the liquid nitrogen. The flow of the liquid nitrogen is controlled by two separate temperature controllers (Omega, type CNi3233), one for the body and one for the endcap, coupled to On/Off solenoid valves. Heating is achieved using tantalum wires that are weaved four times in and out of ceramic tubes placed throughout the drift cell and connected in series. There are ten ceramic tubes in total: eight found in the body and two in the endcap. DC voltage applied to the tantalum is used to heat the cell and is generated from AC voltage converted using separate isolation transformers and rectifiers. DC voltage is used over AC voltage because the ceramic tubes become conductive when heated to higher temperatures which runs the risk of interfering with the voltage that is applied to the drift cell entrance and exit. The heating temperature is controlled using separate controllers for the body and endcap (Omega, type CN3251). The controllers used for both heating and cooling keep the temperatures within ± 1 °C of the set point. The temperatures of the cell body and endcap are monitored using two sets of thermocouple wires (each set consisting of two wires) connected to a temperature readout (Omega, DP4642).

Neutral reagent and/or inert buffer gases used for experiments enter the drift cell through a flexible stainless steel tube with ceramic breakers to ensure that the tube is isolated from the drift cell voltage. The pressure and flow rate are controlled using mass flow controllers (MKS 1479A) or a needle metering valve (Swagelok, SS-22RS4 with 0.25 in outer diameter). Each gas that is fed into the drift cell is controlled with a separate controller or valve and is mixed prior to entering the line inside of the vacuum chamber. The pressure inside the drift cell is measured using capacitance manometer (MKS Baratron type 626) that is connected to the cell body using a stainless steel tube

with ceramic breakers similar to the tube used for reagent gases and monitored 2 channel digital readout (MKS, PR4000) with an accuracy of ± 1 mTorr.

The reagent vapor/gas and inert buffer gas (usually helium) within the drift cell create a high pressure region within the vacuum system and thus the gas/vapor mixture flows out of the drift cell through the entrance and exit apertures. Ion injected into the drift cell undergo collisions with the gas exiting the drift cell entrance aperture resulting in complete thermalization of the ions as they enter the drift cell.^{71,87,104,105} The maximum pressure of the gas in the drift cell is dependent on the drift cell entrance and exit aperture and the pumping speed of the diffusion pump attached to the chamber. With 4 Torr of He gas in the cell, the lowest obtainable pressure is roughly 4.5×10^{-5} Torr using the current setup of the system. This is the upper limit to avoid arcing of the drift cell with other ion optics in the chamber.

Ions that exit the drift cell are focused and guided into the forth chamber by a second stack of three Einzel Lenses. It is important to note that the ions that leave the drift cell are both product ions as well as unreacted ions. The drift cell entrance and exit as well as the first and second Einzel Lens stacks voltages are supplied by ABB Extrel power supply setup. This setup includes a QMS DC Power supply (Model 813370), Merlin QMS Controller (3500 series), and a 150-QC quadrupole power supply (model J304). The Merlin QMS Controller and Merlin Software (version 2.4.0) allow remote control of the applied voltages.

2.4.4. Detection of Ions - Electron Multiplier Detector

The ions entering the forth chamber are analyzed using a second quadrupole mass-filter in either a fixed-ion mode or scan mode. The fixed-ion mode is used to scan an individual reactant or product ion and obtain its arrival time distribution (ATD). An ATD is a function of the time that an ion takes to be detected after injection into the drift cell. The intensity of the ion is the integration

of the area under the ATD.^{71,106} In scan mode the intensity of all ions are monitored after they exit the drift cell. Scan mode is what is used to obtain full mass spectra during experimentation while fixed-ion mode is used for thermochemical and structural determination experiments (discussed in Chapter 3).

Ions are detected by an electron multiplier detector with a conversion dynode (De-Tech, 402A-H) which is coupled to the second quadrupole. Cations produced throughout the experiment and scanned by the second quadrupole strike the surface of the conversion dynode, which has a high negative voltage of -5 kV, causing the generation of electrons. These electrons are accelerated down the multiplier tube due to the potential difference between the dynode and multiplier tube where a less negative voltage is applied. The voltage applied to the multiplier tube is dependent on the abundance of the signal and the age of the multiplier. As electrons strike the surface of the multiplier tube, more electrons are ejected and cascaded down the tube. The current signal generated is then amplified using a counting pre-amplifier (MTS-100). Since the signal is a multi-electron process and noise is a single electron process, the signal-to-noise ratio (S/N) is increased using an adjustable discriminator on the pre-amplifier. The resulting signal is then processed and displayed using Merlin software (Extrel, version 2.4.0).

The second quadrupole as well as the dynode and multiplier voltages are supplied by ABB Extrel power supply setup. This setup includes a QMS DC Power supply, Merlin QMS Controller, and a 150-QC quadrupole power supply. The Merlin QMS Controller and Merlin Software (version 2.4.0) allow remote control of the applied voltages.

2.4.5. Ion Energy and Injection Energy

The energy of an ion generated by electron impact ionization (relative to ground) within a quadrupole mass filter is defined as the voltage applied to the ion region lens of the axial electron

impact ionizer on the first quadrupole mass filter in the second chamber (where the ions are generated).⁹⁴ The entire housing of the quadrupole mass filter is floated to a fixed voltage and this voltage is added to the ion region. This makes the effective ion energy the sum of the ion region lens and quadrupole floating voltages. Floating the quadrupole allows higher ion energies to be effectively handled by the quadrupole mass filter.

Since the resolution of the quadrupole is dependent on the residence time of the ions in the quadrupole which is decreased with higher ion energies (discussed previously), a DC voltage is applied to quadrupole mass filter to adjust the residence time of the ion in the quadrupole mass filter. This voltage is called the “pole bias” and aids in adjusting the resolution of the quadrupole mass filter. The axial kinetic energy of an ion in a quadrupole mass filter is therefore the difference between the overall ion energy and the pole bias as shown in equation 2.6:

$$IE = (IR + FQ) - PB \quad (2.6)$$

where IE is the ion energy within a quadrupole mass filter, IR is the ion region voltage, FQ is the floating quadrupole voltage, and PB is the pole bias voltage. For most experiments, the ion energy is set between 10-30 eV.

A separate important ion energy parameter to consider during experimentation is the injection energy of an ion as it enters the drift cell. This energy is effectively the kinetic energy of the ion as it enters the drift cell. The injection energy (also referred to as the laboratory frame) is defined as the difference between the ion energy and the drift cell entrance. The injection energy should only be slightly higher than the energy that is required for the ions to enter the drift cell against the drift cell gas outflow. If the injection energy is too low, the ions are not able to enter the drift cell leading to low signal intensity. If the injection energy is too high, two possible effects arise. The first is that the ions enter too deeply into the drift cell before they are fully thermalized

causing inaccurate drift residence making results from time dependent studies unusable. The second effect of high injection energy is the fragmentation of the parent ion. This will cause poor signal intensity of the products and reactants of the desired reaction process. The fragments may also undergo secondary reactions causing the collection thermochemical and kinetic information difficult. As the ions exit the drift cell, they are said to be reacted and have roughly the same kinetic energy as the drift cell exit.

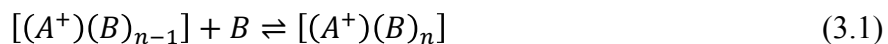
Chapter 3: Experimental Measurements

The following sections of this chapter outlines in detail the experimental measurements that are used throughout the rest of the dissertation.

3.1. Thermochemistry Measurements

The use of ion mobility mass spectrometry (IMMS) has been shown as an effective way to perform thermochemical measurement experiments.¹⁰⁷ This is achieved by mass selecting an ion of interest using the first quadrupole in the second chamber and injecting this selected ion into the drift cell in 30-50 μs pulses. When the ion enters the drift cell, equilibrium between the injected ion and the product cluster is achieved because to the high number of collisions that occur between the injected ion and the drift cell outflow gas. The number of collisions that occurs is typically higher than 10^4 . Low electric field (the difference between the drift cell entrance and the drift cell exit lenses) is used to ensure that there is minimal collisional heating and the ions involved in the reaction have enough time to reach equilibrium.¹³ Since equilibrium is achieved, the concentrations of the reactant and product clusters ions are measured by collecting the arrival time distributions (ATDs) for each ion or by taking the relative peak intensities from mass spectra.

The thermochemical experiments performed throughout this dissertation follow the same general ion-neutral reaction as shown in Equation 3.1:



where A^+ is the injected ion, B is the reactant or solvent molecule that is found in the drift cell, and $n = 0, 1, 2, 3, \dots$; these terms will be used for the following discussion. Equilibrium for this reaction is said to occur when three conditions are met. The first condition is that there is a constant ratio of the product and reactant ion intensities when changing the electric field of the drift cell at

constant temperature and pressure. The second condition is product and reactant ions have equal residence times as obtained from their ATDs. The third condition is that the equilibrium constant is independent of the pressure of the neutral reactant in the drift cell. The equilibrium constant, K_{eq} , is measured as follows (Equation 3.2):

$$K_{\text{eq}} = \frac{I_{(A^+ \cdot B_n)}}{I_{(A^+ \cdot B_{n-1})}} \times \frac{760}{P_B} \quad (3.2)$$

where $I_{(A^+ \cdot B_n)}$ and $I_{(A^+ \cdot B_{n-1})}$ are the integrated intensities of the product and reactant ions respectively as obtained by the ATDs and P_B is the pressure of the neutral gas/vapor filling the drift cell in Torr.¹⁰⁸

Using the following well-defined concepts of thermodynamics²⁹:

$$\Delta G^\circ = \Delta H^\circ - T\Delta S^\circ \quad (3.3)$$

$$\Delta G^\circ = -RT \ln K_{\text{eq}} \quad (3.4)$$

and rearranging Equations 3.3 and 3.4 to Equation 3.5 (linearized van't Hoff equation):

$$-R \ln K_{\text{eq}} = \frac{\Delta H^\circ}{T} - \Delta S^\circ \quad (3.5)$$

a van't Hoff plot is obtained by plotting $-R \ln K_{\text{eq}}$ as a function of $1000/T$ using the temperature of the drift cell and the K_{eq} obtained previously. This plot is a linear function whose slope is the enthalpy change (ΔH°) with units of kcal mol⁻¹ and intercept is the entropy change (ΔS°) of the ion-neutral reaction in units of cal mol⁻¹ K⁻¹ when $R = 1.987$ cal mol⁻¹ K⁻¹.

3.2. Mobility Measurements and Structure Determination

Ion mobility mass spectrometry (IMMS) is a well-established analytical technique that is used to analyze a wide variety of compounds in ambient conditions including explosives, drugs, and chemical warfare agents.^{21,31-33,109} IMMS is considered gas phase ion chromatography by measuring the drift the drift time of an ion in an inert buffer gas (typically He, N₂, or Ar) under the

influence of a weak uniform electric field. Using drift time, the collision cross-section (Ω) of the ion can be directly measured. Since the motion of the ion is dependent on electric field, the geometric shape of the ion can be directly measured.^{17,89,110-115} By differentiating the geometric shapes of an ion, separate isomers of the same structure as well as conformers of the same m/z can be experimentally measured.¹⁹ Ion mobility spectrometry is therefore the only way to directly measure an ion's collision cross section.

3.2.1. Mobility Measurements

Ion mobility experiments measure the mobility value of the ion, which is a measure of how rapidly the ion travels through a buffer gas under a weak electric field. For all experiments, the ion studied is mass-selected by the first quadrupole mass-filter in the second chamber, focused by the first stack of Einzel Lenses, and injected into the drift cell at an injection energy just above the energy necessary to introduce the ions into the drift cell against the outflow of buffer gas from the drift cell. This outflow of gas is where the ions are thermalized prior to entering the drift cell entrance. Inside the drift cell, the ions are accelerated through the electric field along the electric field axis and since the drift cell contains a homogeneous pressure of buffer gas, the ions are decelerated due to the frictional force with the buffer gas.^{34,89,110,115} Throughout all experiments, He is used as the buffer gas since it allows for theoretical tools to be used for molecular structure.¹¹⁶ The frictional force of the buffer gas causes the ions to stay in the drift cell for a longer time. If the ions remain in the drift cell for enough time, the electric field of the entire drift cell is considered uniform. When this condition is met, an equilibrium state is reached and the ions move with a constant velocity called the “drift velocity.”¹¹⁷

The mobility value (K) obtained from experiments is defined as the velocity of the ions as they travel through the drift cell buffer gas divided by the electric field across the drift region as shown by Equation 3.6:

$$K = \frac{\vec{v}_d}{\vec{E}} \quad (3.6)$$

where \vec{v}_d is the drift velocity and \vec{E} is the electric field across the drift region. These variables are further defined in Equations 3.7 and 3.8 respectively with l as the drift cell length in cm (5 cm for the drift cell used), t_d is the drift time in seconds, and V is the drift cell voltage.¹¹⁰

$$\vec{v}_d = \frac{l}{t_d} \quad (3.7)$$

$$\vec{E} = \frac{V}{l} \quad (3.8)$$

The mobility values are normalized to standard temperature and pressure conditions resulting in the reduced mobility (K_0) of the ion. By calculating the reduced mobility, the results obtained using different cell conditions are comparable. It should be noted that the drift velocity is inversely proportional to the number density of the gas in the drift cell (N) so $K \propto NK_0$. Therefore, the reduced mobility is calculated using equation 3.9:

$$K_0 = \frac{P}{P_0} \frac{T_0}{T} K = \frac{P}{760} \frac{273.15}{T} K \quad (3.9)$$

where P is the pressure of the buffer gas in Torr, T is the temperature of the drift cell in Kelvin, and P_0 and T_0 are the STP values in Torr and Kelvin respectively.¹³

By combining Equations 3.6 and 3.9 and substituting \vec{E} from Equation 3.8 yields Equation 3.10:

$$t_d = \left(\frac{l^2 \cdot T_0}{T \cdot P_0} \frac{1}{K_0} \right) \frac{P}{V} + t_0 \quad (3.10)$$

where t_0 is the effective time the ion spends outside the drift cell before reaching the detector.¹¹⁸

All mobility measurements are carried out in a low-field limit so that an ion's drift velocity is small compared to the thermal velocity. By doing this, the mobility is independent of the field strength. To measure the mobility of an ion, a gated mass-selected ion pulse is injected into the drift cell and the arrival time distributions (ATD) are measured over a range of drift cell voltages at a fixed pressure and temperature. The reduced mobility is obtained from the slope of a line plotting the drift time (t_d) versus P/V and using Equation 3.10. The drift time is the maximum of the collected ATDs. Typically, a corrected drift time and therefore reduced mobility is used for subsequent calculations since the collected ATDs have Gaussian-like shape, the distortion generated by the drift cell exit is corrected by Equation 3.11:

$$t_d(\text{corrected}) = t_{obs} + \frac{4D}{v_d^2} \quad (3.11)$$

where t_{obs} is the observed arrival time collected from the ATD maximum and D is the diffusion coefficient.¹⁰³ The diffusion coefficient is related to the measured mobility under low-field conditions by the Einstein equation using Equation 3.12:

$$D = D_L = D_T = K \frac{k_B T}{ze} \quad (3.12)$$

where D_L is the longitudinal diffusion coefficient, D_T is the transverse diffusion coefficient, k_B is Boltzmann's constant, z is the number of charges, and e is the elementary charge (1.60×10^{-19} Coulombs).¹¹⁸

The resolution of an ion mobility instrument is measured using Equation 3.13:

$$\text{Resolution} = \frac{t}{\Delta t} = \frac{l}{\Delta x} = \sqrt{\frac{\pi V e}{4 k_B T}} \quad (3.13)$$

where Δt is the pulse width of the ion packet, e is the charge on the ion, and Δx is the spread of a cloud of identical ions due to diffusion. This spread variable is used to account for the random part of motion and is defined by Equation 3.14:

$$\Delta x = \sqrt{\frac{4k_B T l}{\pi E e}} = \sqrt{\frac{4k_B T l^2}{\pi V e}} \quad (3.14)$$

where all variables are previously defined.¹¹⁹ From Equation 3.12 the resolution is enhanced by a variety of methods. The pulse width is generally changed in practice by changing the length of the gate for the ion packet. For increased resolution, shorter pulse widths are recommended. Other ways that resolution could be increased include using a longer drift tube (although not feasible in practice), high drift voltages, or lower drift temperatures.

When using high drift voltages to increase the resolution, a higher buffer gas density (N) should be used to prevent arcing of the drift cell.¹²⁰ Higher buffer gas density also ensures that the ions are completely thermalized before entering the drift cell and that neutral molecules do not enter the drift cell.²¹ Since the buffer gas density plays a role in the resolution of mobility measurements, the field intensity used is generally expressed as E/N and represents the intensity drift field expressed in units of Townsend (T_d) where $1 T_d = 10^{-17} V \cdot cm^2$.¹¹⁸ For low field conditions to be met, the E/N is generally $< 6 T_d$. If low field conditions are met, the ion drift velocity is small compared to the thermal velocity. When this occurs, ion mobility is independent of field strength.¹¹⁰ To achieve a low E/N value, the drift cell is typically filled with 2-5 Torr of He buffer gas and the ions are injected in narrow pulses of 30-50 μs with the ion gate located just prior to the drift cell entrance.¹⁰

For all ion mobility experiments discussed, there are three assumptions made for low field conditions. These have been mentioned previously and are^{103,118,121}:

1. The measured mobility is independent of the drift field
2. The ion drift time is the maximum of a Gaussian-type distribution
3. Ions injected into the drift cell are thermalized and excess kinetic energy is lost before penetrating significantly into the drift cell.

A discussion of how each of these conditions are met follows.

Verifying the first condition requires the calculation of the effective temperature of the ions as they drift through the electric field. This is done using Equation 3.15:

$$T_{eff} = T_g + \frac{M_d v_d^2}{3k_B} \quad (3.15)$$

where T_{eff} is the effective temperature, T_g is the buffer gas temperature, M_b is the mass of the buffer gas, and v_d is the drift voltage.¹¹⁸ The effective temperature arrives from two sources: the thermal temperature from the buffer gas and the effect of the drift field on temperature. At higher applied fields, the effective temperature is only 9% higher than the buffer gas temperature and causes only a 2% increase in the measured mobilities.¹⁹

The second condition is satisfied by comparing the experimental ATD by an ATD produced with transport theory under similar experimental conditions. These calculated ATDs are simulated as a monoionic species traveling through a cylindrical drift tube. The ion flux ($\phi(t)$) of the ion as it exits the drift tube through an orifice of area a is calculated using Equation 3.16:

$$\phi(t) = \frac{sae^{-\alpha t}}{4\sqrt{\pi D_L t}} \left(v_d + \frac{l}{t} \right) \left(1 - \exp\left(-\frac{r_0^2}{4D_T t} \right) \right) \exp\left(-\frac{(l - v_d t)^2}{4D_L t} \right) \quad (3.16)$$

where s is the surface density of the injected ions, α is the reaction frequency, r is the radius of the disk of injected ions, and all other variables are previously defined. The reaction frequency is set to 0 for an inert buffer gas, but usually accounts for ion loss resulting from reactions with the drift gas.^{87,110}

The third condition is met when the depth that the ions travel before being thermalized must be known. Using hard sphere theory (further discussion in Section 3.2.3.1) the energy of the ion after n collisions is calculated using Equation 3.17:

$$E_f = E_i M^n \quad (3.17)$$

where E_f is the final energy of the ion, E_i is the initial energy of the ion (the injection energy), and M is the reduced mass. The reduced mass is defined as:

$$M = \frac{M_i^2 + M_b^2}{(M_i + M_b)^2} \quad (3.18)$$

with M_i representing the mass of the injected ion and M_b is the mass of the inert buffer gas. Assuming that the injection energy is 13 eV and the collision rate coefficient is $10^{-9} \text{ cm}^3 \text{ s}^{-1}$ (typical number for experiments), the final E_f required for thermalization (when $E_f = k_B T$) is achieved in approximately 24 collisions. The time necessary for these collisions to occur is calculated using the equation:

$$t = \frac{n}{N \cdot k} \quad (3.19)$$

where all variables are previously defined. Using typical experimental parameters of drift cell pressure of 3.5 Torr, 298 K drift cell temperature, 24 collisions, and a collision rate coefficient of $10^{-9} \text{ cm}^3 \text{ s}^{-1}$ thermalization occurs in 0.2 μs . With a known time of thermalization, the distance that the ions travel into the drift cell can be calculated using Equation 3.20:

$$d = \int_0^t v_d + v_i M^{\frac{nkT}{2}} dt \quad (3.20)$$

where v_d is the drift velocity, v_i is the initial velocity, and M is calculated using Equation 3.18. Continuing with this example, the ions travel less than 0.2% of the drift cell before being completely thermalized.

3.2.2. Experimental Structure Determination

The reduced mobilities discussed above are used to directly calculate the collision cross section of an ion, which is a measure of the size of an ion and allows for separation of different isomers and conformers of the same m/z ratio.^{17,89,110-115} The measured reduced mobility (K_0) is related to the collision cross section (Ω) using the Equation 3.21:

$$K_0 = \frac{3ze}{16N_0} \left(\frac{2\pi}{k_B T} \right)^{(1/2)} \left[\frac{1}{\mu^{1/2} \Omega^{(1,1)}} \right] \quad (3.21)$$

where K_0 is the reduced mobility, z is the number of elementary charges, e is the elementary electron charge (1.60×10^{-19} Coulombs), N_0 is the buffer gas number density, k_B is Boltzmann's constant, T is the temperature of the drift cell, μ is the reduced mass of the ion, and $\Omega^{(1,1)}$ is the collision cross section (in \AA^2). From this equation, it is clear that the separation of molecular conformers with differences in their collision cross section (their shape or size) are achieved by measuring differences in the reduced mobilities of ions as they travel through a buffer gas.^{1,122} Ions with open geometries will have larger collision cross sectional areas and reach the detector at later arrival times since these ions will undergo more collisions. On the other hand, an isomer with a more compact structure will undergo fewer collisions resulting in shorter arrival times and therefore smaller collision cross sectional areas.^{123,124}

3.2.3. Theoretical Methods of Calculating Mobilities and Collision Integrals

The experimental reduced mobility and collision cross section values discussed in previous sections can be compared to theoretical values with the Mobcal program using structural input from density functional theory (DFT) and *ab-initio* calculations.^{10,125-127} These theoretical methods use various interaction potentials and approximations to simulate collisions of injected ions with buffer gas. The interactions and approximations used include: exact hard sphere approximation,

projection approximation, and trajectory calculation. All three of these are discussed in detail in the following subsections.

3.2.3.1. Exact Hard Sphere Approximation

In the exact hard sphere approximation, the ion and helium buffer gas are considered hard spheres and the hard sphere potential is used for computation of the collision interactions.¹²⁸ The collision cross section for this approximation is the sum of the van der Waals radii of the colliding species, shown in Equation 3.22:

$$\Omega^{(1,1)} = \sigma_{HS} \quad (3.22)$$

where $\Omega^{(1,1)}$ is the collision cross section and σ_{HS} are the van der Waals radii for a given ion.¹²⁴

These calculations are performed by orienting the ion randomly in a rectangular plane. Hard sphere radii are then drawn around each atom of the ion in the plane. Random points are then selected within this plane and a collision occurs if the point is within the sum of an ion atom's hard sphere radius and the hard sphere radius of a He buffer gas atom. More points are randomly selected as well as different orientations and the average collision cross sections for different orientations are calculated.¹²⁴

The exact hard sphere approximation is useful for convex structures and gives temperature independent collision cross sections since temperature conditions are not considered in calculations.¹²⁴ However, this method ignores multiple scattering collisions and any long-range interactions between the polyatomic ion and buffer gas ions. The approximation also does not consider the temperature-dependence of a collision cross section of an ion. In addition, collision cross sections for concave structures are not well approximated using the exact hard sphere approximation.^{124,128}

3.2.3.2. Projection Approximation

The projection approximation has similarities to the hard sphere exact approximation, but instead of using the hard sphere potential it relies on the 12, 6, 4-interaction potential (Lennard-Jones + ion induced dipole potential). Unlike the exact hard sphere approximation, long-range interactions are considered as is the temperature-dependence on the collision cross section.¹²⁸ These considerations are observed when calculating the collision cross section at low temperatures where higher collision cross sections were estimated. This was attributed to the long-range attractive interactions of the the individual atoms of an ion and the buffer gas atoms.

Projection approximation uses the interaction potential equation:

$$V(R) = \frac{n\varepsilon}{n(3 + \gamma) - 12(1 + \gamma)} \left[\frac{12}{n} (1 + \gamma) \left(\frac{r}{R}\right)^n - 4\gamma \left(\frac{r}{R}\right)^6 - 3(1 - \gamma) \left(\frac{r}{R}\right)^4 \right] \quad (3.23)$$

where $V(R)$ is the potential energy, n the exponent that describes the ion-neutral repulsion ($n = 12$ when using Lennard-Jones Potentials), ε is the depth of the potential well, r is the position of the potential well, γ is the ratio of the relative contributions of the R^{-6} and R^{-4} terms, and R is the distance between a specific atom in a polyatomic ion and a helium atom.¹²⁸ The value of R is obtained using tabulated collision integrals of atom-atom collisions and the equation:

$$R_{coll.} = \left(\frac{\Omega(T)^{(1,1)}}{\pi} \right)^{1/2} \quad (3.24)$$

where $\Omega(T)^{(1,1)}$ is the tabulated collision integrals of atom-atom collisions. At larger R values asymptotic behavior is observed.¹²⁸

The potential energy, $V(r)$, can be simplified using the sum of of the $V_{n,6}(R)$ and $V_4(R)$ terms (Equation 3.25) where $V_{n,6}(R)$ and $V_4(R)$ are defined in Equations 3.26 and 3.27 respectively.

$$V(r) = V_{n,6}(R) + V_4(R) \quad (3.25)$$

$$V_{n,6}(R) = \frac{n\varepsilon_{LJ}}{n-6} \left[\frac{6}{n} \left(\frac{r_{LJ}}{R} \right)^n - \left(\frac{r_{LJ}}{R} \right)^6 \right] = \varepsilon_{LJ} \left[\left(\frac{r_{LJ}}{R} \right)^{12} - 2 \left(\frac{r_{LJ}}{R} \right)^6 \right] \text{ for } n = 12 \quad (3.26)$$

$$V_4(R) = -\frac{q^2\alpha}{2R^4} \quad (3.27)$$

The values for ε_{LJ} and r_{LJ} are determined by taking the experimental collision integrals and best fitting them leading to a more accurate description of the system under investigation. The variable α is the reaction frequency that accounts for the loss of ions as a result of reactions with the drift gas and q is the charge on a particular atom.¹²⁸

3.2.3.3. Trajectory Calculation

Trajectory calculations use a potential composed of 12, 6-Lennard-Jones and long-range (ion induced dipole) potentials.¹²⁵ The collision cross section measured by this method is calculated by averaging the function of the scattering angle over the impact parameter. This means that the function is an average of the momentum transfer cross section over the relative velocity between the ion and neutral atom. Of the three methods discussed, this is the most computationally extensive, but it yields results that are the most reliable when compared to experimental values. This is especially true in multiple scattering cases and when long-range attractive interactions are significant.¹²⁵

3.3. Theoretical Calculations

To support the experimental results of thermochemical and mobility experiments previously discussed, density functional theory (DFT) and *ab-initio* calculations using the Gaussian 03 and Gaussian 09 packages are used to calculate the lowest energy structures of the various ion-neutral reactions discussed in subsequent chapters.^{129,130} For DFT calculations, the Becke three-parameter, Lee-Yang-Parr (B3LYP), Minnesota 11 (M11), and the meta hybrid M06-2X levels of theory are used.^{79,80,131} In these calculations, the 6-311++G** or cc-pVTZ basis sets

are used for geometry optimizations and energy calculations with all electrons included. Vibrational analysis was also used to verify the lack of any imaginary frequencies and to check for any transition states.⁸⁶ Frequency calculations at a given level of theory were performed on an optimized geometry to obtain the zero point vibrational energy (ZPVE), the energy of a molecule at absolute zero. This allows all binding energies calculated to be corrected for this energy. Corrections for the basis-set superposition error (BSSE), when the basis set of two or more atoms within a structure overlap, were corrected using the counterpoise method of the Gaussian software.^{129,130} The total spin, $\langle s^2 \rangle$, for all calculations was 0.75-0.77 which allows for a lack of spin contamination for open shell ions.^{81,83}

Chapter 4: Stepwise Solvation of the Naphthalene Radical Cation by Small Polar Molecules

4.1. Introduction

Ionic hydrogen bonding (IHB) interactions occur between a hydrogen donor, usually radical ions or protonated molecules, and a hydrogen acceptor, examples include neutral polar molecules such as water, methanol, ammonia, hydrogen cyanide, and acetonitrile. The bond strengths of IHBs are higher than typical hydrogen bonds with bond energies reaching up to 35 kcal mol⁻¹, roughly a third the energy of a traditional covalent bond.⁵ IHBs are important in many fields including radiation chemistry, electrochemistry, self-assembly in supramolecular chemistry, and ion induced nucleation.^{5,66,132,133} IHBs also have roles in biological systems including peptides, protein folding, proton transport, enzyme active centers, and molecular recognition.^{7,133} Ionized polycyclic aromatic hydrocarbons (PAH) molecules can form IHBs when subjected to ionizing UV radiation.^{53,55,60,68}

Unconventional carbon-based IHBs form when ionized hydrocarbons contain CH groups that act as the hydrogen donor and the hydrogen acceptors are the electron lone pairs on heteroatoms of the neutral molecule such as O or N, π electrons in olefin double bonds, and aromatic conjugated systems.⁶⁴ Such an unconventional carbon-based CH ^{δ^+} ...O IHB is observed in the hydration of several ionized including benzene (C₆H₆^{•+}), cyclic C₃H₃⁺, cyclobutadiene (C₄H₄^{•+}), and phenylacetylene (C₈H₆^{•+}).^{9,10,28,35,69} Stronger conventional hydrogen bonds can also occur when nitrogen-containing organic ions interact with water where NH⁺...O hydrogen bonds form as seen in protonated pyridine or protonated pyrimidine.^{5,8,134}

Other unconventional IHBs can form besides those involving oxygen as the neutral molecule. Polar molecules containing lone pairs of electrons such as hydrogen cyanide and

acetonitrile can form $\text{CH}^{\delta+}\cdots\text{N}$ IHBs. Hydrogen cyanide (HCN) can serve as both a hydrogen donor and a lone pair acceptor and thus form linear hydrogen bonded chains where the PAH radical ion attaches to “*externally solvate*” the ion. Acetonitrile on the other hand cannot form these linear chains and thus CH_3CN molecules bind to multiple $\text{CH}^{\delta+}$ sites of the PAH radical cation and “*internally solvates*” the ion.

Previous studies have shown that polycyclic aromatic hydrocarbon (PAH) radical cations have unusual stability in amorphous water ices up to 120 K, but there are no laboratory studies investigating the gas phase interactions of PAH radical ions with simple molecules.^{54,55} In this chapter, the first studies of the IHB interactions between the naphthalene radical cation and the astrophysically relevant molecules water, methanol, hydrogen cyanide, and acetonitrile in the gas phase using the mass-selected ion mobility (IMMS) technique are presented.^{56,57,74} Thermochemical ion-neutral equilibrium measurements were conducted at different temperatures to yield the enthalpy and entropy changes of the stepwise solvation of the naphthalene radical cation with these neutral molecules. The nature of these interactions was investigated using density functional theory (DFT) calculations of the low energy structures of the $\text{C}_{10}\text{H}_8^{*+}(\text{H}_2\text{O})_n$, $\text{C}_{10}\text{H}_8^{*+}(\text{CH}_3\text{OH})_n$, $\text{C}_{10}\text{H}_8^{*+}(\text{HCN})_n$, and $\text{C}_{10}\text{H}_8^{*+}(\text{CH}_3\text{CN})_n$ for $n = 1-6$ clusters to give the binding energy. To investigate the hydrogen bonding character of the IHB formed between the oxygen of the neutral molecule, alcohols with longer aliphatic chains were investigated. The specific alcohols include: ethanol, 1-propanol, 2-propanol, 1-butanol, and 2-butanol. For the $\text{C}_{10}\text{H}_8^{*+}(\text{ROH})_n$ ($\text{R} = \text{Et}, 1\text{-Pr}, 2\text{-Pr}, 1\text{-Bu}, \text{and } 2\text{-Bu}$) studies, the structures and binding energies of $n = 1-3$ clusters were calculated.

The results indicate that the naphthalene radical cation is “*externally-solvated*” by water, methanol, and hydrogen cyanide. In these cases, the naphthalene radical cation is attached to a

chain of water, methanol, or hydrogen cyanide. In the cases of acetonitrile and the other alcohols with 2, 3, and 4 carbons, the neutral molecule interacts directly with the naphthalene radical cation to form “*internally solvated*” structures. For the methanol studies, proton transfer products such as $(C_{10}H_7^{\bullet})H^+(CH_3OH)_n$ can be produced at low temperatures. Such products could lead to the formation of a reactive naphthalene radical ($C_{10}H_7^{\bullet}$) on the surface of ice grains of methanol in interstellar medium.

Overall this series of studies aims to establish an understanding of hydrogen bonding interactions between naphthalene radical cations within clusters of polar molecules relevant to astrophysical environments on a molecule level. The computational results provide insights into the factors that determine the energetics and structures of the naphthalene radical cation with small polar molecules as a model system for the solvation of PAH ions within clusters of these neutral molecules.

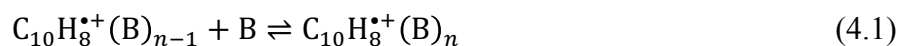
4.2. Experimental Section

All experiments were performed with the VCU mass-selected ion mobility mass spectrometer with details of the system outlined in Chapter 2. During experiments, 50-80 psi (\approx 2500-3600 Torr) ultra-high purity helium (AirGas) seeded with 0.74-3.76 Torr naphthalene vapor generated from heating solid naphthalene (Aldrich, \geq 99 %) stored in a sealed stainless steel/glass bubbler to 50-70 °C was pulsed through a supersonic nozzle (500 μ m) into a source vacuum chamber maintained at a background pressure of 10^{-7} Torr. Following this supersonic expansion, the naphthalene radical cation ($C_{10}H_8^{\bullet+}$) was generated by electron impact ionization using an electron energy of 60-70 eV which is enough to ionize any organic ions of interest. The $C_{10}H_8^{\bullet+}$ ions were mass-selected by a quadrupole mass-filter before being injected into a drift cell (in 25-50 μ s pulses) containing helium (AirGas, Research Grade) or a mixture of helium and the neutral

reagent vapor: H₂O (deionized), D₂O (Sigma-Aldrich, 99.9 % D atoms), methanol (CH₃OH, Fisher, laboratory grade), ethanol (EtOH, Fisher), 1-propanol (1-PrOH, Sigma-Aldrich, anhydrous 99.7 %), 2-propanol (2-PrOH, Fisher, ACS reagent grade), 1-butanol (1-BuOH, Sigma-Aldrich, anhydrous 99.8 %), 2-butanol (2-BuOH, Sigma-Aldrich, anhydrous 99.5%), hydrogen cyanide (HCN, preparation discussed later), or acetonitrile (CH₃CN, Sigma-Aldrich, \geq 99.9 %). Flow controllers (MKS #1479A) were used to maintain a constant pressure inside the drift cell within ± 1 mTorr. The temperature of the drift cell was controlled to ± 1 K using four temperature controllers. To cool the drift cell, liquid nitrogen was used by flowing it through solenoid valves. The reaction products that exit the drift cell were identified by scanning a second quadrupole mass-filter located after the drift cell and arrival time distributions (ATDs) were collected by monitoring the intensity of each ion as a function of time. The injection energies used in experiments (10-14 eV, laboratory frame) are only slightly higher than the minimum energies required to introduce the ions against the neutral reactant/He vapor mixture outflow at the drift cell entrance orifice. Most ion thermalization occurred outside of the drift cell by collisions with the gas mixture molecules escaping the drift cell entrance orifice.

The HCN gas used for experiments was prepared by sealing 5-8 g of NaCN (Sigma-Aldrich, 97 %) in a 500 mL stainless steel/glass bubbler. The solid was then pumped using an Edwards 30 mechanical pump (E2M, 250 V, 33.0 m³ hr⁻¹ pumping speed) to 20 Torr monitored by a Baratron pressure gauge (MKS-626A13TBD). Approximately 2.5-4 mL of pure sulfuric acid (H₂SO₄, Sigma-Aldrich, 99.999%) was added to the bubbler via a stainless steel tube extension on the bubbler fitted with valves on each side to ensure vacuum of the NaCN. The sulfuric acid was then “dropped” into the bubbler where it reacted with the NaCN immediately producing HCN gas.

The equilibrium reaction that all experiments followed throughout this series of studies in this chapter is represented by Equation 4.1:



where B is the neutral molecule: H₂O, CH₃OH, EtOH, 1-PrOH, 2-PrOH, 1-BuOH, 2-BuOH, HCN, or CH₃CN respectively. This reaction is said to be in equilibrium when: (1) the ATDs of the product and reactant ions have equal arrival times and (2) there is a constant ratio of the integrated intensities of product and reactant ion over a range of drift cell field voltage thus changing the residence time of the ions at a constant temperature and pressure. Once equilibrium is established, the equilibrium constant, K_{eq} , is measured using the equation:

$$K_{\text{eq}} = \frac{[\text{C}_{10}\text{H}_8^{*\cdot+}(\text{B})_n]}{[\text{C}_{10}\text{H}_8^{*\cdot+}(\text{B})_{n-1}][\text{B}]} = \frac{I_{[\text{C}_{10}\text{H}_8^{*\cdot+}(\text{B})_n]}}{I_{[\text{C}_{10}\text{H}_8^{*\cdot+}(\text{B})_{n-1}]}P_{\text{B}}} \quad (4.2)$$

where $I_{[\text{C}_{10}\text{H}_8^{*\cdot+}(\text{B})_n]}$ and $I_{[\text{C}_{10}\text{H}_8^{*\cdot+}(\text{B})_{n-1}]}$ are the integrated intensities of the ATDs of the reactant and product ions or the intensity of the ion peak on a mass spectrum and P_{B} is the partial pressure of the neutral vapor in atmospheres inside the drift cell. The equilibrium constant is measured at different temperatures to form a van't Hoff plot (using the van't Hoff equation as shown in Equation 3.5) where the ΔH° and ΔS° values are obtained from the slope and intercept respectively. All data was repeated at least three times with average values used in discussion.

4.3. Theoretical Calculations

Density functional theory calculations of the lowest energy structures for the various structural isomers of the cluster ions were performed using the Gaussian 03 and Gaussian 09 program suite.^{129,130} The $(\text{C}_{10}\text{H}_8^{*\cdot+})(\text{H}_2\text{O})_n$ and $(\text{C}_{10}\text{H}_8^{*\cdot+})(\text{CH}_3\text{OH})_n$ for $n = 1-6$ and the $(\text{C}_{10}\text{H}_8^{*\cdot+})(\text{ROH})_n$ for R=Et, 1-Pr, 2-Pr, 1-Bu, and 2-Bu and $n = 1-3$ were performed at the B3LYP/6-311++G^{**} level of theory using the Gaussian 03 program suite.¹²⁹ Calculations of the

(C₁₀H₈^{•+})(H₂O) and (C₁₀H₈^{•+})(CH₃OH) complexes were also carried out at the M06-2X/6-311++G(d,p) level using the Gaussian 09 program suite for comparison with the B3LYP method.¹³⁰ Calculations for the cluster ions (C₁₀H₈^{•+}(HCN)_n and (C₁₀H₈^{•+})(CH₃CN)_n for n = 1-2 were performed using the M06-2X and ω97XD methods within the 6-311++G** basis set of the Gaussian 09 program suite.^{79,80,130,135-137} For the larger clusters of C₁₀H₈^{•+}(HCN)_n and C₁₀H₈^{•+}(CH₃CN)_n for n = 3-6, B3LYP/6-311++G** calculations were performed using the Gaussian 09 program suite.¹³⁰ Vibrational frequency calculations were also performed for all the optimized geometries at the same level of theory in order to obtain zero point vibrational energy (ZPVE) and to verify the absence of imaginary frequencies.¹³⁰ For all calculations the binding energy (ΔE) was calculated at 0 K and was calculated using the equation:

$$\Delta E_{[(C_{10}H_8^{•+})(B)_n]} = \left(E_{[(C_{10}H_8^{•+})(B)_{n-1}]} + E_{[B]} \right) - E_{[(C_{10}H_8^{•+})(B)_n]} \quad (4.3)$$

where $E_{[(C_{10}H_8^{•+})(B)_{n-1}]}$, $E_{[B]}$, $E_{[(C_{10}H_8^{•+})(B)_n]}$ and are the total electronic energies of the lowest energy isomers of the reactant ion, neutral molecule represented by B, and the product of the reaction shown in equation 4.1. Corrections to the basis set superposition error (BSSE) were only made for the C₁₀H₈^{•+}(H₂O) and C₁₀H₈^{•+}(CH₃OH) complexes because the corrections were small (0.5-0.7 kcal/mol)

4.4. Results and Discussion

This discussion divides the results into five systems with each section containing the results for the interactions of the naphthalene radical cation with a neutral polar molecule or class of neutral molecules. These sections are: (1) water; (2) methanol; (3) 2, 3, and 4 carbon alcohols (EtOH, 1-PrOH, 2-PrOH, 1-BuOH, and 2-BuOH); (4) hydrogen cyanide; and (5) acetonitrile. A comparison of these interactions in general follows the results.

4.4.1. Study of the Energies and Structures of the Stepwise Hydration of the Naphthalene Radical Cation

4.4.1.1. Mass Spectra and Thermochemical Results for the Hydration of Naphthalene^{•+}

The mass spectra obtained following the injection of mass-selected naphthalene radical cations ($C_{10}H_8^{\bullet+}$, $Naph^+$) into the drift cell containing He or a mixture of water vapor (H_2O , W) and He are shown in Figure 6. A reference mass spectrum of $C_{10}H_8^{\bullet+}$ injected into the drift cell containing only He (Figure 6a) shows that only the naphthalene radical cation is present at $m/z = 128$. In the presence of 0.60 Torr H_2O vapor (W) mixed with He in the drift cell at 298 K (Figure 6b), the first association product $C_{10}H_8^{\bullet+}(H_2O)$ ($m/z = 146$) is present along with small intensities corresponding to the clusters $C_{10}H_8^{\bullet+}(H_2O)_n$ for $n = 2-4$ ($m/z = 164, 182, \text{ and } 200$ respectively) and protonated water clusters $H^+(H_2O)_n$ for $n = 6-11$ ($m/z = 109, 127, 145, 163, 181, \text{ and } 199$ respectively). Upon further cooling of the drift cell, the intensity of the $C_{10}H_8^{\bullet+}(H_2O)$ cluster increases and at 249 K (Figure 6d), small peaks corresponding to $C_{10}H_8^{\bullet+}(H_2O)_n$ clusters for $n = 2-6$ ($m/z = 164, 182, 200, 218, \text{ and } 236$ respectively) are detected. In addition, protonated water clusters, $H^+(H_2O)_n$ for $n = 7-13$ ($m/z = 127, 145, 163, 181, 199, 217, \text{ and } 235$ respectively), are present when cooling the drift cell. The presence of very small ion intensities of the protonated water clusters is most likely due to the injection energies of the injected naphthalene radical cations, which could induce the ionization of water inside the drift cell followed by proton transfer to form the observed protonated water clusters.

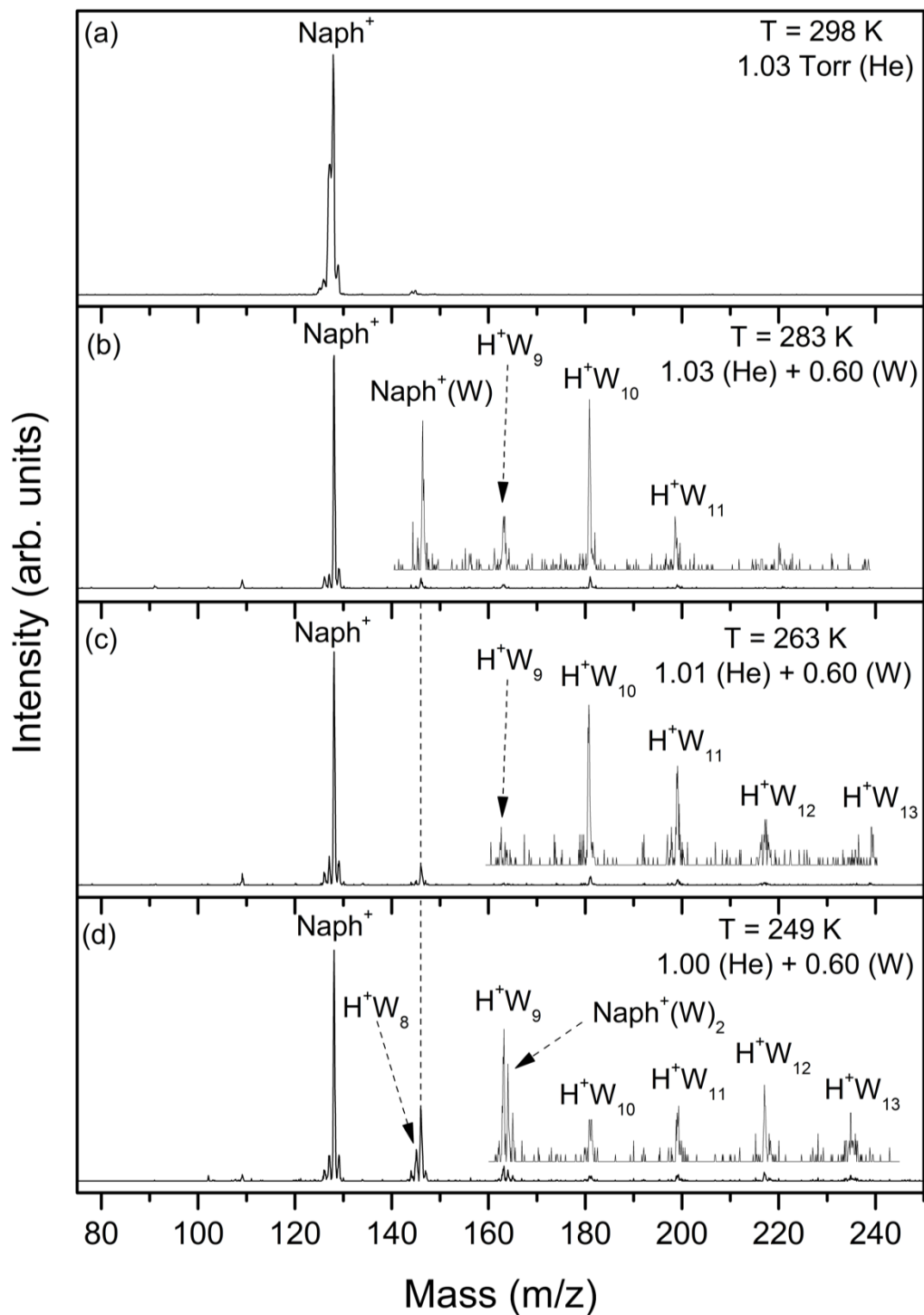
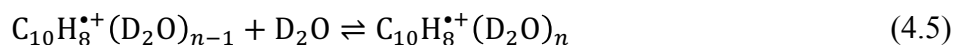
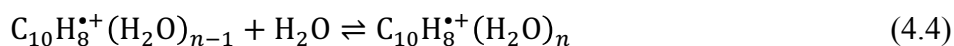


Figure 6. Mass spectra obtained resulting from the injection of the mass-selected naphthalene radical cation ($\text{C}_{10}\text{H}_8^{+\cdot}$, Naph^+) into He gas (a) or He/water (H_2O , W) vapor mixture (b-d) at different pressures (Torr) and temperatures (K) as indicated.

The association reactions of water (H₂O and D₂O) with the naphthalene radical cation are represented by Equations 4.4 and 4.5:



The equilibrium constants are measured for Equations 4.4 and 4.5 using Equation 4.2 by obtaining the peak intensities of the naphthalene radical cation (C₁₀H₈^{•+}) and the first association product (C₁₀H₈^{•+}(W) for W = H₂O or D₂O), and the pressure of the water. By taking the equilibrium constants at different temperatures, a van't Hoff plot for the formation of the C₁₀H₈^{•+}(W) (for W = H₂O or D₂O) cluster using Equation 3.5 is produced as shown in Figure 7. The resulting -ΔH° and -ΔS° values for C₁₀H₈^{•+}(H₂O) are obtained from the slope and intercept of the van't Hoff plot respectively are 7.8 ± 1 kcal mol⁻¹ and 19.5 ± 2 cal mol⁻¹ K⁻¹ (Figure 7a). The -ΔH° and -ΔS° values are obtained for C₁₀H₈^{•+}(D₂O) in the same manner (Figure 7b) and resulted in the values 8.0 ± 1 kcal mol⁻¹ and 19.9 ± 2 cal mol⁻¹ K⁻¹ for the -ΔH° and -ΔS° respectively. The results using D₂O are the same as those obtained for H₂O showing that the isotope effect is smaller than the experimental accuracy of ± 1 kcal mol⁻¹. The thermochemistry results for the naphthalene radical cation are very similar to that of benzene suggesting a similar mechanism of binding.⁹

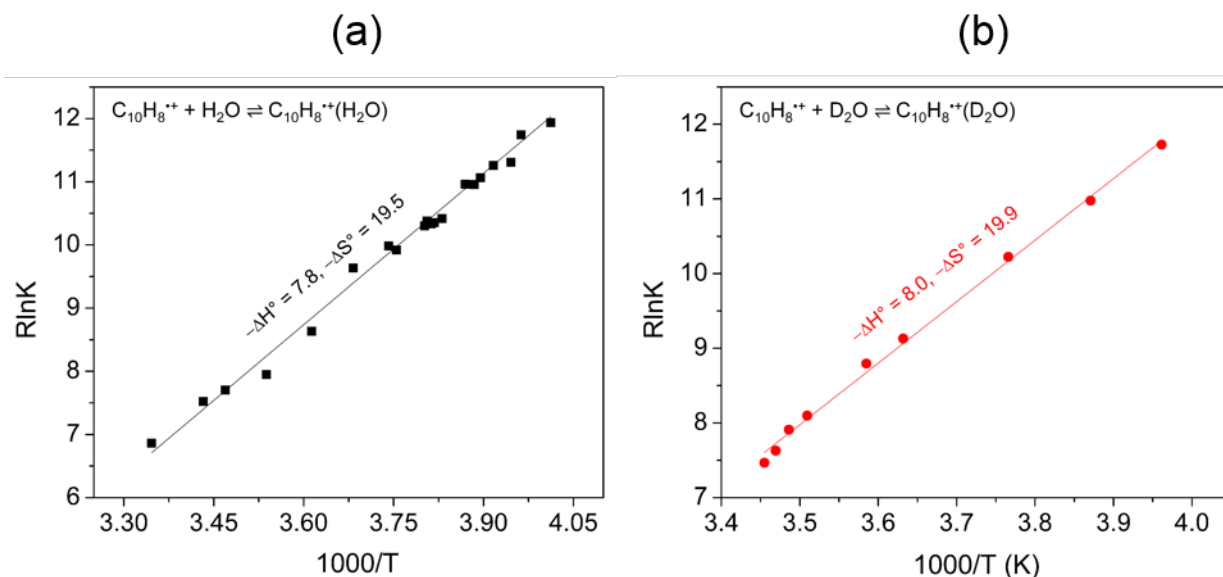


Figure 7. van't Hoff plots for the temperature dependence of the equilibrium constants of the association reaction of naphthalene radical cation with water where H₂O is shown in (a) and D₂O shown in (b). The resulting $-\Delta H^\circ$ and $-\Delta S^\circ$ are in (kcal mol⁻¹) and (cal mol⁻¹ K⁻¹) respectively. The error for the measurements are ± 1 kcal mol⁻¹ for $-\Delta H^\circ$ and ± 2 cal mol⁻¹ K⁻¹ for $-\Delta S^\circ$.

4.4.1.2. Calculated Structures and Binding Energies for Naphthalene^{•+}(H₂O)_n Clusters

The calculated structures and binding energies (ΔE) and enthalpies ($-\Delta H$ calc) of the four lowest energy isomers for the C₁₀H₈^{•+}(H₂O) cluster at the B3LYP/6-311++G** level are shown in Figure 8a. These calculations as well as subsequent calculations in this chapter were performed by Dr. Isaac Kwame Attah. The lowest energy isomers have bifurcated structures with the water bonding to two CH^{δ+} hydrogens as shown in Figure 8a(i) and a(ii) via an ionic hydrogen bonding (IHB). This bifurcated structure is similar to what is observed for the hydrated benzene radical cation.^{9,138} The other two structures shown have a single IHB, Figure 8a(iii), and an ion-dipole structure, Figure 8a(iv), with the water molecule above the plane of the naphthalene radical cation.

The structures with IHBs, Figure 8a(i-iii), have significantly larger binding energies than the ion-dipole structure, Figure 8a(iv). The results indicate that the structure of the C₁₀H₈^{•+}(H₂O) complex is most likely the bifurcated structures seen in Figure 8a(i) and a(ii) with calculated

binding energies of 7.7 and 6.8 kcal mol⁻¹ and calculated enthalpies of 7.8 and 6.7 kcal mol⁻¹ respectively. These values are in agreement with the experimentally determined value of 7.8 ± 1 kcal mol⁻¹. These structures are interesting because the structures with two IHBs of 2.3 Å for Figure 8a(ii) and 2.4 Å and 2.6 Å for Figure 8a(ii) between the two CH^{δ+} centers of the naphthalene cation and the oxygen atom of the water molecule have slightly higher binding energies than the structure with the shorter 2.1 Å IHB. All three IHB structures, Figure 8a(i)-(iii), have similar energies and with the possibility of small entropy contributions suggests that all three may be present in the experimental measurements.

The binding energy of the lowest energy isomer of the C₁₀H₈⁺⁺(H₂O) complex was also calculated using the M06-2X method. This calculation results in a binding energy higher in value than that calculated by B3LYP (9.3 kcal mol⁻¹ vs 7.7 kcal mol⁻¹ respectively, Table 1). This calculated result is also higher than the experimental value of 7.8 ± 1 kcal mol⁻¹. When considering the experimental uncertainty of ± 1 kcal mol⁻¹, the two calculated values appear similar, but the B3LYP correctly predicts the binding energy.⁵⁶ This is unlike most cases where weak van der Waals (vdW) interactions are predicted since the M06-2X method is more accurate than the B3LYP method in those structure.^{65,79,108}

Table 1. Experimental thermochemistry (ΔH° and ΔS°)^a for the formation of C₁₀H₈⁺⁺(H₂O) and C₁₀H₈⁺⁺(D₂O) clusters and the calculated binding energies (ΔE , corrected ZPVE) and enthalpies ($-\Delta H$ calc) at the B3LYP/6-311++G** (ΔE and $-\Delta H$ calc) and M06-2X/6-311++G** (ΔE only) levels of C₁₀H₈⁺⁺(H₂O)_n for n = 1-6.

Cluster	$-\Delta H^\circ$	$-\Delta S^\circ$	ΔE (B3LYP)	ΔE (M06-2X)	$-\Delta H$ (Calc)
C ₁₀ H ₈ ⁺⁺ (H ₂ O)	7.8	19.5	7.7 (7.1) ^b	9.3	7.8
C ₁₀ H ₈ ⁺⁺ (D ₂ O)	8.0	19.9	-	-	-
C ₁₀ H ₈ ⁺⁺ (H ₂ O) ₂	-	-	8.4	-	8.6
C ₁₀ H ₈ ⁺⁺ (H ₂ O) ₃	-	-	7.8	-	8.2
C ₁₀ H ₈ ⁺⁺ (H ₂ O) ₄	-	-	7.6	-	7.9
C ₁₀ H ₈ ⁺⁺ (H ₂ O) ₅	-	-	7.4	-	7.7
C ₁₀ H ₈ ⁺⁺ (H ₂ O) ₆	-	-	7.0	-	7.5

^a Units, estimated error: $\Delta H^\circ \pm 1$ kcal mol⁻¹ and $\Delta S^\circ \pm 2$ cal mol⁻¹ K⁻¹

^b Corrected for BSSE

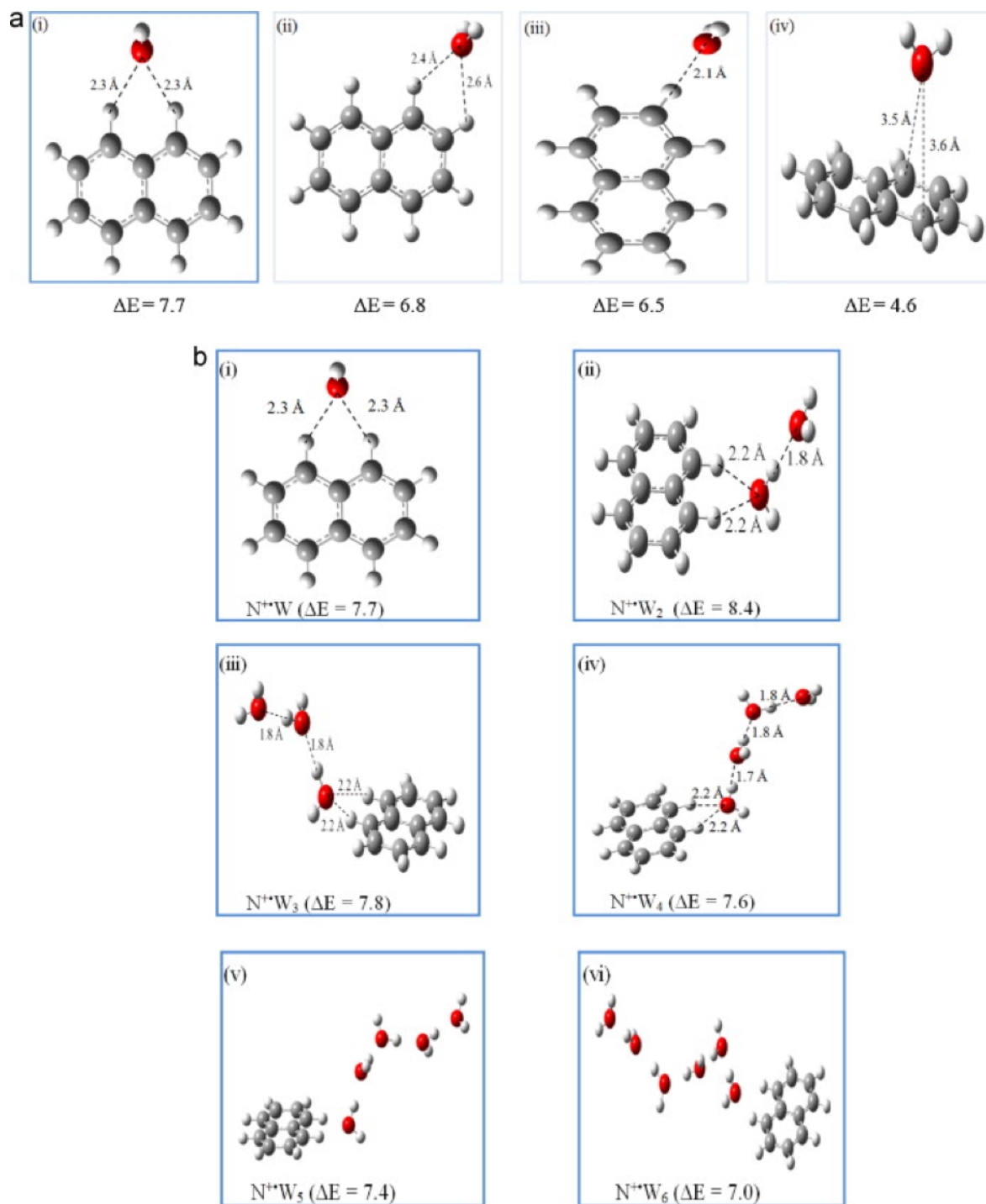


Figure 8. DFT structures and binding energies (ΔE , kcal mol⁻¹, calculated using Equation 4.3) of: (a) the four lowest energy isomers of the $C_{10}H_8^+(H_2O)$ cluster obtained at the B3LYP/6-311++G** level and (b) the lowest energy structures of the $C_{10}H_8^+(H_2O)_n$ clusters for $n = 1-6$ obtained at B3LYP/6-311++G** level.

The structure of a second water adding to the naphthalene radical cation to form the $C_{10}H_8^{++}(H_2O)_2$ complex forms an “*externally solvated*” structure (shown in Figure 8b(ii)) where the two water molecules hydrogen bond to each other forming a dimer with the naphthalene radical cation is external to this dimer. The calculated binding energy of this isomer is $8.4 \text{ kcal mol}^{-1}$ and the calculated enthalpy is $8.6 \text{ kcal mol}^{-1}$. For the “*internally solvated*” structure, both water molecules are bonded to the naphthalene radical cation making the ion “inside” the solvent (water in this case). When compared to “*internally solvated*” structures (Figure 9b-d), the calculated binding energy of the “*externally solvated*” isomer is higher by 1.2, 2.1, and $2.6 \text{ kcal mol}^{-1}$ with similar difference observed with the calculated enthalpies.

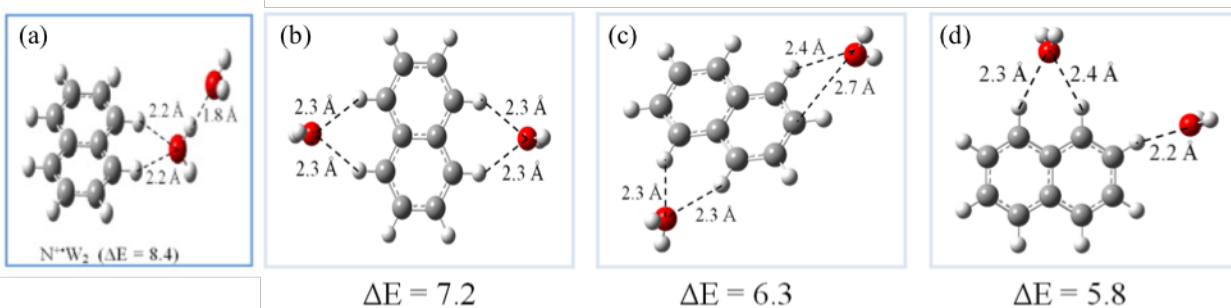


Figure 9. DFT structures and binding energies (ΔE , kcal mol^{-1} , calculated using Equation 4.3) for (a) the lowest energy “*externally solvated*” isomer of the $C_{10}H_8^{++}(H_2O)_2$ cluster and (b-d) higher energy “*internally solvated*” isomers with corresponding binding energies.

The calculated lowest energy isomer of the third addition of water to the naphthalene radical cation to form the $C_{10}H_8^{++}(H_2O)_3$ cluster, shown in Figure 8b(iii), shows the third water adding to the hydrogen bonded chain of water molecules to continue to “*externally solvate*” the naphthalene radical cation. The calculated binding energy is $7.8 \text{ kcal mol}^{-1}$ and the calculated enthalpy is slightly higher at $8.2 \text{ kcal mol}^{-1}$. Other higher energy isomers are shown in Figure 10b-d. A second “*externally solvated*” structure is calculated with a bifurcated structure where a central water molecule is bonded to two CH groups of the naphthalene radical cation and the other two water molecules are bound to separate hydrogen atoms of the the central water. This structure,

shown in Figure 10c, has a calculated binding energy and enthalpy of 6.7 kcal mol⁻¹. Two additional structures are calculated with the naphthalene radical cation being both “*internally*” and “*externally solvated*.” These structures, shown in Figure 10b and d, have binding energies and enthalpies of 6.9 and 6.0 kcal mol⁻¹ respectively. Here two water molecules “*internally solvating*” the naphthalene radical cation and a third “*externally solvation*” the cation via hydrogen bonding to one of the water molecules.

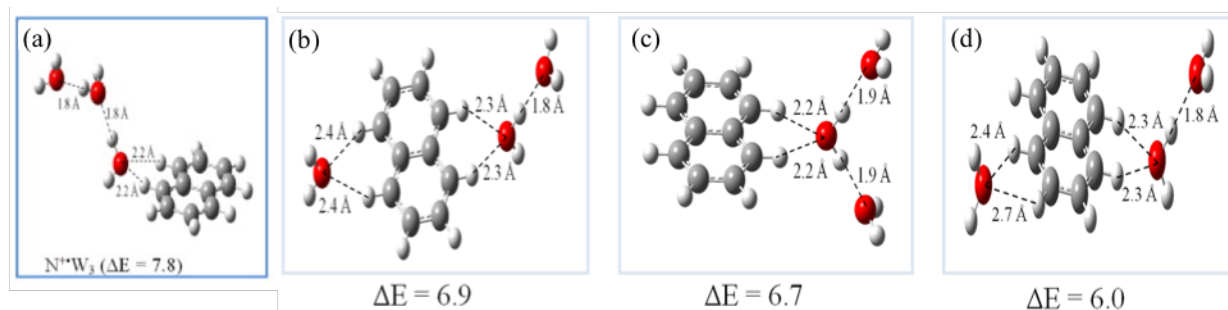


Figure 10. DFT structures and binding energies (ΔE , kcal mol⁻¹, calculated using Equation 4.3) for (a) the lowest energy “*externally solvated*” isomer of the C₁₀H₈⁺(H₂O)₃ cluster and (b-d) higher energy isomers with corresponding binding energies.

The calculated lowest energy isomer for the C₁₀H₈⁺(H₂O)₄ cluster, shown in Figure 8b(iv), has a calculated binding energy of 7.6 kcal mol⁻¹ and calculated enthalpy of 7.9 kcal mol⁻¹. This structure consists of a hydrogen-bonded chain of four water molecules attached to the naphthalene radical cation by two IHB from the oxygen atom of the first water in the chain to two CH^{δ+} groups of the naphthalene radical cation. This “*external solvation*” pattern continues for higher energy isomers (Figure 11c and d), but with different arrangements of the water molecules within the hydrogen bonded tetramer. These isomers were calculated to have calculated binding energies and enthalpies of 6.3 and 6.2 kcal mol⁻¹ respectively. A third higher energy isomer was calculated to have a mixed “*internal*” and “*external solvation*” structure, shown in Figure 11b, and has a binding energy of 6.8 kcal mol⁻¹ and calculated enthalpy of 6.7 kcal mol⁻¹.

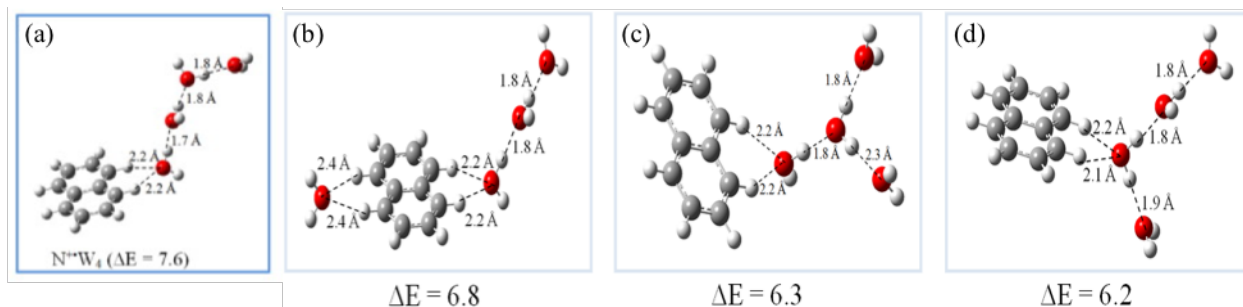


Figure 11. DFT structures and binding energies (ΔE , kcal mol⁻¹, calculated using Equation 4.3) for (a) the lowest energy isomer of the $C_{10}H_8^{++}(H_2O)_5$ cluster and (b-d) higher energy isomers with corresponding binding energies.

The pattern of “*external solvation*” continues for the calculated lowest energy isomers for $C_{10}H_8^{++}(H_2O)_5$ and $C_{10}H_8^{++}(H_2O)_6$ clusters. The structures for the lowest energy isomers of these clusters are shown in Figure 8b(v) and (vi) and have calculated binding energies of 7.4 and 7.0 kcal mol⁻¹ and calculated enthalpies of 7.7 and 7.5 kcal mol⁻¹ respectively. Higher energy isomers for both $C_{10}H_8^{++}(H_2O)_5$ and $C_{10}H_8^{++}(H_2O)_6$ clusters are shown in Figure 12 and Figure 13 respectively. In both cases, no cyclic structures among the water molecules are formed. Favorable structures appear to be those with extended hydrogen bonded chains where subsequent water additions have constant binding energies for $C_{10}H_8^{++}(H_2O)_n$ clusters and little change from 8 kcal mol⁻¹ for $n = 1-4$ to 7 kcal mol⁻¹ for $n = 5$ and 6.⁶⁹ This type of binding is similar to the binding energy of non-cyclic chain IHB clusters to the energy of a neutral water-water hydrogen bond of 5 kcal mol⁻¹ after 4-6 solvent molecules because the ionic interaction decreases as the number of solvent molecules increases.^{64,69}

Hydrated clusters of protonated molecules (such as H_3O^+) have different bonding behavior than that of a neutral water chain. Here the first four binding energies usually decrease significantly before reaching the vaporization of bulk water (10 kcal mol⁻¹). This convergence involves the formation of two neutral water-water hydrogen bonds in three-dimensional structures.⁶⁴ Since the energy change in the stepwise hydration of both $C_6H_6^{++}(H_2O)_n$ and $C_{10}H_8^{++}(H_2O)_n$ is relatively

constant in binding energy compared to protonated species, the notion of non-cyclic water structures is supported.

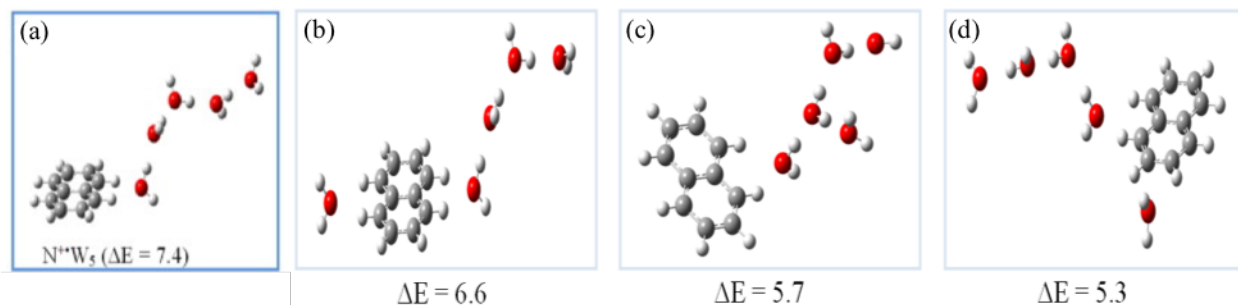


Figure 12. DFT structures and binding energies (ΔE , kcal mol⁻¹, calculated using Equation 4.3) for (a) the lowest energy isomer of the $C_{10}H_8^+(H_2O)_5$ cluster and (b-d) higher energy isomers with corresponding binding energies.

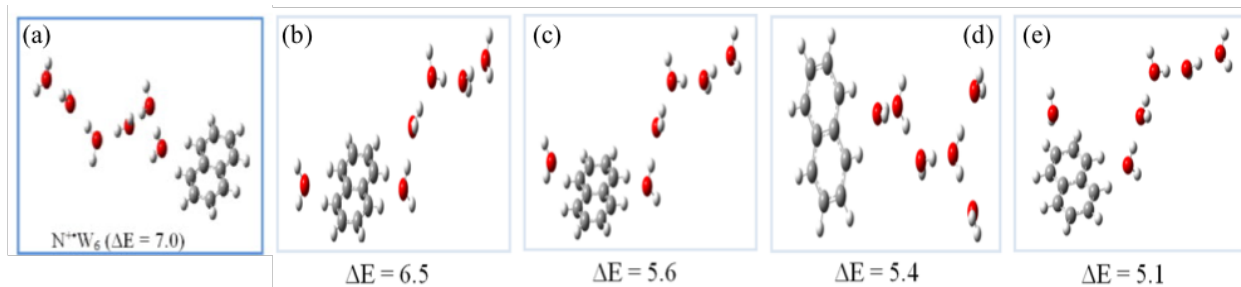


Figure 13. DFT structures and binding energies (ΔE , kcal mol⁻¹, calculated using Equation 4.3) for (a) the lowest energy isomer of the $C_{10}H_8^+(H_2O)_6$ cluster and (b-d) higher energy isomers with corresponding binding energies.

Although cyclic water structures are not seen in $C_6H_6^+(H_2O)_n$ clusters, for clusters $n \leq 4$ the structures tend to be “*internally solvated*” compared to the “*externally solvated*” $C_{10}H_8^+(H_2O)_n$ clusters. This means that conventional hydrogen bonding in water is more favorable than the unconventional IHB between the $CH^{\delta+}$ sites of the naphthalene radical cation. This “*external solvation*” for naphthalene (and by extrapolation larger PAH molecules) suggests that the large organic molecule remains accessible on the surface of water nanodroplets. This has implications in regard to the reactivity of large PAH ions in interstellar medium since the ion can interact with incoming small molecules under UV irradiation. These interactions can lead to the formation of complex organics on the surface of these icy grains.⁵⁶

4.4.2. Study of the Energies and Structures of the Stepwise Solvation of Naphthalene^{•+} with Methanol

4.4.2.1. Mass Spectra and Thermochemical Results for Naphthalene^{•+}(CH₃OH)_n Clusters

The mass spectra obtained following the injection of mass-selected naphthalene radical cation (C₁₀H₈^{•+}, Naph^{•+}) into the drift cell containing He or a mixture of methanol (CH₃OH, M) and He are shown in Figure 14. A reference mass spectrum of C₁₀H₈^{•+} into the drift cell containing only He (Figure 14a) shows that only the naphthalene radical cation is present at $m/z = 128$ at 298 K. In the presence of 0.51 Torr of methanol vapor (M) mixed with He in the drift cell at 299 K (Figure 14b), the protonated methanol cluster H⁺(CH₃OH)₅ is present ($m/z = 161$), but no association products of methanol to the naphthalene radical cation are observed. The first association product, C₁₀H₈^{•+}(CH₃OH) ($m/z = 160$), is present when the drift cell is cooled to 279 K (Figure 14c) along with protonated methanol clusters H⁺(CH₃OH)_n for $n = 5$ and 6 ($m/z = 161$ and 193). When the drift cell is cooled to 249 K (Figure 14e), the C₁₀H₈^{•+}(CH₃OH)_n for $n = 1$ and 2 ($m/z = 160$ and 192) and protonated methanol clusters H⁺(CH₃OH)_n for $n = 5-7$ ($m/z = 161, 193,$ and 225 respectively) are observed. At lower temperatures (below 240 K), the intensities of the peaks associated with naphthalene, C₁₀H₈^{•+} and C₁₀H₈^{•+}(CH₃OH)_n for $n = 1, 2$, decrease and eventually disappear at 238 K. At this point, only protonated methanol clusters H⁺(CH₃OH)_n for $n = 5-9$ ($m/z = 161, 193, 225, 257,$ and 289) are observed along with small intensities of the C₁₀H₈^{•+}(CH₃OH)_n for $n = 3-5$ as shown in Figure 14f.

The injection energies of the naphthalene cations to induce ionization and proton transfer does not explain the simultaneous disappearance of the naphthalene-containing ions and the appearance of the protonated methanol clusters H⁺(CH₃OH)_n for $n \geq 5$ at temperatures less than 240 K. This type of result suggests that the larger C₁₀H₈^{•+}(CH₃OH)_n clusters for $n \geq 5$ undergo intracuster dissociative proton transfer (DPT) reactions to produce the large H⁺(CH₃OH) clusters

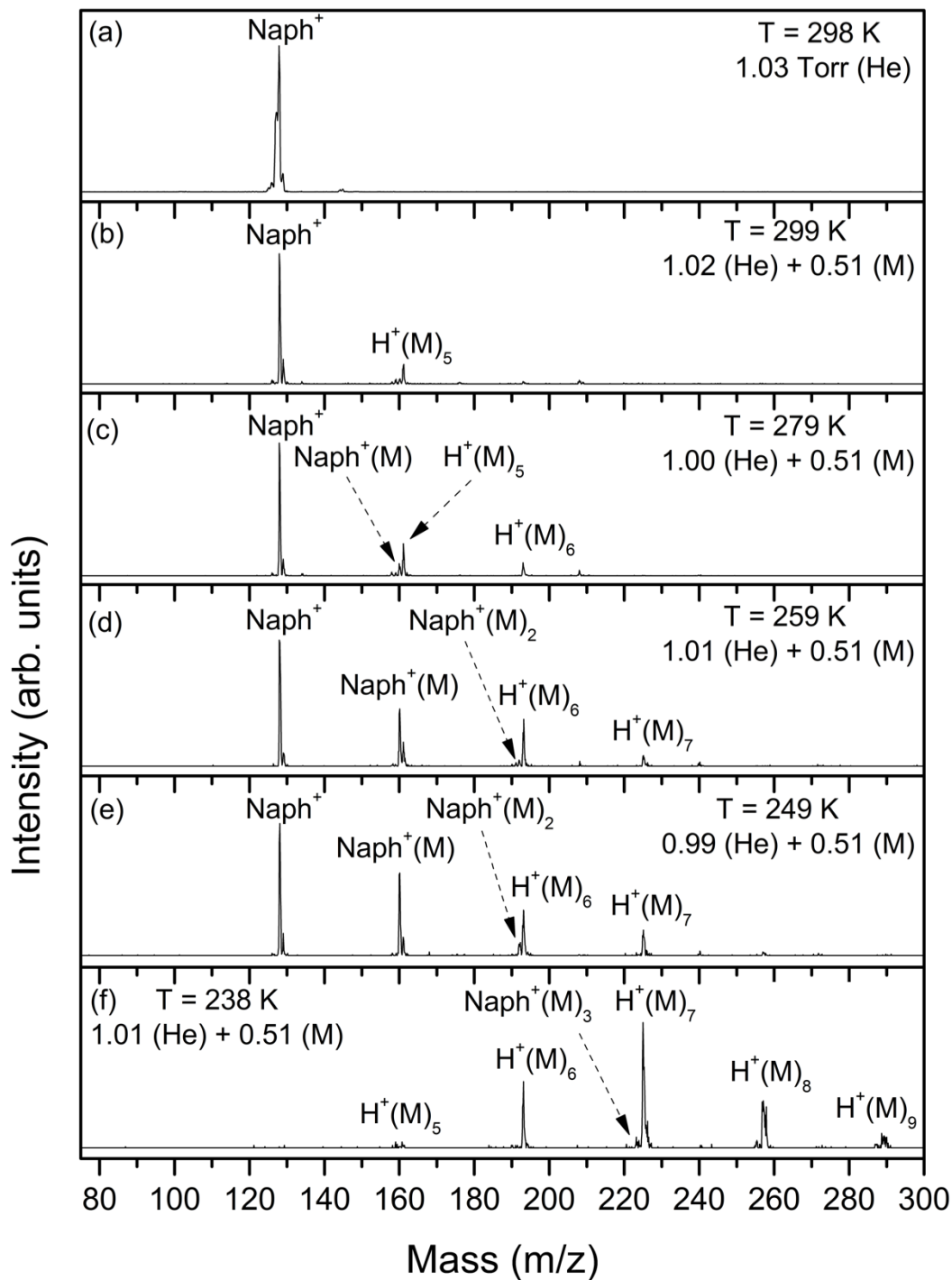
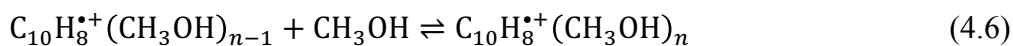


Figure 14. Mass spectra obtained resulting from the injection of the mass-selected naphthalene radical cation ($\text{C}_{10}\text{H}_8^{+\cdot}$, Naph^+) into He gas (a) or He/methanol (M) vapor mixture (b-f) at different pressures (Torr) and temperatures (K) as indicated.

for $n = 5-9$ and the naphthalene radical ($C_{10}H_7^{\bullet}$) based on the mass spectrum shown in Figure 14f.⁵⁶ This type of reaction is observed in the hydration of benzene in the clusters $C_6H_6^{*+}(H_2O)_n$ for $n \geq 4$.⁶⁹ The higher proton affinity (PA) of the naphthalene radical ($C_{10}H_7^{\bullet}$, 234 kcal mol⁻¹)¹³⁹ compared to the phenyl radical ($C_6H_5^{\bullet}$, 212 kcal mol⁻¹)⁶⁹ and the higher PA of methanol (182 kcal mol⁻¹)^{2,140} compared to water (167 kcal mol⁻¹)^{2,140} make the PT reaction within the $C_{10}H_8^{*+}(CH_3OH)_n$ clusters exothermic at $n = 5$. Detailed explanation for this interaction is found in Section 4.4.2.3.

The association reaction of methanol to the naphthalene radical cation is represented by Equation 4.6:



The equilibrium constants are measured for this reaction using Equation 4.2 by obtaining the peak intensities of the naphthalene radical cation ($C_{10}H_8^{*+}$) and the association products, $C_{10}H_8^{*+}(CH_3OH)_n$ for $n = 1$ and 2, and the pressure of the methanol in the drift cell. By taking the equilibrium constants at different temperatures, a van't Hoff plot for the formation of $C_{10}H_8^{*+}(CH_3OH)_n$ cluster of $n = 1$ and 2 using Equation 3.5 is produced as shown in Figure 15. The resulting $-\Delta H^\circ$ and $-\Delta S^\circ$ values for Equation 4.6 are obtained from the slope and intercept of the van't Hoff plot respectively are 8.3 ± 1 kcal mol⁻¹ and 19.7 ± 2 cal mol⁻¹ K⁻¹ for the $C_{10}H_8^{*+}(CH_3OH)$ product and 8.6 ± 1 kcal mol⁻¹ and 23.1 ± 2 cal mol⁻¹ K⁻¹ for the $C_{10}H_8^{*+}(CH_3OH)_2$ product. These results are similar to those found with water suggesting the formation of a chain like structures are possible for $C_{10}H_8^{*+}(CH_3OH)_n$ for $n \leq 5$.⁵⁶

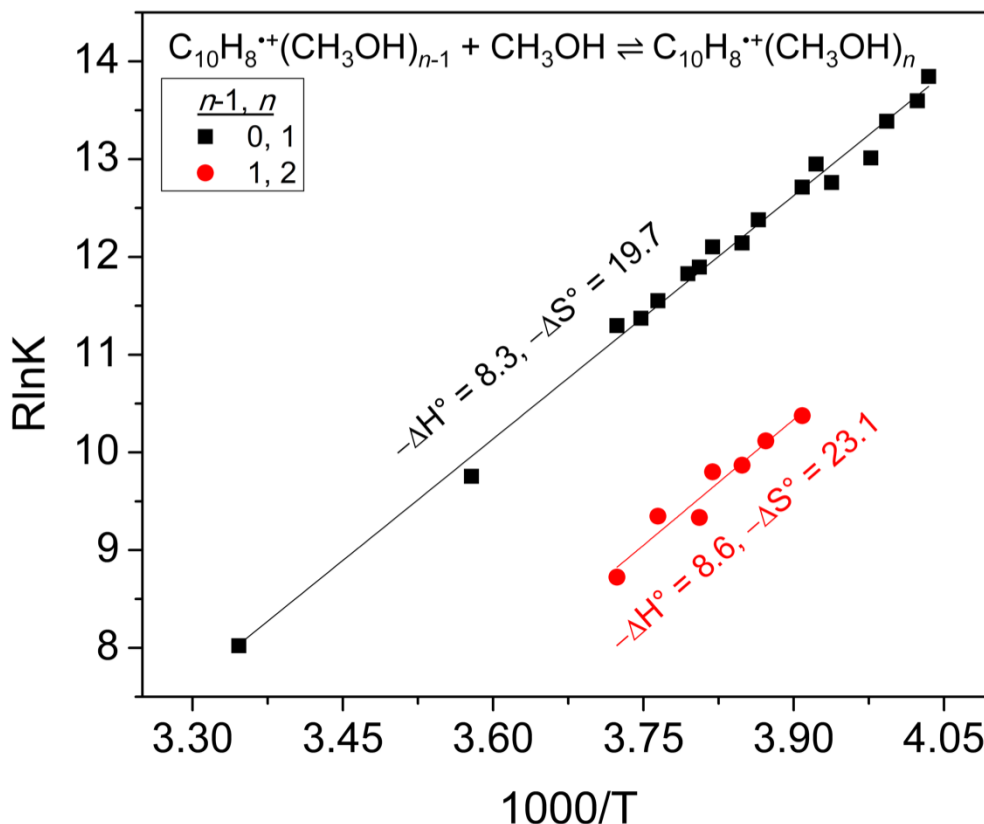


Figure 15. van't Hoff plots of the temperature dependence of the equilibrium constants for the association reaction of the naphthalene radical cation with methanol for the first and second solvation steps. The resulting $-\Delta H^\circ$ and $-\Delta S^\circ$ are in (kcal mol^{-1}) and ($\text{cal mol}^{-1} \text{K}^{-1}$) respectively. The error for the measurements are $\pm 1 \text{ kcal mol}^{-1}$ for $-\Delta H^\circ$ and $\pm 2 \text{ cal mol}^{-1} \text{K}^{-1}$ for $-\Delta S^\circ$.

4.4.2.2. Calculated Structures and Binding Energies for Naphthalene⁺(CH₃OH)_n Clusters

To support the experimental thermochemistry results, the calculated lowest energy structures for the $C_{10}H_8^+(CH_3OH)_n$ for $n = 1-6$ using B3LYP/6-311++G** are shown in Figure 16. The M06-2X method was also used and just as what is observed with water (see Section 4.4.1.2), the results slightly over estimate the interaction between the naphthalene radical cation and methanol when compared to the experimental results. These calculations were performed by Dr. Isaac Kwame Attah. For the $C_{10}H_8^+(CH_3OH)$ cluster (structure (i) in Figure 16), the calculated binding energy using the B3LYP method is $8.4 \text{ kcal mol}^{-1}$ and $9.9 \text{ kcal mol}^{-1}$ for the M06-2X compared to the experimental $-\Delta H^\circ$ value of $8.3 \pm 1 \text{ kcal mol}^{-1}$ and the calculated $-\Delta H$ of 7.9 kcal

mol^{-1} . This difference is due to the experimental $-\Delta H^\circ$ value being an ensemble of multiple isomers versus the calculated structure of a single isomer.

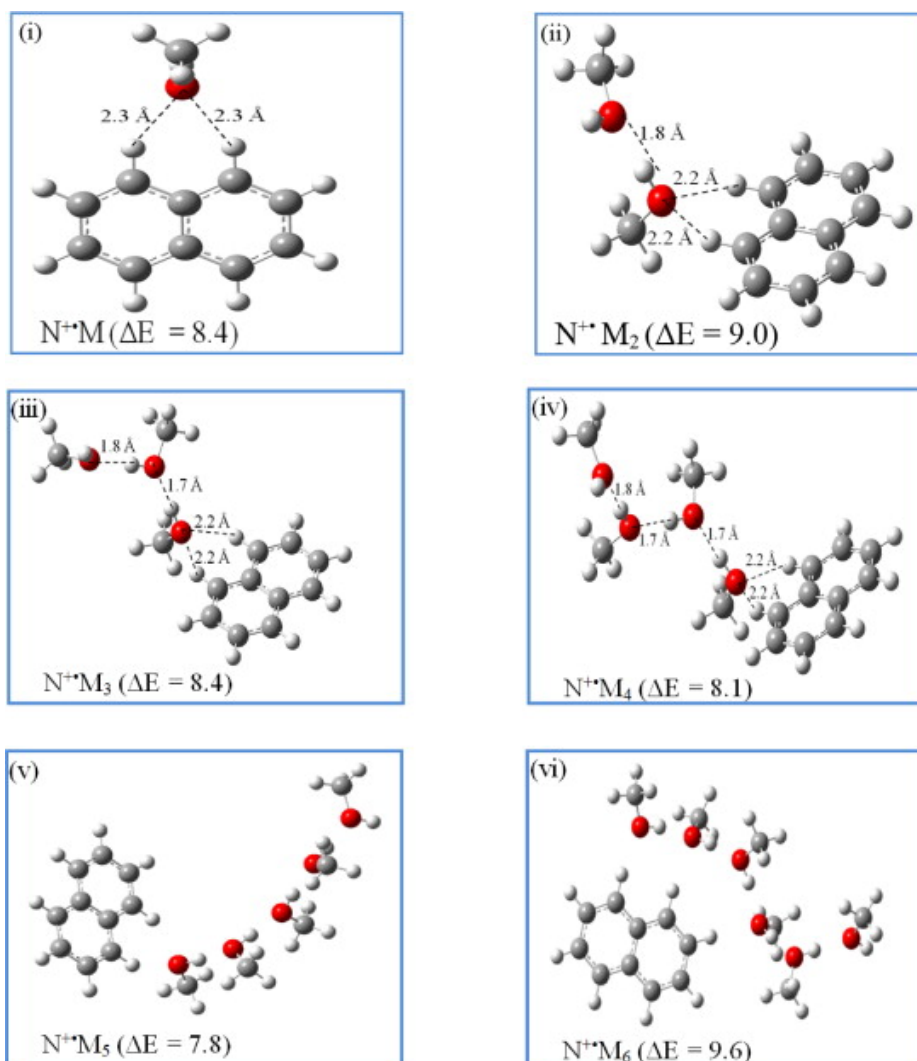


Figure 16. DFT structures and binding energies (ΔE , kcal mol^{-1} , calculated using Equation 4.3) of the lowest energy isomers of the lowest energy isomers of the $\text{C}_{10}\text{H}_8^{+\bullet}(\text{CH}_3\text{OH})_n$ clusters (N^+M_n) for $n = 1-6$ obtained at the B3LYP/6-311++G** level.

Structures of $\text{C}_{10}\text{H}_8^{+\bullet}(\text{CH}_3\text{OH})_n$ clusters for $n = 2-6$ are shown in Figure 16(ii)-(vi) and are similar to what is observed in the calculations for the hydrated naphthalene radical cation. The pattern of “*external solvation*” structures with hydrogen bonding chain are the lowest energy structures. The binding energies, ΔE , and calculated $-\Delta H$ for the stepwise solvation of the naphthalene radical cation by methanol remains relatively constant at $8 \pm 1 \text{ kcal mol}^{-1}$. A summary

of the individual binding energies along with comparisons to experimental values when available are summarized in Table 2. The hydrogen-bonded methanol chain that is attached to the naphthalene radical cation shown in Figure 16 (iv), (v), and (vi) is relevant to the deprotonation of the naphthalene radical cation by a methanol sub-cluster. This become exothermic in $C_{10}H_8^{*\cdot+}(CH_3OH)_n$ cluster for $n \geq 5$ as discussed in 4.4.2.3.

Table 2. Experimental thermochemistry (ΔH° and ΔS°)^a of the formation of $C_{10}H_8^{*\cdot+}(CH_3OH)_n$ clusters for $n = 1-2$ and the calculated binding energies (ΔE , corrected ZPVE) at the B3LYP/6-311++G** (ΔE and ΔH) and M06-2X/6-311++G** levels (ΔE only) for $C_{10}H_8^{*\cdot+}(CH_3OH)_n$ cluster for $n = 1-6$.

Cluster	$-\Delta H^\circ$	$-\Delta S^\circ$	ΔE (B3LYP)	ΔE (M06-2X)	$-\Delta H$ (Calc)
$C_{10}H_8^{*\cdot+}(CH_3OH)$	8.3	19.7	8.4 (7.8) ^b	9.9	7.9
$C_{10}H_8^{*\cdot+}(CH_3OH)_2$	8.6	23.1	9.0	-	8.7
$C_{10}H_8^{*\cdot+}(CH_3OH)_3$	-	-	8.4	-	8.3
$C_{10}H_8^{*\cdot+}(CH_3OH)_4$	-	-	8.1	-	7.8
$C_{10}H_8^{*\cdot+}(CH_3OH)_5$	-	-	7.8	-	7.5
$C_{10}H_8^{*\cdot+}(CH_3OH)_6$	-	-	9.6	-	9.5

^a Units, estimated error: $\Delta H^\circ \pm 1 \text{ kcal mol}^{-1}$ and $\Delta S^\circ \pm 2 \text{ cal mol}^{-1} \text{ K}^{-1}$

^b Corrected for BSSE

Figure 17 shows calculated structures of higher energy where a chain of three, four, or five methanol molecules are attached to one side of the naphthalene radical cation and the remaining methanol molecule forms a second bifurcated IHB on the opposite site of the cation. This is similar to the $C_{10}H_8^{*\cdot+}(H_2O)_n$ clusters for $n = 4-6$.

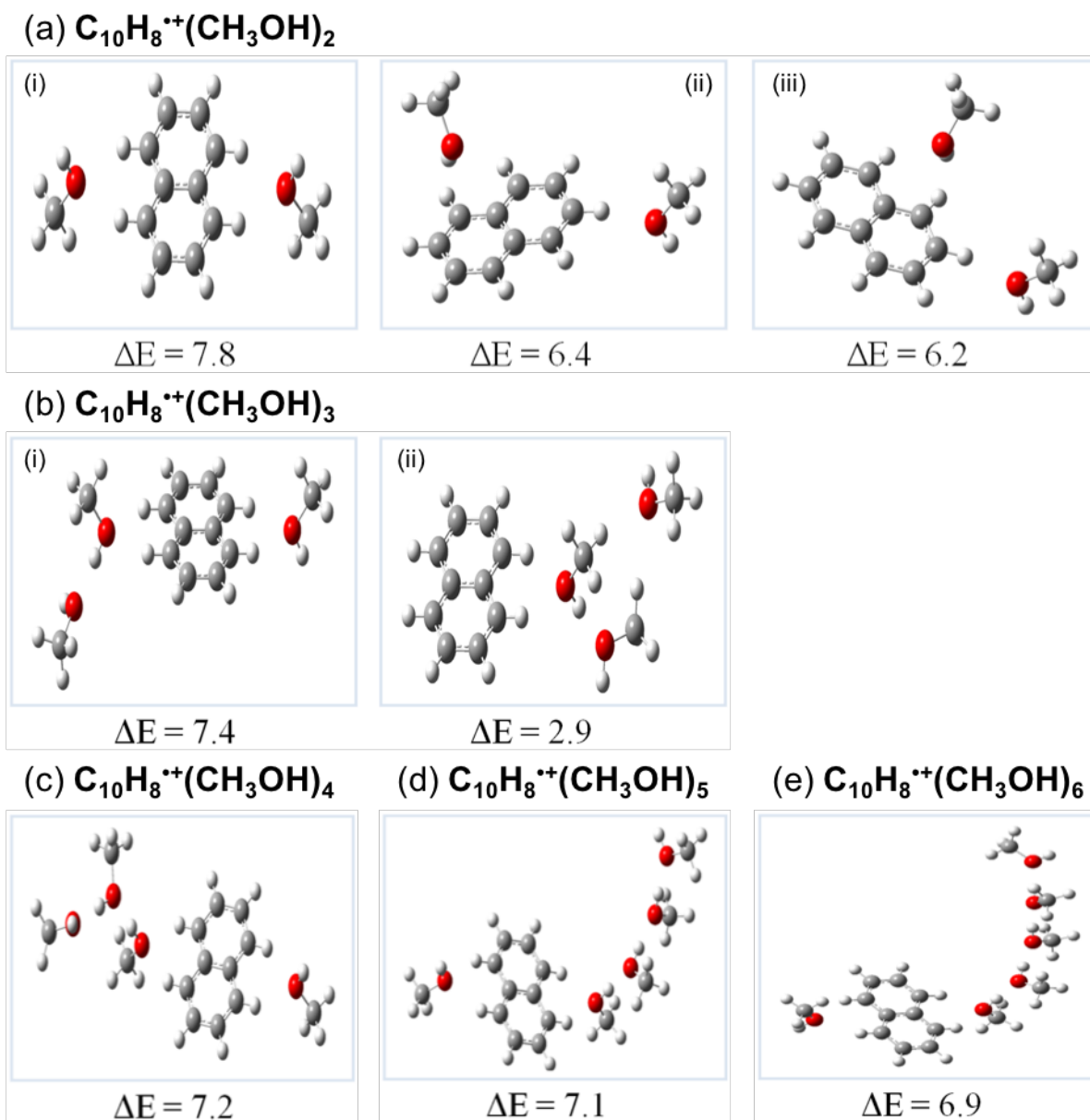


Figure 17. DFT Structures and binding energies (ΔE , kcal mol⁻¹, calculated using Equation 4.3) for higher energy isomers of the $C_{10}H_8^{++}(CH_3OH)_n$ clusters for $n = 2-6$ obtained at the B3LYP/6-311++G** level.

4.4.2.3. Deprotonation of Naphthalene⁺ by Methanol Clusters

As mentioned in previous sections, the mass spectra of $C_{10}H_8^{++}(CH_3OH)_n$ clusters at low temperatures suggest that larger clusters can undergo intracuster dissociative proton transfer (DPT) reactions to produce the protonated methanol clusters $H^+(CH_3OH)_n$ for $n \geq 5$ that are observed in Figure 14f. This series of intracuster DPT reactions can occur within the

$C_{10}H_8^{*\cdot}(CH_3OH)_n$ clusters if the proton transfer of the naphthalene radical cation to the methanol subcluster is exothermic. The energy from this proton transfer must also be sufficient enough to dissociate the now $C_{10}H_7^{\cdot} \cdots H^+(CH_3OH)_n$ cluster. The cluster size (n) of the $C_{10}H_8^{*\cdot}(CH_3OH)_n$ at which the proton transfer becomes exothermic can be determined by comparing the proton affinity (PA) of the naphthyl radical ($C_{10}H_7^{\cdot}$) and the methanol subcluster $(CH_3OH)_n$ for $n = 2-6$. The calculated PA for $C_{10}H_7^{\cdot}$ is $234.5 \text{ kcal mol}^{-1}$ and the calculated PA for methanol clusters $(CH_3OH)_n$ for $n = 2-6$ are 211, 224, 231, 234, and $237 \text{ kcal mol}^{-1}$ respectively.^{139,140} These results show that the PT from $C_{10}H_8^{*\cdot}$ to the $(CH_3OH)_n$ subcluster becomes thermoneutral at $n = 5$ and exothermic at $n > 5$. This type of interaction is not observed in $C_{10}H_8^{*\cdot}(H_2O)_n$ clusters because at $n = 6$ the PA for the $(H_2O)_6$ cluster is $217 \text{ kcal mol}^{-1}$ making the intracluster DPT endothermic.¹⁴⁰

The mass spectrum at 238 K (Figure 14f) supports these theoretical results where the signal for the naphthalene-containing ions disappears and only protonated methanol clusters $H^+(CH_3OH)_n$ for $n \geq 5$ are present. This indicates that at low temperatures, methanol molecules will cluster with the naphthalene radical cation to form $C_{10}H_8^{*\cdot}(CH_3OH)_n$ clusters and then the equilibrium shifts when $n \geq 5$. Here DPT occurs within the $C_{10}H_8^{*\cdot}(CH_3OH)_n$ cluster to generate naphthyl radical ($C_{10}H_7^{\cdot}$) and protonated methanol clusters $H^+(CH_3OH)_n$ of $n \geq 5$.⁵⁶

To investigate the structures of this intracluster DPT process, the structures of the clusters formed by the association of the naphthyl radical ($C_{10}H_7^{\cdot}$) with protonated methanol clusters ($H^+(CH_3OH)_n$ for $n = 4-6$) were calculated. Figure 18 shows the lowest energy structures and corresponding binding energies of the $C_{10}H_7^{\cdot} \cdots (CH_3OH)_{4-6}$ clusters. As the size of the cluster increases from $n = 4$ to $n = 6$, the binding energy of the protonated methanol cluster to the naphthyl radical decreases. For the $H^+(CH_3OH)_4$ cluster, the binding energy of the protonated methanol cluster to the naphthyl radical was calculated to be $6.5 \text{ kcal mol}^{-1}$ and decrease to $5.4 \text{ kcal mol}^{-1}$

for the $\text{H}^+(\text{CH}_3\text{OH})_5$ cluster and $4.5 \text{ kcal mol}^{-1}$ for the $\text{H}^+(\text{CH}_3\text{OH})_6$ cluster. This decrease in binding energy is explained by the fact that the charge of the protonated methanol cluster becomes more delocalized and further away from the naphthyl radical as the size of the subcluster increases thus decreasing the charge-induced dipole interaction between the naphthyl radical and the protonated methanol subcluster. When size of the protonated methanol subcluster becomes large enough, the effect of the charge is negligible and the binding energy is similar to that of the neutral system. The increase in size (n) of the methanol subcluster also results in the proton transfer interaction from the naphthalene radical cation to the methanol subcluster in $\text{C}_{10}\text{H}_8^{*\cdot}(\text{CH}_3\text{OH})_n$ to become more exothermic as n increases. Since the binding of the $\text{C}_{10}\text{H}_7^* \cdots \text{H}^+(\text{CH}_3\text{OH})_n$ clusters decreases with increasing n , the dissociation of the $\text{C}_{10}\text{H}_8^{*\cdot}(\text{CH}_3\text{OH})_n$ clusters into the naphthyl radical and protonated methanol clusters will occur at lower temperatures. This is what is observed in the mass spectrum shown in Figure 14f.

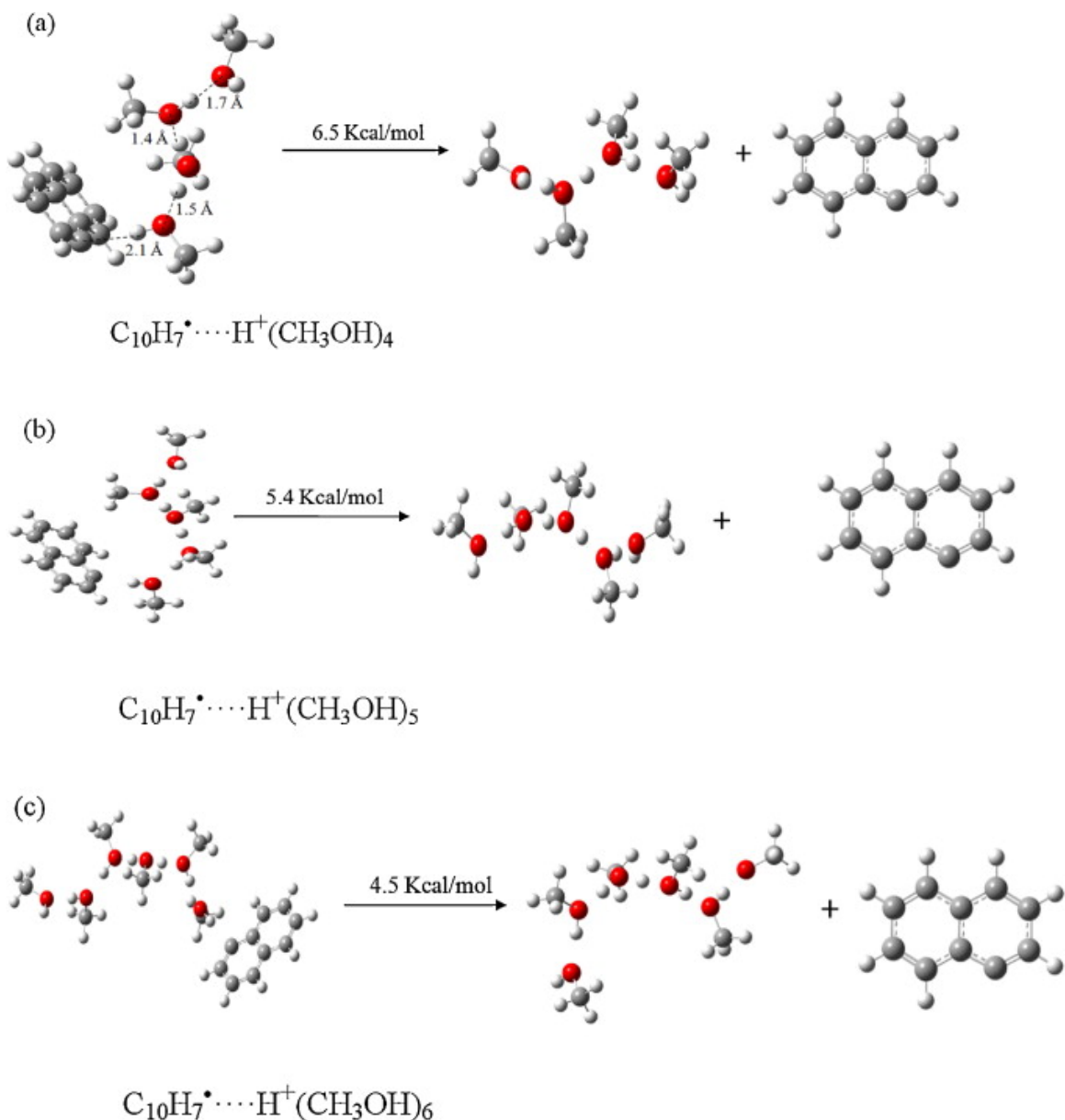


Figure 18. DFT structures and binding energies of the lowest energy structures of the $C_{10}H_7^+$ $H^+(CH_3OH)_n$ clusters for $n = 4-6$ as obtained at the B3LYP/6-311++G** level.

4.4.3. Study of the Energies and Structures of the Stepwise Solvation of Naphthalene^{•+} with Primary and Secondary Alcohols of 2, 3, and 4 Carbons

The solvation of naphthalene^{•+} with methanol resulted in interesting intracluster proton transfer interactions resulting in naphthyl radical molecules and protonated methanol clusters at low temperatures.⁵⁶ This is in part because of the hydrogen bonded chain of methanol molecules that forms upon the “*external solvation*” of the naphthalene radical cation. With larger organic

alcohols, the charge would be more delocalized and thus the investigation of these interactions is of interest. The thermochemistry and theoretical binding energy were also calculated to observe any trends with increasing size of the carbon chain. In the following section, the solvation of the naphthalene radical cation to produce $C_{10}H_8^{*+}(ROH)_n$ with R = Et, 1-Pr, 2-Pr, 1-Bu, and 2-Bu was investigated.

4.4.3.1. Mass Spectra and Thermochemical Results for Naphthalene^{*+}(ROH) Clusters

The mass spectra obtained following the injection of the mass-selected naphthalene radical cation ($C_{10}H_8^{*+}$, $Naph^+$) into the drift cell containing helium or a mixture of helium with the vapor of various alcohols are shown in Figure 19-Figure 23. The first mass spectrum for each figure is a reference mass spectrum of mass-selected $C_{10}H_8^{*+}$ injected into the drift cell containing roughly 1.0 Torr He. In all cases the only major peak is at $m/z = 128$, which is assigned to the naphthalene radical cation.

In the case of ethanol (Figure 19, EtOH), only the naphthalene radical cation is present at 301 K as a major peak (Figure 19b) with a very small peak at $m/z = 185$ corresponding to the fourth protonated ethanol cluster, $H^+(EtOH)_4$, also observed. The first association product, $C_{10}H_8^{*+}(EtOH)$ ($m/z = 174$), is observed when the naphthalene radical cation is injected into the drift cell containing 0.92 Torr ethanol at 274 K (Figure 19c) as a minor peak. At this temperature, the fifth protonated ethanol cluster, $H^+(EtOH)_5$, is observed as a minor peak at $m/z = 231$. The $C_{10}H_8^{*+}(EtOH)$ peak continues to be the only product observed until the drift cell temperature is 228 K, just above the point at which ethanol freezes (Figure 19e). Here the first and second association products, $C_{10}H_8^{*+}(EtOH)_n$ for $n = 1$ and 2, are present ($m/z = 174$ and 220) as well as protonated ethanol clusters, $H^+(EtOH)_n$ for $n = 5-7$, are also present ($m/z = 231, 277,$ and 323). The presence of the protonated ethanol clusters was most likely due to the injection energy of the

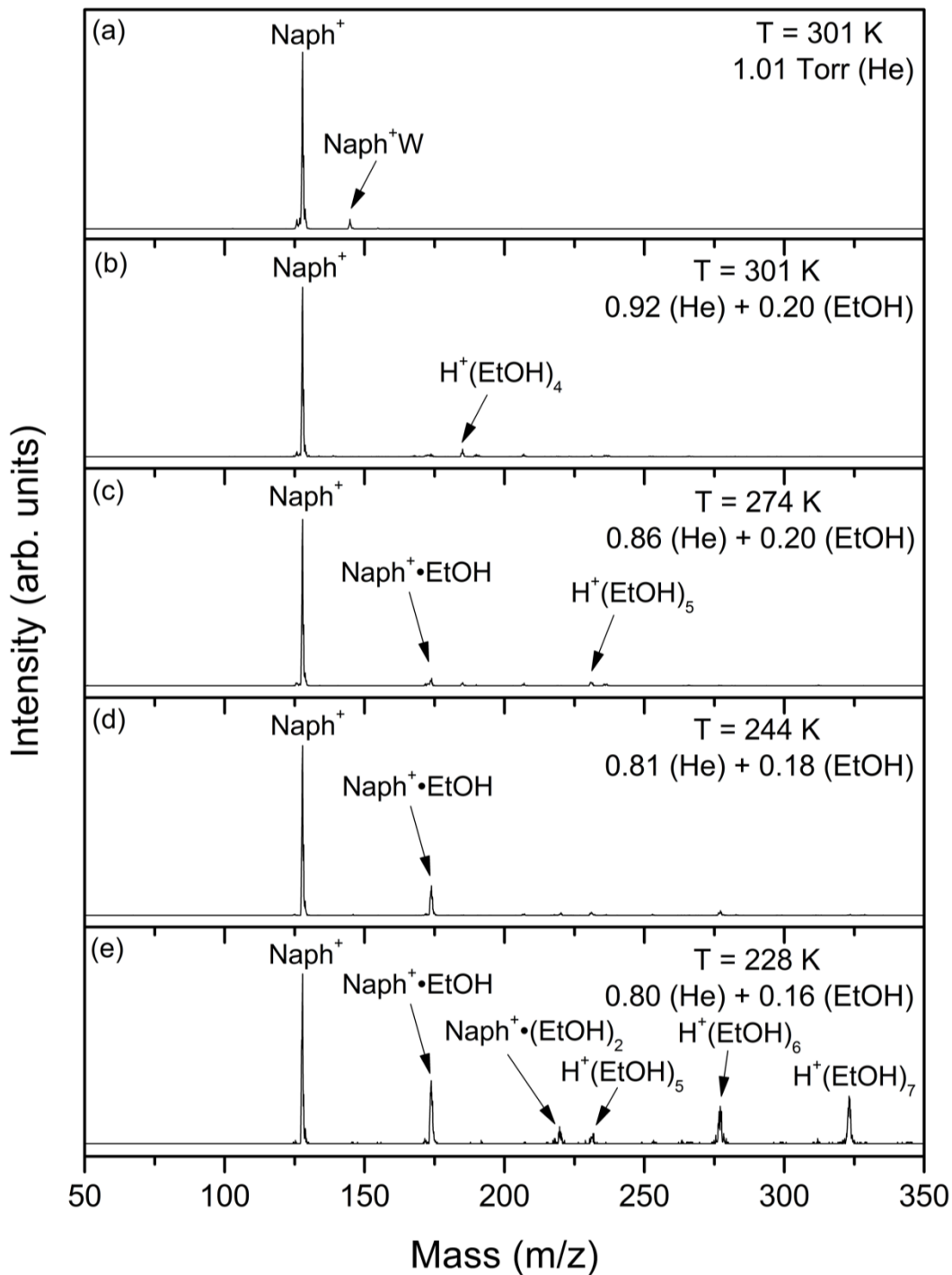


Figure 19. Mass spectra resulting from the injection of the mass-selected naphthalene radical cations ($\text{C}_{10}\text{H}_8^{\bullet+}$, Naph^+) into He gas (a) or He/ethanol (EtOH) vapor mixture (b-e) at different pressures (Torr) and temperatures (K) as indicated.

injected naphthalene radical cation which could induce the ionization of the ethanol inside the drift cell followed by proton transfer to form the observed protonated ethanol clusters. Since the naphthalene containing ions remain throughout the entire experiment, and the naphthalene radical cation remains the major peak, the DPT interactions seen in methanol are most likely not observed here.

The mass spectra obtained following the injection of naphthalene radical cation ($C_{10}H_8^{*\cdot+}$, $Naph^+$) into the drift cell containing propanol are shown in Figure 20 and Figure 21. Mass spectra obtained for 1-propanol (1-PrOH, *n*-propanol) are shown in Figure 20 and for 2-propanol (2-PrOH, *iso*-propanol) are shown Figure 21. The first association product of 1-propanol $C_{10}H_8^{*\cdot+}(1-PrOH)$ ($m/z = 188$), is not present when the naphthalene radical cation is injected into the drift cell containing 0.35 Torr 1-PrOH at 297 K (Figure 20b), but the fourth protonated 1-propanol cluster, $H^+(1-PrOH)_4$, at $m/z = 241$ is present as a minor peak. The $C_{10}H_8^{*\cdot+}(1-PrOH)$ peak is observed when $C_{10}H_8^{*\cdot+}$ is injected into 0.92 Torr 1-PrOH at 274 K (Figure 20c), but as a minor peak. As the temperature of the drift cell is decreased, the intensity of the $C_{10}H_8^{*\cdot+}(1-PrOH)$ peak slowly increases and is the only product present until just above the freezing point of 1-PrOH in the drift cell at 249 K (Figure 20f); at this point, the $C_{10}H_8^{*\cdot+}(1-PrOH)$ peak is the only association product present, but protonated 1-propanol clusters, $H^+(1-PrOH)_n$ for $n = 5-7$ ($m/z = 301, 361, \text{ and } 421$), are also present as minor peaks.

Similar results are observed when $C_{10}H_8^{*\cdot+}$ was injected into the drift cell containing 2-propanol vapor (2-PrOH) and He (Figure 21). Again the fourth protonated 2-propanol cluster, $H^+(2-PrOH)_4$ at $m/z = 241$, is present at 301 K (Figure 21b). When $C_{10}H_8^{*\cdot+}$ is injected into the drift cell containing 0.27 Torr 2-PrOH at 272 K (Figure 21c), the first association product, $C_{10}H_8^{*\cdot+}(2-PrOH)$ ($m/z = 188$), is present at low intensity compared to the parent naphthalene radical cation. The

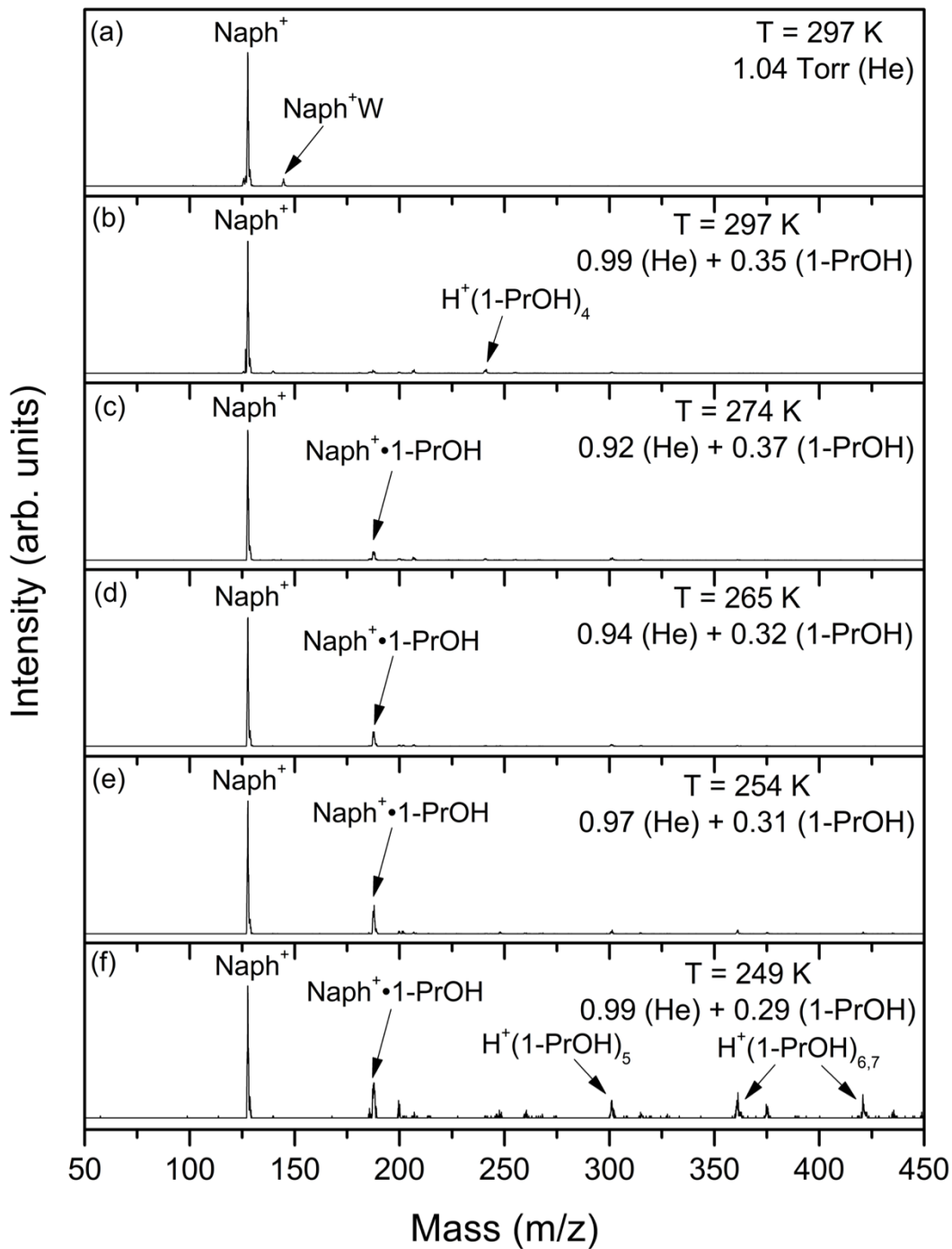


Figure 20. Mass spectra resulting from the injection of the mass-selected naphthalene radical cations ($\text{C}_{10}\text{H}_8^{+\bullet}$, Naph^+) into He gas (a) or He/1-propanol (1-PrOH) vapor mixture (b-f) at different pressures (Torr) and temperatures (K) as indicated.

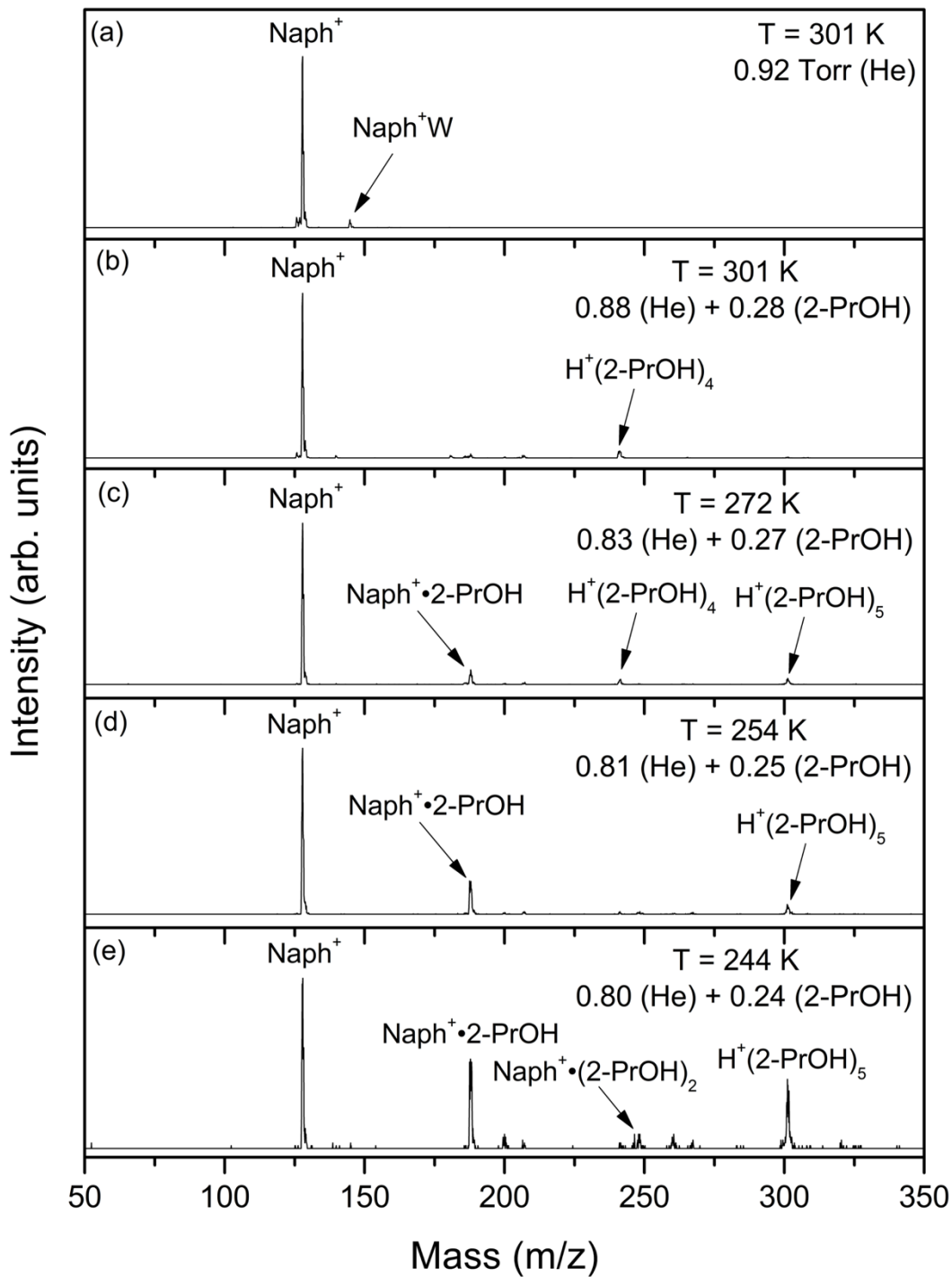


Figure 21. Mass spectra resulting from the injection of the mass-selected naphthalene radical cations ($\text{C}_{10}\text{H}_8^+$, Naph^+) into He gas (a) or He/2-propanol (2-PrOH) vapor mixture (b-e) at different pressures (Torr) and temperatures (K) as indicated.

forth and fifth protonated 2-propanol cluster are also present, $H^+(2\text{-PrOH})_n$ for $n = 4-5$, at $m/z = 241$ and 301 . The intensity of the $C_{10}H_8^{*+}(2\text{-PrOH})$ peak continued to increase and is the only association product peak observed until 244 K (Figure 21e), the temperature just above where the 2-propanol would freeze in the drift cell. At this temperature, the second association product, $C_{10}H_8^{*+}(2\text{-PrOH})_2$ ($m/z = 248$), is observed as a minor peak. The fifth protonated 2-propanol cluster, $H^+(2\text{-PrOH})_5$, is also observed at an intensity nearly equal to that of the first association product. The presence of the protonated propanol clusters observed in both Figure 20 and Figure 21 is due to charge transfer interactions much like with ethanol.

The mass spectra obtained following the injection of the naphthalene radical cation ($C_{10}H_8^{*+}$, Naph^+) into the drift cell containing butanol are shown in Figure 22 and Figure 23. The mass spectra for 1-butanol (1-BuOH, *n*-butanol) are shown in Figure 22 and for 2-butanol (2-BuOH, *sec*-butanol) are shown in Figure 23. When $C_{10}H_8^{*+}$ is injected into the drift cell containing 0.41 Torr 1-butanol at 305 K (Figure 22b) the first association product, $C_{10}H_8^{*+}(1\text{-BuOH})$, $m/z = 202$ is observed at an intensity much weaker than the parent naphthalene radical cation peak. The intensity of this ion increases slightly as the temperature of the drift cell decreased and just above the point at which 1-butanol freezes in the drift cell at 263 K (Figure 22e), it is still the only association product observed. The only protonated 1-butanol cluster observed during this series of mass spectra is the fifth protonated 1-butanol cluster, $H^+(1\text{-BuOH})_5$, at $m/z = 371$. This cluster is only observed at the lowest temperature observed (Figure 22e).

When the drift cell contained 0.29 Torr 2-butanol at 300 K (Figure 23b), the naphthalene radical cation was the major peak observed and the protonated dimer of 2-butanol, $H^+(2\text{-BuOH})$ was observed with a much lower intensity at $m/z = 149$. Similar to what was observed with 1-butanol, when the drift cell contained 0.28 Torr of 2-butanol at 273 K (Figure 23c), the first

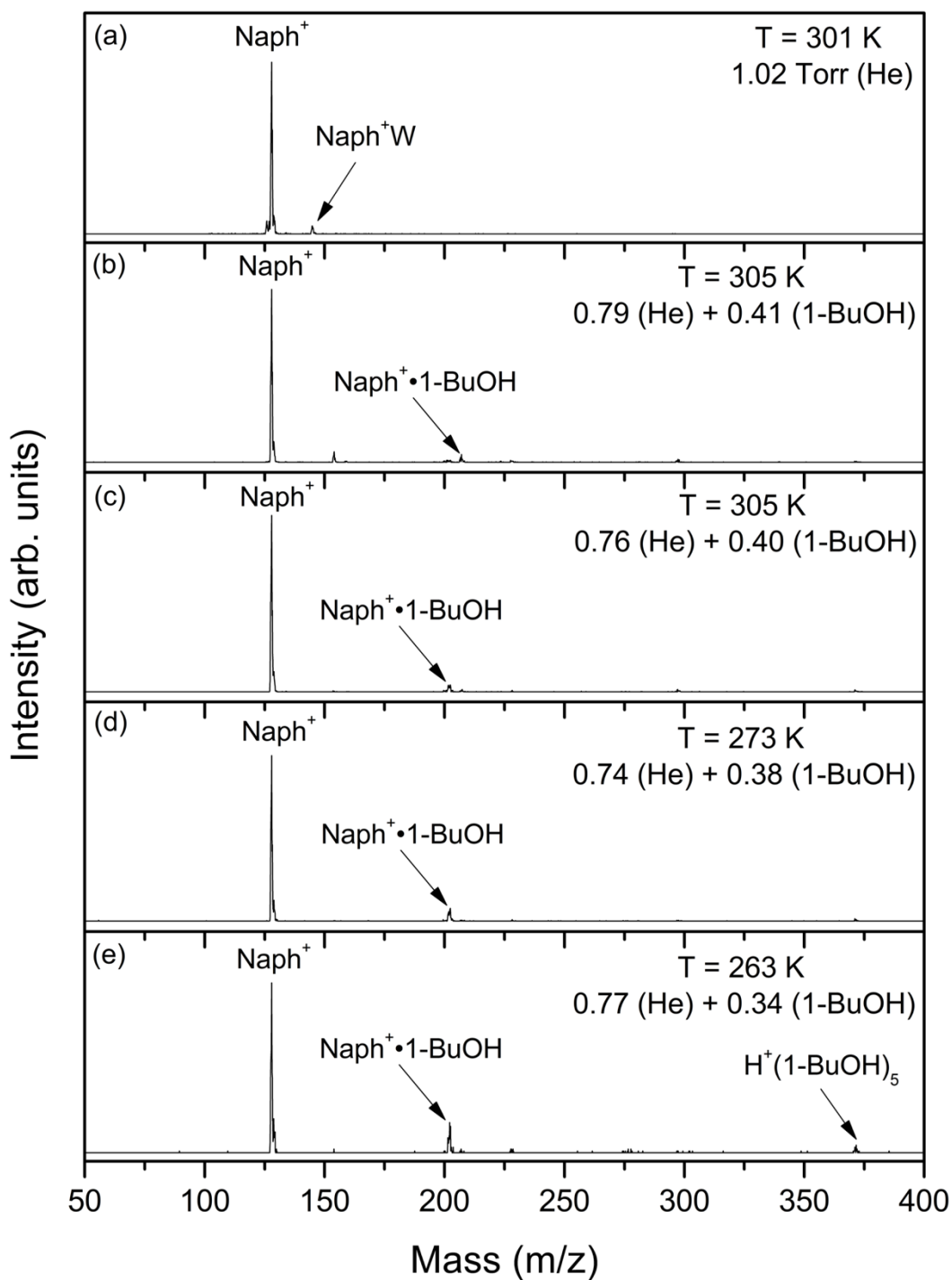


Figure 22. Mass spectra resulting from the injection of the mass-selected naphthalene radical cations ($\text{C}_{10}\text{H}_8^{+\cdot}$, Naph^+) into He gas (a) or He/1-butanol (1-BuOH) vapor mixture (b-e) at different pressures (Torr) and temperatures (K) as indicated.

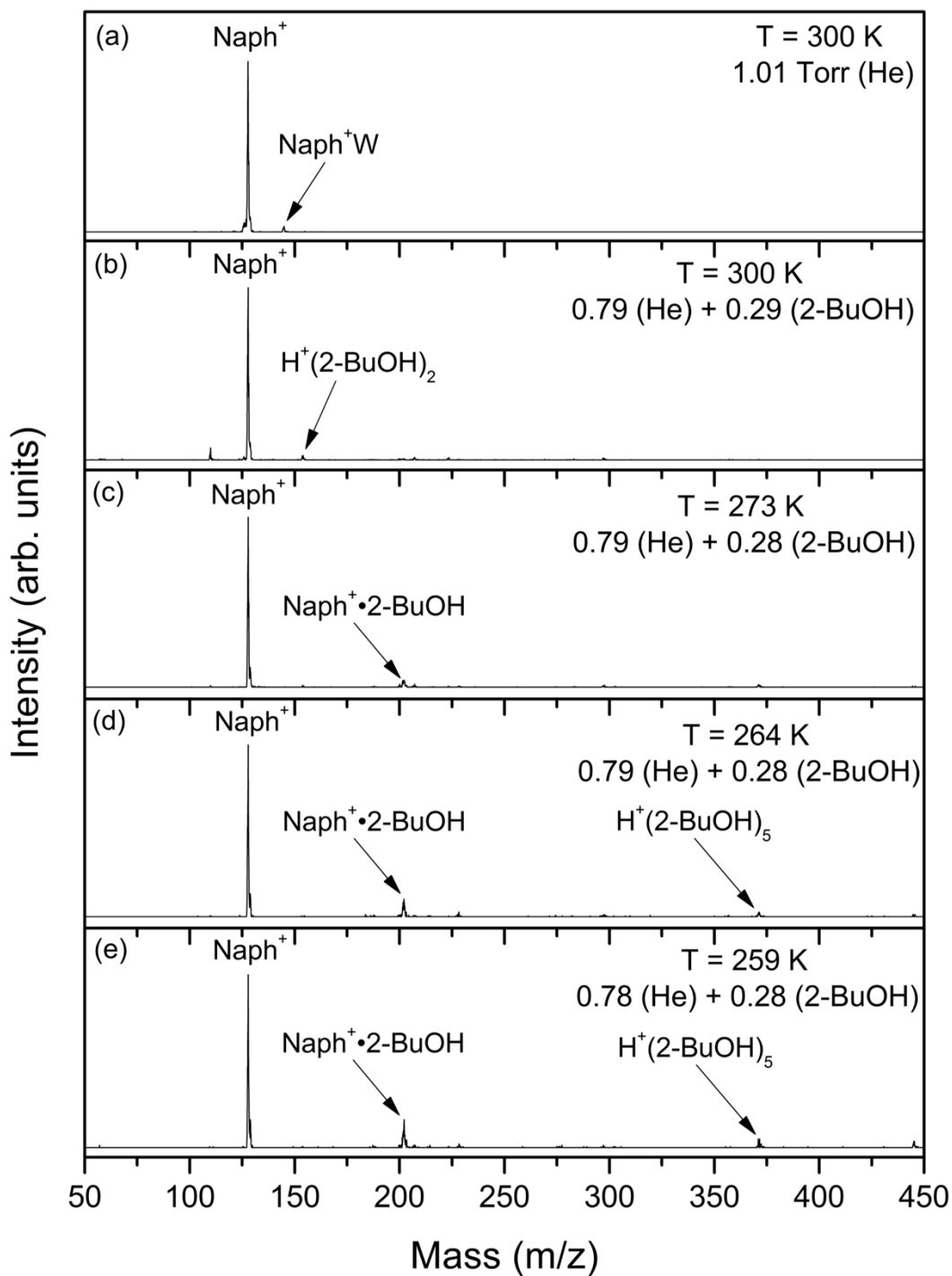
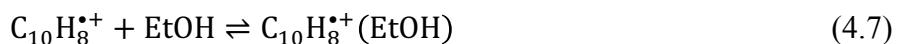


Figure 23. Mass spectra resulting from the injection of the mass-selected naphthalene radical cations ($\text{C}_{10}\text{H}_8^{+\bullet}$, Naph^+) into He gas (a) or He/2-BuOH (2-BuOH) vapor mixture (b-e) at different pressures (Torr) and temperatures (K) as indicated.

association product, $C_{10}H_8^{*\cdot+}(2-BuOH)$ ($m/z = 202$), is observed as a minor peak. At this temperature, no protonated 2-butanol clusters are observed. The intensity of the $C_{10}H_8^{*\cdot+}(2-BuOH)$ peak continues to increase slowly as the temperature of the drift cell is lowered, but the intensity is still low compared to the naphthalene radical cation at 259 K (Figure 23e). The fifth protonated 2-butanol cluster, $H^+(2-BuOH)_5$, at $m/z = 371$ is the only protonated 2-butanol cluster observed at $T < 273$ K.

The stepwise solvation reaction of the naphthalene radical cation with primary and secondary alcohols of two, three, and four carbons (EtOH, 1-PrOH, 2-PrOH, 1-BuOH, and 2-BuOH) are represented by Equations 4.7-4.11:



The equilibrium constants are measured for these reactions using Equation 4.2 by obtaining the peak intensities of the naphthalene radical cation ($C_{10}H_8^{*\cdot+}$) and the observed association products and the pressure of the alcohol. By measuring the equilibrium constants at different temperatures, a van't Hoff plot for the formation of the first association product using Equation 3.5 is produced for each alcohol as shown in Figure 24. The resulting $-\Delta H^\circ$ and $-\Delta S^\circ$ values for Equation 4.4 are obtained from the slope and intercept of the van't Hoff plot respectively and are summarized in Table 3. The van't Hoff plot for the formation of the $C_{10}H_8^{*\cdot+}(EtOH)$ cluster, represented by Equation 4.7, is shown in Figure 24b. The resulting $-\Delta H^\circ$ and $-\Delta S^\circ$ values are 7.8 ± 1 kcal mol⁻¹ and 15.2 ± 2 cal mol⁻¹ K⁻¹. These values are similar to those obtained for the first association

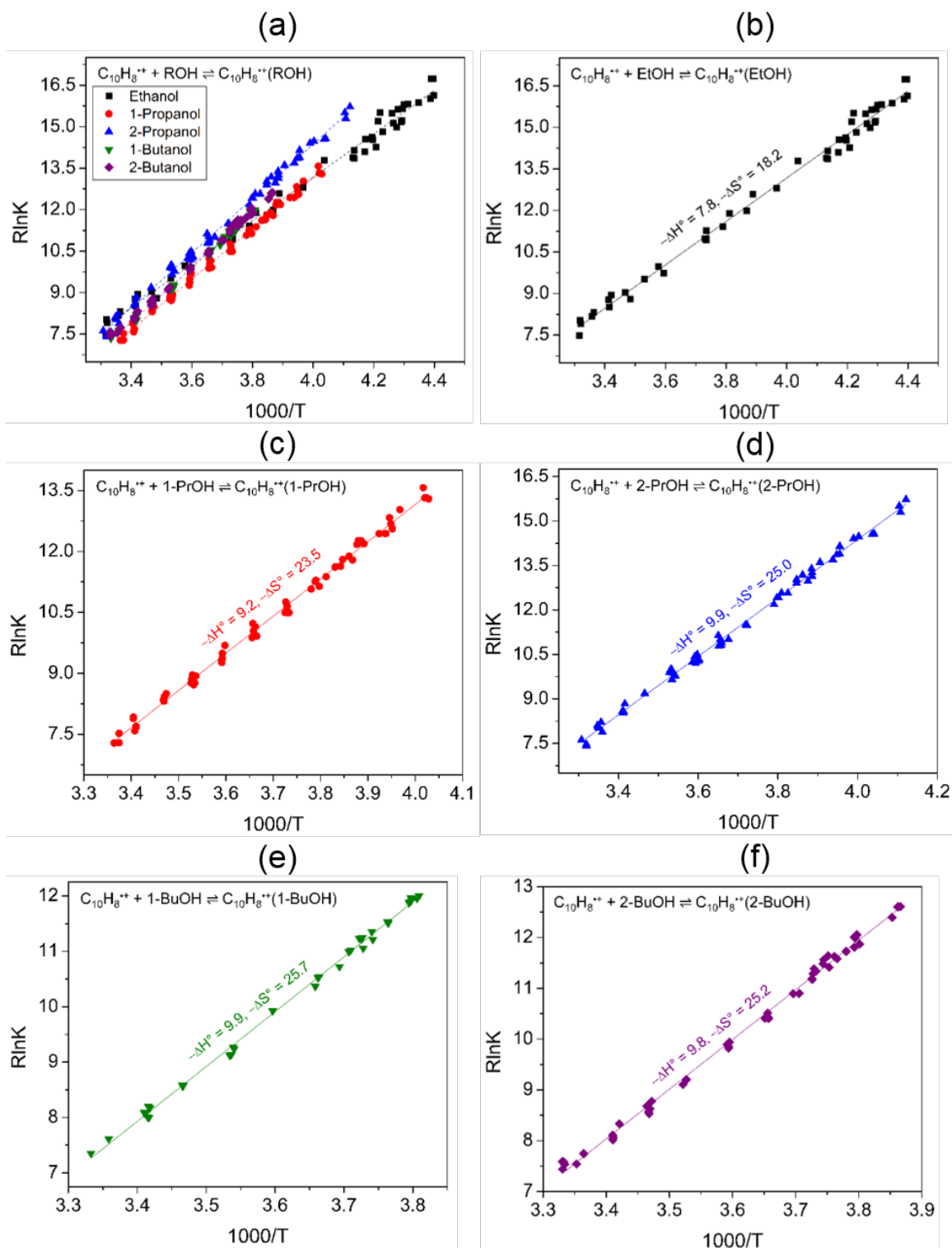


Figure 24. van't Hoff plots for the temperature dependence of the equilibrium constants of the association reaction of naphthalene radical cation with ethanol (b), 1-propanol (c), 2-propanol (d), 1-butanol (e), and 2-butanol (e) for the first solvation step. The resulting ΔH° and ΔS° are in (kcal mol⁻¹) and (cal mol⁻¹ K⁻¹) respectively. The experimental error for these measurements are ± 1 kcal mol⁻¹ and ± 2 cal mol⁻¹ K⁻¹. A composite of all plots is shown in (a).

products of the naphthalene radical cation to water and methanol.⁵⁶ Based on the overlapping ATDs of the naphthalene radical cation and the first association product with ethanol, $C_{10}H_8^{*+}(EtOH)$, at a sequence of temperatures from 243 K to 233 K, the reaction represented by Equation 4.7 is said to be in equilibrium (Figure 25).

Table 3. Measured thermochemistry ($-\Delta H^\circ$ and $-\Delta S^\circ$)^a of the formation of $C_{10}H_8^{*+}(ROH)$ clusters for R = Et, 1-Pr, 2-Pr, 1-Bu, and 2-Bu and the calculated binding energies (ΔE), enthalpies ($-\Delta H$), and Gibbs Free Energies (ΔG) at the B3LYP/6-311++G** level for the lowest energy isomers of $C_{10}H_8^{*+}(ROH)_n$ cluster for R = Et, 1-Pr, 2-Pr, 1-Bu, and 2-Bu and $n = 1-3$.

Cluster	n	$-\Delta H^\circ$	$-\Delta S^\circ$	ΔE (B3LYP)	$-\Delta H$ (calc)	ΔG (calc)
$C_{10}H_8^{*+}(EtOH)_n$	1	7.8	15.2	8.4	7.8	0.4
	2	-	-	8.6	8.2	0.3
	3	-	-	7.2	6.6	1.8
$C_{10}H_8^{*+}(1-PrOH)_n$	1	9.2	23.5	8.0	7.3	0.9
	2	-	-	8.1	7.6	0.8
	3	-	-	6.7	6.1	3.5
$C_{10}H_8^{*+}(2-PrOH)_n$	1	9.9	25.0	8.8	8.1	0.6
	2	-	-	8.4	7.8	0.5
	3	-	-	7.6	7.1	1.8
$C_{10}H_8^{*+}(1-BuOH)_n$	1	9.9	25.7	9.3	8.6	0.2
	2	-	-	8.9	8.4	0.1
	3	-	-	7.9	7.2	2.0
$C_{10}H_8^{*+}(2-BuOH)_n$	1	9.8	25.2	8.3	7.6	1.0
	2	-	-	8.2	7.6	1.0
	3	-	-	7.0	6.2	2.4

^a Units, estimated experimental error: $\Delta H^\circ \pm 1$ kcal mol⁻¹ and $\Delta S^\circ \pm 2$ cal mol⁻¹ K⁻¹

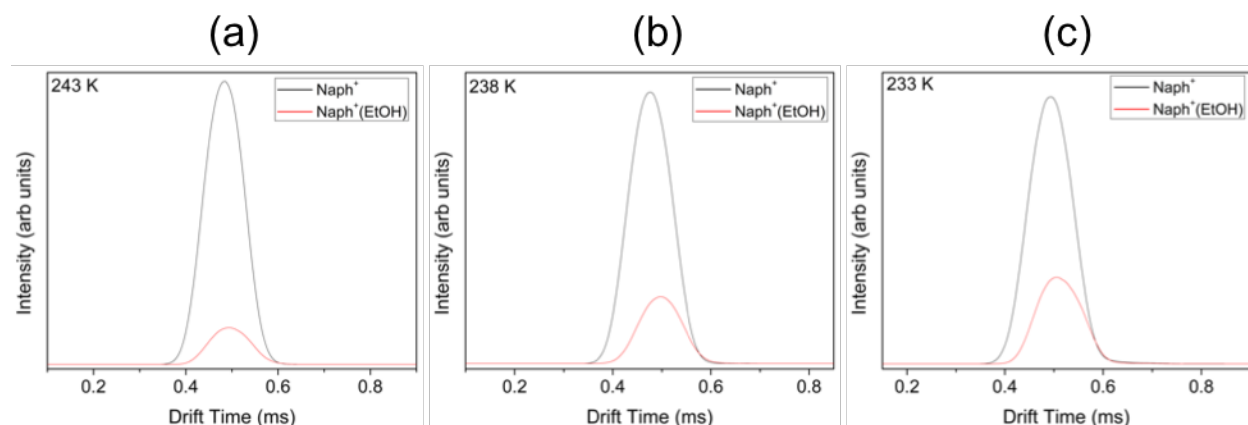


Figure 25. Arrival time distributions (ATDs) of the naphthalene radical cation ($Naph^+$) and the first association product with ethanol, $C_{10}H_8^{*+}(EtOH)$ ($Naph^+(EtOH)$), obtained following the injection of the mass-selected naphthalene radical cation into a He/EtOH vapor mixture at: (a) 243 K, (b) 238 K, and (c) 233 K. Similar ATD overlap suggests the reaction is in equilibrium.

The $-\Delta H^\circ$ and $-\Delta S^\circ$ values obtained for the formation of the first association product of 1-propanol to the naphthalene, $C_{10}H_8^{++}(1-PrOH)$, are $9.2 \pm 1 \text{ kcal mol}^{-1}$ and $23.5 \pm 2 \text{ cal mol}^{-1} \text{ K}^{-1}$ (Figure 24c). The reaction used for these values, Equation 4.8, is assumed to be in equilibrium based on the overlapping ATDs taken for the naphthalene radical cation and the first association product $C_{10}H_8^{++}(1-PrOH)$ at 258 K 263 K (Figure 26). The thermochemistry results for the formation of the association product of the secondary alcohol 2-propanol to the naphthalene radical cation, $C_{10}H_8^{++}(2-PrOH)$, are similar to those obtained for 1-propanol. Here the $-\Delta H^\circ$ and $-\Delta S^\circ$ values were $9.9 \pm 1 \text{ kcal mol}^{-1}$ and $25.0 \pm 2 \text{ cal mol}^{-1} \text{ K}^{-1}$ (Figure 24d). Again the reaction for the formation of $C_{10}H_8^{++}(2-PrOH)$ was assumed to be in equilibrium based on the overlapping ATDs taken for the naphthalene radical cation and the first association product $C_{10}H_8^{++}(2-PrOH)$ at 263 K and 258 K (Figure 27).

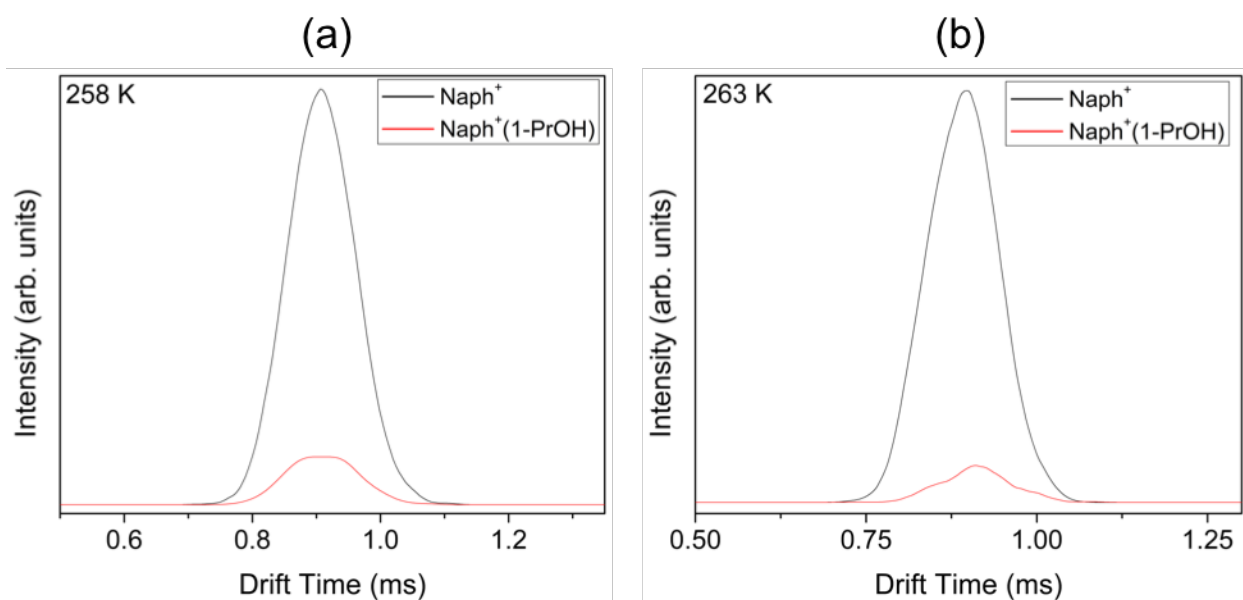


Figure 26. Arrival time distributions (ATDs) of the naphthalene radical cation ($Naph^+$) and the first association product with 1-propanol, $C_{10}H_8^{++}(1-PrOH)$ ($Naph^+(1-PrOH)$), obtained following the injection of the mass-selected naphthalene radical cation into He/1-PrOH vapor mixture at: (a) 258 K and (b) 263 K. Similar ATD overlap suggests the reaction is in equilibrium.

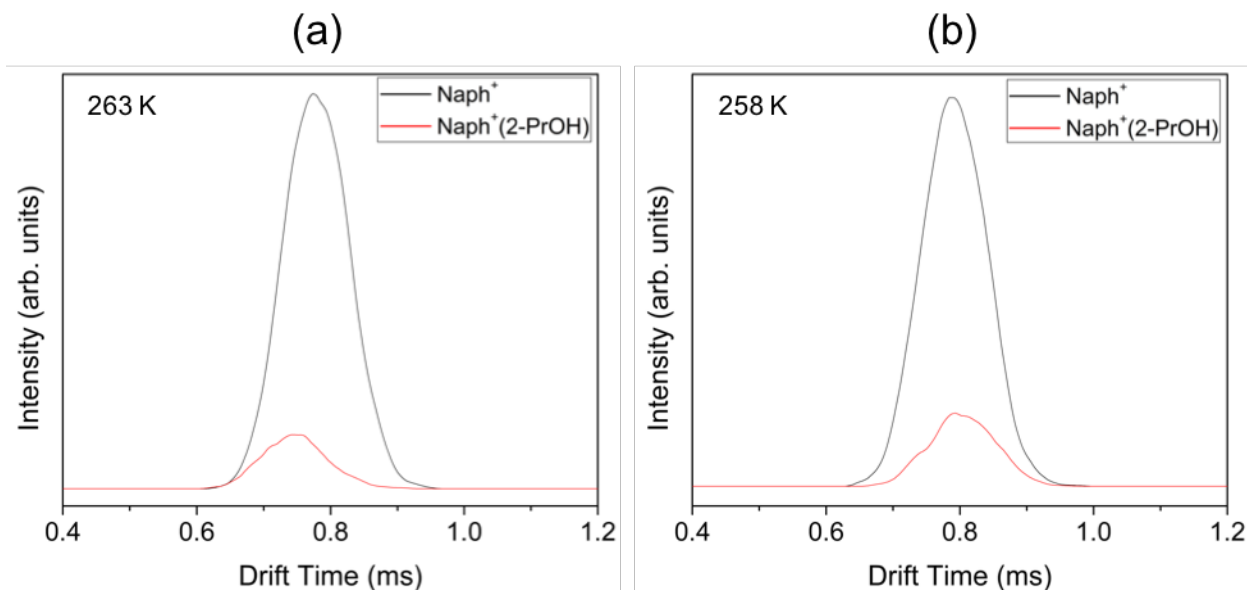


Figure 27. Arrival time distributions (ATDs) of the naphthalene radical cation ($\text{Naph}^{\bullet+}$) and the first association product with 2-propanol, $\text{C}_{10}\text{H}_8^{\bullet+}(\text{2-PrOH})$ ($\text{Naph}^{\bullet+}(\text{2-PrOH})$), obtained following the injection of the mass-selected naphthalene radical cation into He/2-PrOH vapor mixture at: (a) 263 K and (b) 258 K. Similar ATD overlap suggests the reaction is in equilibrium.

The thermochemistry results for the solvation of the naphthalene radical cation with both the primary and secondary butanol alcohols, 1-BuOH and 2-BuOH, are very similar. The $-\Delta H^\circ$ and $-\Delta S^\circ$ values are $9.9 \pm 1 \text{ kcal mol}^{-1}$ and $25.7 \pm 2 \text{ cal mol}^{-1} \text{ K}^{-1}$ for 1-butanol (Figure 24e) and $9.8 \pm 1 \text{ kcal mol}^{-1}$ and $25.2 \pm 2 \text{ cal mol}^{-1} \text{ K}^{-1}$ for 2-butanol (Figure 24f). The $-\Delta H^\circ$ values for these alcohols are similar to those using propanol (both 1-propanol and 2-propanol). This suggests that the binding of small primary and secondary alcohols to the naphthalene radical cation forms a $\text{CH}^{\delta+}\cdots\text{O}$ IHB between alcohol and the PAH naphthalene radical cation.

4.4.3.2. Calculated Structures and Binding Energies of Naphthalene^{•+}(ROH) Clusters

The lowest energy isomers for the first three association products of the injection of the naphthalene radical cation into the drift cell containing a gas/vapor mixture of He and small primary and secondary alcohols with two, three, or four carbons were calculated at the B3LYP/

6-311++G** level of theory with the calculated binding energies, enthalpies, and Gibbs free energies are summarized in Table 3.

The calculated structures and binding energies, ΔE , for the first three association products of ethanol to the naphthalene radical cation, $C_{10}H_8^{*\cdot+}(EtOH)_n$ where $n = 1-3$, are shown in Figure 28. The structure of the first association product $C_{10}H_8^{*\cdot+}(EtOH)$ (Figure 28a) is similar to that observed with water and methanol where the oxygen of the ethanol forms a bifurcated IHB structure with two $CH^{\delta+}$ hydrogens of the naphthalene radical cation.⁵⁶ The calculated binding energy of this structure is $\Delta E = 8.4 \text{ kcal mol}^{-1}$ and the calculated $-\Delta H$ is $7.8 \text{ kcal mol}^{-1}$ (which is closer to the experimental value). A lower energy isomer of the $C_{10}H_8^{*\cdot+}(EtOH)$ cluster with a single IHB between the ethanol and naphthalene radical cation was also calculated, as shown in Figure 29a(ii), with a binding energy, ΔE , of $7.0 \text{ kcal mol}^{-1}$ and calculated $-\Delta H$ of $6.2 \text{ kcal mol}^{-1}$. Considering the experimentally measured enthalpy change for the formation of the $C_{10}H_8^{*\cdot+}(EtOH)$ cluster of $-\Delta H^{\circ} = 7.8 \pm 1 \text{ kcal mol}^{-1}$, the lowest energy structure is preferred, but a mixture could still be present.

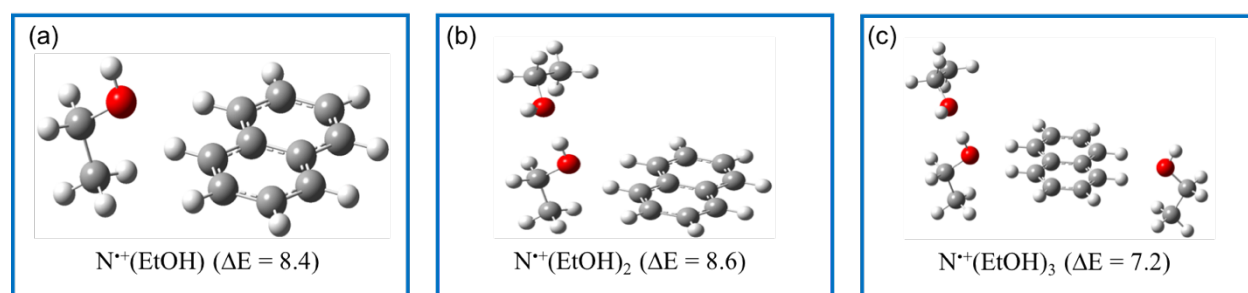
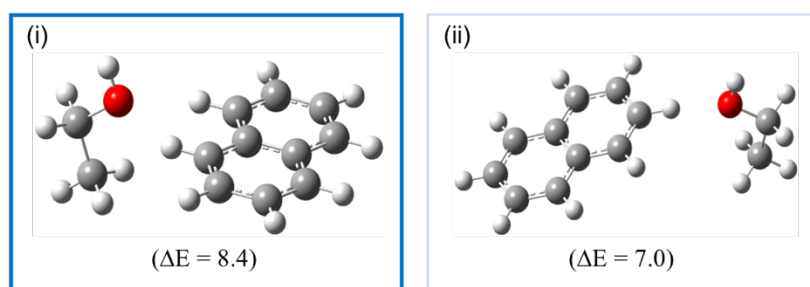


Figure 28. DFT structures and binding energies ($\Delta E \text{ kcal mol}^{-1}$, calculated according to Equation 4.3) of the lowest energy isomers of the $C_{10}H_8^{*\cdot+}(EtOH)_n$ clusters for $n = 1-3$ obtained at the B3LYP/6-311++G** level.

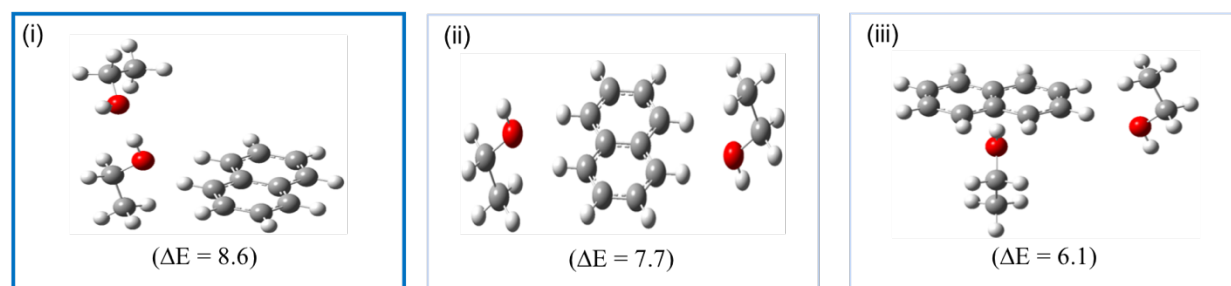
The lowest energy isomer for the second association product is an “*externally solvated*” structure (Figure 28b) with a ΔE of $8.6 \text{ kcal mol}^{-1}$ and a calculated $-\Delta H$ of $8.2 \text{ kcal mol}^{-1}$. This structure is similar to that of the $C_{10}H_8^{*\cdot+}(CH_3OH)_2$ cluster where the second alcohol begins a chain of molecules attached to the naphthalene radical cation.⁵⁶ However, a higher energy “*internally*

solvated^p structure with a binding energy of $\Delta E = 7.7$ kcal mol⁻¹ and a calculated $-\Delta H$ of 7.0 kcal mol⁻¹, shown in Figure 29b(ii), is within the experimental uncertainty of ± 1 kcal mol⁻¹ and therefore could also be present. A structure where the second ethanol add in a way where ion-dipole interactions observed in the plane of the naphthalene rings is shown in Figure 29b(iii). In this case, the calculated binding energy lower with a ΔE of 6.1 kcal mol⁻¹ with a calculated $-\Delta H$ of 5.3 kcal mol⁻¹.

(a) C₁₀H₈^{•+}(EtOH)



(b) C₁₀H₈^{•+}(EtOH)₂



(c) C₁₀H₈^{•+}(EtOH)₃

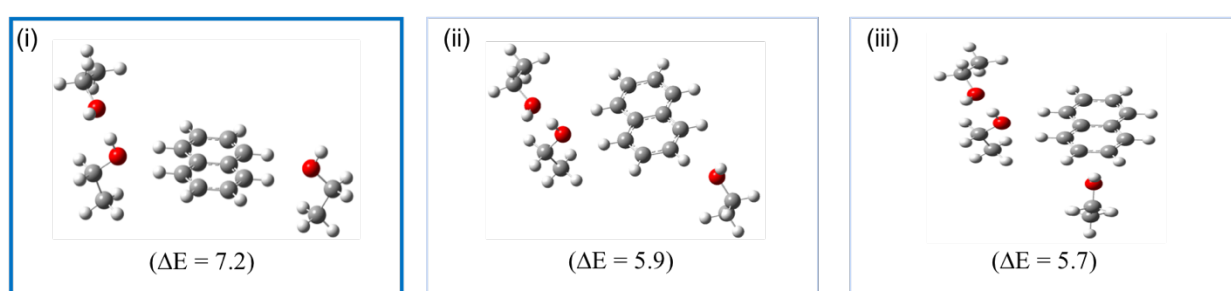


Figure 29. DFT Structures and binding energies (ΔE , kcal mol⁻¹, calculated according to Equation 4.3) for higher energy isomers of the C₁₀H₈^{•+}(EtOH)_n clusters for $n = 1-3$ obtained at the B3LYP/6-311++G** level.

Calculated isomers of the third association product of ethanol to the naphthalene radical cation, C₁₀H₈^{•+}(EtOH)₃, show that the third ethanol molecule forms a second IHB to the

naphthalene radical cation. The lowest energy isomer (Figure 28c) has a calculated binding energy, ΔE , of 7.2 kcal mol⁻¹ and a calculated $-\Delta H$ of 6.6 kcal mol⁻¹. In this structure, the third ethanol forms a bifurcated IHB on the opposite side of the naphthalene that is the same as that formed by the first ethanol. If the ethanol forms a single IHB similar to that calculated in Figure 29a(ii), the binding energy is 5.9 kcal mol⁻¹ with a calculated $-\Delta H$ of 5.2 kcal mol⁻¹ as shown in Figure 29c(ii). Should the ethanol interact with the C₁₀H₈^{•+}(EtOH)₂ cluster in an ion-dipole fashion, the calculated binding energy is low, $\Delta E = 5.7$ kcal mol⁻¹, as is the calculated $-\Delta H$ (5.0 kcal mol⁻¹) as shown in Figure 29c(iii). The formation of a second IHB is unlike methanol where there is strong evidence that methanol molecules form a H-bonded chain to “*externally solvated*” the naphthalene radical cation. This is interesting when compared to IR studies of the ethanol dimer which has at least two hydrogen bonded linear conformers.¹⁴¹ Crystal structure studies of ethanol clusters show that the unit cell consists of four ethanol molecules that form a ring-like structure that then has an infinite zigzag pattern.¹⁴¹⁻¹⁴³ However it appears here that ring structures are not preferred for lower additions of ethanol. Differences between the calculated binding energies and the calculated enthalpies are likely due to entropy contributions which is seen with the increasing calculated ΔG as the cluster size increases as observed in Table 3.

The lowest energy structures for the first three additions of 1-propanol to the naphthalene radical cation resulting in the C₁₀H₈^{•+}(1-PrOH)_{*n*} with *n* = 1-3 association products are shown in Figure 30. For the first association product, the 1-propanol binds to the naphthalene radical cation via a bifurcated IHB that is observed with other polar molecules studied with a calculated binding energy, ΔE , of 8.0 kcal mol⁻¹ and calculated enthalpy of 7.3 kcal mol⁻¹. A higher energy isomer for the C₁₀H₈^{•+}(1-PrOH) cluster where a single IHB is formed between the oxygen of the 1-propanol molecule and a CH^{δ+} hydrogen of the naphthalene radical cation, structure shown in Figure 31a(ii),

the calculated binding energy is much lower with a ΔE value of $6.7 \text{ kcal mol}^{-1}$ and calculated $-\Delta H$ of $5.9 \text{ kcal mol}^{-1}$. The second 1-propanol molecule “*externally solvates*” the naphthalene radical cation in a similar fashion as ethanol (structure shown in Figure 30b) and has a similar calculated binding energy of $8.1 \text{ kcal mol}^{-1}$ and calculated enthalpy of $7.6 \text{ kcal mol}^{-1}$. Interestingly, an “*internally solvated*” structure shown in Figure 31b(ii) with two bifurcated IHBs has a calculated binding energy of $7.2 \text{ kcal mol}^{-1}$ and calculated enthalpy of $6.6 \text{ kcal mol}^{-1}$ that is within the experimental error of $\pm 1 \text{ kcal mol}^{-1}$. This would suggest that such a structure is possible and is reinforced when low energy structures of the third association product of 1-propanol to the naphthalene radical cation are calculated. The calculated binding energy of the third 1-propanol molecule is lower than what is observed in lower additions with a ΔE value of $6.7 \text{ kcal mol}^{-1}$ and calculated $-\Delta H$ of $6.1 \text{ kcal mol}^{-1}$ (Figure 30c). The lowest energy structure of the $\text{C}_{10}\text{H}_8^{*\cdot+}(\text{1-PrOH})_3$ shows that the third 1-propanol binds to either the “*externally*” or “*internally solvated*” $\text{C}_{10}\text{H}_8^{*\cdot+}(\text{1-PrOH})_2$ structures with a lower binding energy. A drop in binding energy is not observed with small alcohols suggesting that this is an effect of the chain length. A higher energy ion-dipole structure, shown in Figure 31c(ii), with a binding energy of $5.5 \text{ kcal mol}^{-1}$ and calculated enthalpy of $4.8 \text{ kcal mol}^{-1}$ is slightly more stable than a fully “*externally solvated*” structure with a binding energy of $5.2 \text{ kcal mol}^{-1}$ and calculated enthalpy of $4.4 \text{ kcal mol}^{-1}$, calculated structure shown in Figure 31c(iii).

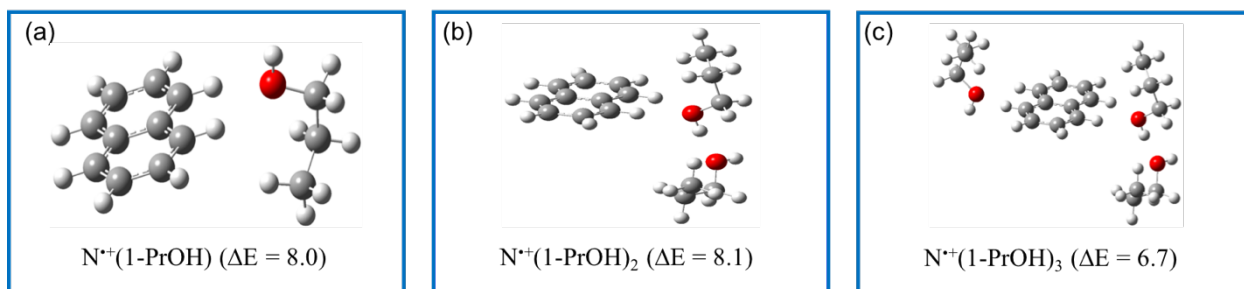
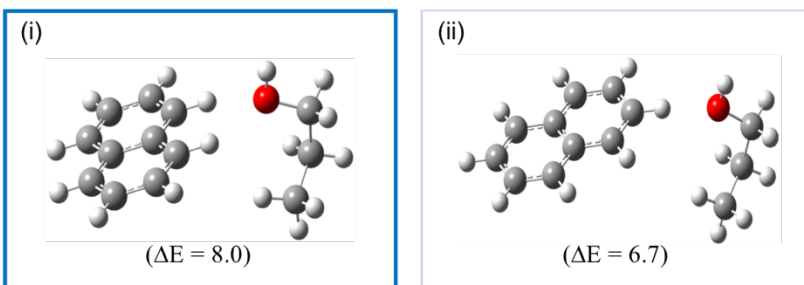
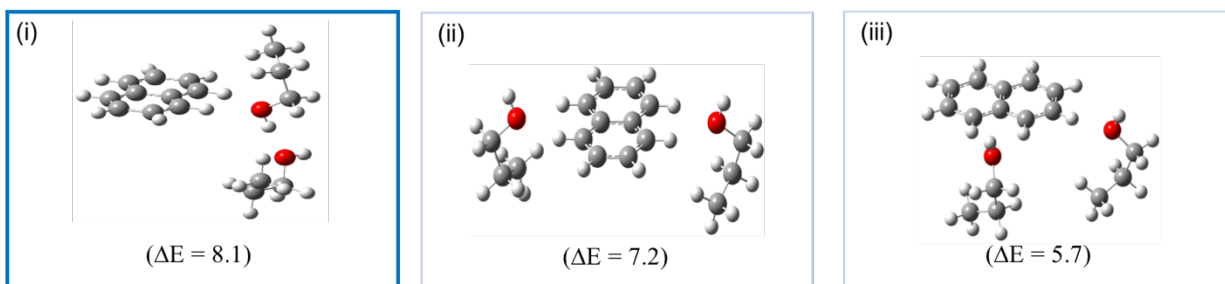


Figure 30. DFT structures and binding energies ($\Delta E \text{ kcal mol}^{-1}$, calculated according to Equation 4.3) of the lowest energy isomers of the $\text{C}_{10}\text{H}_8^{*\cdot+}(\text{1-PrOH})_n$ clusters for $n = 1-3$ obtained at the B3LYP/6-311++G** level.

(a) $C_{10}H_8^{+}(1-PrOH)$



(b) $C_{10}H_8^{+}(1-PrOH)_2$



(c) $C_{10}H_8^{+}(1-PrOH)_3$

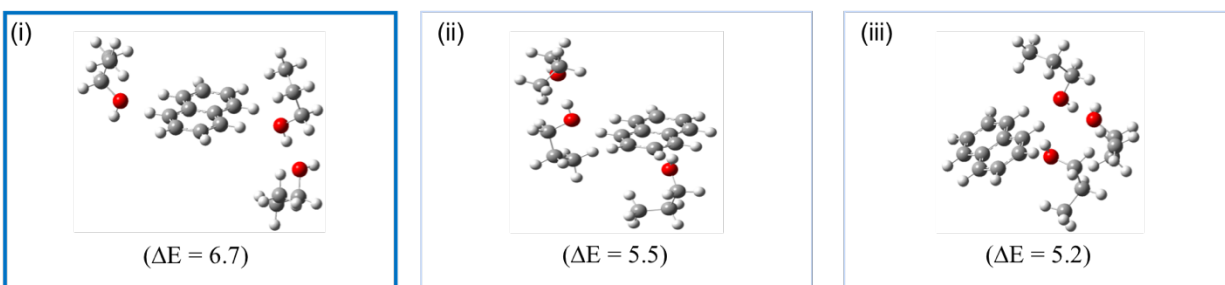


Figure 31. DFT Structures and binding energies (ΔE , kcal mol⁻¹, calculated according to Equation 4.3) for higher energy isomers of the $C_{10}H_8^{+}(1-PrOH)_n$ clusters for $n = 1-3$ obtained at the B3LYP/6-311++G** level.

The first association product of 2-propanol to the naphthalene radical cation forms a bifurcated IHB structure that is similar to what is observed with other polar molecules with a calculated binding energy of 8.8 kcal mol⁻¹ and calculated enthalpy of 8.1 kcal mol⁻¹ (Figure 32a). A higher energy isomer with a single IHB, structure shown in Figure 33a(ii), has a binding energy of 7.3 kcal mol⁻¹ and calculated $-\Delta H$ of 6.4 kcal mol⁻¹. The lowest energy isomer of the $C_{10}H_8^{+}(2-PrOH)_2$ cluster shows that the second 2-PrOH molecule forming a hydrogen bonded chain of 2-propanol molecules and thus “*externally solvating*” the naphthalene radical cation (Figure 32b).

The calculated binding energy, ΔE , of this isomer is $8.4 \text{ kcal mol}^{-1}$ and calculated $-\Delta H$ of $7.8 \text{ kcal mol}^{-1}$. An “*internally solvated*” structure where the 2-propanol molecules form two separate IHBs with the naphthalene radical cation has a very similar calculated binding energy as the “*externally solvated*” structure with a ΔE value of $8.0 \text{ kcal mol}^{-1}$ and $-\Delta H$ value of $7.2 \text{ kcal mol}^{-1}$ with the structure shown in Figure 33b(ii). An ion-dipole structure was also calculated, structure shown in Figure 33b(iii), but the calculated binding energy is much lower where $\Delta E = 6.3 \text{ kcal mol}^{-1}$ and calculated $-\Delta H = 5.4 \text{ kcal mol}^{-1}$. The calculations for the $\text{C}_{10}\text{H}_8^{*+}(\text{2-PrOH})_3$ cluster resulted in two isomers of nearly identical binding energies. A fully “*externally solvated*” structure that is similar to that of methanol has a calculated binding energy of $\Delta E = 7.6 \text{ kcal mol}^{-1}$ and calculated $-\Delta H = 7.1 \text{ kcal mol}^{-1}$ (Figure 32c).⁵⁶ A structure where there are two bifurcated IHBs for two 2-propanol molecules and a third 2-proanol forming to a hydrogen bonded chain has a calculated binding energy of $\Delta E = 7.5 \text{ kcal mol}^{-1}$, structure shown in Figure 33c(ii).

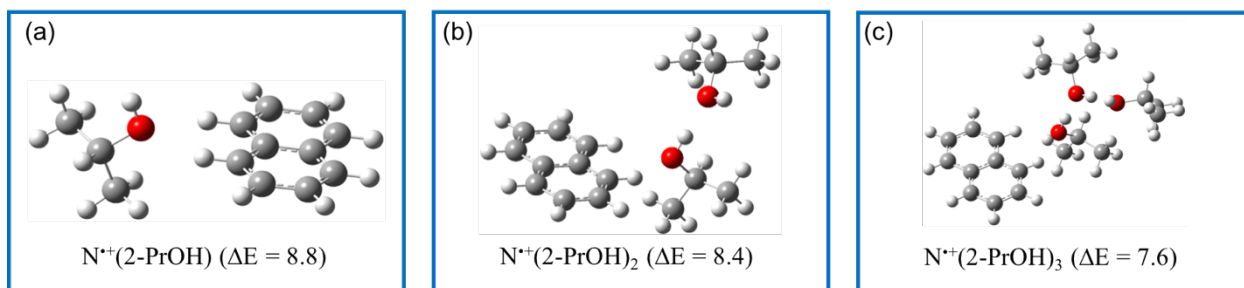
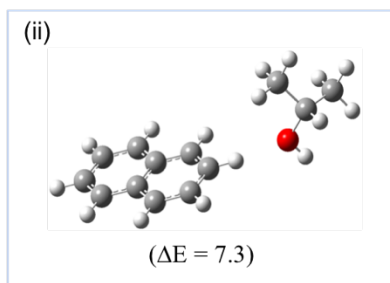
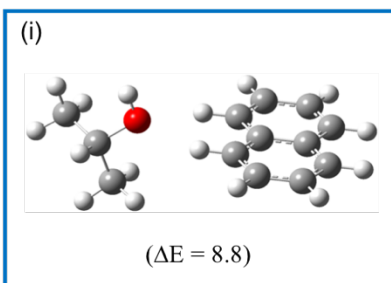
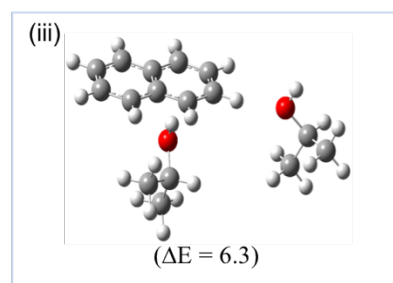
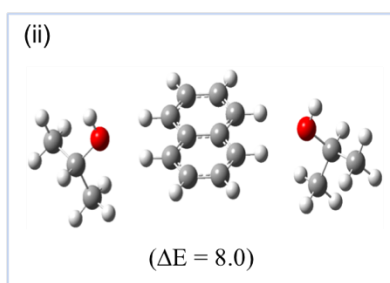
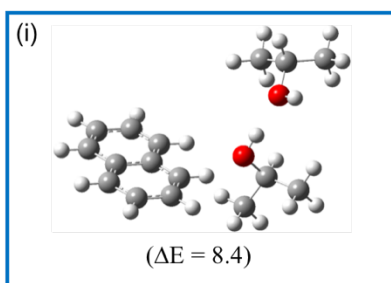


Figure 32. DFT structures and binding energies ($\Delta E \text{ kcal mol}^{-1}$, calculated according to Equation 4.3) of the lowest energy isomers of the $\text{C}_{10}\text{H}_8^{*+}(\text{2-PrOH})_n$ clusters for $n = 1-3$ obtained at the B3LYP/6-311++G** level.

(a) $C_{10}H_8^{++}(2-PrOH)$



(b) $C_{10}H_8^{++}(2-PrOH)_2$



(c) $C_{10}H_8^{++}(2-PrOH)_3$

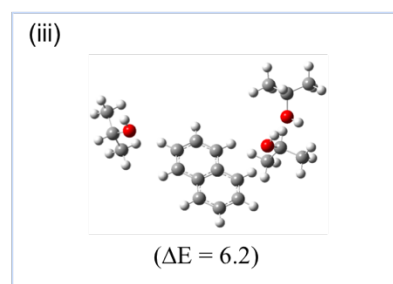
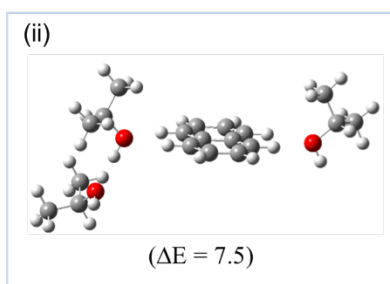
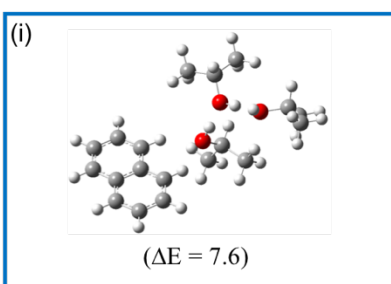


Figure 33. DFT Structures and binding energies (ΔE , kcal mol⁻¹, calculated according to Equation 4.3) for higher energy isomers of the $C_{10}H_8^{++}(2-PrOH)_n$ clusters for $n = 1-3$ obtained at the B3LYP/6-311++G** level.

The structure of the $C_{10}H_8^{++}(1-BuOH)$ cluster is similar to that previously discussed and has a calculated binding energy of 9.3 kcal mol⁻¹ and calculated enthalpy of 8.6 kcal mol⁻¹ (Figure 34a). The single IHB structure for the first addition of 1-butanol to the naphthalene radical, structure shown in Figure 35a(ii), has a ΔE of 7.6 kcal mol⁻¹ and calculated $-\Delta H$ of 6.8 kcal mol⁻¹ indicating that the bifurcated IHB structure is preferred. An “externally solvated” structure for the $C_{10}H_8^{++}(1-BuOH)_2$ structure (Figure 34b) is the low energy structure where $\Delta E = 8.9$ kcal mol⁻¹ and calculated $-\Delta H = 8.4$ kcal mol⁻¹. “Internally solvated” structures with two bifurcated IHBs between the 1-butanol and the the naphthalene radical cation with the orientation of the 1-butnaol

molecules differing, structures shown in Figure 35b(ii) and Figure 35b(iii), have relatively similar calculated binding energies to the “*externally solvated*” structure with ΔE values of 8.4 and 8.2 kcal mol⁻¹ and calculated $-\Delta H$ values of 7.7 and 7.2 kcal mol⁻¹ respectively. The third 1-butanol molecule binds in a similar fashion as small alcohols with a binding energy of 7.9 kcal mol⁻¹ and calculated enthalpy of 7.2 kcal mol⁻¹ (Figure 34c). If the third 1-butanol molecule adds via a single IHB, as observed in Figure 35c(ii) and Figure 35c(iii) with differing orientations of the 1-butanol, the binding energies are 6.3 and 6.1 kcal mol⁻¹ and calculated enthalpy of 5.5 and 5.2 kcal mol⁻¹ indicating that the bifurcated IHB stabilizes the third addition of 1-butanol to the naphthalene radical cation.

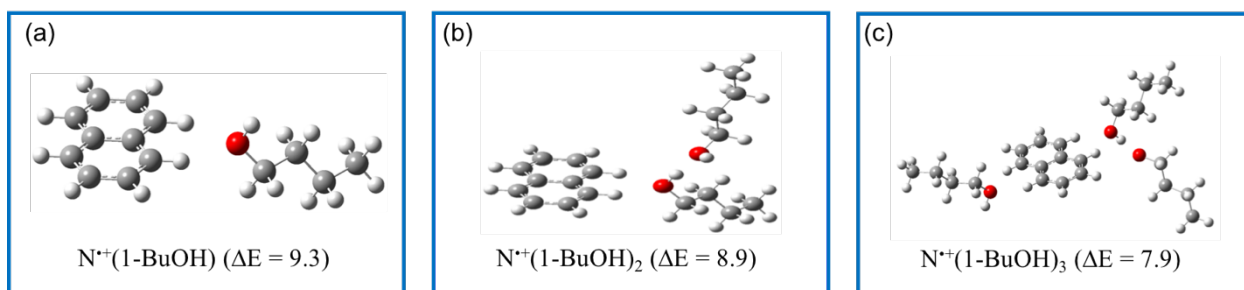
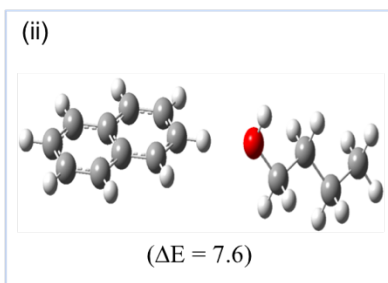
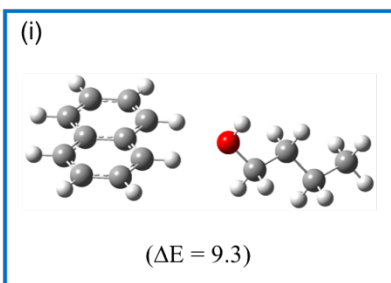
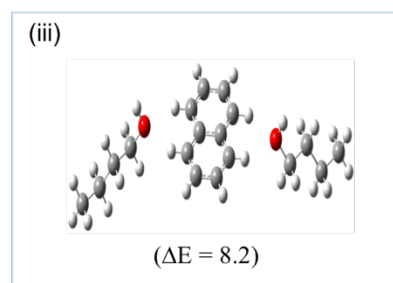
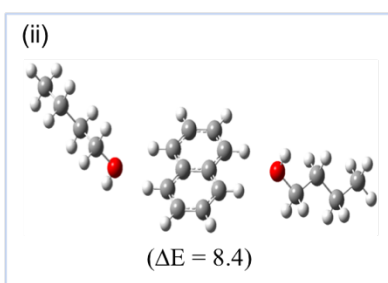
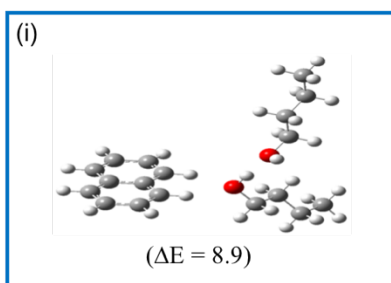


Figure 34. DFT structures and binding energies (ΔE kcal mol⁻¹, calculated according to Equation 4.3) of the lowest energy isomers of the $C_{10}H_8^{+\bullet}(1-BuOH)_n$ clusters for $n = 1-3$ obtained at the B3LYP/6-311++G** level.

(a) $C_{10}H_8^{*+}(1-BuOH)$



(b) $C_{10}H_8^{*+}(1-BuOH)_2$



(c) $C_{10}H_8^{*+}(1-BuOH)_3$

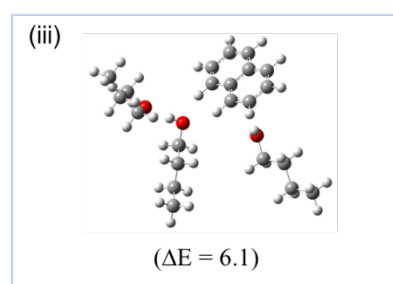
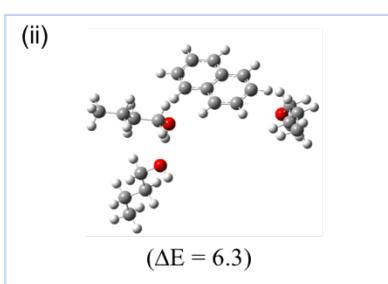
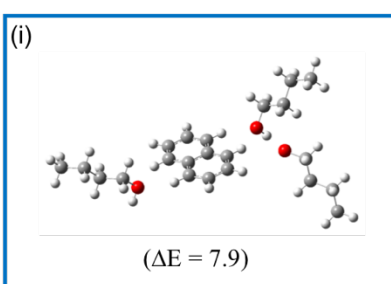


Figure 35. DFT Structures and binding energies (ΔE , kcal mol⁻¹, calculated according to Equation 4.3) for higher energy isomers of the $C_{10}H_8^{*+}(1-BuOH)_n$ clusters for $n = 1-3$ obtained at the B3LYP/6-311++G** level.

The bifurcated IHB structure for the $C_{10}H_8^{*+}(2-BuOH)$ cluster has a calculated binding energy of 8.3 kcal mol⁻¹ and calculated enthalpy of 7.6 kcal mol⁻¹ (Figure 36a) and the lower energy single IHB structure has a binding energy of 6.9 kcal mol⁻¹ and calculated enthalpy of 6.1 kcal mol⁻¹, structure shown in Figure 37a(ii). The lowest energy isomer of the $C_{10}H_8^{*+}(2-BuOH)_2$ cluster (Figure 36b) is an “*externally solvated*” structure with a calculated binding energy of $\Delta E = 8.2$ kcal mol⁻¹ and calculated $-\Delta H = 7.6$ kcal mol⁻¹. A second “*internally solvated*” structure with two IHBs, structure shown in Figure 37b(ii), of higher energy also possible with a calculated binding energy of $\Delta E = 7.4$ kcal mol⁻¹ and $-\Delta H = 6.7$ kcal mol⁻¹. If the second 2-butnaol molecule binds

with a single IHB, structure shown in Figure 37b(iii), the calculated binding energy is lower with $\Delta E = 6.1 \text{ kcal mol}^{-1}$ and $-\Delta H = 5.3 \text{ kcal mol}^{-1}$. The third association product of 2-butanol to the naphthalene radical cation is similar to that observed in 2-propanol with the structure with two bifurcated IHBs (Figure 36c) having a calculated binding energy nearly identical to that of the purely “*externally solvated*” structure, shown in Figure 37c(ii), with binding energies of 7.0 and $6.8 \text{ kcal mol}^{-1}$ and calculated enthalpies of 6.2 and $6.3 \text{ kcal mol}^{-1}$ respectively.

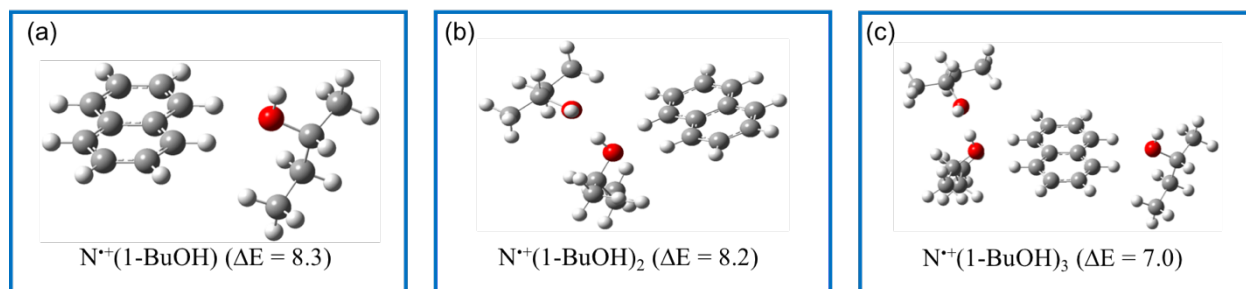
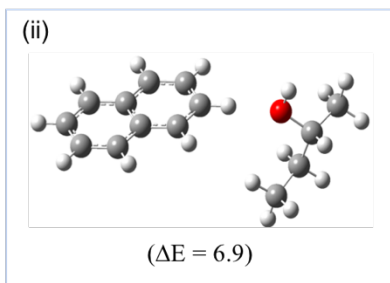
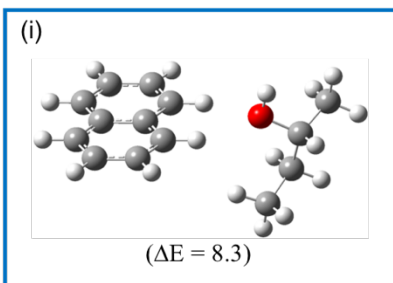


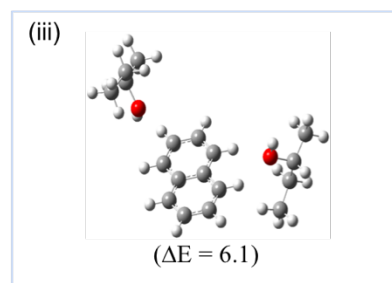
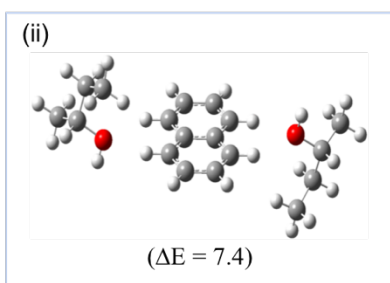
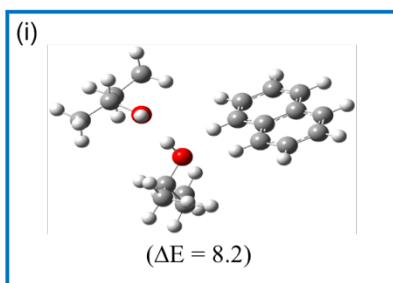
Figure 36. DFT structures and binding energies ($\Delta E \text{ kcal mol}^{-1}$, calculated according to Equation 4.3) of the lowest energy isomers of the $\text{C}_{10}\text{H}_8^+(2\text{-BuOH})_n$ clusters for $n = 1\text{-}3$ obtained at the B3LYP/6-311++G** level.

The size of the aliphatic chain on the alcohol shows no significant impact on the hydrogen bonding properties of the first addition of an alcohol to the naphthalene radical cation when compared to methanol.⁵⁶ This could be explained by the similar dipole moments of all alcohols and that the hydrogen bonding strength of the primary alcohol clusters is relatively unchanged based on IR cavity ringdown laser absorption spectroscopy.^{2,141} The calculated structures also show that secondary alcohols (2-propanol and 2-butanol) behave in the same manner as primary alcohols. Interestingly an ensemble of structures appears to be present as the alcohols increase in size. The higher entropy values observed with the longer aliphatic chains could be explained by a restriction of the structures since the value measured in entropy loss. There seems to be greater entropy contribution with the shorter aliphatic chains when the ΔG values of Table 3 are considered.

(a) $C_{10}H_8^{++}(1-BuOH)$



(b) $C_{10}H_8^{++}(1-BuOH)_2$



(c) $C_{10}H_8^{++}(1-BuOH)_3$

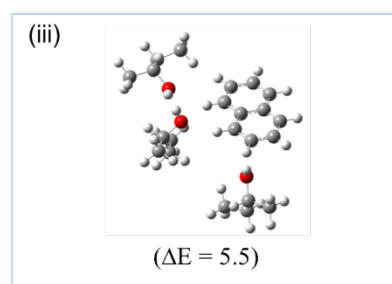
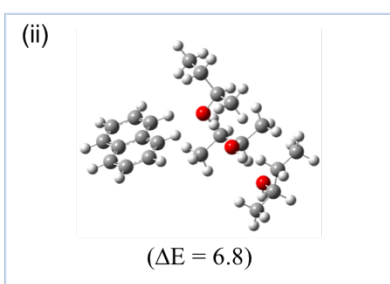
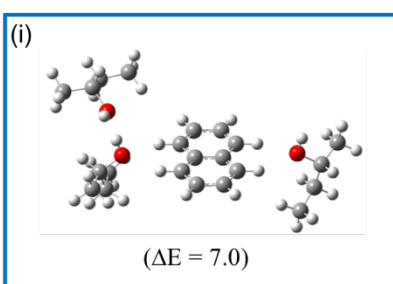


Figure 37. DFT Structures and binding energies (ΔE , kcal mol⁻¹, calculated according to Equation 4.3) for higher energy isomers of the $C_{10}H_8^{++}(1-BuOH)_n$ clusters for $n = 1-3$ obtained at the B3LYP/6-311++G** level.

4.4.4. Study of the Energies and Structures of the Stepwise Solvation of Naphthalene⁺⁺ by HCN

4.4.4.1. Mass Spectra and Thermochemical Results for Naphthalene⁺⁺(HCN)_n clusters

The mass spectra obtained following the injection of mass-selected naphthalene radical cation ($C_{10}H_8^{++}$, $Naph^+$) into the drift cell containing He or a He/HCN gas mixture are shown in Figure 38. When the mass-selected $C_{10}H_8^{++}$ is injected into the drift cell containing 0.83 Torr He at 301 K (Figure 38a), the mass spectrum shows no dissociation products, which is consistent with the low injection energy (13.8 eV), and the $C_{10}H_8^{++}$ was the major peak ($m/z = 128$). The small

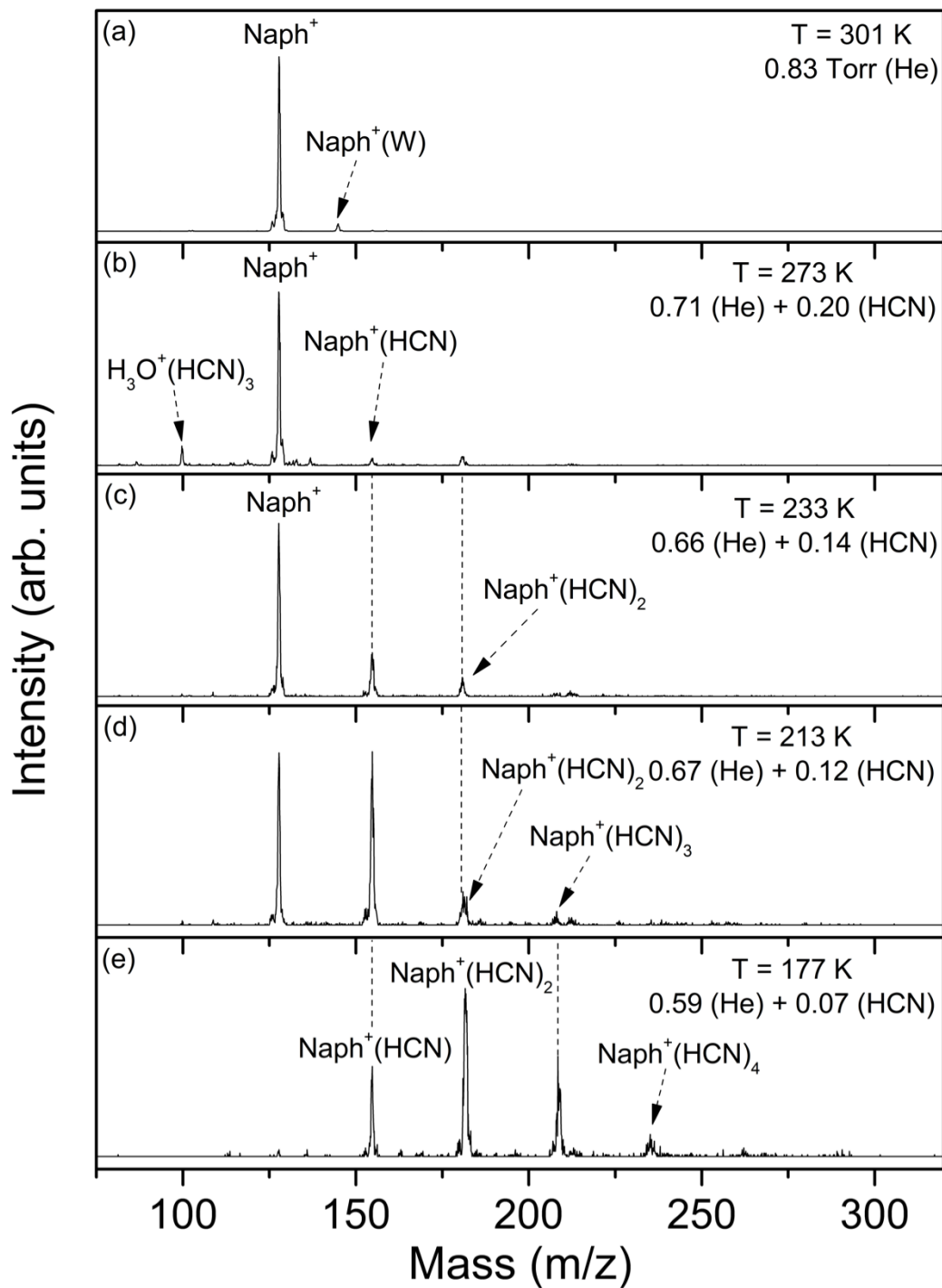
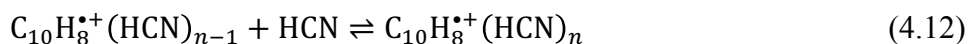


Figure 38. Mass spectra resulting from the injection of the mass-selected naphthalene radical cation ($\text{C}_{10}\text{H}_8^+$, Naph^+) into He gas (a) or He/HCN vapor mixture (b-e) at different pressures (Torr) and decreasing temperatures (K) as indicated.

peak observed at $m/z = 146$ corresponds to the $C_{10}H_8^{*+}(H_2O)$ ion (Naph⁺(W) in Figure 38a) and is present due to the trace amount of water vapor in the drift cell. When the drift cell is cooled to 273K with 0.20 Torr HCN, the first two association products of $C_{10}H_8^{*+}(HCN)_n$ for $n = 1$ and 2 ($m/z = 155$ and 182) are present as shown in Figure 38b. There is also a small peak at $m/z = 100$ which is assigned to $H_3O^+(HCN)_3$ cluster ion formed by three HCN molecules associating with a central hydronium ion. The three IHBs formed between the nitrogen atoms of the HCN and the hydrogen atoms of the core hydronium ion formed a stable solvation shell leading to an increased intensity. This peak disappeared when the water freezes at lower temperatures. Also with decreasing temperatures, the major cluster series $C_{10}H_8^{*+}(HCN)_n$ increases in intensity with a shift towards larger n values (Figure 38c-e). At 177 K, the lowest temperature achieved before condensation of the HCN, the naphthalene radical cation peak is not present and the $C_{10}H_8^{*+}(HCN)_n$ cluster peaks for $n = 1-4$ were the dominate peaks present (Figure 38e).

The association reaction of HCN with the naphthalene radical cation is represented by Equation 4.12:



The equilibrium constants are measured for Equation 4.12 using Equation 4.2 by obtaining the peak intensities of the the stepwise association of neutral HCN to the $C_{10}H_8^{*+}$ ion at different temperatures and using Equation 3.5 the van't Hoff plots for each association step is produced as shown in Figure 39. The resulting $-\Delta H^\circ$ and $-\Delta S^\circ$ values for Equation 4.12 are obtained from the slope and intercept of the van't Hoff plot respectively are calculated and summarized in Table 4.

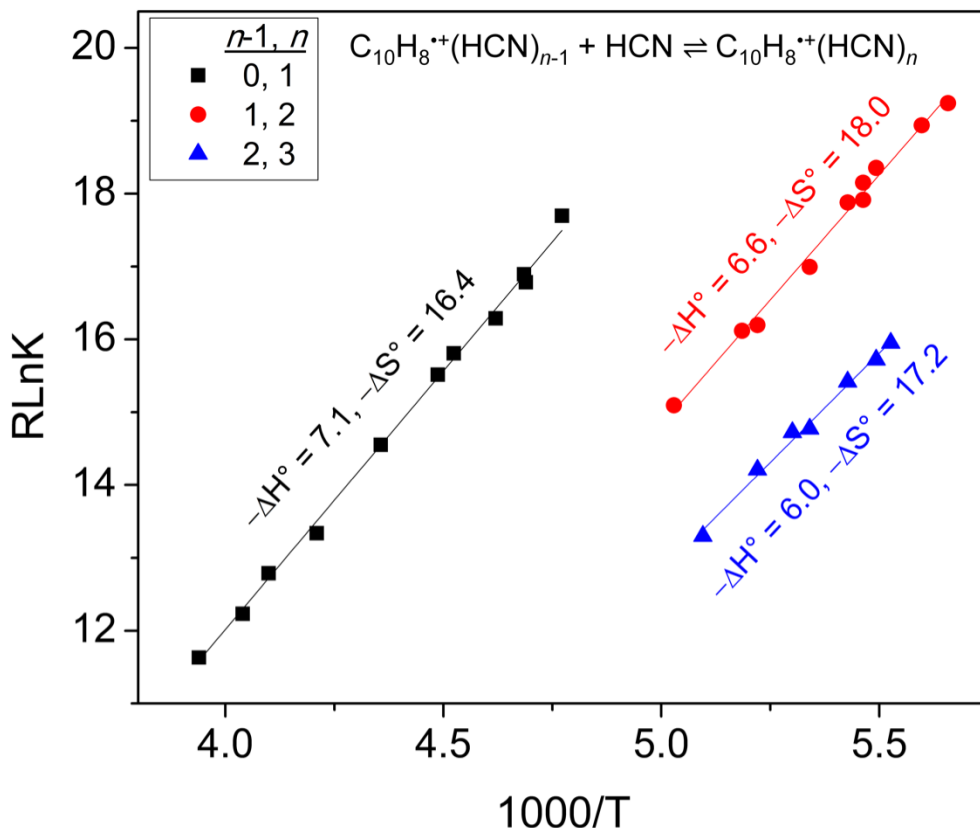


Figure 39. van't Hoff plots for the temperature dependence of the equilibrium constants of the association reaction of naphthalene radical cation with HCN for the first, second, and third solvation steps. The resulting ΔH° and ΔS° are in (kcal mol^{-1}) and ($\text{cal mol}^{-1} \text{K}^{-1}$) respectively. The experimental error for the $-\Delta H^\circ$ and $-\Delta S^\circ$ values are $\pm 1 \text{ kcal mol}^{-1}$ and $\pm 2 \text{ cal mol}^{-1} \text{K}^{-1}$ respectively.

Table 4. Measured thermochemistry ($-\Delta H^\circ$ and $-\Delta S^\circ$)^a of the formation of $\text{C}_{10}\text{H}_8^{\bullet+}(\text{HCN})_n$ clusters for $n = 1-3$ and the calculated binding energies (ΔE , corrected ZPVE) and enthalpies ($-\Delta H$ calc) at the B3LYP/6-311++G** (ΔE and $-\Delta H$ calc), M06-2X/6-311+G**, and ω 97X-D/6-311+G** levels for $\text{C}_{10}\text{H}_8^{\bullet+}(\text{H}_2\text{O})_n$ cluster for $n=1-4$.

n	$-\Delta H^\circ$	$-\Delta S^\circ$	ΔE (B3LYP)	ΔE (M06-2X)	ΔE (ω 97X-D)	$-\Delta H$ (calc)
1	7.1	16.4	7.8	9.1	8.8	7.4
2	6.6	18.0	7.5	8.4	8.1	7.4
3	6.0	17.2	7.0	-	-	6.4
4	-	-	7.8	-	-	7.1

^a Units, estimated error for experimental measurements: $\Delta H^\circ \pm 1 \text{ kcal mol}^{-1}$ and $\Delta S^\circ \pm 2 \text{ cal mol}^{-1} \text{K}^{-1}$

The thermochemical results indicate that the binding energies of the first three HCN molecules are similar with values of $6-7 \pm 1 \text{ kcal mol}^{-1}$. This would suggest the presence of multiple binding sites with comparable energies for the HCN molecules to attach to the naphthalene radical cation. The first site would involve $\text{CH}^{\delta+}\cdots\text{N}$ unconventional hydrogen bonding where the

naphthalene radical cation acts as the proton donor to the lone pair of electrons on the nitrogen atom of the HCN molecule. Subsequent HCN molecules could attach to different $\text{CH}^{\delta+}$ sites of the naphthalene radical cation or form linear H-bonded chains by attachment to the first HCN molecule associated with the naphthalene radical cation as observed in water and methanol.^{56,57}

Throughout the course of the experiment, ATDs were taken to ensure that the reaction between the naphthalene radical cation and neutral HCN as written in Equation 4.12 is in equilibrium. Based on the ATDs shown in Figure 40, the reaction is considered to be in equilibrium since the similar arrival times and overlapping ATDs for the naphthalene radical cation and the first three association products, $\text{C}_{10}\text{H}_8^{++}(\text{HCN})_n$ for $n = 1-3$, at 263, 233, and 183 K was observed.

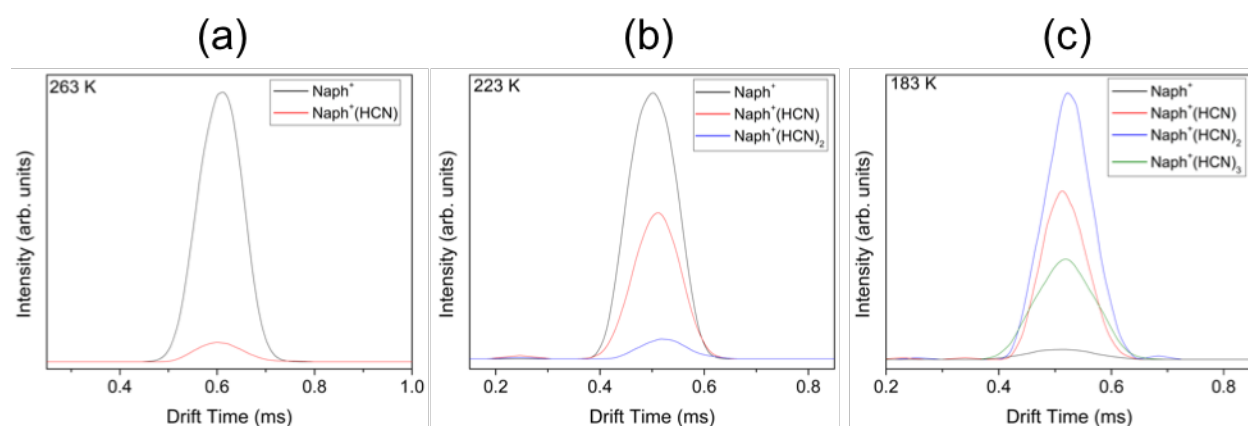


Figure 40. Arrival time distributions (ATDs) of the naphthalene radical cation (Naph^+) and the first three association products with HCN, $\text{C}_{10}\text{H}_8^{++}(\text{HCN})_n$ for $n = 1-3$ ($\text{Naph}^+(\text{HCN})_n$ for $n = 1-3$), obtained following the injection of the mass-selected naphthalene radical cation into the drift cell containing a He/HCN gas mixture at: (a) 263 K, (b) 223 K, and 183. Similar ATD overlap suggests the reaction is in equilibrium.

4.4.4.2. Calculated Structures and Binding Energies of Naphthalene⁺⁺(HCN)_n Clusters

Insights into the roles of naphthalene-HCN and HCN-HCN interactions in the energetics of the structures of $\text{C}_{10}\text{H}_8^{++}(\text{HCN})_n$ clusters are obtained by calculating the binding energies of the lowest energy structures of the $\text{C}_{10}\text{H}_8^{++}(\text{HCN})_n$ clusters using DFT calculations, which were performed by Dr. Isaac Kwame Attah. For these calculations, three levels of theory were used: M06-2X, ω 97X-D, and B3LYP levels using the 6-311++G** basis set with all results being

summarized in Table 4, which also includes the calculated enthalpy values for the lowest energy isomer at the B3LYP/6-311++G** level of theory. Similar to the methanol and water clusters, the M06-2X and ω 97X-D functional are known to be accurate for van der Waals (vdW) and weak ion-molecule interactions.^{56,57,65,79,127,144} Since the results using the B3LYP functional are closer to the experimental results compared to those using the M06-2X and ω 97X-D functionals, only the B3LYP functional was used for subsequent calculations of larger $C_{10}H_8^{*+}(HCN)_n$ clusters where $n = 3$ and 4.^{57,67}

All three functionals predicted the lowest energy isomer of $C_{10}H_8^{*+}(HCN)$ to have a bifurcated structure where the HCN molecule binds to two $CH^{\delta+}$ hydrogen atoms from the two condensed rings of the naphthalene radical cation. The distance of these bonds are 2.44 Å for the M06-2X and ω 97X-D functionals (Figure 41 structure 1-a) and 2.51 Å for the B3LYP functional (Figure 43 structure 1-a). This geometry continues the trend observed in association of water, methanol, and various alcohols with the naphthalene radical cation, but also the association of HCN with the benzene cation.^{56,69,145} The calculated binding energy of the lowest energy isomer of $C_{10}H_8^{*+}(HCN)$ cluster using the B3LYP functional is 7.8 kcal mol⁻¹ (structure 1-a of Figure 43) which is in agreement with the experimental $-\Delta H^\circ$ value of 7.1 ± 1 kcal mol⁻¹ and calculated $-\Delta H$ value of 7.4 kcal mol⁻¹. The M06-2X and ω 97X-D functionals overestimate the binding energy where the values of ΔE are 9.1 and 8.8 kcal mol⁻¹ for each functional respectively (structure 1-a in Figure 41). The geometry of three other structural isomers for the $C_{10}H_8^{*+}(HCN)$ cluster were calculated using the M06-2X and ω 97X-D and are shown in structures 1-b, 1-c, and 1-d in Figure 41. Structures 1-b and 1-c show the HCN binding in a bifurcated IHB structure, but between different $CH^{\delta+}$ groups as those in structure 1-a with binding energies of $\Delta E = 8.3$ and 7.9 kcal mol⁻¹ for the M06-2X functional and 8.4 and 7.9 kcal mol⁻¹ for the ω 97X-D functional respectively.

Structure 1-d shows the HCN above the plane of the naphthalene radical cation with the nitrogen atom pointing to the plane of the cation in an ion-dipole structure with a binding energy of $\Delta E = 7.4 \text{ kcal mol}^{-1}$ for the M06-2X functional and $8.0 \text{ kcal mol}^{-1}$ for the ω 97X-D functional. Overall the M06-2X and ω 97X-D functionals result in the same low energy structures and similar binding energies. The B3LYP functional does result in lower calculated binding energies, but these values are closer to the experimental $-\Delta H^\circ$ values making it more accurate.⁵⁷

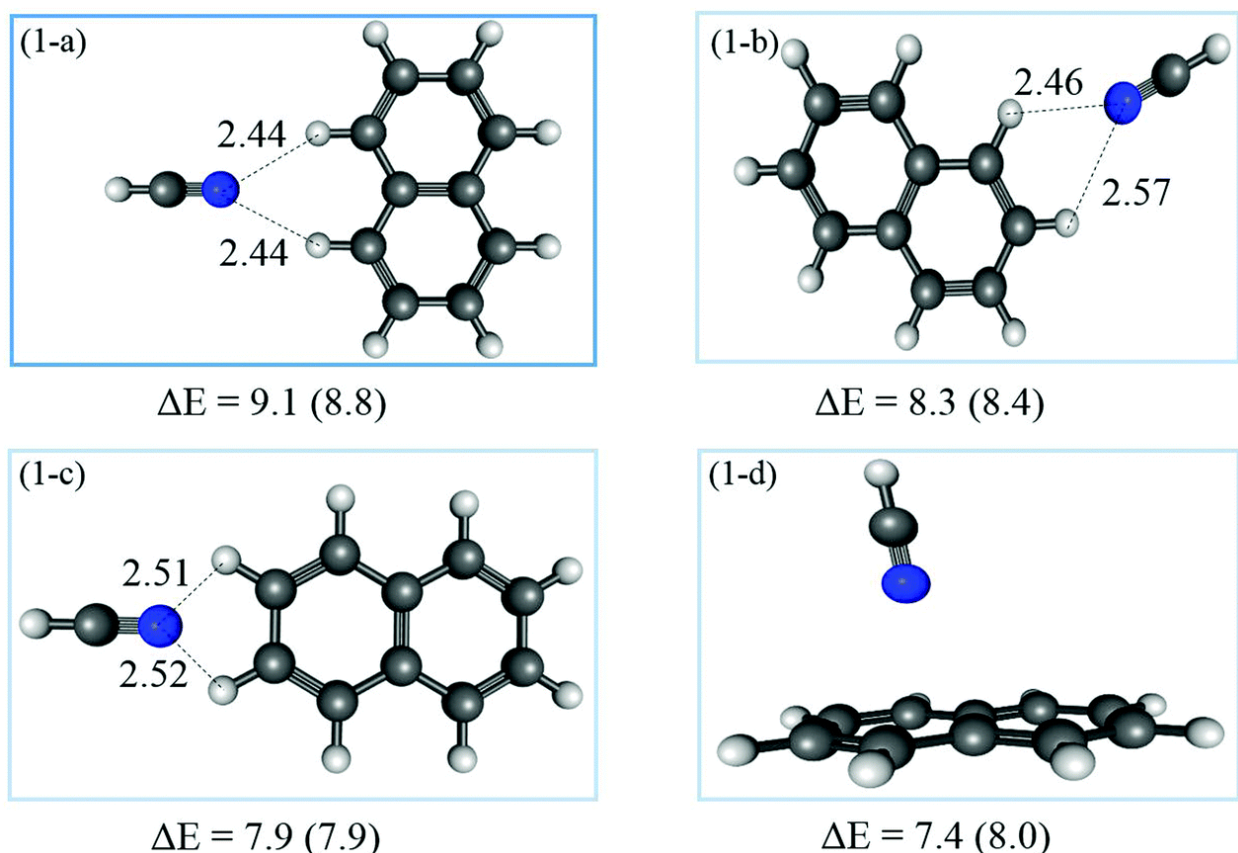


Figure 41. Structures of the four lowest energy isomers of the $C_{10}H_8^{++}(HCN)$ complex obtained using two functionals: M06-2X and ω 97X-D, within the 6-311+G** basis set. The calculated energies ΔE in kcal mol^{-1} are given using M06-2X and ω 97X-D (in parenthesis) methods.

The structures of six isomers for the $C_{10}H_8^{++}(HCN)_2$ cluster using the M06-2x and ω 97X-D functionals as shown in Figure 42 where the calculated binding energies range from 8.4 to $6.0 \text{ kcal mol}^{-1}$. The lowest energy isomer (structure 2-a in Figure 42) has an “*internally solvated*” structure where the second HCN molecule forming a second bifurcated IHB with the naphthalene radical

cation with a binding energy of 8.4 and 8.1 kcal mol⁻¹ for the M06-2X and ω 97X-D functionals respectively. An “*externally solvated*” structure was calculated (structure 2-b in Figure 42) and resulted in a binding energy of 8.0 kcal mol⁻¹ for both the M06-2X and ω 97X-D functionals. The small difference between structures 2-a and 2-b in Figure 42 indicates that the HCN IHB interaction with the CH^{δ+} group of the naphthalene radical cation (CH^{δ+} ... NCH) is similar to the hydrogen bonding interaction with the second HCN molecules (NCH ... NCH).

This is supported when the M06-2X and ω 97X-D functional results are compared to those using the B3LYP functional; in this case, the “*externally solvated*” structure is the lower energy structure, with a binding energy of $\Delta E = 7.5$ kcal mol⁻¹ and calculated $-\Delta H = 7.4$ kcal mol⁻¹ (structure 2-a in Figure 43), compared to the “*internally solvated*” structure where the calculated binding energy was $\Delta E = 7.2$ kcal mol⁻¹ and calculated $-\Delta H = 6.7$ kcal mol⁻¹ (structure 2-b in Figure 43). Similar structures are produced using all three functionals, but the M06-2X and ω 97X-D functionals overestimate the binding energies when compared to the experimental $-\Delta H^\circ$ value of 6.6 ± 1 kcal mol⁻¹. This trend is to to what was observed with water and methanol.⁵⁶ With this in mind, the B3LYP functional at the 6-311++G** level was used to calculate the lowest energy structures of the C₁₀H₈^{•+}(HCN)_n for n = 3 and 4. The resulting structures and calculated binding energies are shown in Figure 43.⁵⁷

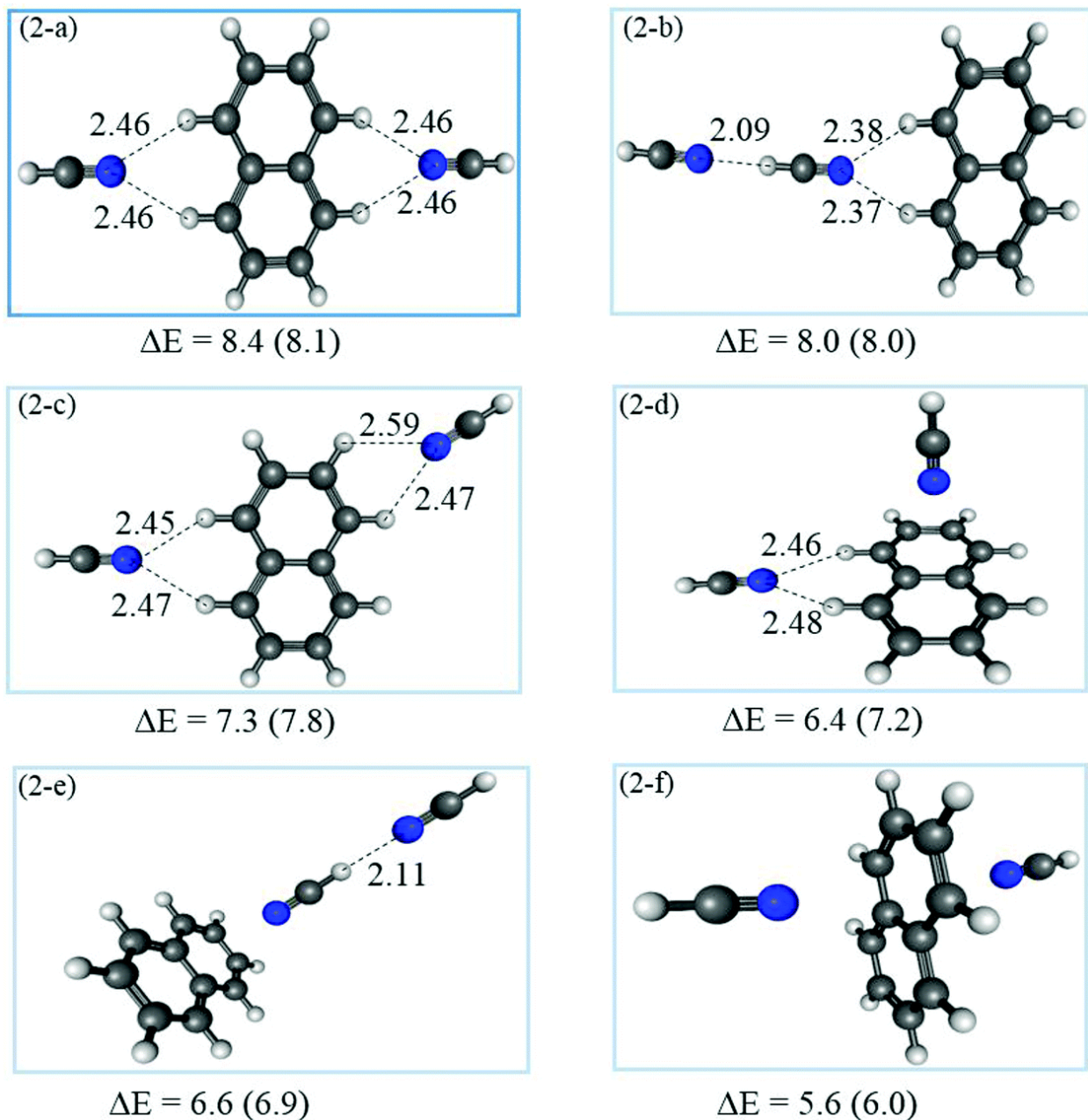


Figure 42. Structures of the six lowest energy isomers of the $C_{10}H_8^{++}(HCN)_2$ complex obtained used two functionals: M06-2X and ω 97X-D, within the 6-311+G** basis set. The calculated energies ΔE in kcal mol^{-1} are given using M06-2X and ω 97X-D (in parenthesis) methods.

The lowest energy isomers of the third and fourth association steps of $C_{10}H_8^{++}(HCN)_n$ clusters where $n = 3$ and 4 show that the solvation of the naphthalene radical cation by HCN will form bifurcated hydrogen bonding sites ($CH^{\delta+} \cdots NCH$) with the ring hydrogen atoms on opposite sides of the naphthalene radical cation (structures 3-a and 4-a in Figure 43). The calculated binding

energies for these clusters were $\Delta E = 7.0$ and $7.8 \text{ kcal mol}^{-1}$ for the third and fourth association products respectively. In addition, the calculated enthalpies of these clusters were $-\Delta H = 6.4$ and $7.1 \text{ kcal mol}^{-1}$ respectively. A purely “*externally solvated*” structure for the $\text{C}_{10}\text{H}_8^{\bullet+}(\text{HCN})_3$ is shown as structure 3-b in Figure 43 where the HCN molecules form an extended hydrogen bonded chain and had a calculated binding energy of $\Delta E = 6.7 \text{ kcal mol}^{-1}$ and a calculated enthalpy of $-\Delta H = 6.5 \text{ kcal mol}^{-1}$. Although this is possible for the third association product, it does not appear to be the case for the fourth association product as shown in structure 4-a and 4-b in Figure 43 which shows a preference for forming two bifurcated hydrogen bonding interactions along the opposite side of the naphthalene radical cation where the calculated binding energy and enthalpy was 7.8 and $7.1 \text{ kcal mol}^{-1}$ for structure 4-a versus 6.5 and $6.4 \text{ kcal mol}^{-1}$ for structure 4-b.

The small energy difference between the different isomers implies that an ensemble of different configurations could exist for these clusters. This would mean that the measured $-\Delta H^\circ$ values is an average of the binding energies of different structures. Since the measured $-\Delta H^\circ$ values are obtained using equilibrium thermochemical measurements, it can be assumed that the different configurations are populated thermally.⁵⁷

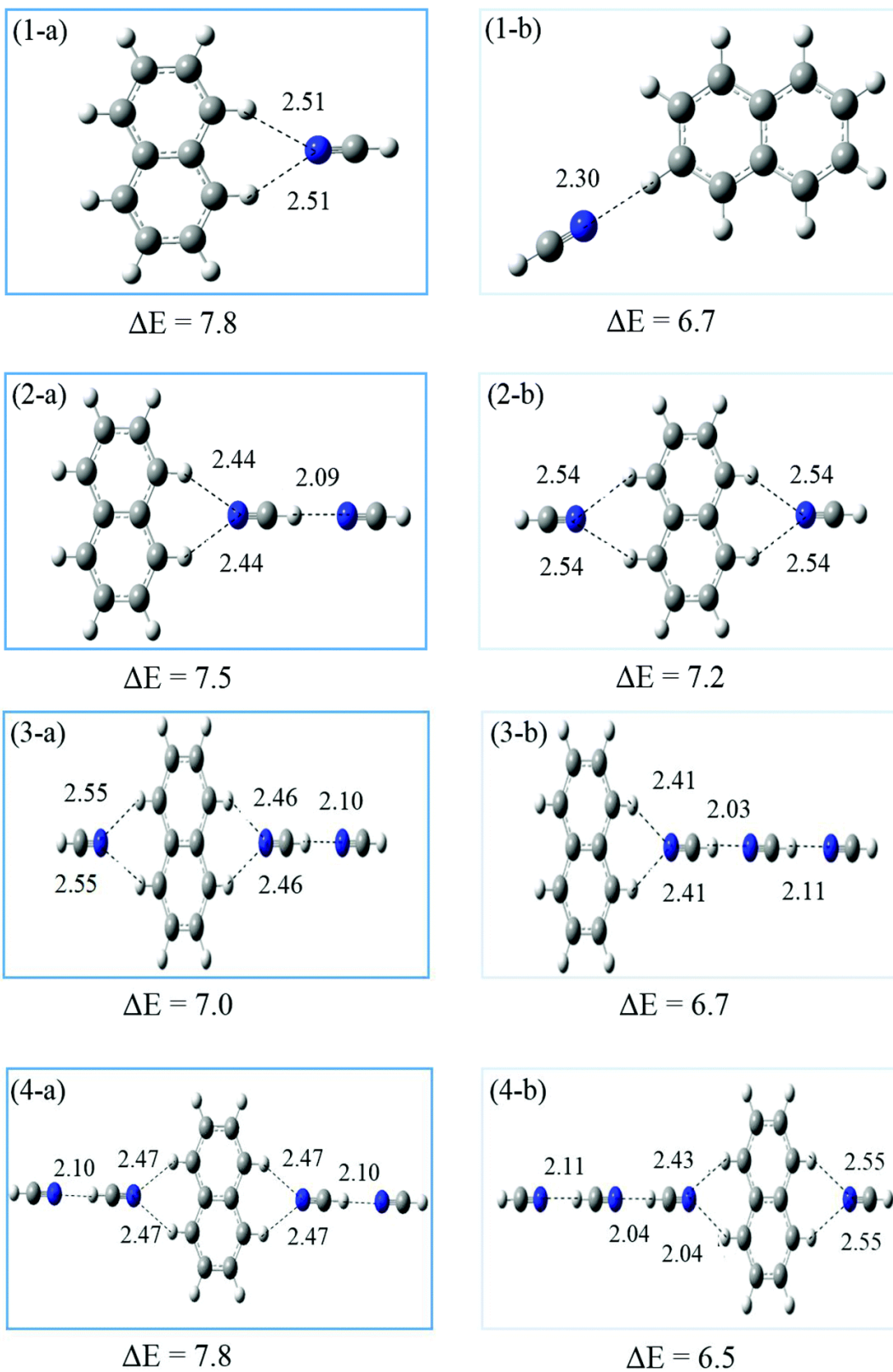


Figure 43. Structures of the two lowest energy isomers of the $C_{10}H_8^+(HCN)_n$ clusters for $n = 1-4$ obtained using the B3LYP method within the 6-311++G** basis set. The calculated energies ΔE are given in kcal mol^{-1} .

4.4.5. Study of the Energies and Structures of the Stepwise Solvation of Association of Naphthalene^{•+} by Acetonitrile

4.4.5.1. Mass Spectra and Thermochemical Results for Naphthalene^{•+}(CH₃CN)_n clusters

The mass spectra obtained following the injection of mass-selected naphthalene radical cation (C₁₀H₈^{•+}, Naph^{•+}) into the drift cell containing He or 0.25-0.17 Torr acetonitrile (CH₃CN, A) vapor in He at different temperatures are shown in Figure 44. When the mass-selected C₁₀H₈^{•+} is injected into the drift cell containing 0.83 Torr He at 292 K (Figure 44a), no dissociation products are observed, which is consistent with the low injection energy (13.8 eV). The C₁₀H₈^{•+} is the major peak of this mass spectrum with a $m/z = 128$. The small peak observed at $m/z = 146$ corresponds to the C₁₀H₈^{•+}(H₂O) ion (Naph^{•+}(W) in Figure 44a) and is present due to the trace amount of water vapor in the drift cell. At 301 K, when the drift cell contained 0.25 Torr CH₃CN, most of the naphthalene radical cations are incorporated into C₁₀H₈^{•+}(CH₃CN)_n clusters for $n = 1$ and 2 ($m/z = 169$ and 210) as shown in Figure 44b. When compared to the HCN experiments at 273 K (Figure 38b), the mass spectra indicates that binding of CH₃CN to the naphthalene radical cation is significantly stronger than HCN. This is confirmed by the observation of C₁₀H₈^{•+}(CH₃CN)_n cluster for $n = 1-3$ ($m/z = 169, 210, \text{ and } 251$) at 301 K (Figure 44b) while only $n = 1$ and 2 are weakly observed for C₁₀H₈^{•+}(HCN)_n clusters at 273 K (Figure 38b). At the lowest temperature used for CH₃CN experiments (212 K), the C₁₀H₈^{•+}(CH₃CN)_n clusters for $n = 2-5$ ($m/z = 210, 251, 292, \text{ and } 333$ respectively) are the most prominent ions observed and the peak associated with the naphthalene radical cation is not present (Figure 44d).⁵⁷

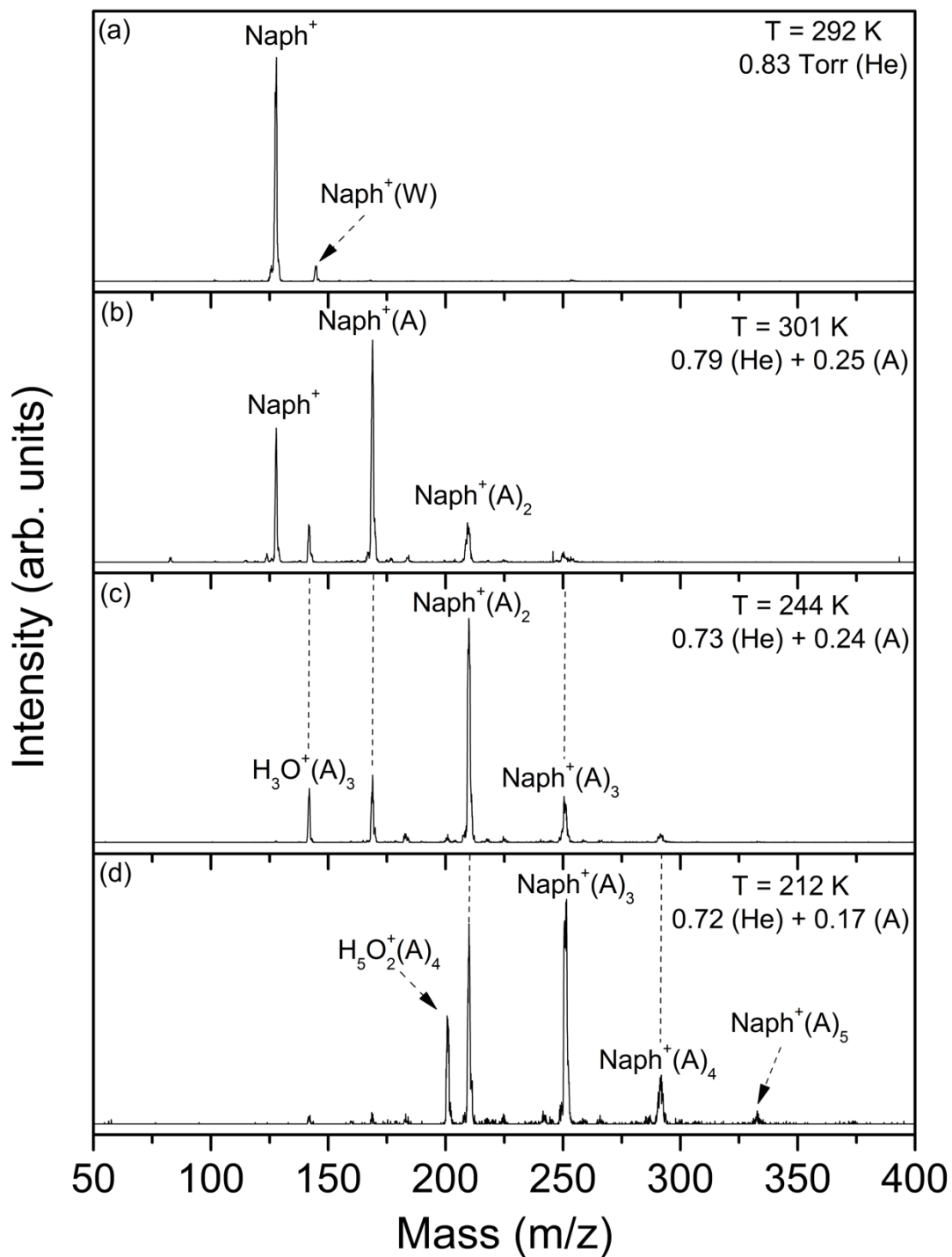
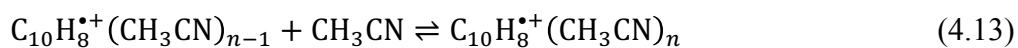


Figure 44. Mass spectra resulting from the injection of the naphthalene radical cation ($\text{C}_{10}\text{H}_8^{+\cdot}$, Naph^+) into He gas (a) or He/ CH_3CN vapor mixture (b-d) at different pressures (Torr) and decreasing temperatures (K) as indicated.

Other ions observed in the mass spectra of Figure 44 include the $\text{H}_3\text{O}^+(\text{CH}_3\text{CN})_3$ cluster at $m/z = 142$ which appears at 301 K and 244 K (Figure 44b and c). This ion is the first solvent shell of the three acetonitrile molecules around the hydronium ion, which is similar to that seen in HCN experiments (Figure 38b).¹⁴⁶ At 212 K the $\text{H}_3\text{O}^+(\text{CH}_3\text{CN})_3$ ion nearly disappears, but the $\text{H}_5\text{O}_2^+(\text{CH}_3\text{CN})_4$ cluster ion appears at $m/z = 201$ (Figure 44d). This peak indicates the formation of a protonated water dimer core (H_5O_2^+) solvated by four acetonitrile molecules through four unconventional $\text{OH}^{\delta+}\cdots\text{N}$ IHBs.¹⁴⁷ The presence of water at these lower temperatures can be explained by the trace amounts found in acetonitrile liquid that is difficult to remove due to the strong interaction between water and acetonitrile in the liquid phase.¹⁴⁸

The association reaction of CH_3CN with the naphthalene radical cation is represented by Equation 4.13:



The equilibrium constants are measured for Equation 4.13 using Equation 4.2 by obtaining the peak intensities of the stepwise association of CH_3CN with the $\text{C}_{10}\text{H}_8^{*\cdot+}$ ion at different temperatures and using Equation 3.5, van't Hoff plots for each association step were produced as shown in Figure 45. The resulting $-\Delta H^\circ$ and $-\Delta S^\circ$ values for Equation 4.13 are obtained from the slope and intercept of the van't Hoff plot respectively and the results are summarized in Table 5.

Table 5. Measured thermochemistry ($-\Delta H^\circ$ and $-\Delta S^\circ$)^a of the formation of $\text{C}_{10}\text{H}_8^{*\cdot+}(\text{CH}_3\text{CN})_n$ clusters for $n = 1-5$ and the calculated binding energies (ΔE , corrected ZPVE), enthalpies ($-\Delta H$ calc), and Gibbs free energies (ΔG calc) at the B3LYP/6-311++G**, M06-2X/6-311+G**, and ω 97X-D/6-311+G** levels for $\text{C}_{10}\text{H}_8^{*\cdot+}(\text{CH}_3\text{CN})_n$ cluster for $n = 1-6$.

n	$-\Delta H^\circ$	$-\Delta S^\circ$	ΔE (B3LYP)	ΔE (M06-2X)	ΔE (ω 97X-D)	$-\Delta H$ calc	ΔG calc
1	11.3	20.9	10.8	12.2	12.1	10.0	3.1
2	9.2	17.3	9.7	11.3	10.5	8.9	2.2
3	7.2	15.0	7.1	-	-	6.3	0.2
4	8.0	23.2	6.5	-	-	5.6	0.2
5	7.7	22.1	4.6	-	-	3.7	1.5
6	-	-	4.5	-	-	3.6	1.6

^a Units, estimated error: $\Delta H^\circ \pm 1 \text{ kcal mol}^{-1}$ and $\Delta S^\circ \pm 2 \text{ cal mol}^{-1} \text{ K}^{-1}$

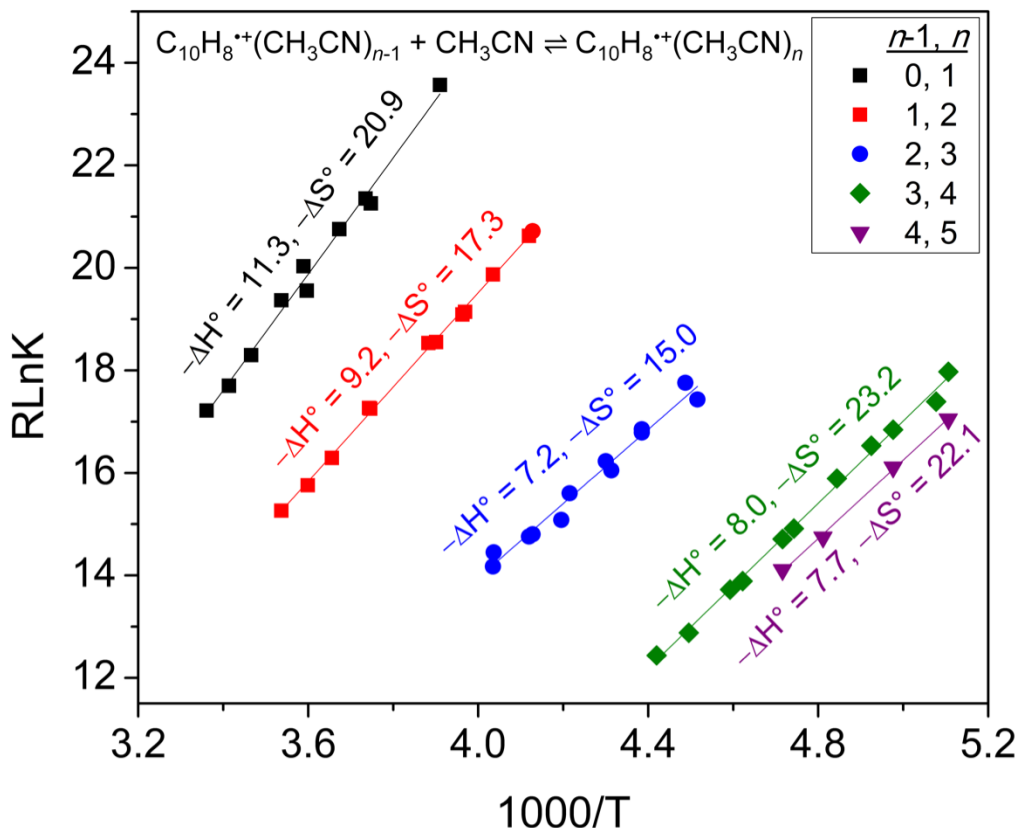


Figure 45. van't Hoff plots for the temperature dependence of the equilibrium constants of the association reaction of naphthalene radical cation with acetonitrile for the first five solvation steps. The resulting $-\Delta H^\circ$ and $-\Delta S^\circ$ are in (kcal mol^{-1}) and ($\text{cal mol}^{-1} \text{K}^{-1}$) respectively. The experimental error for the $-\Delta H^\circ$ and $-\Delta S^\circ$ values are $\pm 1 \text{ kcal mol}^{-1}$ and $\pm 2 \text{ cal mol}^{-1}$ respectively.

The thermochemical results indicate that the binding energies of the first three acetonitrile molecules to the naphthalene radical cation have decreasing values for $-\Delta H^\circ$ from $11.3 \pm 1 \text{ kcal mol}^{-1}$ for the first solvation product $C_{10}H_8^{+\cdot}(CH_3CN)$ to $7.2 \pm 1 \text{ kcal mol}^{-1}$ for the third solvation product $C_{10}H_8^{+\cdot}(CH_3CN)_3$. The fourth and fifth association products of CH_3CN to the naphthalene radical cation have similar $-\Delta H^\circ$ values of 8.0 ± 1 and $7.7 \pm 1 \text{ kcal mol}^{-1}$ respectively, which are similar to value of the third association product. ATDs for the fourth and fifth association products were taken at 223 and 208 K as shown in Figure 46. The fact that the ATDs overlap and have similar arrival times suggest that the reaction between the naphthalene radical cation and acetonitrile as shown in Equation 4.13 is in equilibrium.

The increase in entropy for the fourth and fifth association products could be explained by the possibility of multiple structures present with binding energies that average to the measured binding energy. In addition the thermochemical measurements are stepwise and therefore measure the addition of a single acetonitrile molecule to the $C_{10}H_8^{*+}(CH_3CN)_n$ cluster and therefore the entropy increase is due to more restriction of the cluster formed by Equation 4.13 due to loss of degrees of freedom compared to the reactant cluster. The calculated Gibbs free energy values in Table 5 help to explain this larger entropy contribution to the binding energies of the $C_{10}H_8^{*+}(CH_3CN)_n$ clusters where the lower ΔG is a results of a larger contribution of the $-T\Delta S$ term. Since the larger clusters are observed only at lower temperatures, entropy has a larger contribution in that term.

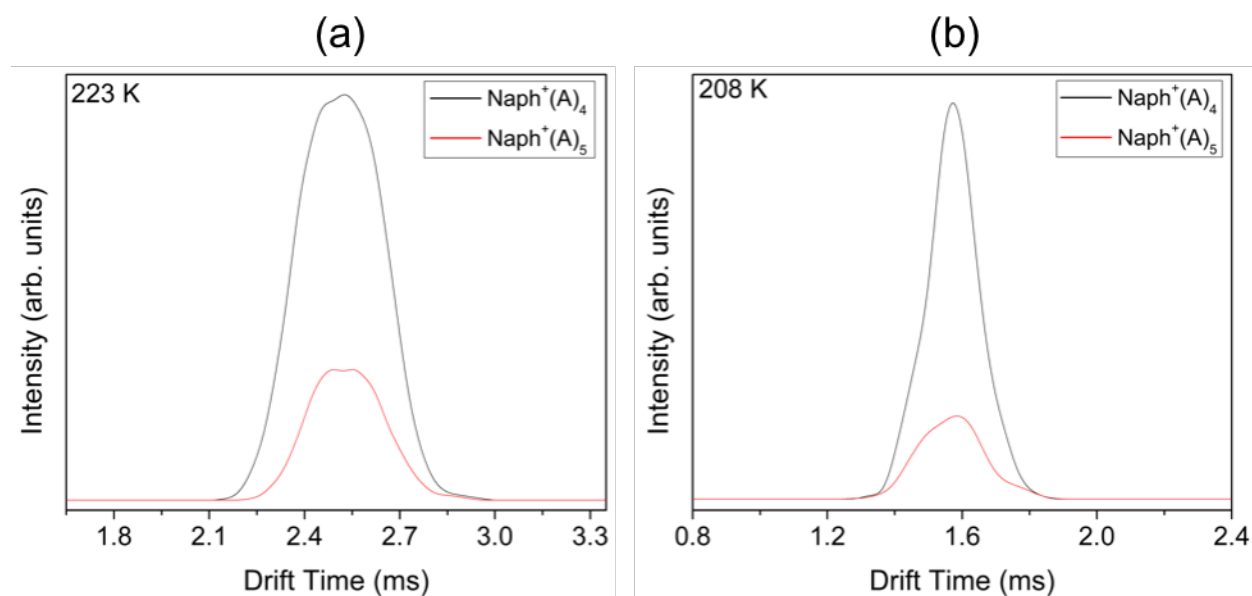


Figure 46. Arrival time distributions (ATDs) of the fourth and fifth association products of the naphthalene radical cation with acetonitrile (A), $C_{10}H_8^{*+}(CH_3CN)_n$ for $n = 4$ and 5 ($Naph^+(A)_n$ $n = 4, 5$), obtained following the injection of the mass-selected naphthalene radical cation into the drift cell containing He/ CH_3CN vapor mixture at: (a) 223 K and (b) 208 K. Similar ATD overlap suggests the reaction is in equilibrium.

4.4.5.2. Calculated Structures Binding Energies of Naphthalene^{•+}(CH₃CN)_n Clusters

The interactions of acetonitrile to the naphthalene radical cation and the energetics of the structures of the C₁₀H₈^{•+}(CH₃CN)_n clusters are obtained by calculating the binding energies (ΔE) and enthalpies ($-\Delta H$) of the lowest energy structures of the C₁₀H₈^{•+}(CH₃CN)_n clusters using DFT calculations. For these calculations, three levels of theory are used, M06-2X, ω 97X-D, and B3LYP functionals within the 6-311++G** basis set for all calculations. The lowest energy results of these calculations and comparison to experimental values are summarized in Table 5. Figure 47 displays the optimized structures of the four lowest energy isomers of the C₁₀H₈^{•+}(CH₃CN) cluster calculated at the M06-2X/6-311+G** and ω 97X-D/6-311+G** levels. The resulting calculated binding energies, ΔE , range from 12.2 and 12.1 kcal mol⁻¹ to 10.6 kcal mol⁻¹ for the M06-2X and ω 97X-D respectively. These values are in good agreement with the experimental $-\Delta H^\circ$ value of 11.3 ± 1 kcal mol⁻¹. As is the trend with all other polar molecules discussed, the lowest energy isomer (structure 1-a in Figure 47) has a bifurcated structure where the nitrogen atom of acetonitrile interacts with two CH ^{$\delta+$} hydrogen atoms belonging to the two condensed rings of the naphthalene radical cation. The other isomers for the C₁₀H₈^{•+}(CH₃CN) cluster are similar to those of C₁₀H₈^{•+}(HCN) (shown in Figure 41). The results show that this type of bifurcated IHB structure represents the most favorable interaction geometries between the nitrogen lone pair in HCN and CH₃CN molecule and the CH ^{$\delta+$} site of the naphthalene radical cation.

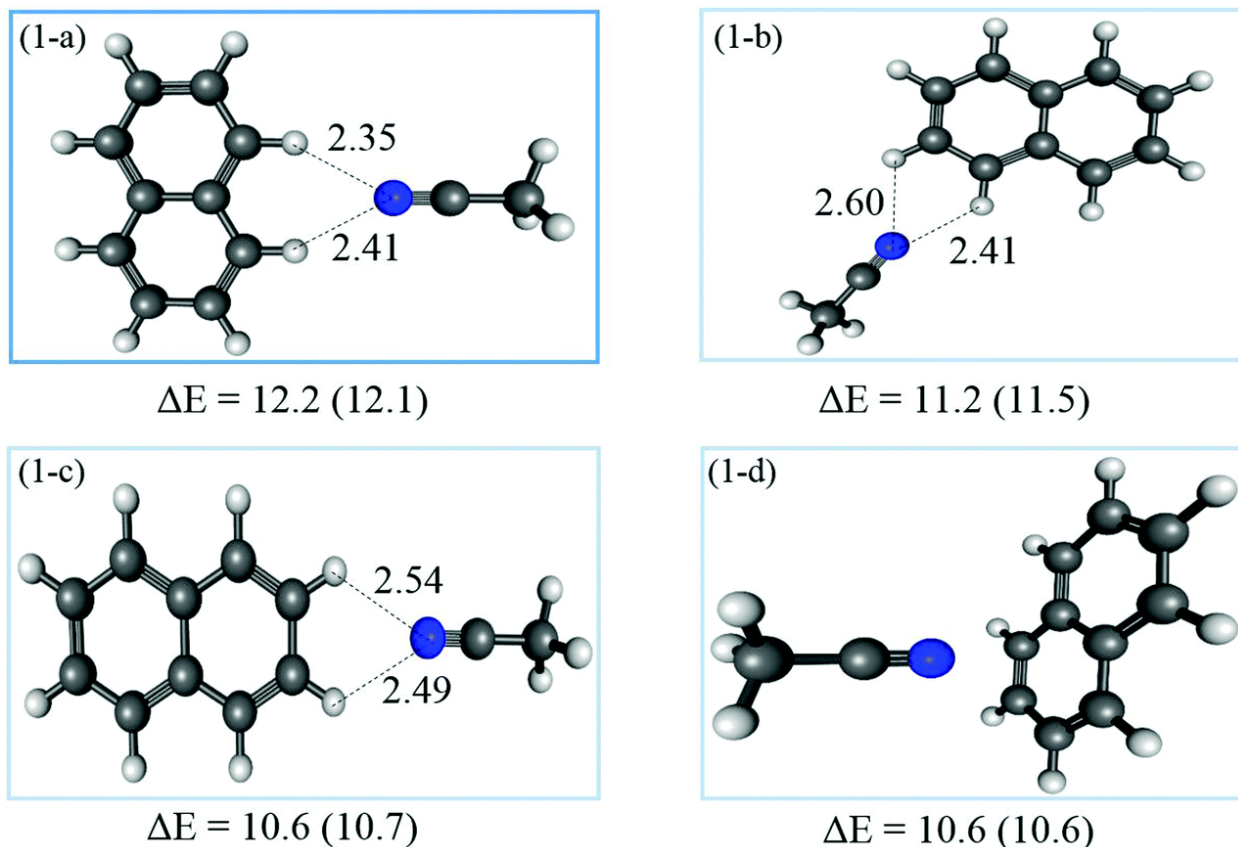


Figure 47. Structures of the four lowest energy isomers of the $C_{10}H_8^{++}(CH_3CN)$ complex obtained using two functionals: M06-2X and ω 97X-D, within the 6-311+G** basis set. The calculated energies ΔE in kcal mol^{-1} are given using M06-2X and ω 97X-D (in parenthesis) methods.

The lowest energy isomers of the $C_{10}H_8^{++}(CH_3CN)_2$ cluster calculated using the M06-2X and ω 97X-D functionals are shown in Figure 48 and have a broad range of binding energies ($\Delta E=11.3$ - $7.6 \text{ kcal mol}^{-1}$). Such differences in binding energies result in three different types of geometries: (1) double bifurcated IHB structures (structures 2-a, 2-b, and 2-c in Figure 48), (2) perpendicular and bifurcated structures (structures 2-d and 2-e in Figure 48), and (3) double perpendicular structures (structure 2-f in Figure 48). The lowest energy isomer has a double bifurcated structure IHB structure (structure 2-a in Figure 48) with a calculated binding energy of $11.3 \text{ kcal mol}^{-1}$ for the M06-2X functional and $10.5 \text{ kcal mol}^{-1}$ for the ω 97X-D. These calculated binding energies again overestimate the binding energy when compared to the experimental $-\Delta H^\circ$ value of $9.2 \pm 1 \text{ kcal mol}^{-1}$.

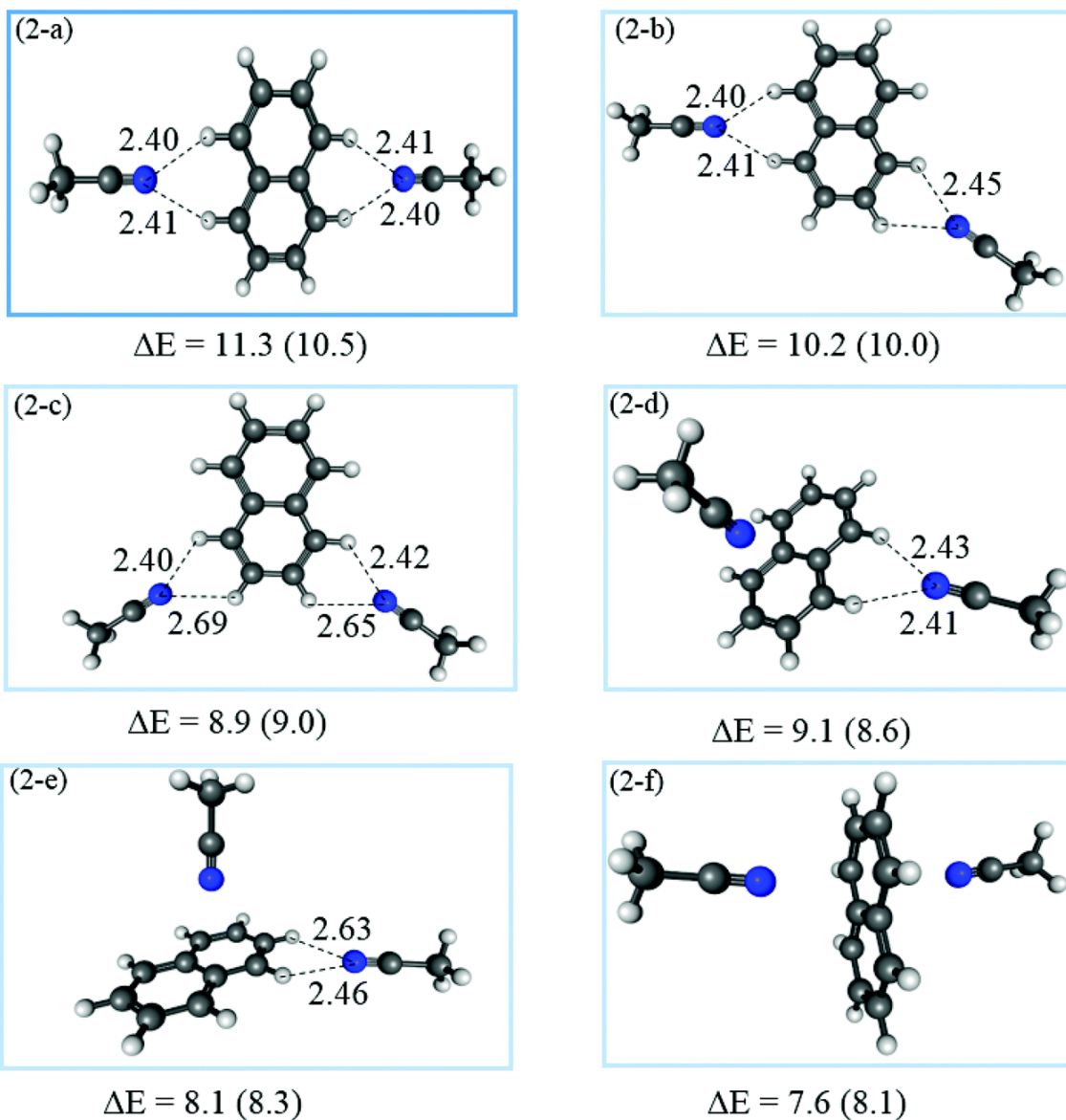


Figure 48. Structures of the six lowest energy isomers of the $C_{10}H_8^+(CH_3CN)_2$ complex obtained used two functionals: M06-2X and ω 97X-D, within the 6-311+G** basis set. The calculated energies ΔE in kcal mol^{-1} are given using M06-2X and ω 97X-D (in parenthesis) methods.

Just as in the HCN calculations, the B3LYP functional predicts the same lowest energy structures of the $C_{10}H_8^+(CH_3CN)_n$ clusters for $n = 1$ and 2 as the M06-2X and ω 97X-D functionals. The resulting structures using B3LYP/6-311++G** are shown in Figure 49. The calculated binding energies, ΔE , of the $C_{10}H_8^+(CH_3CN)_n$ clusters for $n = 1$ and 2 are 10.8 and 9.7 kcal mol^{-1} respectively which is in better agreement with the experimental $-\Delta H^\circ$ values of 11.3 ± 1 and 9.2 ± 1 kcal mol^{-1} than the M06-2X and ω 97X-D functionals (Figure 47 and Figure 48).

For larger association products of $C_{10}H_8^{*+}(CH_3CN)_n$ clusters for $n = 3-6$, structures and binding energies were only calculated at the B3LYP/6-311++G** level as shown in Figure 49. These structures build on the bifurcated IHB structure motif until the naphthalene radical cation is saturated at the fourth association product of $C_{10}H_8^{*+}(CH_3CN)_4$ (seen in structure 4-a in Figure 49). The resulting calculated binding energies for the $C_{10}H_8^{*+}(CH_3CN)_n$ clusters where $n = 3$ and 4 ($\Delta E=7.1$ and 6.5 kcal mol⁻¹ respectively) are in agreement with the experimental $-\Delta H^\circ$ values (7.2 ± 1 and 8.0 ± 1 kcal mol⁻¹ respectively). The differences here can be explained by the possibility of other structures present in addition to the lowest energy isomer. It is interesting to note that the calculated Gibbs free energy of the $C_{10}H_8^{*+}(CH_3CN)_n$ clusters for $n = 3$ and 4 are 0.2 kcal mol⁻¹ suggesting restriction in the formation of the cluster as the first solvation layer of acetonitrile around the naphthalene radical cation due to entropic contributions.

The lowest energy structures for the fifth and sixth association products, $C_{10}H_8^{*+}(CH_3CN)_n$ with $n = 5$ and 6 (structures 5-a and 6-a in Figure 49), show evidence of saturation of the IHB sites on the naphthalene cation by four acetonitrile molecules with the fifth and sixth acetonitrile molecules coordinated through weak $CH_3 \cdots N$ interactions ($CH_3^{\delta+} \cdots N\equiv C-CH_3 \cdots N\equiv C-CH_3$). In higher energy structures for the fifth and sixth association products, $C_{10}H_8^{*+}(CH_3CN)_n$ with $n = 5$ and 6 (structures 5-b and 6-b in Figure 49) show the fifth and sixth acetonitrile molecules forming perpendicular structures through the $N \cdots$ naphthalene ring interactions above and below the plane of the naphthalene radical cation. The higher energy structures also show greatly reduced calculated binding energies of $\Delta E = 3.8$ and 2.1 kcal mol⁻¹ respectively. The fifth and sixth association products $C_{10}H_8^{*+}(CH_3CN)_n$ with $n = 5$ and 6 represent the complete solvation of the naphthalene radical cation with acetonitrile molecules.

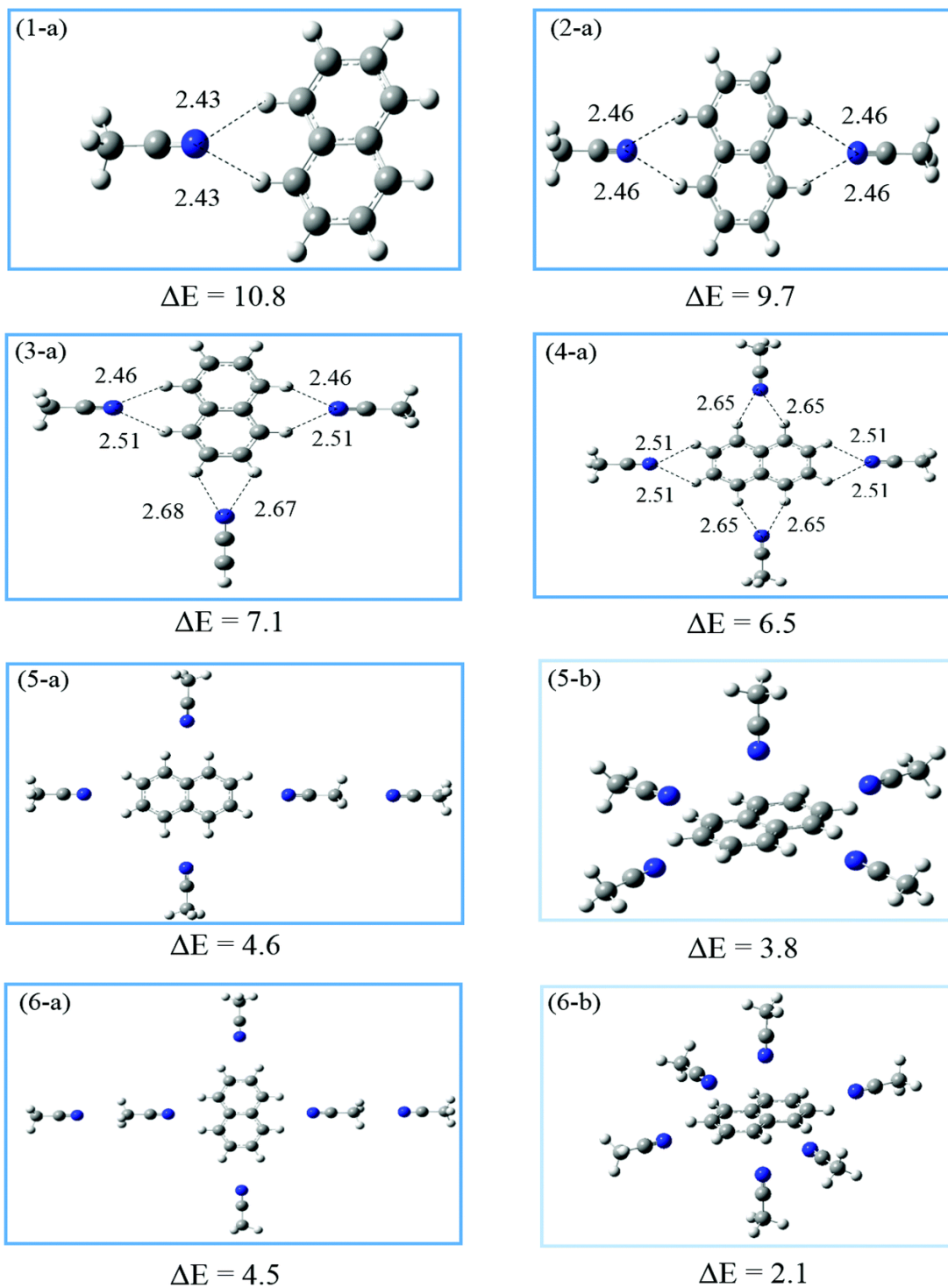


Figure 49. Structures of the lowest energy isomers of the $C_{10}H_8^+(CH_3CN)_n$ clusters for $n = 1-4$ and the two lowest energy isomers for $n = 5$ and 6 obtained using the B3LYP method within the 6-311++G** basis set. The calculated energies ΔE are given in kcal mol^{-1}

4.5. Summary and Conclusions

Equilibrium thermochemical measurements using the mass-selected ion mobility drift cell technique have been utilized to investigate the binding energies and entropy changes associated with the stepwise association of various small polar molecules with the naphthalene radical cation in the $C_{10}H_8^{*+}(B)_n$ clusters where B is the small polar molecules (water, methanol, ethanol, 1-propanol, 2-propanol, 1-butanol, 2-butanol, hydrogen cyanide, and acetonitrile). The association enthalpies ($-\Delta H^\circ$) for the various polar molecules with the naphthalene radical cation are summarized in Table 6. The nearly similar values of $-\Delta H^\circ$ for water, methanol, ethanol, and HCN of roughly $8 \pm 1 \text{ kcal mol}^{-1}$ are smaller than that of acetonitrile ($11.3 \pm 1 \text{ kcal mol}^{-1}$). This can be explained by the stronger ion dipole interaction in the $C_{10}H_8^{*+}(CH_3CN)$ given that the dipole moment is 3.92 Debye compared to the 1.55-2.98 Debye for the other polar molecules.² For both $C_{10}H_8^{*+}(HCN)_n$ and $C_{10}H_8^{*+}(CH_3CN)_n$ clusters, the sequential binding energy decreases stepwise to about 6-7 kcal mol^{-1} by three HCN or CH_3CN molecules, approaching the macroscopic enthalpy of vaporization of liquid HCN ($6.0 \text{ kcal mol}^{-1}$) or liquid acetonitrile ($7.9 \text{ kcal mol}^{-1}$).² For all other molecules, the measured $-\Delta H^\circ$ values for the first association products are below that of the enthalpy of vaporization.

The lowest energy structures of the first association for all cases consist of unconventional bifurcated hydrogen bonding of the oxygen or nitrogen atom to two $CH^{\delta+}$ hydrogen atoms from the two condensed rings of the naphthalene radical cation. Further water and methanol show that for $n = 2-6$, the naphthalene radical cation is “*externally solvated*” and is bonded through unconventional $CH^{\delta+}\cdots OHR$ ($R = H$ or CH_3) hydrogen bonds to a conventional hydrogen bonding chain of H_2O or CH_3OH molecules. HCN molecules follows as similar pattern, but in $C_{10}H_8^{*+}(HCN)_2$, the second HCN molecule forms another bifurcated hydrogen bond between the

nitrogen atom and two CH hydrogen atoms on the opposite side of the two condensed rings of the naphthalene radical cation. Subsequent HCN molecules form conventional linear hydrogen bonding chains involving HCN \cdots HCN interactions among the associated HCN molecules resulting in “*externally solvated*” structures. These structures allow the PAH ion to reside on the surface of ice grains in interstellar medium where reactions with incoming organic molecules in addition to UV irradiation can take place to produce a variety of complex organics in space.

For the C₁₀H₈⁺(CH₃CN)_n clusters for n = 1-6, “*internally solvated*” structures are favored where the acetonitrile molecules are directly interacting with the naphthalene cation through CH^{δ+} \cdots N unconventional ionic hydrogen bonds. Complete solvation is observed after the C₁₀H₈⁺(CH₃CN)₆ cluster. With these “*internally solvated*” structures, the organic component becomes isolated inside the ice and may not be accessible for reactions with incoming molecules or for efficient photochemical processes by UV irradiation.

For the other alcohols studied, ethanol, 1-propanol, 2-propanol, 1-butanol, and 2-butanol, there appears to be a mixture of structures where the calculated binding energy of the second addition forms both a double bifurcated IHB “*internally solvated*” structure as well as a fully “*externally solvated*” structure. The third association product will fill the empty site of the second addition. Testing longer aliphatic chains and tertiary alcohols will allow full characterization of the CH^{δ+} \cdots OHR IHB that is formed with the PAH ions like naphthalene.

Intracluster dissociative proton transfer reactions within the C₁₀H₈⁺(CH₃OH)_n clusters producing naphthyl radical (C₁₀H₇[•]) and protonated methanol clusters become exothermic at n ≥ 5. The deprotonation of the naphthalene radical cation by methanol clusters could lead to the generation of reactive naphthalene radicals that could participate in rich photochemistry with small organic molecules leading to further organic synthesis in space.

Table 6. Summary of measured $-\Delta H^\circ$ (kcal mol⁻¹) of the association of small polar molecules with naphthalene radical cation to form C₁₀H₈^{•+}(B)_n clusters where B is the small polar molecule indicated. Estimated error for $-\Delta H^\circ$ is ± 1 kcal mol⁻¹. The enthalpy of vaporization (ΔH_{vap} , kcal mol⁻¹) and dipole moments (in Debye) for these molecules are also shown.²

<i>n</i>	$-\Delta H^\circ$ (kcal mol ⁻¹)								
	H ₂ O	CH ₂ OH	EtOH	1-PrOH	2-PrOH	1-BuOH	2-BuOH	HCN	CH ₃ CN
1	7.8	8.3	7.8	9.2	9.9	9.9	9.8	7.1	11.3
2	-	8.6	-	-	-	-	-	6.6	9.2
3	-	-	-	-	-	-	-	6.0	7.2
4	-	-	-	-	-	-	-	-	8.0
5	-	-	-	-	-	-	-	-	7.7
ΔH_{vap}	9.7	9.0	10.1	11.3	10.7	12.4	12.0	6.0	7.9
Dipole Moment (Debye)	1.85	1.69	1.69	1.68	1.66	1.66	1.66	2.98	3.92

Chapter 5: Interactions of the Naphthalene Radical Cation with Acetylene and Olefin Molecules

5.1. Introduction

Acetylene (C_2H_2) is the smallest organic molecules than can be polymerized and is present in interstellar space and solar nebulae.^{41,108,149-157} Molecules found in outer space are subjected to ionizing radiation making ion-molecule processes an area of interest for the formation of complex organics, clustering, and polymerization in astrochemical environments.^{41,54,55,60,108,150,158,159} The variety of reactions that can be studied grows when the range of temperature and pressure conditions in outer space environments are considered.^{41,153,157}

Previous studies have studied acetylene as both an ion and a neutral in ion-neutral interactions.^{106,108,160-166} Ionized acetylene have been shown to form cyclic covalent ions such as cyclobutadiene ($C_4H_4^{*+}$) and benzene ($C_6H_6^{*+}$) within ionized acetylene clusters of $(C_2H_2)_n$ via associative charge transfer (ACT) reactions. These cyclic ions can act as nucleation centers for acetylene where the cyclic ion catalyzes intracluster reactions leading to complex organics such as naphthalene.^{160,167,168}

The polymerization of olefin molecules such as propene (C_3H_6), and isobutene (C_4H_8) have been investigated previously to observe entropy barriers and to further understand the kinetics of polymerization.^{169,170} Activation of the polymerization of isobutene was also shown via charge transfer interactions with organic cations, in particular with the benzene radical cation.^{170,171} The understanding of the polymerization energetics of these molecules are of interest since it allows for optimization of industrial processes as well as understanding reactions resulting in large organic molecules that occur in higher temperature flames and low-temperature interstellar medium.¹⁶⁹ The structure of the ethylene dimer and trimer have been investigated previously using

IR spectroscopy and DFT calculations, but no studies report it's ability to bind to aromatic ions.¹⁷²⁻

174

In this chapter, the experimental results for the thermochemistry of the condensation of acetylene onto the naphthalene radical cation are reported. To further test the the binding and possible polymerization of unsaturated aliphatic molecules via charge transfer interactions with an organic cation initiator, the thermochemistry for the olefin molecules ethylene, propylene, and isobutylene were obtained.^{169,170} The results offer the first step in understanding the binding and structures of naphthalene^{•+}(aliphatic)_n clusters. Interestingly, despite similar ionization potentials, no polymerization of the acetylene or olefin neutral was observed as was in the case with benzene or toluene.^{169,175} With theoretical calculations, the results can offer insights into the growth kinetics and formation mechanisms of complex organics as has been observed with benzene.^{108,160,161}

5.2. Experimental Section

All experiments are performed with the VCU mass-selected ion mobility spectrometer with details of the system outlined in Chapter 2. During experiments, 50-80 psi (\approx 2500-3600 Torr) ultra high purity helium (AirGas) seeded with roughly 0.74-3.76 Torr naphthalene vapor generated from heating solid naphthalene (Aldrich, \geq 99 %) stored in a sealed glass-metal bubbler to 50-70°C is pulsed through a supersonic nozzle (500 μ m) into a source vacuum chamber maintained at a background pressure of 10^{-7} Torr. Following this supersonic expansion, the naphthalene radical cation ($C_{10}H_8^{•+}$) is generated by electron impact ionization using an electron energy of 60-70 eV which is enough to ionize any organic ions of interest. The $C_{10}H_8^{•+}$ ions are mass-selected by a quadrupole mass-filter before being injected into a drift cell (in 25-50 μ s pulses) containing helium (AirGas, Research Grade) or a mixture of helium and the neutral reagent gas: acetylene (C_2H_2 , BOC Gasses, dissolved UN1001, 99.999 %), ethylene (C_2H_4 , Aldrich, \geq 99.5%), propylene (C_3H_6 ,

Aldrich, $\geq 99\%$), or isobutene (C_4H_8 , 2-methyl propene, Aldrich, 99%). Flow controllers (MKS #1479A) are used to maintain a constant pressure inside the drift cell within ± 1 mTorr. The temperature of the drift cell is controlled to ± 1 K using four temperature controllers. To cool the drift cell, liquid nitrogen is used by flowing it through solenoid valves. The reaction products that exit the drift cell are identified by scanning a second quadrupole mass-filter located after the drift cell and arrival time distributions (ATDs) are collected by monitoring the intensity of each ion as a function of time. The injection energies used in experiments (10-14 eV, laboratory frame) are only slightly higher than the minimum energies required to introduce the ions against the neutral reactant/He vapor mixture outflow at the drift cell entrance orifice. Most ion thermalization occurs outside of the drift cell by collisions with the gas mixture molecules escaping the drift cell entrance orifice.

The dissolved acetylene contains residual acetone and is “scrubbed” to ensure no side reactions with contaminants when the gas is used in the drift cell. The acetylene is first bubbled through concentrated sulfuric acid (Fisher, Certified ACS Plus) and neutralized by flowing over a 5 M NaOH solution (Fisher, Certified ACS Grade pellets). To dry the gas and remove any residual water, the acetylene flows through a drying tube containing P_2O_5 (Alfa Aesar, 98%) followed by Drierite™ drying beads (Drierite, anhydrous $CaSO_4$). From here, the scrubbed acetylene is introduced like any other neutral reagent into the drift cell.

The equilibrium reaction that all experiments follow throughout this series of studies is represented by Equation 5.1:



where B is the neutral molecule (C_2H_2 , C_2H_4 , C_3H_6 , or C_4H_8 respectively). This reaction is said to be in equilibrium when: (1) the ATDs of the product and reactant ions have equal arrival times and

(2) there is a constant ratio of the integrated intensities of product and reactant ion over a range of drift cell field voltage thus changing the residence time of the ions at a constant temperature and pressure. Once equilibrium is established, the equilibrium constant, K_{eq} , is measured using the equation:

$$K_{\text{eq}} = \frac{[\text{C}_{10}\text{H}_8^{\bullet+}(\text{B})_n]}{[\text{C}_{10}\text{H}_8^{\bullet+}(\text{B})_{n-1}][\text{B}]} = \frac{I_{[\text{C}_{10}\text{H}_8^{\bullet+}(\text{B})_n]}}{I_{[\text{C}_{10}\text{H}_8^{\bullet+}(\text{B})_{n-1}]}P_{\text{B}}} \quad (5.2)$$

where $I_{[\text{C}_{10}\text{H}_8^{\bullet+}(\text{B})_n]}$ and $I_{[\text{C}_{10}\text{H}_8^{\bullet+}(\text{B})_{n-1}]}$ are the integrated intensities of the ATDs of the reactant and product ions or the intensity of the ion peak on a mass spectrum and P_{B} is the partial pressure of the neutral vapor in atmospheres inside the drift cell. The equilibrium constant is measured at different temperatures to form a van't Hoff plot (using the van't Hoff equation as shown in Equation 3.5) where the ΔH° and ΔS° values are obtained from the slope and intercept respectively. All data was repeated at least three times with average values used in discussion.

5.3. Results and Discussion

5.3.1. Mass Spectra and Thermochemistry Results for Naphthalene^{•+}(C₂H₂)_n clusters

The mass spectra obtained following the injection of the mass-selected naphthalene radical cation ($\text{C}_{10}\text{H}_8^{\bullet+}$, Naph^+) into the drift cell containing He or C_2H_2 are shown in Figure 50. Following the injection of the mass-selected $\text{C}_{10}\text{H}_8^{\bullet+}$ into the drift cell containing 0.83 Torr He at 292 K, the mass spectrum obtained (Figure 50a) shows no dissociation products with the $\text{C}_{10}\text{H}_8^{\bullet+}$ being the major peak ($m/z = 128$), which is consistent with the low injection energy (13.8 eV). The small peak observed at $m/z = 146$ corresponds to the $\text{C}_{10}\text{H}_8^{\bullet+}(\text{H}_2\text{O})$ ion ($\text{Naph}^+(\text{W})$ in Figure 50a) and is present due to the trace amount of water vapor in the drift cell. When the naphthalene radical cation is injected into the drift cell containing 0.50 Torr C_2H_2 at 172 K (Figure 50b) the first association product, $\text{C}_{10}\text{H}_8^{\bullet+}(\text{C}_2\text{H}_2)$ ($m/z = 154$), is present, but at low intensity. However, a peak at $m/z = 153$,

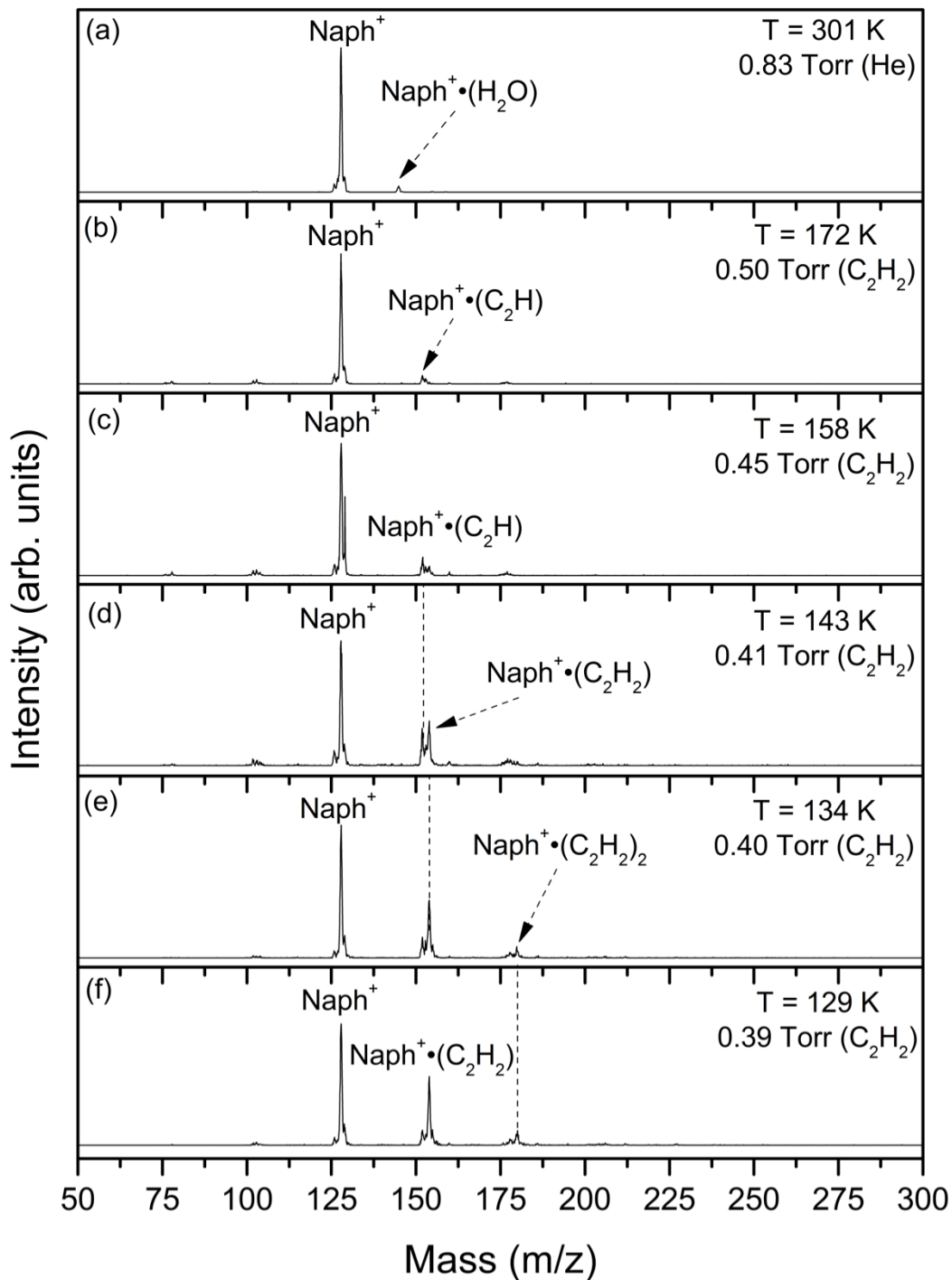
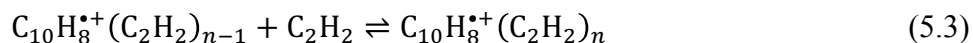


Figure 50. Mass spectra resulting from the injection of the mass-selected naphthalene radical cation ($\text{C}_{10}\text{H}_8^{+\bullet}$, Naph^+) into He gas (a) or acetylene (C_2H_2) gas (b-f) at different pressures (Torr) and temperatures (K) as indicated.

which is associated with $C_{10}H_8^{*+}(C_2H)$, is observed at higher intensity than the first association product of acetylene as well as the naphthalene radical cation. As the drift cell is cooled, the intensity of the $C_{10}H_8^{*+}(C_2H)$ peak decreases while the intensity of the $C_{10}H_8^{*+}(C_2H_2)$ increases. At 143 K (Figure 50d), the $C_{10}H_8^{*+}(C_2H_2)$ peak is the major peak of the acetylene-containing series along with the second addition product $C_{10}H_8^{*+}(C_2H_2)_2$ ($m/z = 180$) begins to appear. The same $C_{10}H_8^{*+}(C_2H)_n$ or $C_{10}H_8^{*+}(C_2H_2)(C_2H)$ peak ($m/z = 179$) is present at this temperature. Just above the condensation temperature of acetylene (129 K, Figure 50f), the $C_{10}H_8^{*+}$, $C_{10}H_8^{*+}(C_2H_2)$, and $C_{10}H_8^{*+}(C_2H_2)_2$ are the only measurable products. No acetylene clustering products are observed as observed in Chapter 4 with polar molecules.

The association reaction of acetylene with the naphthalene radical cation is represented by Equation 5.3:



The equilibrium constants were measured for Equation 5.3 using Equation 5.2 by obtaining the peak intensities of the stepwise association of C_2H_2 with the $C_{10}H_8^{*+}$ ion at different temperatures and using Equation 3.5 the van't Hoff plots for each association step was produced as shown in Figure 51. The resulting $-\Delta H^\circ$ and $-\Delta S^\circ$ values for Equation 5.3 are obtained from the slope and intercept of the van't Hoff plot respectively are calculated and summarized in Table 7.¹⁰⁸

Table 7. Measured thermochemistry ($-\Delta H^\circ$ and $-\Delta S^\circ$)^a of the formation of $C_{10}H_8^{*+}(C_2H_2)_n$ clusters for $n = 1-3$ as well as reference values for $C_6H_6^{*+}(C_2H_2)_n$ ¹⁰⁸ clusters for $n = 1-4$.

<i>n</i>	Benzene [$C_6H_6^{*+}(C_2H_2)_n$] ¹⁰⁸		Naphthalene [$C_{10}H_8^{*+}(C_2H_2)_n$]	
	$-\Delta H^\circ$	$-\Delta S^\circ$	$-\Delta H^\circ$	$-\Delta S^\circ$
1	4.0	11.4	3.3	10.9
2	3.8	12.0	3.0	10.7
3	3.6	13.7	3.1	11.4
4	3.1	10.8	-	-

^a Units, estimated error: $\Delta H^\circ \pm 1$ kcal mol⁻¹ and $\Delta S^\circ \pm 2$ cal mol⁻¹ K⁻¹

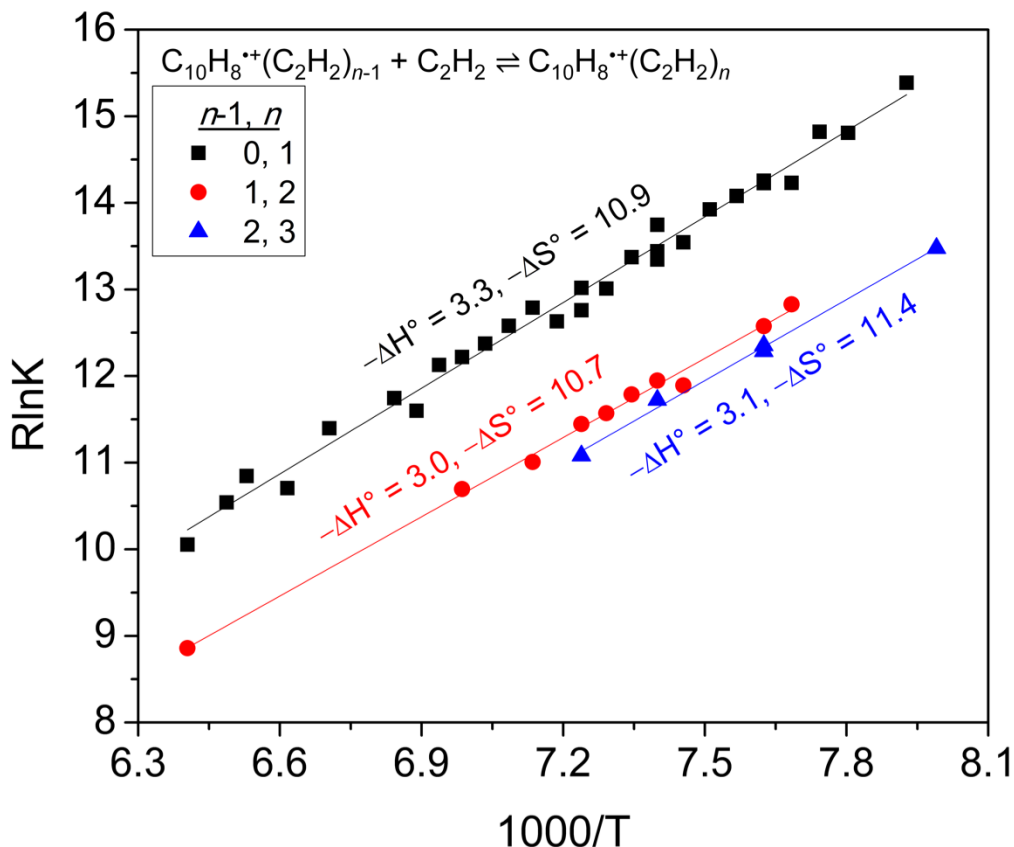


Figure 51. van't Hoff plots for the temperature dependence of the equilibrium constants of the association reaction of naphthalene radical cation with acetylene for the first three solvation steps. The resulting ΔH° and ΔS° are in (kcal mol⁻¹) and (cal mol⁻¹ K⁻¹) respectively. The error for the measurements are ± 1 kcal mol⁻¹ for $-\Delta H^\circ$ and ± 2 cal mol⁻¹ K⁻¹ for $-\Delta S^\circ$.

The thermochemistry results indicate that the binding energies for the first three association products $C_{10}H_8^{+\bullet}(C_2H_2)_n$ for $n = 1-3$ are nearly identical in values of 3.0 ± 1 kcal mol⁻¹. This is unlike the decrease that is observed in ion-neutral interactions with increasing n as in hydrogen cyanide or acetonitrile solvation.⁵⁷ Such $-\Delta H^\circ$ values suggests that there are multiple binding sites around the naphthalene radical cation with each having comparable energies. These binding sites would involve $CH^{\delta+} \cdots \pi$ hydrogen bonding where the proton donor is the naphthalene radical cation to the π system of the $C\equiv C$ bond of acetylene. The reaction shown in Equation 5.3 is in equilibrium based on the overlapping ATDs for the naphthalene radical cation and the first and second additions taken at 168 K and 138 K as shown in Figure 52.

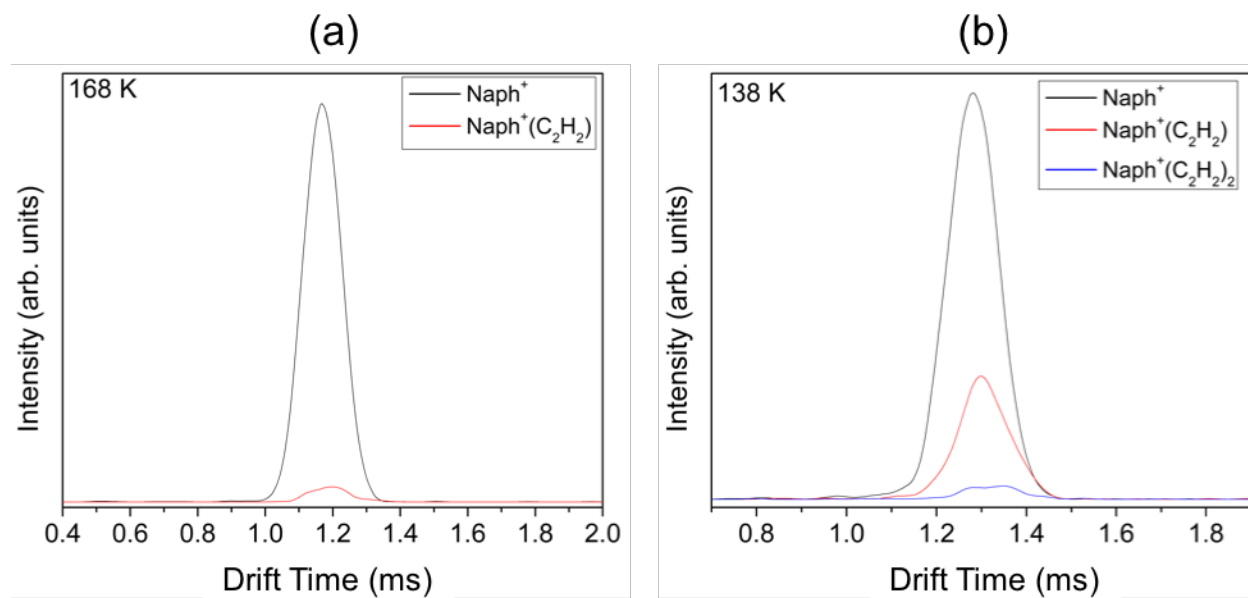


Figure 52. Arrival time distributions (ATDs) of the naphthalene radical cation (Naph⁺) and the first two association products with acetylene, C₁₀H₈⁺(C₂H₂)_n for *n* = 1 and 2 (Naph⁺(C₂H₂)_n for *n* = 1 and 2), obtained following the injection of the mass-selected naphthalene radical cation into C₂H₂ at: (a) 168 K and (b) 138 K. Similar ATD overlap suggests the reaction is in equilibrium.

The thermochemistry results are similar to what was observed in C₆H₆⁺(C₂H₂)_n clusters, however slightly lower $-\Delta H^{\circ}$ values are observed with the naphthalene radical cation which is explained by the more diffuse charge on the bicyclic naphthalene.¹⁰⁸ Larger clusters than the ones observed are required for associative charge transfer processes to occur which would explain the lack of acetylene clusters in the mass spectra.¹⁰⁸ Further insights into the possible structures that the C₁₀H₈⁺(C₂H₂)_n take require DFT calculations which will be completed in the future.

5.3.2. Association of Neutral Olefin Molecules with the Naphthalene Radical Cation

To test the possible polymerization and binding of unsaturated aliphatic molecules, the thermochemistry experiments of three olefin molecules were performed. The selected olefin molecules for these experiments are: ethylene (C₂H₄), propylene (C₃H₆), and isobutene (2-methylpropene, C₄H₈). The mass spectra following the injection of the mass-selected naphthalene radical cation into the drift cell containing He, the olefin gas (for ethylene and propylene), or a gas

mixture of He/isobutene are shown in Figure 53-Figure 55. In all cases, the first mass spectrum in each figure (Figure 53a, Figure 54a, and Figure 55a) shows the injection of naphthalene radical cation into He. In all cases, the naphthalene radical cation (Naph^+ , $m/z = 128$) is the major peak observed with no fragmentation. In both Figure 53a and Figure 55a there is a second minor peak at $m/z = 146$ which is assigned to the naphthalene $^{*+}$ -water association product. The presence of the peak is due to trace water in the drift cell.

When the naphthalene is injected into the drift cell containing 0.40 Torr C_2H_4 at 155 K (Figure 53b) a peak at $m/z = 153$ associated with $\text{C}_{10}\text{H}_8^{*+}(\text{C}_2\text{H}_3)$ is a minor peak aside from the parent naphthalene radical cation peak observed. This behavior is similar to the results using acetylene. Further cooling to 134 K (Figure 53c) results in the observation of the first association product, $\text{C}_{10}\text{H}_8^{*+}(\text{C}_2\text{H}_4)$ ($m/z = 184$), but was minor compared to the peak associated with the naphthalene radical cation. By 115 K (Figure 53e), the second association product $\text{C}_{10}\text{H}_8^{*+}(\text{C}_2\text{H}_4)_2$ is present and the first association product has nearly the same intensity as the naphthalene radical cation. Just above the temperature where the ethylene begins to condense (110 K, Figure 53f), the first association product is the major peak with the second association product and naphthalene radical cation are also present, but at lower intensities.

In the case of propylene, the same trend of a deprotonated first association product appearing prior to a shift to the first association product continues (Figure 54b-c). At 144 K (Figure 54d), the second association product is observed at $m/z = 212$ with it becoming the major peak at 129 K (Figure 54f). In addition, the third and fourth association products are also present at 129 K, just above the point at which the propylene condenses in the drift cell. Small peaks observed are due to fragmentation and impurities of the propylene gas based on a reference EI spectrum.²

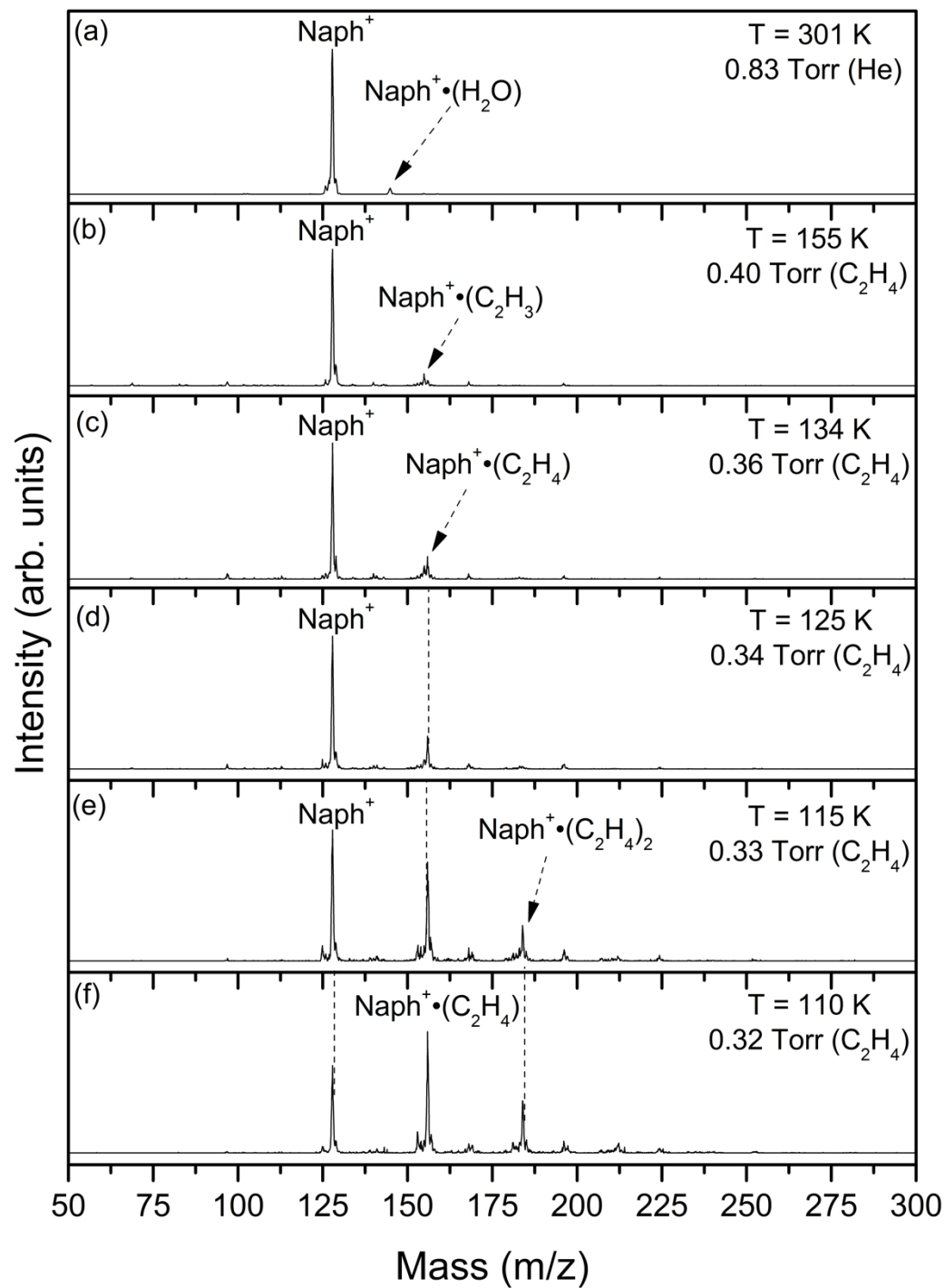


Figure 53. Mass spectra resulting from the injection of the mass-selected naphthalene radical cation ($C_{10}H_8^{+\bullet}$, $Naph^+$) into He gas (a) or ethylene (C_2H_4) gas (b-f) at different pressures (Torr) and temperatures (K) as indicated.

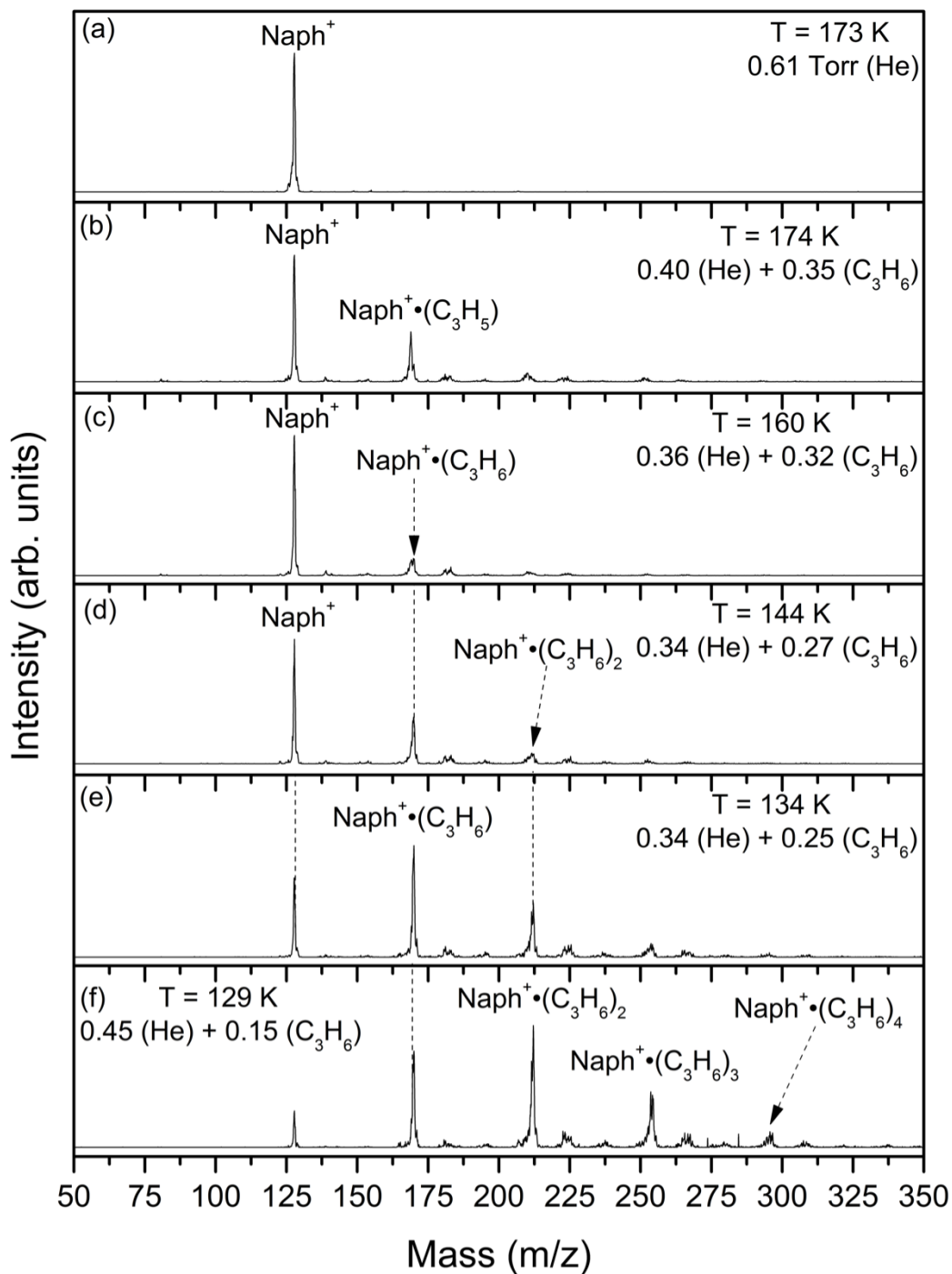
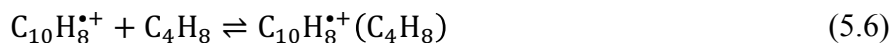
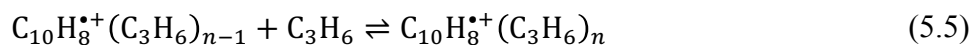
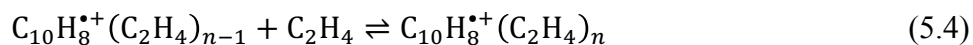


Figure 54. Mass spectra resulting from the injection of the mass-selected naphthalene radical cation ($\text{C}_{10}\text{H}_8^{+\bullet}$, Naph^+) into He gas (a) or He/propylene (C_3H_6) gas mixture (b-f) at different pressures (Torr) and temperatures (K) as indicated.

When the naphthalene radical cation is injected into isobutene, the protonated isobutene cluster $\text{H}^+(\text{C}_4\text{H}_8)_3$ where *is* observed (Figure 55b-e). This is similar to what is observed with associative charge transfer with benzene, but with smaller clusters and at lower intensities when using the naphthalene radical cation as is done in the present study.¹⁶⁹⁻¹⁷¹ This is in part due to the lower IE of naphthalene compared to that of benzene (8.14 vs. 9.24 eV respectively).² In addition, peaks at $m/z = 110$ and 145 are present and are associated with protonated isobutene clustering with minor fragments and impurities of the isobutene gas.² The first association product $\text{C}_{10}\text{H}_8^{*\dagger}(\text{C}_4\text{H}_8)$ is present as at 200 K (Figure 55b) and continues to be a minor peak until the condensation of isobutene at 169 K (Figure 55e).

The association reactions of the olefins studied (ethylene, propylene, and isobutene) with the naphthalene radical cation are represented by Equations 5.4-5.6:



The equilibrium constants are measured for these reactions using Equation 5.2 by obtaining the peak intensities of the naphthalene radical cation ($\text{C}_{10}\text{H}_8^{*\dagger}$) and the observed association products, and the pressure of the olefin in the drift cell. By measuring the equilibrium constants at different temperatures, a van't Hoff plot for the formation of the first association product using Equation 3.5 is produced for each olefin neutral gas as shown in Figure 56 (for C_2H_4), Figure 58 (for C_3H_6), and Figure 60 (for C_4H_8) and the results are summarized in Table 8. The measured $-\Delta H^\circ$ for the first three association products $\text{C}_{10}\text{H}_8^{*\dagger}(\text{C}_2\text{H}_4)_n$ where $n = 1-3$ (Figure 56) have similar values of $2.8 \pm 1 \text{ kcal mol}^{-1}$. This would suggest the presence of multiple binding sites with comparable

energies for the C_2H_4 molecules to attach to the naphthalene radical cation in a nature similar to that of acetylene. A time profile

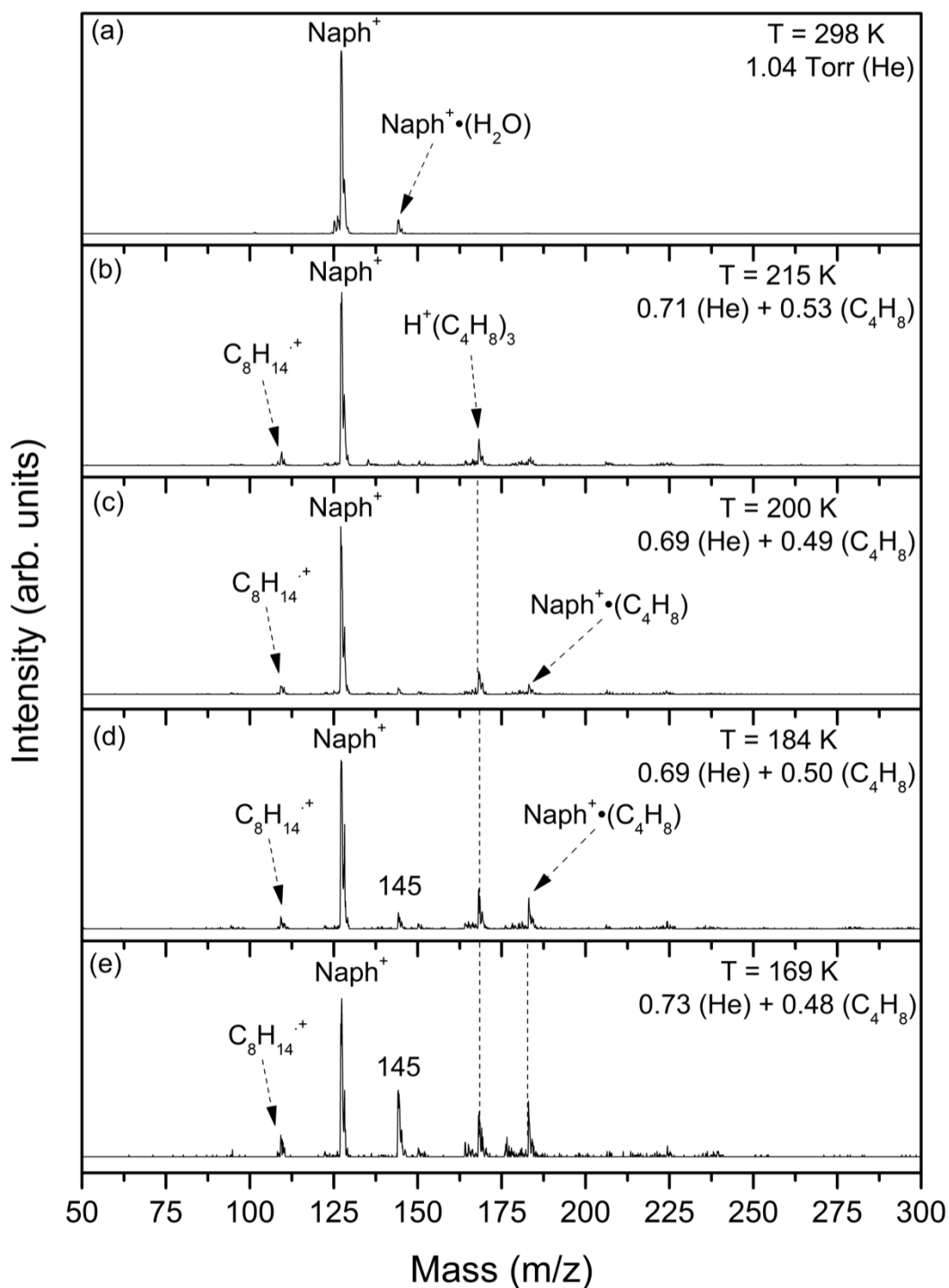


Figure 55. Mass spectra resulting from the injection of the mass-selected naphthalene radical cation ($C_{10}H_8^+$, $Naph^+$) into He gas (a) or He/isobutene (C_4H_8) gas mixture (b-f) at different pressures (Torr) and temperatures (K) as indicated.

(Figure 57) is obtained at 113 K to show that the reaction shown in Equation 5.4, which is used for the thermochemistry results, is in equilibrium. Changing the drift field resulted in relatively similar ion intensity when the results are normalized. Small changes observed at low drift time occur at high drift field and were not used during the experiment. The ATDs used in this time profile has similar arrival times as a second check for equilibrium.

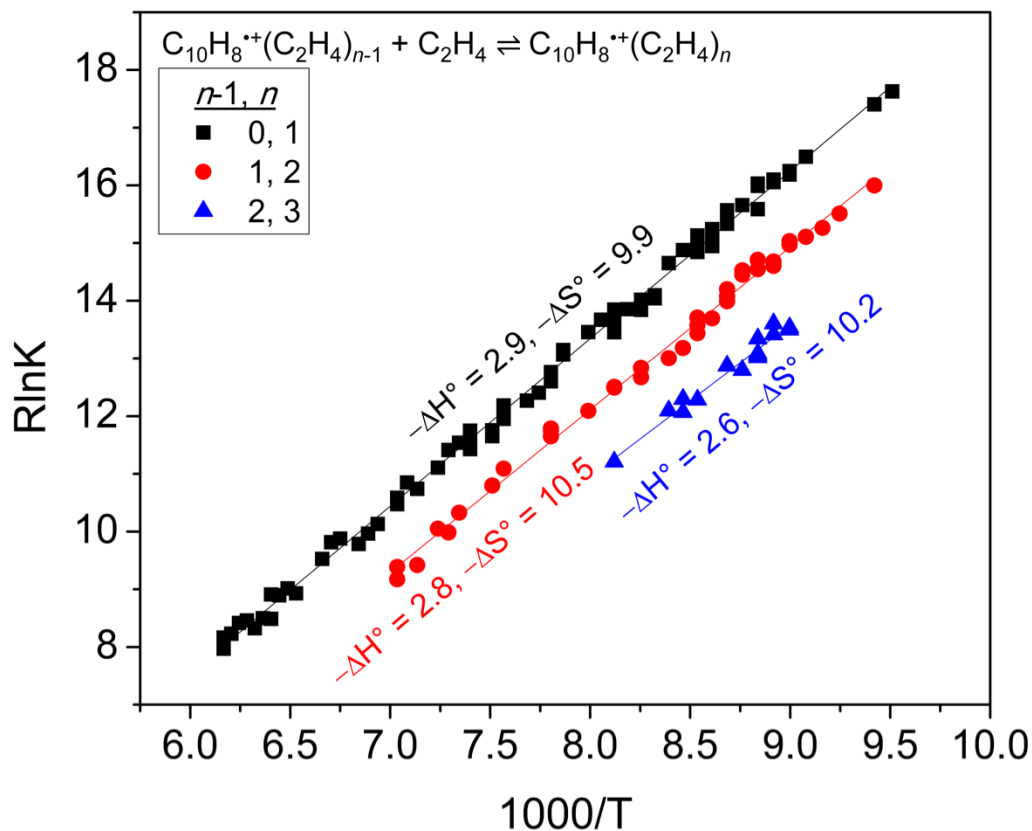


Figure 56. van't Hoff plots for the temperature dependence of the equilibrium constants of the association reaction of naphthalene radical cation with ethylene for the first three solvation steps. The resulting ΔH° and ΔS° are in (kcal mol⁻¹) and (cal mol⁻¹ K⁻¹) respectively. The error for the measurements are ± 1 kcal mol⁻¹ for $-\Delta H^\circ$ and ± 2 cal mol⁻¹ K⁻¹ for $-\Delta S^\circ$.

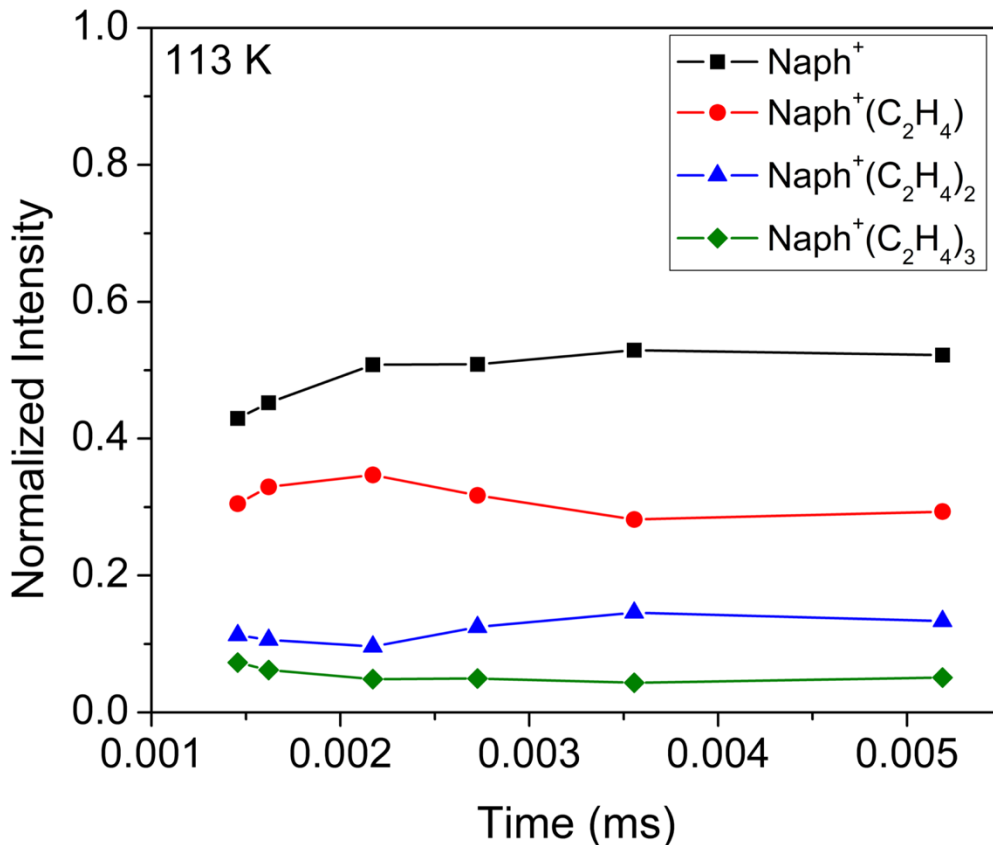


Figure 57. Time profile based on the arrival time distributions (ATDs) of the naphthalene radical cation (Naph^+) and the first three association products with ethylene, $\text{C}_{10}\text{H}_8^{*+}(\text{C}_2\text{H}_4)_n$ for $n = 1-3$ ($\text{Naph}^+(\text{C}_2\text{H}_4)_n$ for $n = 1-3$), obtained following the injection of the mass-selected naphthalene radical cation into He/ C_2H_4 gas mixtures at 113 K.

The same trend for the thermochemistry is observed for the first three association products of propylene $\text{C}_{10}\text{H}_8^{*+}(\text{C}_3\text{H}_6)_n$ for $n = 1-3$ where the experimental $-\Delta H^\circ$ has values of 4.1 ± 1 kcal mol^{-1} (Figure 58). A time profile (Figure 59) is obtained at 113 K to show that the reaction shown in Equation 5.5, which is used for the thermochemistry results, is in equilibrium. Changing the drift field resulted in relatively similar ion intensity when the results are normalized. The ATDs used in this time profile has similar arrival times as a second check for equilibrium.

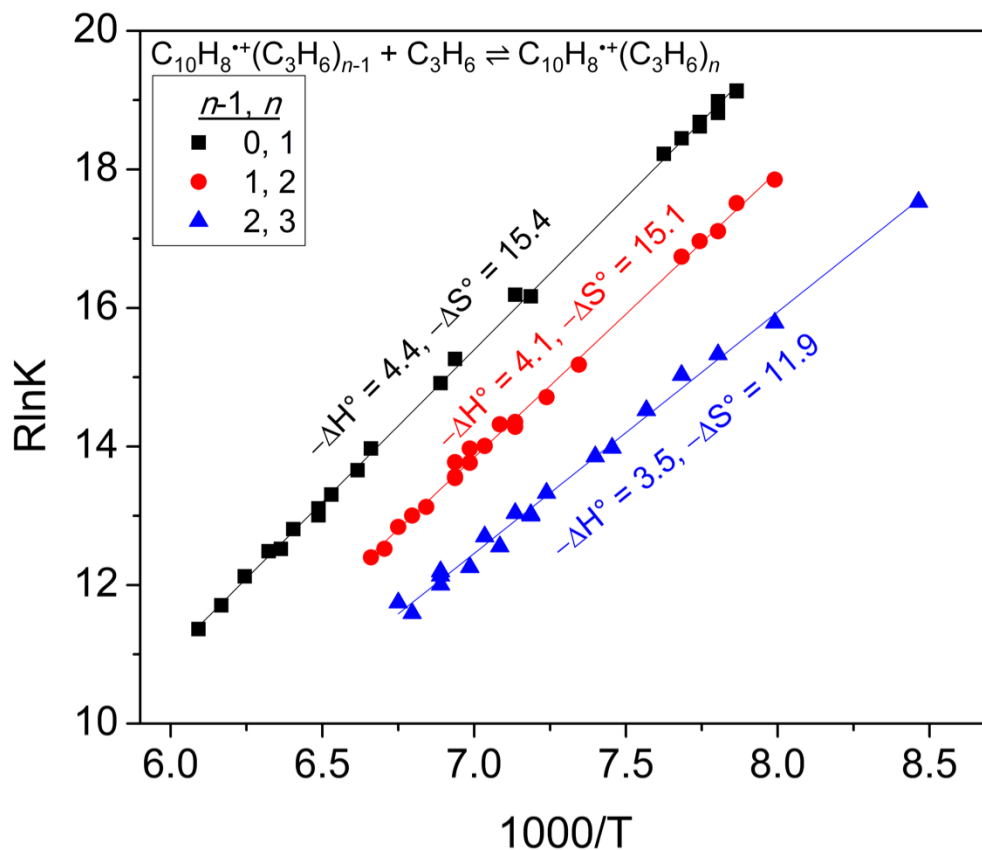


Figure 58. van't Hoff plots for the temperature dependence of the equilibrium constants of the association reaction of naphthalene radical cation with propylene for the first three solvation steps. The resulting ΔH° and ΔS° are in (kcal mol⁻¹) and (cal mol⁻¹ K⁻¹) respectively. The error for the measurements are ± 1 kcal mol⁻¹ for $-\Delta H^\circ$ and ± 2 cal mol⁻¹ K⁻¹ for $-\Delta S^\circ$.

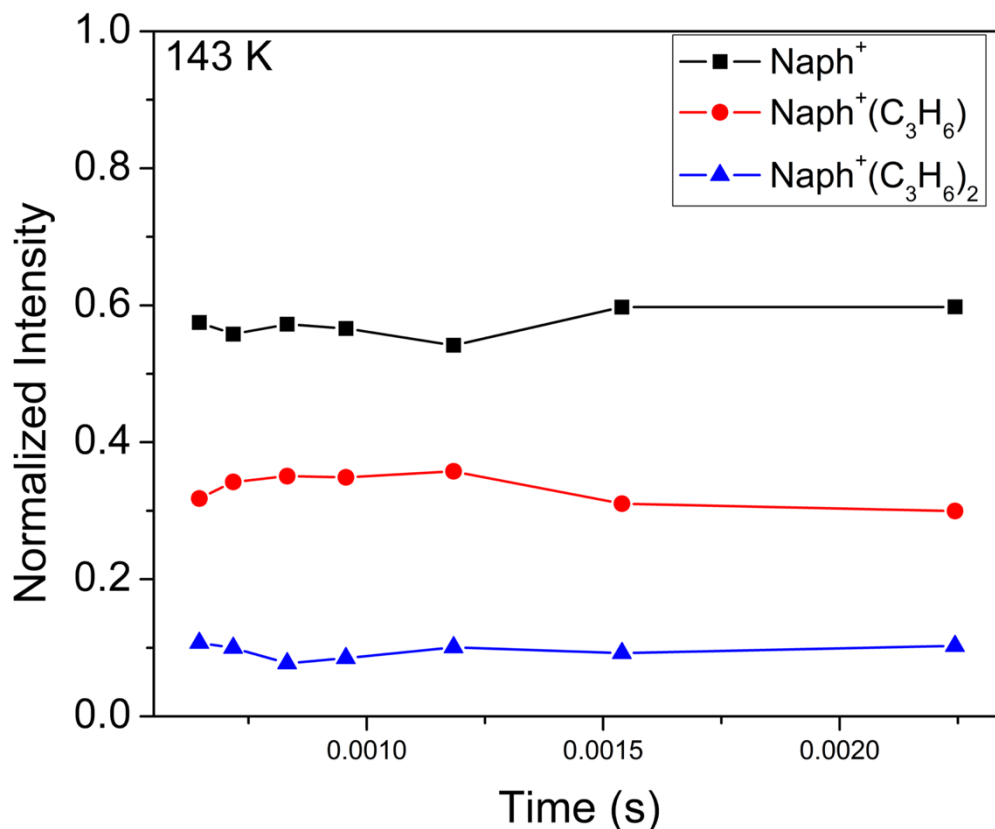


Figure 59. Time profile based on the arrival time distributions (ATDs) of the naphthalene radical cation (Naph^+) and the first two association products with propylene, $\text{C}_{10}\text{H}_8^{*+}(\text{C}_3\text{H}_6)_n$ for $n = 1-2$ ($\text{Naph}^+(\text{C}_3\text{H}_8)_n$ for $n = 1-2$), obtained following the injection of the mass-selected naphthalene radical cation into $\text{He}/\text{C}_3\text{H}_6$ gas mixtures at 143 K.

Only the first association product of isobutene for $\text{C}_{10}\text{H}_8^{*+}(\text{C}_4\text{H}_8)$ is observed (Figure 60) and has a measured $-\Delta H^\circ$ value of $3.5 \pm 1 \text{ kcal mol}^{-1}$. Further insights into the possible structures and binding behavior for the association of alkenes with naphthalene require DFT calculations which will be completed in the future. This would determine whether using the PAH naphthalene could generate polymerization of acetylene and olefins with the naphthalene radical cation as is observed with monocyclic aromatics like benzene and toluene.^{171,175} Time profiles were obtained at 193 K (Figure 61a) and 173 K Figure 61b) to show that the reaction shown in Equation 5.6 used for the thermochemistry results was in equilibrium. Changing the drift field resulted in relatively similar ion intensity when the results are normalized. The ATDs used in this time profile has similar arrival times as a second check for equilibrium.

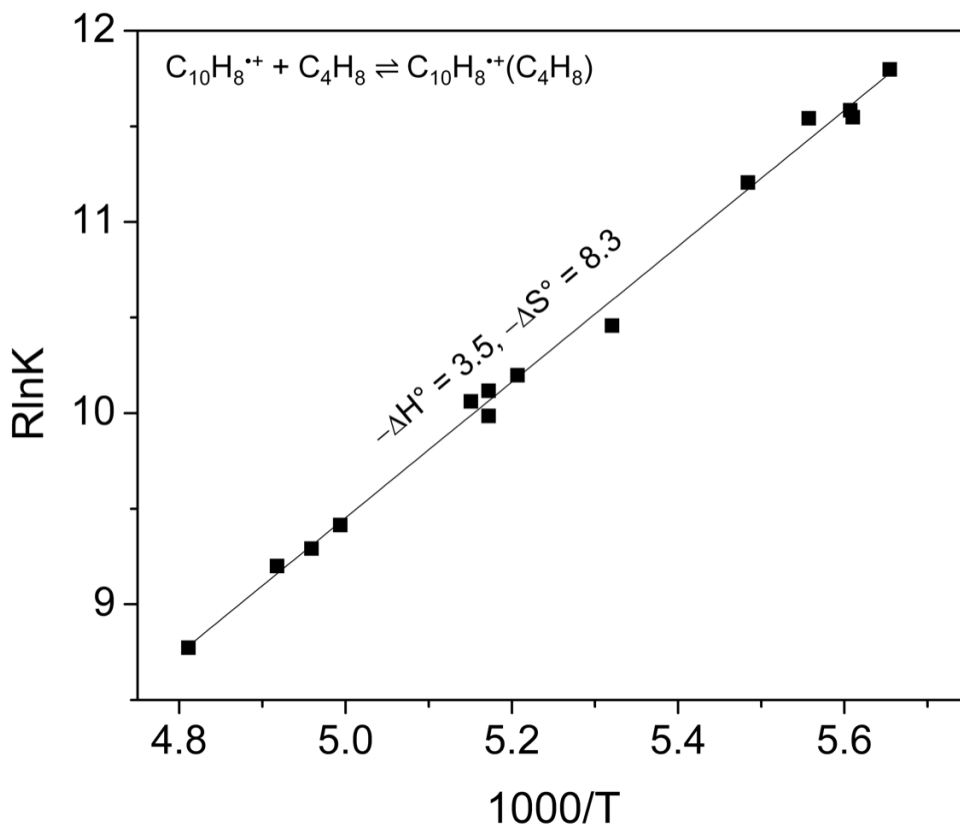


Figure 60. van't Hoff plot for the temperature dependence of the equilibrium constants of the association reaction of naphthalene radical cation with isobutene for the first step. The resulting ΔH° and ΔS° are in (kcal mol^{-1}) and ($\text{cal mol}^{-1} \text{K}^{-1}$) respectively. The error for the measurements are $\pm 1 \text{ kcal mol}^{-1}$ for $-\Delta H^\circ$ and $\pm 2 \text{ cal mol}^{-1} \text{K}^{-1}$ for $-\Delta S^\circ$.

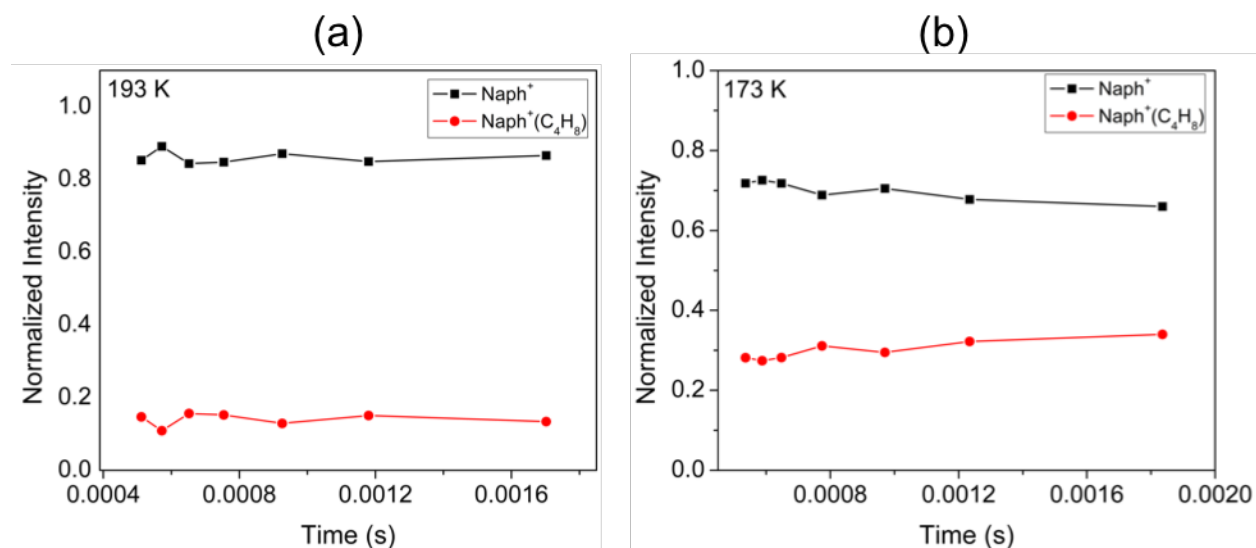


Figure 61. Time profiles based on the arrival time distributions (ATDs) of the naphthalene radical cation ($\text{Naph}^{\bullet+}$) and the first association product with isobutene, $\text{C}_{10}\text{H}_8^{\bullet+}(\text{C}_4\text{H}_8)$ ($\text{Naph}^{\bullet+}(\text{C}_4\text{H}_8)$), obtained following the injection of the mass-selected naphthalene radical cation into $\text{He}/\text{C}_4\text{H}_8$ gas mixtures at: (a) 193 K and (b) 173 K.

Table 8. Measured thermochemistry ($-\Delta H^\circ$ and $-\Delta S^\circ$)^a of the formation of $C_{10}H_8^{*+}(C_mH_{2m})_n$ clusters for ethylene ($m = 2, n = 1-3$), propylene ($m = 3, n = 1-3$), and isobutene ($m = 4, n = 1$).

<i>n</i>	Ethylene [$C_{10}H_8^{*+}(C_2H_4)_n$]		Propylene [$C_6H_6^{*+}(C_3H_6)_n$]		Isobutene [$C_{10}H_8^{*+}(C_4H_8)_n$]	
	$-\Delta H^\circ$	$-\Delta S^\circ$	$-\Delta H^\circ$	$-\Delta S^\circ$	$-\Delta H^\circ$	$-\Delta S^\circ$
1	2.9	9.9	4.4	15.4	3.5	8.3
2	2.8	10.5	4.1	15.1	-	-
3	2.6	10.2	3.5	11.9	-	-

^a Units, estimated error: $\Delta H^\circ \pm 1$ kcal mol⁻¹ and $\Delta S^\circ \pm 2$ cal mol⁻¹ K⁻¹

5.4. Summary and Conclusions

Using the mass-selected ion mobility drift cell technique, equilibrium thermochemical measurements were used to investigate the binding energies and entropy changes associated with the step-wise solvation of the naphthalene radical cation by acetylene and small olefin molecules. The measured $-\Delta H^\circ$ values were relatively constant for each system studied. For $C_{10}H_8^{*+}(C_2H_2)_n$ where $n = 1-3$, the $-\Delta H^\circ$ values were 3.0 ± 1 kcal mol⁻¹. The experimental $-\Delta H^\circ$ for the $C_{10}H_8^{*+}(C_2H_4)_n$ where $n = 1-3$ was nearly identical to that of acetylene at 2.7 ± 1 kcal mol⁻¹ suggesting similar binding and structures. In the case of propylene, observed in $C_{10}H_8^{*+}(C_3H_6)_n$ where $n = 1-3$, the binding is slightly stronger where the $-\Delta H^\circ$ is 4 ± 1 kcal mol⁻¹. The first association product was the only ion observed for isobutene, $C_{10}H_8^{*+}(C_4H_8)$, where the $-\Delta H^\circ$ was 3.5 ± 1 kcal mol⁻¹. In addition, small protonated isobutene cluster peaks were observed suggesting some polymerization. Future theoretical calculations would offer insight into whether or not acetylene condensing on the naphthalene radical cation could produce larger polycyclic aromatic hydrocarbons such as anthracene, phenalene, and phenanthrene.

Chapter 6: Structures and Binding Energies of the Naphthalene₂^{•+} Homodimer and (Naphthalene•Benzene)^{•+} and (Naphthalene•Pyridine)^{•+} Heterodimers

6.1. Introduction

Dimer radical cations of aromatic and polycyclic aromatic hydrocarbons (PAHs) are the smallest intermolecular units that carry a delocalized charge. This makes them of fundamental importance to chemistry, biochemistry, and material science.¹⁷⁶⁻¹⁷⁸ They also provide the basis for understanding photoconductivity and ferromagnetism in organic materials.^{178,179} In biological systems, interactions between the subunits of these dimers have a role in base pair stacking in DNA, drug design, and crystal packing of aromatic molecules.¹⁸⁰⁻¹⁸³ In astrochemistry, polycyclic aromatics are responsible for much of the interstellar extended red emission at 450-899 nm.^{58,60,184,185}

Nitrogen containing heterocyclic molecules are also of interest in several fields including biochemistry, pharmacology, synthetic chemistry, environmental chemistry, and astrochemistry and astrobiology.^{66,73,74,132,186,187} Interactions of these heterocycles with PAHs or PANHs can be seen between nitrogen-containing cations with neutral π systems where effects in protein structure, self-organization, molecular crystals, and molecular recognition occur.^{115,188-195} Observations from meteorite organics show that PAHs and nitrogen containing heterocyclics are present in space and when ionized by interstellar UV radiation can undergo chemistry that can form complex organic molecules and polymers.^{60,196-198}

Benzene (C₆H₆, Bz) and pyridine (C₅H₅N, Pyr) are monocyclic molecules that are used as prototype models for PAHs and PANHs (polycyclic aromatic nitrogen containing hydrocarbons).^{87,115} Naphthalene (C₁₀H₈, Naph) is considered one of the simplest PAHs. When observing the (Naph•Naph)^{•+} and (Bz•Bz)^{•+} homodimers, the unpaired electron of the radical

cation is considered to be shared between the two moieties resulting in extra charge stabilization and ion-induced dipole and dispersion interactions.¹⁷⁸ For benzene, the binding energy of the (Bz•Bz)^{•+} homodimer has been measured as 17.6 ± 1 and 17.4 ± 1 kcal mol⁻¹ for the (C₆H₆)₂^{•+} and (C₆D₆)₂^{•+} systems respectively and is similar to the high-pressure mass spectrometry value of 17.0 kcal mol⁻¹.^{87,199} The large binding energy of this homodimer suggests significant charge resonance interactions that has its maximum in a parallel sandwich-like structure.^{87,199-202} Theoretical density functional theory (DFT) calculations show that two isomers for the (Bz•Bz)^{•+} homodimer are present: a sandwich structure and a T-shaped structure. The sandwich structure was found to be more stable, but only by 1.6 kcal mol⁻¹ making both structures possible based on the thermochemistry measurements.¹¹⁰ Ion mobility experiments of the (Bz•Bz)^{•+} homodimer (theory outlined in Chapter 3) were performed resulting in a collision cross section (Ω) of 71 Å². This value is in agreement with the sandwich structure.¹¹⁰

The cross reaction between the ionized aromatics and the nitrogen containing heterocyclic pyridine have also been studied as a prototype model system for radical cation- π interactions.¹¹⁵ The (benzene•pyridine)^{•+} heterodimer radical cation showed similar charge transfer resonance that stabilizes the dimer and the two moieties are bonded covalently with a bonding energy in excess of 33 kcal mol⁻¹ experimentally (31-38 kcal mol⁻¹ using *ab initio* calculations).¹¹⁵

Using the results for the structures and binding of benzene radical cation homodimer and benzene•pyridine radical cation heterodimer as model systems, comparisons were made for the structure and binding of the naphthalene radical cation homodimer as well as naphthalene•benzene and naphthalene•pyridine radical cation heterodimers. In the case of the (Naph•Naph)^{•+} homodimer, the effect of charge delocalization in the larger naphthalene cation was compared to the benzene cation. For the (Naph•Bz)^{•+} and (Naph•Pyr)^{•+} heterodimers, how the changes in charge

delocalization effects the charge transfer (CT) interactions and binding energy were observed. Dissociation energies of heterodimer radical cations tend to decrease with increasing difference in the ionization energies (ΔIE) of the component molecules. This effect has been observed in heterodimers containing benzene, aniline, and methylnaphthalene with different neutral molecules.¹⁹⁹⁻²⁰¹ This would suggest that the CT interaction in the $(\text{Naph}\cdot\text{Bz})^{+\bullet}$ and $(\text{Naph}\cdot\text{Pyr})^{+\bullet}$ heterodimers is very small due to the large difference in the IEs between naphthalene and benzene or pyridine (roughly 1.1 eV for both heterodimers). The CT contribution to the overall binding energy can only be determined when the most likely structure of the heterodimer is known.

Comparing the binding of the $(\text{Naph}\cdot\text{Bz})^{+\bullet}$ and $(\text{Naph}\cdot\text{Pyr})^{+\bullet}$ heterodimers also gains insight in the radical cation- π interactions that occur when nitrogen containing heterocycles interact with PAHs. The adducts formed could represent a general class of reactions for the radical cation- π interactions.

Presented in this chapter are the ion mobility experiments for the naphthalene radical cation homodimer and the naphthalene•benzene and naphthalene•pyridine radical cation heterodimers. The experimental reduced mobility values were used to calculate the average collision cross sections and showed that the naphthalene radical cation homodimer forms a stacked parallel structure similar to that of the benzene radical cation homodimer. The naphthalene•benzene radical cation homodimer showed that a stacked parallel structure is present at higher temperatures, while a T-shaped structure is present at lower temperatures. The binding of the naphthalene•benzene radical cation heterodimer is lower than that of the benzene or naphthalene radical cation homodimers. The naphthalene•pyridine radical cation heterodimer was found to be a covalent structure with subsequent pyridine molecules formed a hydrogen bonded network with this

covalent dimer. This work presents changes that occur within heterocyclic dimers as larger ring structures are formed.

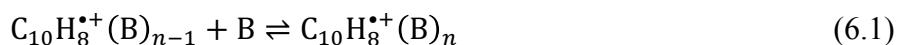
6.2. Experimental Section

All experiments are performed with the VCU mass-selected ion mobility spectrometer with details of the system outlined in Chapter 2. During experiments, 50-80 psi (\approx 2500-3600 Torr) ultra high purity helium (AirGas) seeded with roughly 0.74-3.76 Torr naphthalene vapor generated from heating solid naphthalene (Aldrich, \geq 99 %) stored in a sealed stainless steel/glass bubbler to 50-70 °C is pulsed through a supersonic nozzle (500 μ m) into a source vacuum chamber maintained at a background pressure of 10^{-7} Torr. Following this supersonic expansion, the naphthalene radical cation ($C_{10}H_8^{*+}$) is generated by electron impact ionization using an electron energy of 60-70 eV which is enough to ionize any organic ions of interest. The $C_{10}H_8^{*+}$ ions are mass-selected by a quadrupole mass-filter before being injected into a drift cell (in 25-50 μ s pulses) containing helium (AirGas, Research Grade) or a mixture of helium and the neutral reagent vapor: benzene (C_6H_6 , Aldrich, 99.9 %), benzene-d₆ (Aldrich, 99.96 % D atoms), and pyridine (Aldrich, anhydrous 99.8 %). Flow controllers (MKS #1479A) are used to maintain a constant pressure inside the drift cell within \pm 1 mTorr. The temperature of the drift cell was controlled to \pm 1 K using four temperature controllers. To cool the drift cell, liquid nitrogen is used by flowing it through solenoid valves. The reaction products that exit the drift cell are identified by scanning a second quadrupole mass-filter located after the drift cell and arrival time distributions (ATDs) are collected by monitoring the intensity of each ion as a function of time. The injection energies used in experiments (10-14 eV, laboratory frame) are only slightly higher than the minimum energies required to introduce the ions against the neutral reactant/He vapor mixture outflow at the drift cell

entrance orifice. Most ion thermalization occurs outside of the drift cell by collisions with the gas mixture molecules escaping the drift cell entrance orifice.

Mobility measurements are made by injecting a narrow pulse of ions into the drift cell. The ion injected must be the dimer or heterodimer being observed. The ion gate is located just prior to the cell entrance and chopped the pulse to a narrow, 30-50 μs wide packet, which enters the drift cell. Mobility is determined according to Equation 3.10 by plotting t_d versus P/V . The slope of this plot is inversely proportional to the reduced mobility and the intercept is the time spent outside of the drift cell before detection.

The equilibrium reaction used for the thermochemistry experiments in this series of experiments is represented by the following reaction:



where B is the neutral aromatic molecule, in these experiments that molecule was benzene or pyridine. This reaction is said to be in equilibrium when (1) the ATDs of the product and reactant ions have equal arrival times and (2) there is a constant ratio of the integrated intensities of product and reaction ions over a range of drift cell field voltage thus changing the residence time of the ions at a constant and pressure. Once equilibrium is established, the equilibrium constant, K_{eq} , is measured using the equation:

$$K_{\text{eq}} = \frac{[\text{C}_{10}\text{H}_8^{\bullet+}(\text{B})_n]}{[\text{C}_{10}\text{H}_8^{\bullet+}(\text{B})_{n-1}][\text{B}]} = \frac{I_{[\text{C}_{10}\text{H}_8^{\bullet+}(\text{B})_n]}}{I_{[\text{C}_{10}\text{H}_8^{\bullet+}(\text{B})_{n-1}]}P_{\text{B}}} \quad (6.2)$$

where $I_{[\text{C}_{10}\text{H}_8^{\bullet+}(\text{B})_n]}$ and $I_{[\text{C}_{10}\text{H}_8^{\bullet+}(\text{B})_{n-1}]}$ are the integrated intensities of the ATDs of the reactant and product ions or the intensity of the ion peak on a mass spectrum and P_{B} is the partial pressure of the neutral vapor in atmospheres inside the drift cell. The equilibrium constant was measured at different temperatures to form a van't Hoff plot (using the van't Hoff equation as shown in

Equation 3.5) where the $-\Delta H^\circ$ and $-\Delta S^\circ$ values are obtained from the slope and intercept respectively. All data was repeated at least three times with average values used in discussion.

6.3. Theoretical Calculations

Density functional theory calculations of the lowest energy structures for the various isomers of the cluster ions studied were performed using the Gaussian 09 program suite.¹³⁰ The structures of the naphthalene radical cation homodimer, $(C_{10}H_8)_2^{\bullet+}$ or $Naph_2^{\bullet+}$, was performed at the B3LYP/6-311++G** for the comparisons with the experimental mobility results.^{126,130} Calculations for the naphthalene•benzene radical cation heterodimer, $(C_{10}H_8\bullet C_6H_6)^+$ or $(Naph\bullet Bz)^+$, and the second addition of benzene to the naphthalene radical cation, $C_{10}H_8^{\bullet+}(C_6H_6)_2$ or $Naph^+(Bz)_2$, were carried out at the M11/cc-pVTZ level of theory.^{126,127,203} The structures and binding energies for various isomers of the naphthalene•pyridine radical cation heterodimer, $C_{10}H_8^{\bullet+}(C_5H_5N)$ or $Naph^+(Pyr)$, were carried out at the M06-2X/cc-pVTZ level of theory.⁸⁰ For structural minima of the second addition of pyridine to the naphthalene radical cation, $C_{10}H_8^{\bullet+}(C_5H_5N)_2$ or $Naph^+(Pyr)_2$, a methodology that combines *ab initio* molecular dynamics (QAIMD) starting from random initial orientations followed by gradient-based local optimizations with DFT was used at the M06-2X and M11 level of theory using the cc-pVTZ basis set.

Vibrational frequency calculations were also performed for all the optimized geometries at the same level of theory in order to obtain zero point vibrational energy (ZPVE) and to verify the absence of imaginary frequencies.¹³⁰ For all calculations the binding energy (ΔE) was calculated at 0 K and was calculated using the equation:

$$\Delta E_{[(C_{10}H_8^{\bullet+})(B)_n]} = \left(E_{[(C_{10}H_8^{\bullet+})(B)_{n-1}]} + E_{[B]} \right) - E_{[(C_{10}H_8^{\bullet+})(B)_n]} \quad (6.3)$$

where $E_{[(C_{10}H_8^{\bullet+})(B)_{n-1}]}$, $E_{[B]}$, $E_{[(C_{10}H_8^{\bullet+})(B)_n]}$ and are the total electronic energies of the lowest energy isomers of the reactant ion, neutral molecule represented by B (benzene or pyridine), and

the product of the reaction shown in Equation 6.1. The calculations for this portion were performed by Dr. Martin Head-Gordon and Dr. Roberto Peverati of University of California – Berkeley.

6.4. Results and Discussion

6.4.1. Ion Mobility Measurements and Structures of the (Naphthalene)₂^{•+} Dimer

The mass spectrum obtained following the coexpansion of naphthalene and benzene injected into the drift cell containing helium is shown in Figure 62. The major ions present are the naphthalene radical cation homodimer (Naph₂^{•+}), the naphthalene•benzene radical cation heterodimer [(Naph•Bz)^{•+}], the benzene radical cation homodimer (Bz₂^{•+}), and the naphthalene radical cation (Naph^{•+}). The ATDs and t_d versus P/V plot for the mobility experiments for the naphthalene radical cation homodimer are displayed in Figure 63a and Figure 63b respectively. The excellent linearity in the data shown in Figure 63b indicates that under the low-field regime employed in the mobility experiments ($E/N < 5.0$), the drift velocity of the naphthalene radical cation homodimer is small compared to the thermal velocity and the ion mobility is independent of the field strength. The repeated mobility measurements resulted in reduced mobility of 5.9 ± 0.1 (0.25) $\text{cm}^2 \text{V}^{-1} \text{s}^{-1}$ for the naphthalene radical cation homodimer. The ± 0.1 is the uncertainty in the repeated measurements of the reduced mobility and the 0.25 value is a 4 % experimental error in the mobility measurements.

The measured mobilities at different temperatures are used to calculate average collision cross sections (Ω) for the naphthalene radical cation homodimer in helium using Equation 3.21 and the resulting values are listed in Table 9. The optimized structures of the two isomers, stacked parallel and T shaped, calculated at the B3LYP/6-311++G** level of theory are shown in Figure 64. These structures are used to obtain average collision cross sections using the trajectory

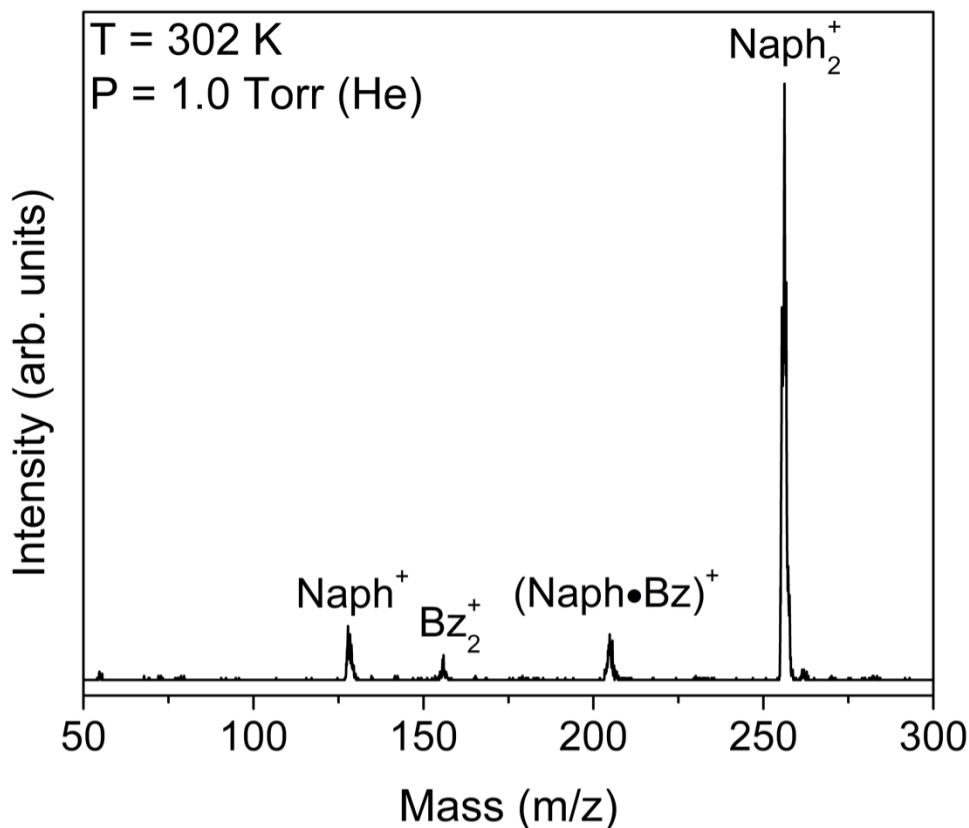


Figure 62. Mass-spectrum of the ions injected into the drift cell containing 1.0 Torr helium at a temperature of 302 K. The ions are formed by 70 eV EI ionization of the neutral clusters generated by a supersonic beam coexpansion of the binary mixture containing naphthalene (Naph) and benzene (Bz) using helium as a carrier gas.

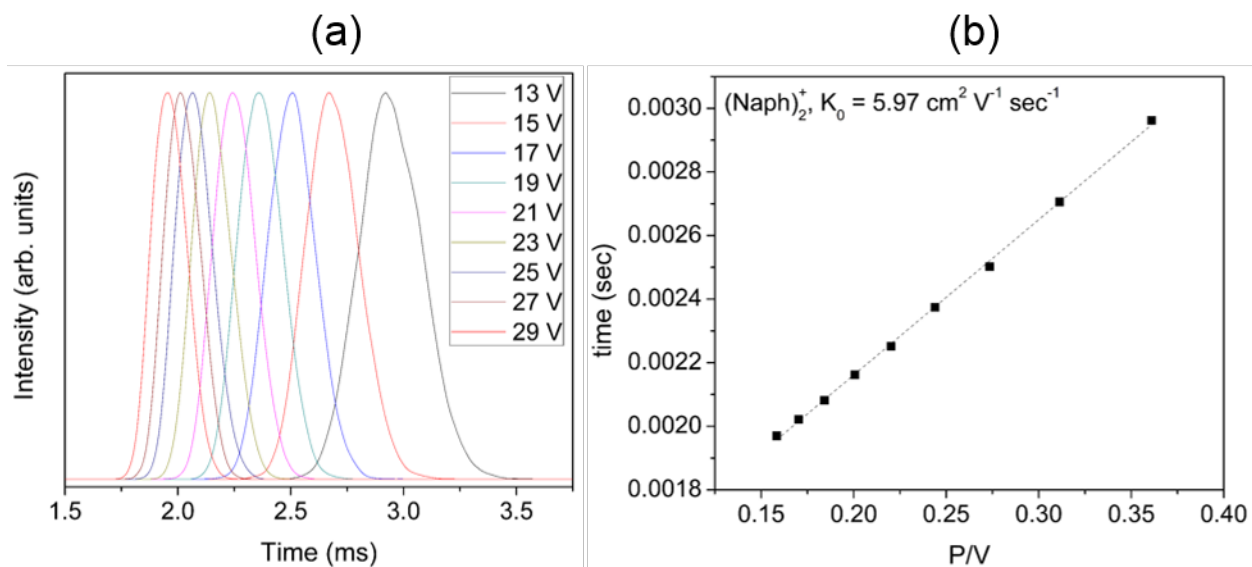


Figure 63. (a) ATDs and (b) t_d versus P/V plot for the naphthalene radical cation homodimer (Naph)₂⁺. All the data are obtained in 4.5 Torr helium at a temperature of 302 K.

calculations which employ a potential of Lennard-Jones (LJ) and ion-induced dipole interactions.^{125,130} The calculated average collision cross sections in helium at the temperatures of the measured mobilities using the trajectory method are also given in Table 9. There is good agreement between the experimental and calculated cross sections for the stacked parallel structure at the three measured temperatures (within 2.5 %). The calculated T-shaped structure is significantly larger (around 20 %) than the measured values at the three temperatures. Since the measured cross sections are close to a single isomer, and not an average of the two, it can be concluded that the naphthalene radical cation homodimer forms a stacked parallel structure at the three measured temperatures. This is supported by the significant contribution from charge resonance interaction to the 17.8 kcal mol⁻¹ binding energy of the naphthalene radical cation homodimer.²⁰⁴

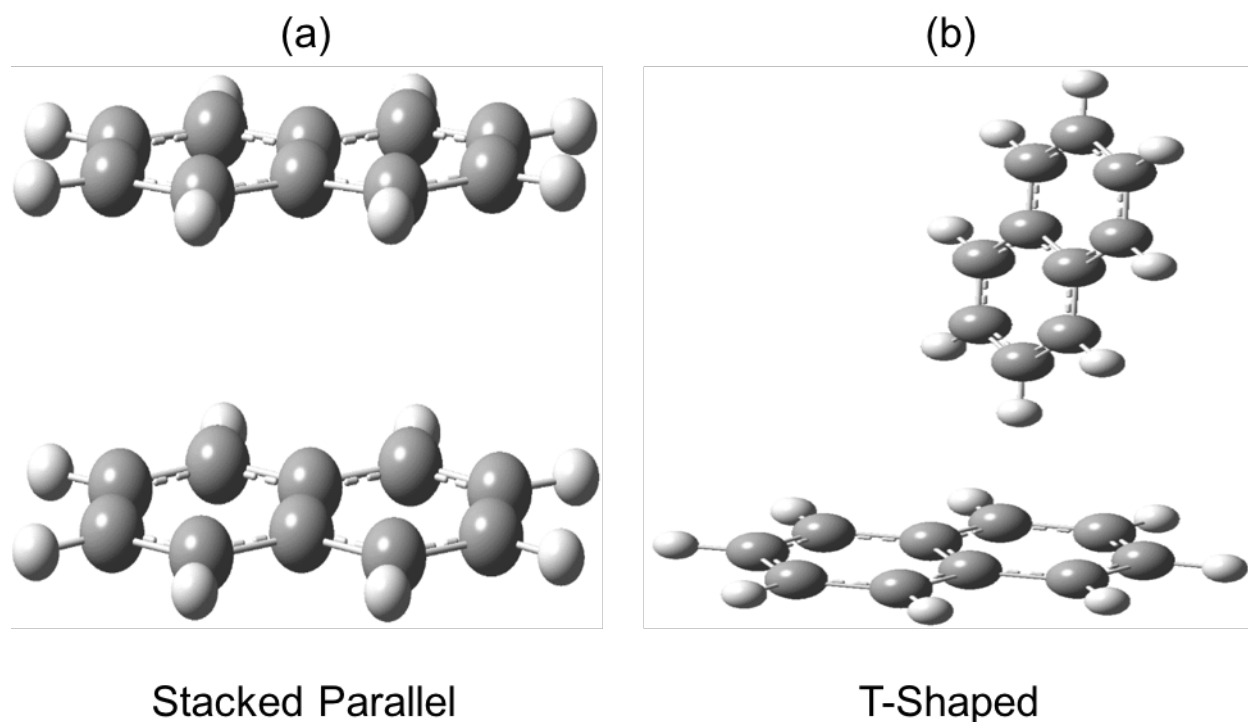
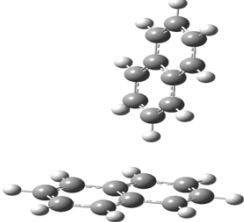


Figure 64. Two classes of isomers for the naphthalene radical cation homodimers: (a) stacked parallel and (b) T-shaped. The structures are optimized at the B3LYP/6-311++G** level of theory.

Table 9. Experimental-based collision cross sections of naphthalene radical cation homodimers in helium at different temperatures and pressures as indicated. The calculated cross sections obtained from the trajectory method¹²⁵ for the stacked parallel and T-shaped structures optimized at the B3LYP/6-311++G** level of theory.¹³⁰ The boldface values represent the best agreement between experimental and calculated cross sections.

T (K)	P (Torr)			
				Ω (\AA^2) Experimental
302	4.1	90.9	93.0	109.9
273	4.0	95.4	94.5	111.4
231	4.0	97.0	97.3	114.2

6.4.2. Structures and Binding of the Solvation of the Naphthalene^{•+} by Benzene

To determine the binding energy and structures of the naphthalene•benzene radical cation heterodimer, two sets of experiments were performed. For measurements of the thermochemistry and binding energy, the naphthalene radical cation was injected into the drift cell containing a helium/benzene vapor mixture (C_6H_6 and C_6D_6 was used) and the $-\Delta H^\circ$ and $-\Delta S^\circ$ were obtained from van't Hoff plots. Mobility experiments following the coexpansion of naphthalene and benzene vapor were used to obtain experimental measurements for the structure of the naphthalene•benzene radical cation heterodimer. The experimental results were coupled with DFT calculations to further understand the structure and binding of the naphthalene•benzene radical cation homodimer.

6.4.2.1. Thermochemical Results and Structures for Naphthalene^{•+}(Benzene)_n Clusters

The mass spectra obtained following the injection of mass-selected naphthalene radical cation ($C_{10}H_8^{•+}$, $Naph^+$) into the drift cell containing He or He/ C_6D_6 vapor mixture are shown in Figure 65. A reference mass spectrum of $C_{10}H_8^{•+}$ injected into the drift cell containing only He

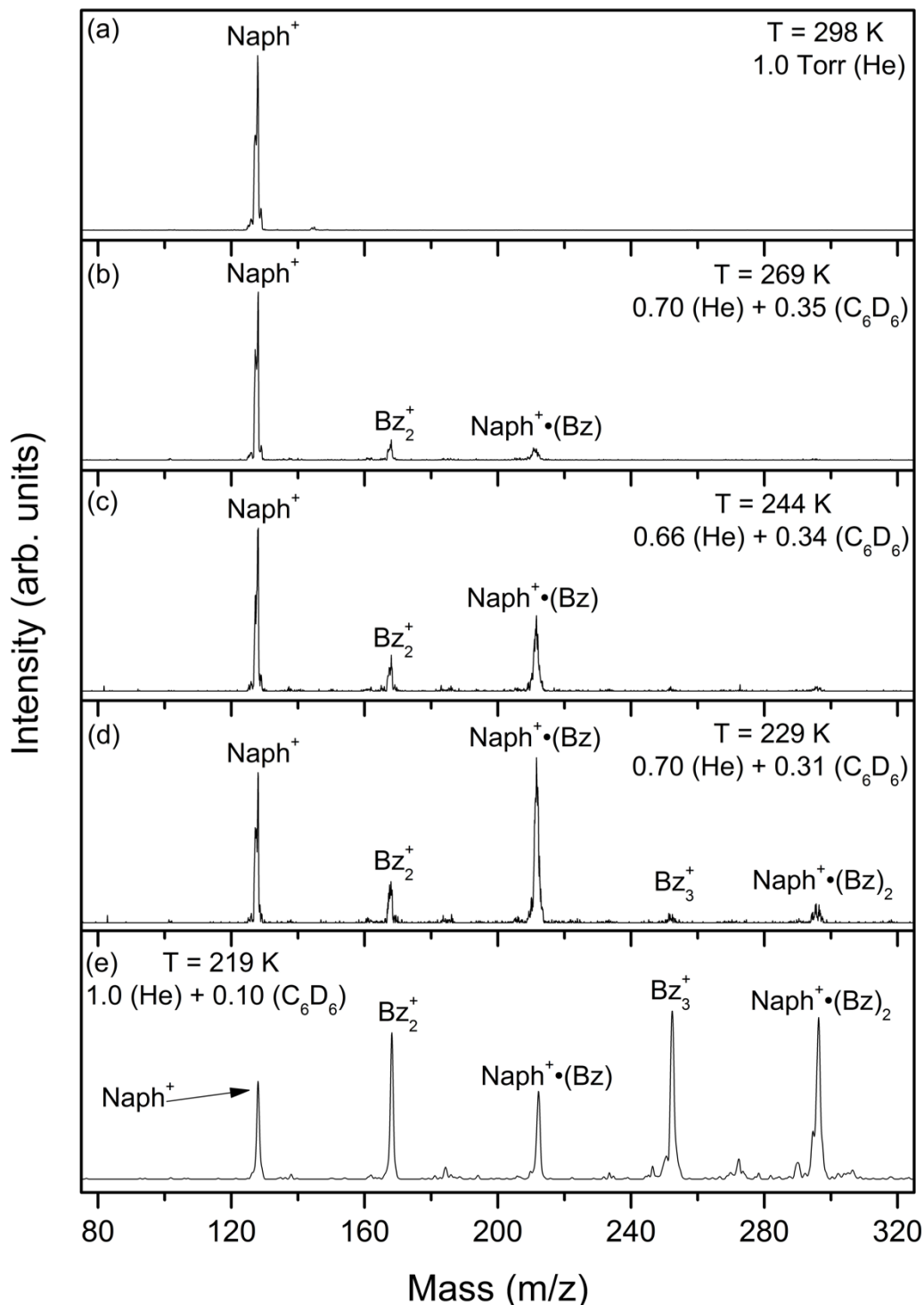
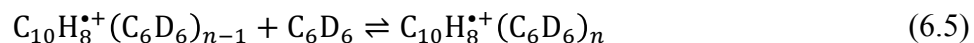
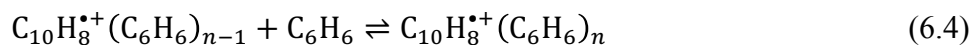


Figure 65. Mass spectra resulting from the injection of the mass-selected naphthalene radical cation ($\text{C}_{10}\text{H}_8^+$, Naph^+) into the drift cell containing He gas (a) or He/benzene (C_6D_6) vapor mixture (b-e) at different temperatures and pressures as indicated.

(Figure 65a) shows that only the naphthalene radical cation is present at $m/z = 128$. In the presence of 0.35 Torr of C_6D_6 vapor in the drift cell at 269 K, the first association product of $C_{10}H_8^{*+}(C_6D_6)$ ($m/z = 212$) is present in addition to the naphthalene radical cation benzene radical cation homodimer [$(C_6D_6)_2^{*+}$, $(Bz)_2$, $m/z = 168$] (Figure 65b). The presence of the $(Bz)_2^{*+}$ suggests direct ionization of a small amount of benzene molecules in the cell by the injection energy of the naphthalene radical cation despite the lack of observable dissociation products. As the temperature decreases, the ion intensity of the $C_{10}H_8^{*+}(C_6D_6)$ heterodimer increases (Figure 65c), and at 229 K, small peaks corresponding to the second association product $C_{10}H_8^{*+}(C_6D_6)_2$ heterotrimer and the benzene radical cation homotrimer $(Bz)_3^{*+}$ are observed, as shown in Figure 65d. At the lowest possible temperature in the drift cell before the benzene vapor freezes (219 K, Figure 65e), a significant decrease in the intensity of the $C_{10}H_8^{*+}(C_6D_6)$ heterodimer ion and a large increase in the intensities of the $C_{10}H_8^{*+}(C_6D_6)_2$ and $(C_6D_6)_3^{*+}$ ions are observed. Small peaks at $m/z = 234$, 236, and 290 are associated with $(C_6H_6)_3^{*+}$, $(C_6D_6)_2(C_6H_6)^{*+}$, and $C_{10}H_8^{*+}(C_6D_6)(C_6H_6)$ respectively and are due to isotope contamination of C_6H_6 in the C_6D_6 sample. The peaks at $m/z = 138$, 184, and 272 are due to pump oil impurities that tend to be observed in the drift cell at high pressures and low temperatures. Similar results were observed when the naphthalene radical cation was injected into He- C_6H_6 vapor mixture as shown in Figure 66.

The observed association reactions of the benzene vapor (C_6H_6 and C_6D_6) with the naphthalene radical cation are represented by Equations 6.4 and 6.5:



The equilibrium constants for Equations 6.4 and 6.5 for $n = 1$ at different temperatures results in van't Hoff plots for the formation of $C_{10}H_8^{*+}(Bz)$ heterodimer for both C_6H_6 and C_6D_6 are shown

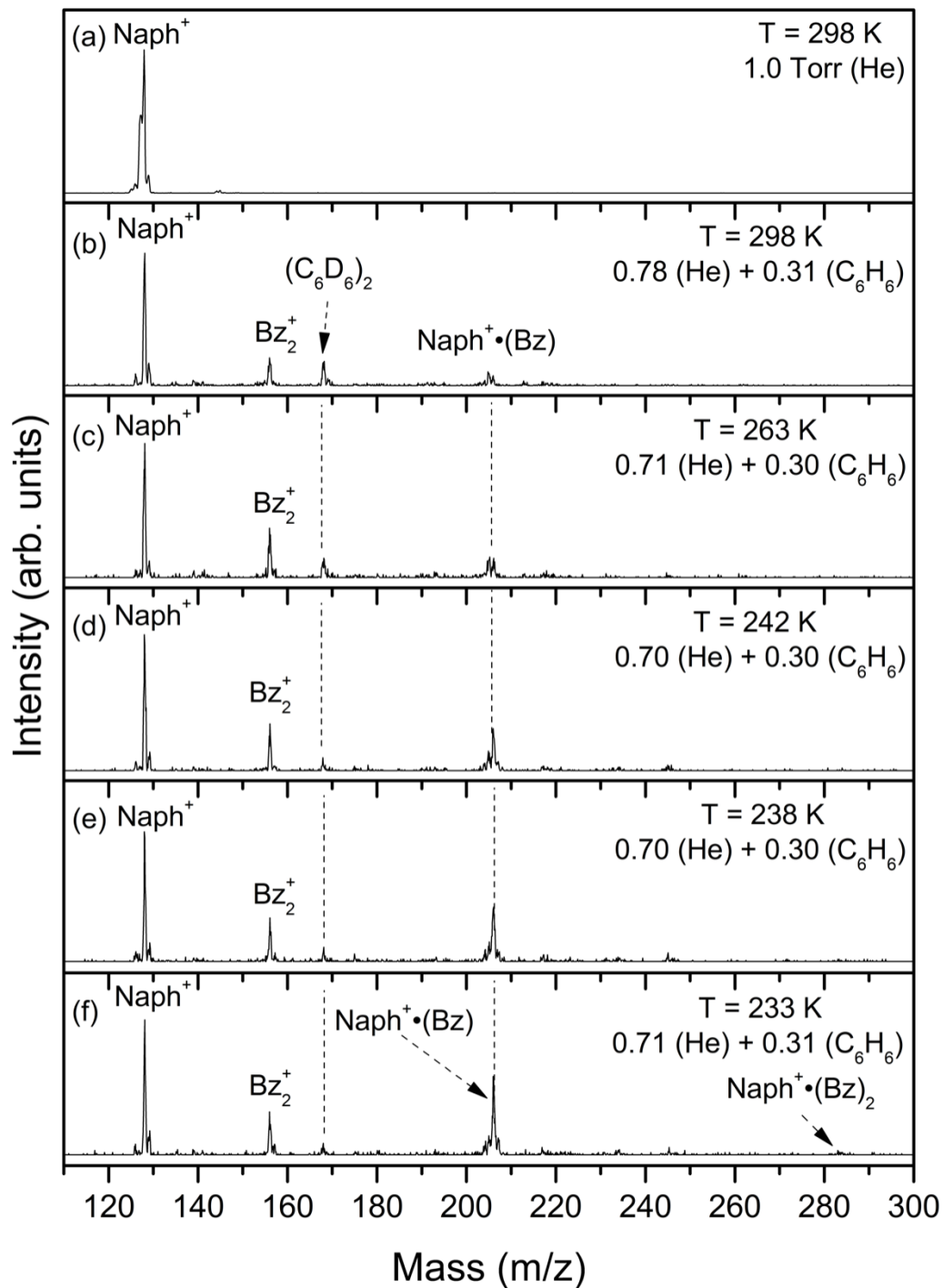


Figure 66. Mass spectra resulting from the injection of the mass-selected naphthalene radical cation ($\text{C}_{10}\text{H}_8^+$, Naph^+) into the drift cell containing He gas (a) or He/benzene (C_6H_6) vapor mixture (b-f) at different temperatures and pressures as indicated.

in Figure 67. The experimental $-\Delta H^\circ$ and $-\Delta S^\circ$ values for the formation of $C_{10}H_8^{++}(C_6H_6)$ are 7.9 ± 1 kcal mol⁻¹ and 18.7 ± 2 cal mol⁻¹ K⁻¹ respectively (Figure 67a). For the formation of $C_{10}H_8^{++}(C_6D_6)$, the resulting $-\Delta H^\circ$ and $-\Delta S^\circ$ values are 8.1 ± 1 kcal mol⁻¹ and 20.2 ± 2 cal mol⁻¹ K⁻¹ respectively (Figure 67b). The measured equilibrium constants and van't Hoff plots are repeated at least three times, and the estimated errors in the $-\Delta H^\circ$ and $-\Delta S^\circ$ values are obtained from standard deviations of van't Hoff plots and from typical uncertainties in thermochemical equilibrium studies. The isotope effects on the enthalpy and entropy changes are smaller than the usual experimental uncertainties of ± 1 kcal mol⁻¹ and ± 2 cal mol⁻¹ K⁻¹ respectively for the experimental measurements.

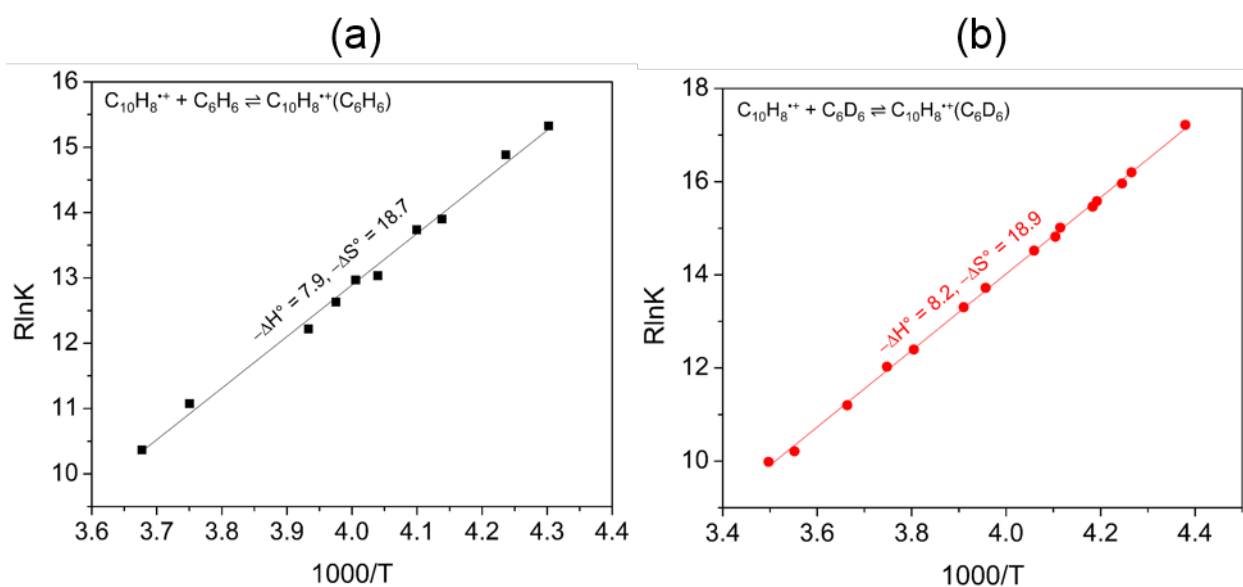


Figure 67. van't Hoff plots for the formation of $C_{10}H_8^{++}(C_6H_6)$ (a) and $C_{10}H_8^{++}(C_6D_6)$ (b) heterodimer cations. Error estimates are ± 1 kcal mol⁻¹ and ± 2 cal mol⁻¹ K⁻¹ for ΔH° and ΔS° respectively.

The measured enthalpy of binding of the $C_{10}H_8^{++}(Bz)$ heterodimer is significantly smaller than that of the Bz_2^{++} and $(C_{10}H_8)_2^{++}$ homodimer, 8 kcal mol⁻¹ vs. 17 and 17.8 kcal mol⁻¹ respectively.^{87,127,199} Two factors could explain this behavior: (1) the delocalization of the charge on the larger naphthalene cation as compared to the benzene cation could lead to weaker charge-

induced dipole interactions with the neutral benzene molecule, and (2) the lack of charge resonance interaction in the $C_{10}H_8^{++}(Bz)$ heterodimer as a result of the large difference in the ionization energies (IE) between naphthalene and benzene (1.1 eV).² ATDs collected at 253 K (Figure 68a) and 228 K (Figure 68b) show that the reaction between the naphthalene radical cation and benzene (C_6D_6) as written in Equation 6.5 is in equilibrium due to similar arrival times.

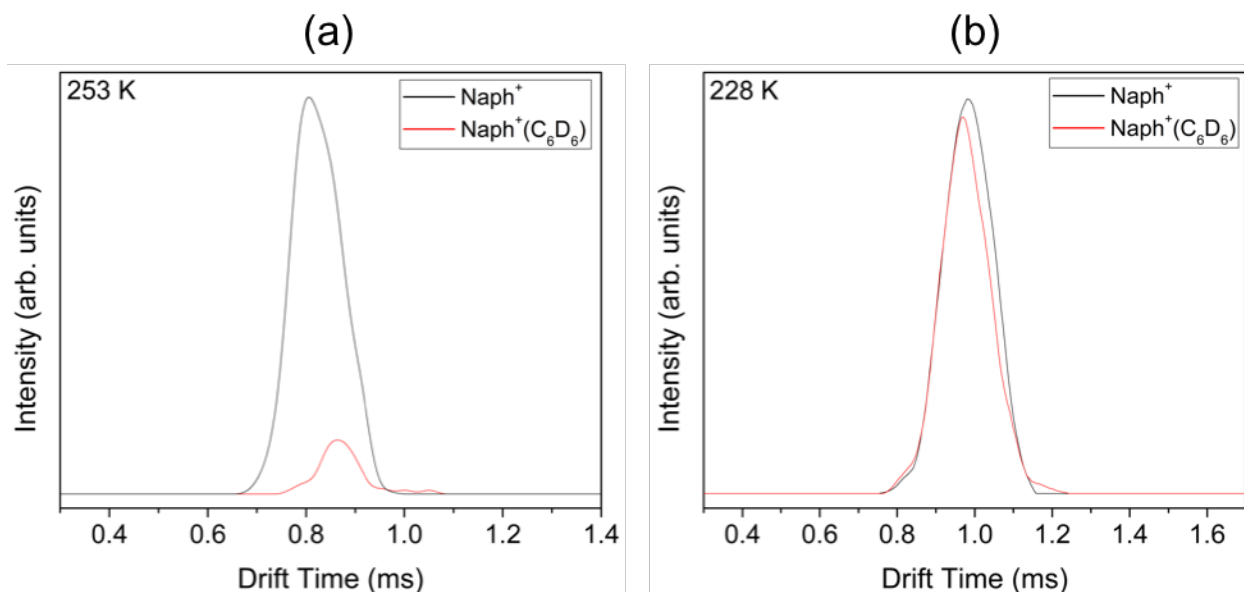


Figure 68. Arrival time distributions (ATDs) of the naphthalene radical cation ($Naph^+$) and the naphthalene⁺⁺(benzene) heterodimer, $C_{10}H_8^{++}(C_6D_6)$ ($Naph^+(C_6D_6)$), obtained following the injection of the mass-selected naphthalene radical cation into a He/ C_6D_6 vapor mixture at: (a) 253 K and (b) 228 K. Similar ATD overlap suggests the reaction is in equilibrium.

The calculated structures of the $C_{10}H_8^{++}(C_6H_6)$ heterodimer resulted in 15 minimum structures that fall into three classes based on the angle between the planes of the naphthalene and benzene molecules: (1) stacked parallel, (2) V-shaped, and (3) T-shaped. The calculated structures using M11/cc-pVTZ are shown in Figure 69. The calculations predict that the stacked parallel isomer (Figure 69a) is the global minimum energy isomer, which is similar to the structure observed with the naphthalene radical cation homodimer.¹²⁶ The V-shaped isomer (Figure 69b) is very close in energy with a difference that is within the experimental error of ± 1 kcal mol⁻¹ and therefore a mixture of the two isomers is possible. Both structures have binding energies that are

slightly higher than the experimental $-\Delta H^\circ$ value measured. Although the T-shaped structure is (Figure 69c) higher energy, it is still within the experimental error of $\pm 1 \text{ kcal mol}^{-1}$ meaning that there are small transition barriers between the minima making all structures present.

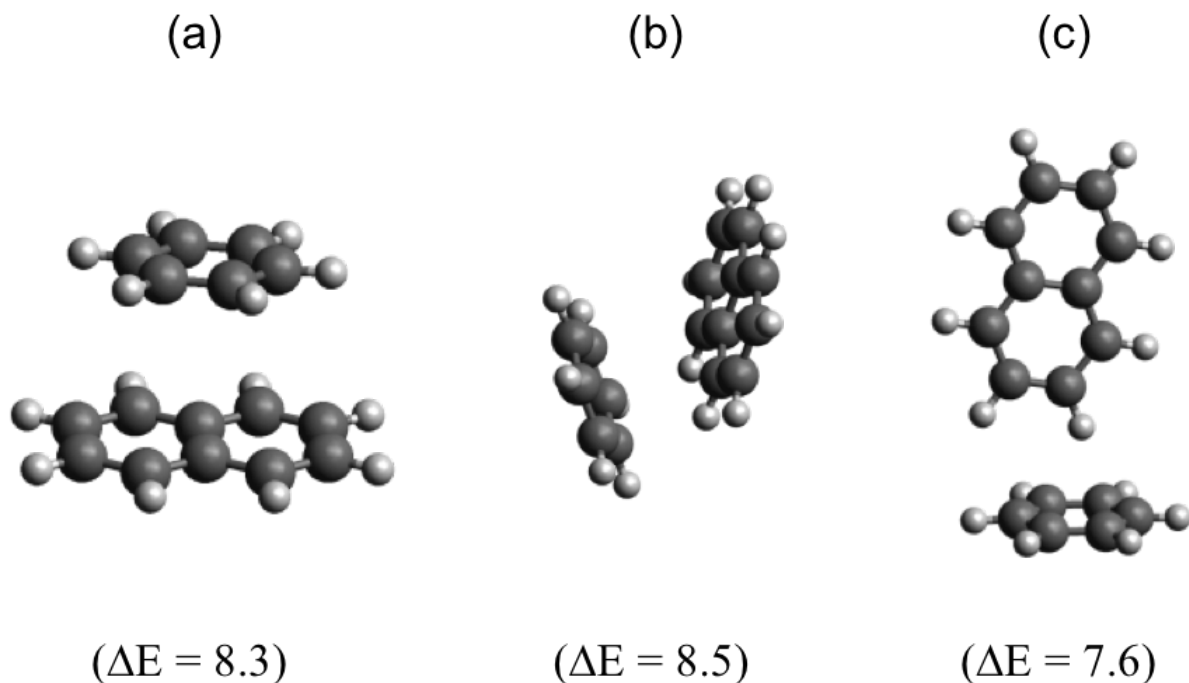


Figure 69. DFT structures and binding energies (ΔE , kcal mol^{-1}) of the three classes of isomers for the naphthalene⁺(benzene) heterodimer: (a) stacked parallel, (b) V-shaped, (c) T-shaped calculated using the M11/cc-pVTZ where the lowest energy isomer is depicted.

The $\text{C}_{10}\text{H}_8^{++}(\text{C}_6\text{D}_6)_2$ was only observed in a small temperature range (215-219 K) and thus it was not possible to measure a van't Hoff plot for the formation of the $\text{C}_{10}\text{H}_8^{++}(\text{C}_6\text{D}_6)_2$ heterotrimer. An alternative method for estimating the value of $-\Delta H^\circ$ for $\text{C}_{10}\text{H}_8^{++}(\text{C}_6\text{D}_6)_2$ is to use equations 3.3-3.5. The ΔG° for Equation 6.5 for $n = 2$ at 219 K is $-4.2 \text{ kcal mol}^{-1}$. Assuming a $-\Delta S^\circ$ of $19 \text{ cal mol}^{-1} \text{ K}^{-1}$, the estimated $-\Delta H^\circ$ for $\text{C}_{10}\text{H}_8^{++}(\text{C}_6\text{D}_6)_2$ is $8.4 \text{ kcal mol}^{-1}$. This value of $-\Delta H^\circ$ is similar to the binding energy of the $\text{C}_{10}\text{H}_8^{++}(\text{C}_6\text{D}_6)$ heterodimer suggesting that a second benzene molecule has a similar interaction with the naphthalene cation as the first benzene molecule. A possible structure is one where the naphthalene radical cation is sandwiched between two neutral benzene molecules.

The calculated structures of the naphthalene^{•+}(benzene)₂ heterotrimer resulted three classes of isomers based on the angle between the planes of the naphthalene and benzene molecules: (1) sandwich, (2) slanted U-shaped, and (3) stacked parallel. The calculated structures using M11/cc-pVTZ are shown in Figure 70. The results show that the global minimum corresponds to the structure where the naphthalene radical cation is sandwiched between two benzene molecules (Figure 70a). The calculated binding energy (ΔE) for this isomer is 9.6 kcal mol⁻¹, which supports the estimated $-\Delta H^\circ$ calculated from the ΔG° value. The planes of the molecules are at a slight angle to each other with the angle between the planes of the benzene molecules and the central naphthalene radical cation are 8° and 6° respectively.

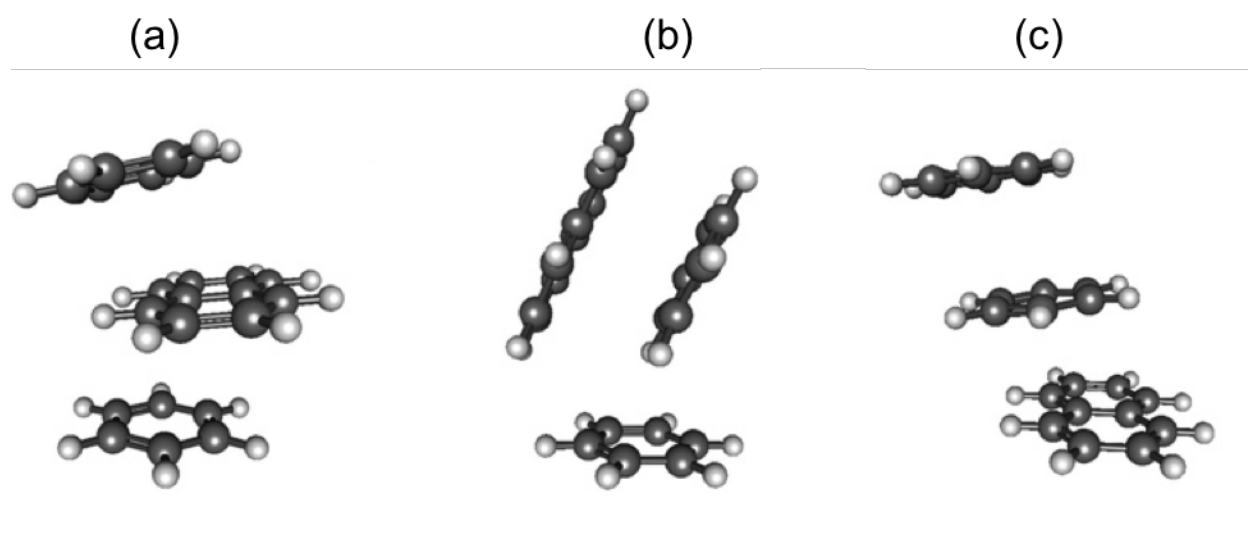


Figure 70. DFT structures for the three classes of isomers for the naphthalene^{•+}(benzene)₂ heterotrimer: (a) sandwich, (b) slanted U-shaped, (c) stacked parallel calculated using the M11/cc-pVTZ where the lowest energy isomer is depicted.

The slanted U-shaped and stacked parallel structures (Figure 70b and c respectively) are higher-energy isomers than the sandwich structure. In the slanted U-shaped structure, the second benzene molecule attached to the side of the stacked parallel naphthalene•benzene radical cation heterodimer. The binding energy of this isomer is 3.5 kcal mol⁻¹ higher than that of the sandwich structure. For the stacked parallel structure, the second benzene molecule is attached to the benzene

side of the of the stacked parallel $C_{10}H_8^{*\cdot+}(C_6H_6)$ heterodimer and the binding energy is 4.7 kcal mol⁻¹ higher than the sandwich structure.

The difference between the binding energies of the first and second benzene molecules relatively small which is relatively unusual when compared to similar systems. The binding energy of the benzene homodimer is 17 kcal mol⁻¹ vs 6 kcal mol⁻¹ for the formation of the benzene homotrimer.¹²⁷ The difference is in part due to the charge delocalization in the system. The formation of the benzene radical cation homodimer is dominated by charge transfer interactions whereas the formation of the homotrimer is polarization-dominant. This causes the charge on the central benzene to increase. The opposite is true in the case of the $C_{10}H_8^{*\cdot+}(C_6H_6)_2$ homotrimer where the charge on the central naphthalene becomes more delocalized.

6.4.2.2. Ion Mobility Measurements for the (Naphthalene•Benzene)^{*+} Heterodimer

The mass spectrum obtained following the coexpansion of naphthalene and benzene injected into the drift cell containing helium is shown in Figure 62. The major ions present are the naphthalene radical cation homodimer ($Naph_2^{*\cdot+}$), the naphthalene•benzene radical cation heterodimer [$(Naph\cdot Bz)^{*\cdot+}$], the benzene radical cation homodimers ($Bz_2^{*\cdot+}$), and the naphthalene radical cation ($Naph^{*\cdot+}$). The ATDs and t_d versus P/V plot for the mobility experiments for the (naphthalene•benzene)^{*+} heterodimer are displayed in Figure 71a and Figure 71b respectively. The excellent linearity in the data shown in Figure 71b indicates that under the low-field regime employed in the mobility experiments ($E/N < 5.0$), the drift velocity of the (naphthalene•benzene)^{*+} heterodimer is small compared to the thermal velocity and the ion mobility is independent of the field strength. The repeated mobility measurements resulted in reduced mobility of 6.5 ± 0.1 (0.25) cm² V⁻¹ s⁻¹ for the naphthalene radical cation homodimer. The ± 0.1 is the uncertainty in the

repeated measurements of the reduced mobility and the 0.25 values is a 4 % experimental error in the mobility measurements.

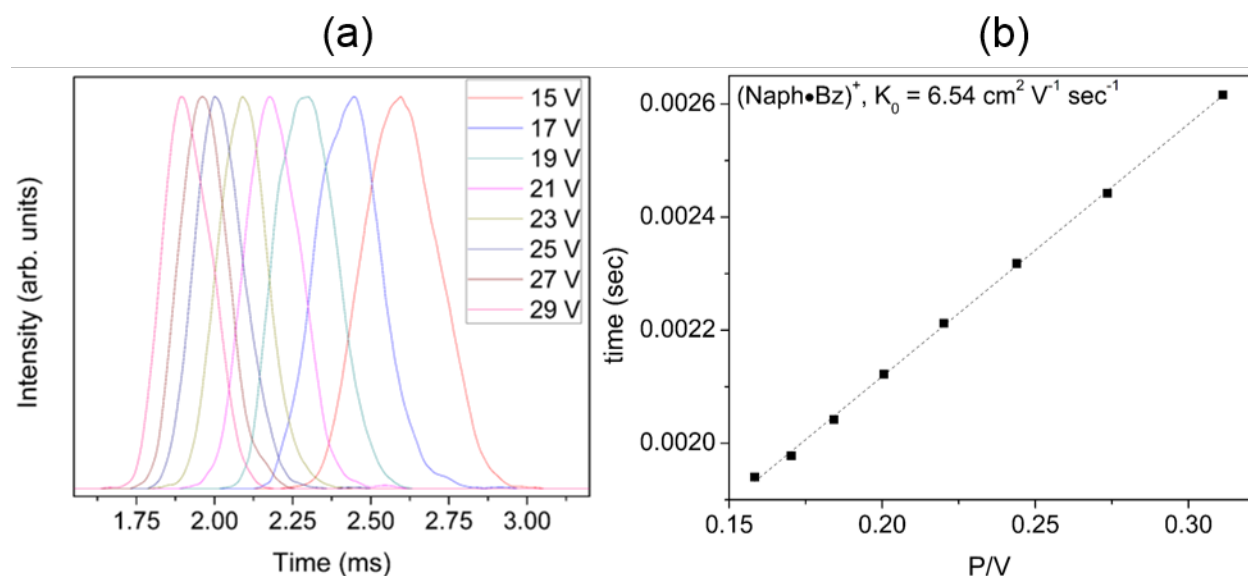
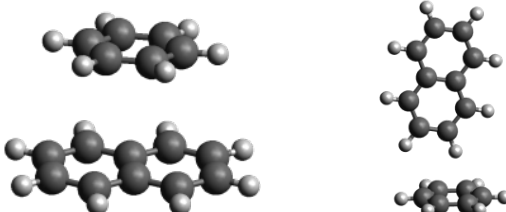


Figure 71. (a) ATDs and (b) t_d versus P/V plot for the naphthalene•⁺(benzene) heterodimer (Naph•Bz)⁺. All the data are obtained in 4.5 Torr helium at a temperature of 302 K.

The measured mobilities at different temperatures are used to calculate average collision cross sections (Ω) for the (naphthalene•benzene)⁺ heterodimer in helium using Equation 3.21 and the resulting values are listed in Table 10. The collision cross section of the naphthalene radical cation homodimer is larger than that of the (naphthalene•benzene)⁺ heterodimer due to the increase in the physical size of the ion. The optimized structures of two isomers used for mobility results, stacked parallel and T shaped, calculated at the B3LYP/6-311++G** level of theory are similar to those calculated by M11/cc-pVTZ shown in Figure 69a and c respectively. These structures were used to obtain average collision cross sections using the trajectory calculations which employ a potential of Lennard-Jones (LJ) and ion-induced dipole interactions.^{125,130} The calculated average collision cross sections in helium at the temperatures of the measured mobilities using the trajectory method are given in Table 10.

Table 10. Experimental-based collision cross sections of naphthalene^{•+}(benzene) heterodimer in helium at different temperatures and pressures as indicated. The calculated cross sections obtained from the trajectory method¹²⁵ for the stacked parallel and T-shaped structures optimized at the B3LYP/6-311++G** level of theory.¹³⁰ The boldface values represent the best agreement between experimental and calculated cross sections. Structures shown are calculated using M11/cc-pVTZ.

T (K)	P (Torr)	Ω (Å ²) Experimental		
			Ω (Å ²) Calculated Stacked Parallel	Ω (Å ²) Calculated T-Shaped
302	4.5	82.4	80.1	88.0
273	3.0	86.2	81.6	89.5
231	4.0	91.0	84.4	92.0

The measured collision cross section of the (naphthalene•benzene)^{•+} heterodimer at 302 K (82.4 Å²) is in good agreement with the calculated value of the stacked parallel structure (80.1 Å²). The experimental results at 302 K are about 9 % less than the T-shape structure of 88.0 Å². This is small compared to the naphthalene radical cation homodimer results where the difference between the stacked parallel and T-shaped structures is 20 %. At 231 K, the measured collision cross section is 91.0 Å², which is in excellent agreement with the calculated value for the T-shaped structure of 92.0 Å². However, at the intermediate temperature of 273 K, the measured collision cross section is 86.2 Å² which is almost the average of the calculated values of the stacked parallel and T-shaped structures, 81.6 and 89.5 Å² respectively. These results suggest that the (naphthalene•benzene)^{•+} heterodimer interconverts between the stacked parallel and T-shaped structures depending on the experimental conditions. The similarity of these collision cross section is also supported by the relatively similar calculated binding energies (roughly 8 kcal mol⁻¹) as previously discussed.^{126,127}

Despite the similarities in both collision cross sections and binding energies, it is still interesting that at lower temperatures, the measured experimental cross sections suggest a lower

abundance of the stacked parallel structure compared to the higher energy T-shaped structure. This could be explained by considering the free energy formation of the stacked parallel and T-shaped isomers. There is a loss of entropy in the formation of both isomers due to the loss of translational, rotational, and vibrational degrees of freedom. It appears however that the entropy loss associated with stacking the naphthalene radical cation and the benzene molecule in a sandwich dimer is more than the entropy loss associated with the assembly of the T-shaped dimer. This suggests that the $T\Delta S$ term of the free energy formation (Equation 3.3) of the T-shape isomer is less positive than the corresponding term in the free energy formation of the stacked parallel isomer. The combination of a small positive $T\Delta S$ term along the the binding energy (represented by the $-\Delta H$ term) could result in a more favorable free energy of the T-shaped isomer at lower temperatures. This unique structural motif is useful for the molecular design and recognition involving charged aromatic systems.

6.4.3. Structure and Binding of the Solvation of Naphthalene^{•+} by Pyridine

6.4.3.1. Mass Spectra and Thermochemical Results for Naphthalene^{•+}(Pyridine)_n Clusters

The mass spectra obtained following the injection of mass-selected naphthalene radical cation ($C_{10}H_8^{•+}$, $Naph^+$) into the drift cell containing He or a He/pyridine (C_5H_5N , Pyr) vapor mixture are shown in Figure 72 and Figure 73. In both Figure 72a and Figure 73a, the mass-selected $C_{10}H_8^{•+}$ was injected into the drift cell containing 1.0 Torr He at 305 K and 304 K respectively. Both mass spectra show no dissociation products that is consistent with the low injection energy (12.8 eV) and the naphthalene radical cation is the major peak ($m/z = 128$). A small peak is observed at $m/z = 146$ in both Figure 72a and Figure 73a that corresponds to the $C_{10}H_8^{•+}(H_2O)$ ion ($Naph^+(W)$) in both mass spectra). The presence of this ion is due to the trace amount of water vapor in the drift cell.

When the naphthalene radical cation is injected into the drift cell containing 0.12 Torr Pyr and 0.91 Torr He at 305 K (Figure 72b), the peak associated with the naphthalene radical cation is negligible and the peak associated with the first association product $C_{10}H_8^{*\bullet}(C_5H_5N)$ at $m/z = 207$ is the major peak. The protonated pyridine dimer ($H^+(Pyr)_2$) at $m/z = 159$ is also present. This protonated dimer is present likely due to proton abstraction and subsequent ionization due to the injection energy of the naphthalene radical cation. Further heating of the drift cell resulted in dissociation of the $C_{10}H_8^{*\bullet}(C_5H_5N)$ association product to the naphthalene radical cation and at 400 K (Figure 72c), the $C_{10}H_8^{*\bullet}$ and $C_{10}H_8^{*\bullet}(C_5H_5N)$ peaks are similar in intensity and the protonated pyridine dimer is somewhat reduced. Further heating of the drift cell continued the dissociation of the $C_{10}H_8^{*\bullet}(C_5H_5N)$ to the $C_{10}H_8^{*\bullet}$ (Figure 72d and e) and at 480 K (Figure 72f) the $C_{10}H_8^{*\bullet}(C_5H_5N)$ is almost completely undetectable. The protonated pyridine dimer also dissociates to protonated pyridine, but the intensity of these peaks are small compared to the $C_{10}H_8^{*\bullet}(C_5H_5N)_n$ series as the temperature of the drift cell increases. From the mass spectra in Figure 72, it is clear that there is some covalent character to the binding of the first pyridine molecule to the naphthalene radical cation, but there is likely other types of binding present because the first association product dissociated at higher temperatures.

To observe subsequent additions of pyridine to the naphthalene radical cation, the drift cell was cooled and the resulting mass spectra are shown in Figure 73. When the naphthalene radical cation is injected into the drift cell containing 0.13 Torr pyridine and 1.04 Torr He at 273 K (Figure 73c), the second association product ($Naph^{*\bullet}(Pyr)_2$) is observed. Subsequent cooling resulted in the formation of higher additions of pyridine to the naphthalene radical cation forming $C_{10}H_8^{*\bullet}(C_5H_5N)_n$ association products with $n = 3$ appearing at 246 K (Figure 73d) and $n = 4$ at 225 K (Figure 73f). In addition to the $C_{10}H_8^{*\bullet}(C_5H_5N)_n$ association products, there is a second series of

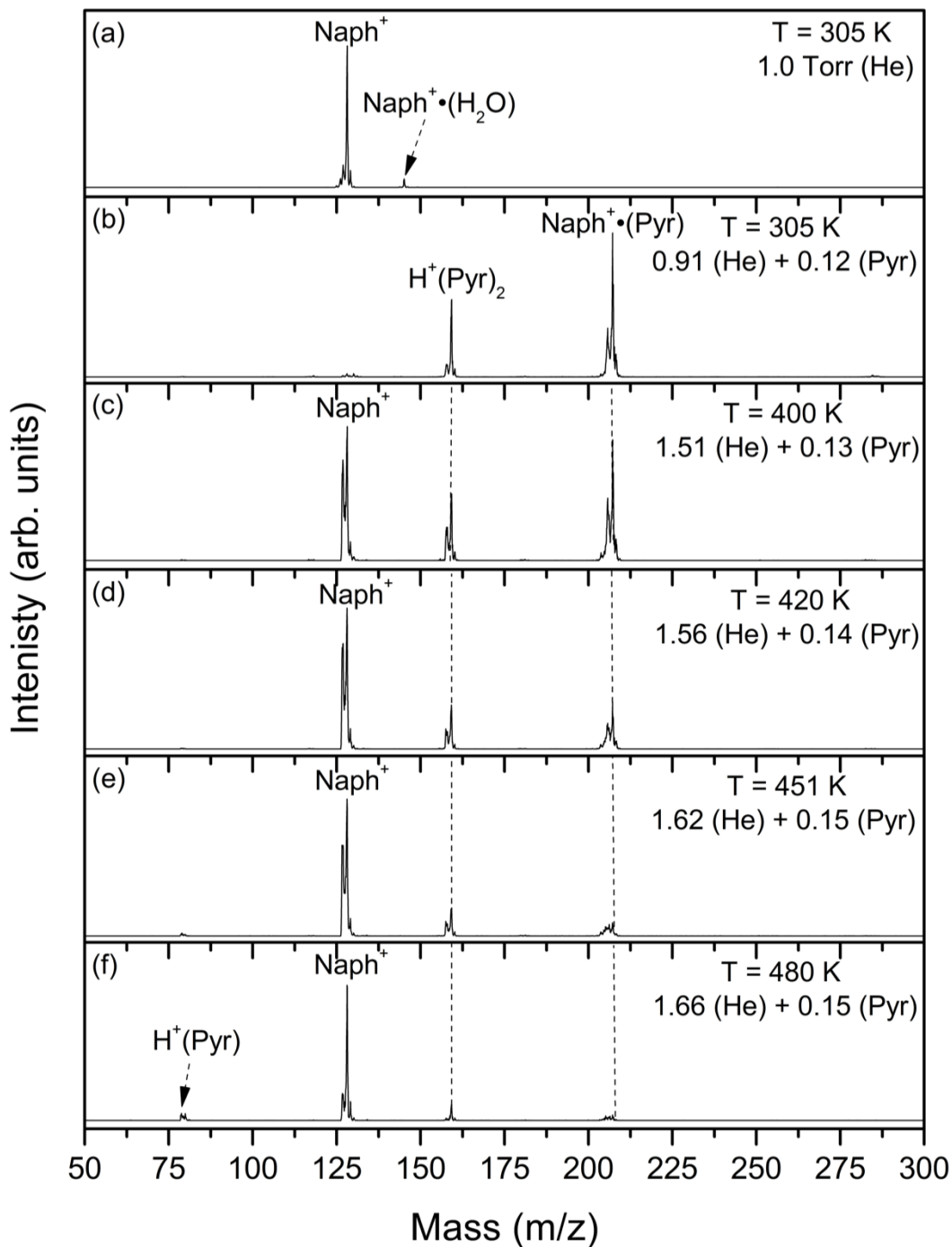


Figure 72. Mass spectra resulting from the injection of the mass-selected naphthalene radical cation ($\text{C}_{10}\text{H}_8^{+\cdot}$, Naph^+) into the drift cell containing He gas (a) or He/pyridine (Pyr) vapor mixture (b-f) at increasing temperatures and pressures as indicated.

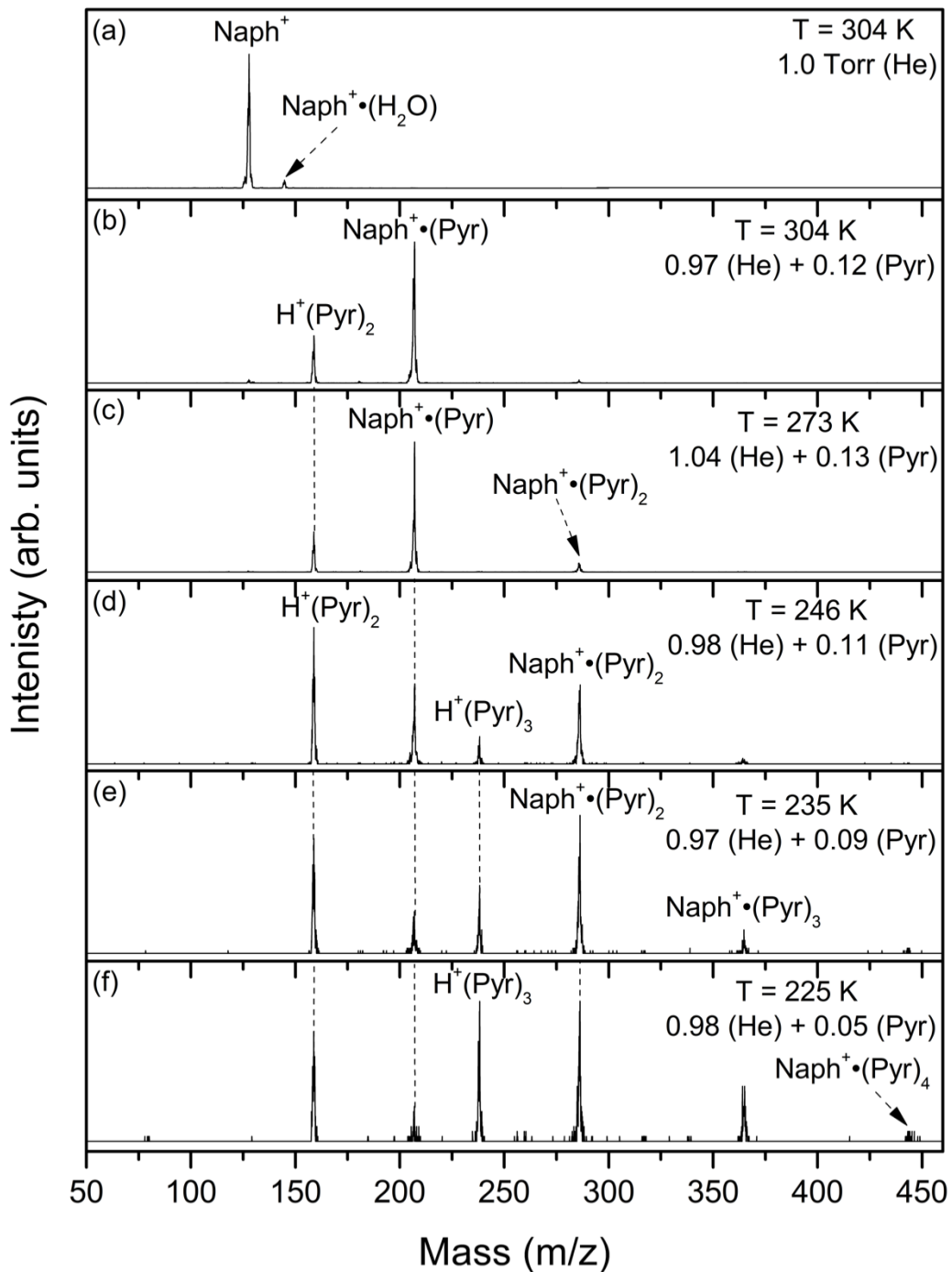
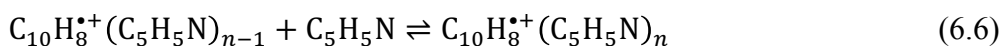


Figure 73. Mass spectra resulting from the injection of the mass-selected naphthalene radical cation ($\text{C}_{10}\text{H}_8^{+\bullet}$, Naph^+) into the drift cell containing He gas (a) or He/pyridine (Pyr) vapor mixture (b-f) at decreasing temperatures and pressures as indicated.

protonated pyridine clusters. The protonated pyridine dimer cation is the dominant peak at 246 K (Figure 73d) with the protonated trimer also observed also observed. At 225 K, the lowest achievable temperature before the pyridine freezes (Figure 73f), the protonated trimer is one of two major peaks present.

The association reaction of pyridine with the naphthalene radical cation is represented by Equation 6.6:



The equilibrium constants were measured for this equation using Equation 6.2 by obtaining the peak intensities of the stepwise association products of $\text{C}_5\text{H}_5\text{N}$ to the $\text{C}_{10}\text{H}_8^{*\cdot}$ ion at different temperatures. Using Equation 3.5, the van't Hoff plots for each association step is produced as shown in Figure 74. The resulting $-\Delta H^\circ$ and $-\Delta S^\circ$ values for Equation 6.6 are obtained from the slope and intercept of the van't Hoff plot respectively and are summarized in Table 11.

Table 11. Measured thermochemistry ($-\Delta H^\circ$ and $-\Delta S^\circ$)^a of the formation of $\text{C}_{10}\text{H}_8^{*\cdot}(\text{C}_5\text{H}_5\text{N})_n$ clusters for $n = 1-4$.

$\text{C}_{10}\text{H}_8^{*\cdot}(\text{C}_5\text{H}_5\text{N})_n$	$-\Delta H^\circ$ (kcal mol ⁻¹)	$-\Delta S^\circ$ (cal mol ⁻¹ K ⁻¹)
1	20.9	33.9
2	11.0	26.9
3	10.9	31.8
4	9.5	27.3

^a Units, estimated error: $\Delta H^\circ \pm 1$ kcal mol⁻¹ and $\Delta S^\circ \pm 2$ cal mol⁻¹ K⁻¹

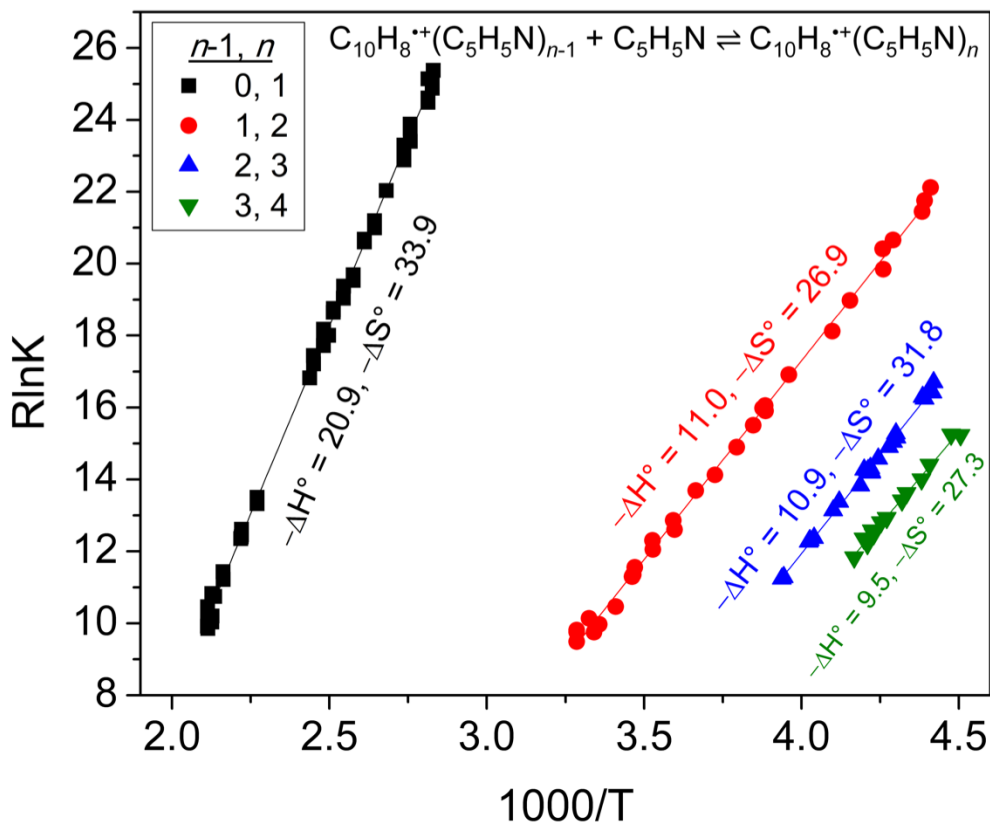


Figure 74. van't Hoff plots for the temperature dependence of the equilibrium constants of the association reaction of naphthalene radical cation with pyridine for the first four solvation steps. The resulting ΔH° and ΔS° are in (kcal mol⁻¹) and (cal mol⁻¹ K⁻¹) respectively. The error for the measurements are ± 1 kcal mol⁻¹ for $-\Delta H^\circ$ and ± 2 cal mol⁻¹ K⁻¹ for $-\Delta S^\circ$.

The formation of the naphthalene^{•+}(pyridine) heterodimer has experimentally measured $-\Delta H^\circ$ and $-\Delta S^\circ$ values of 20.9 ± 1 kcal mol⁻¹ and 33.9 ± 2 cal mol⁻¹ K⁻¹. The binding as measured by the $-\Delta H^\circ$ is significantly higher than the that of the naphthalene^{•+}(benzene) heterodimer of 8 ± 1 kcal mol⁻¹, but lower than that of the benzene^{•+}(pyridine) heterodimer, > 33 kcal mol⁻¹.^{115,127} This behavior could be explained by the fact that there is significant contribution from covalent bond interaction through the formation of a C-N bond, but the possibility of some electrostatic contribution remains. The time profile at 400 K for the naphthalene radical cation, the naphthalene^{•+}(pyridine) heterodimer, and the protonated pyridine dimer is shown in Figure 75. The naphthalene radical cation remains at a constant normalized intensity as the voltage of the drift field is varied. The variations of the naphthalene^{•+}(pyridine) heterodimer and the protonated

pyridine dimer are due to the low intensity of the ATDs taken at low drift field. The lack of any significant change suggests that this reaction is in equilibrium.

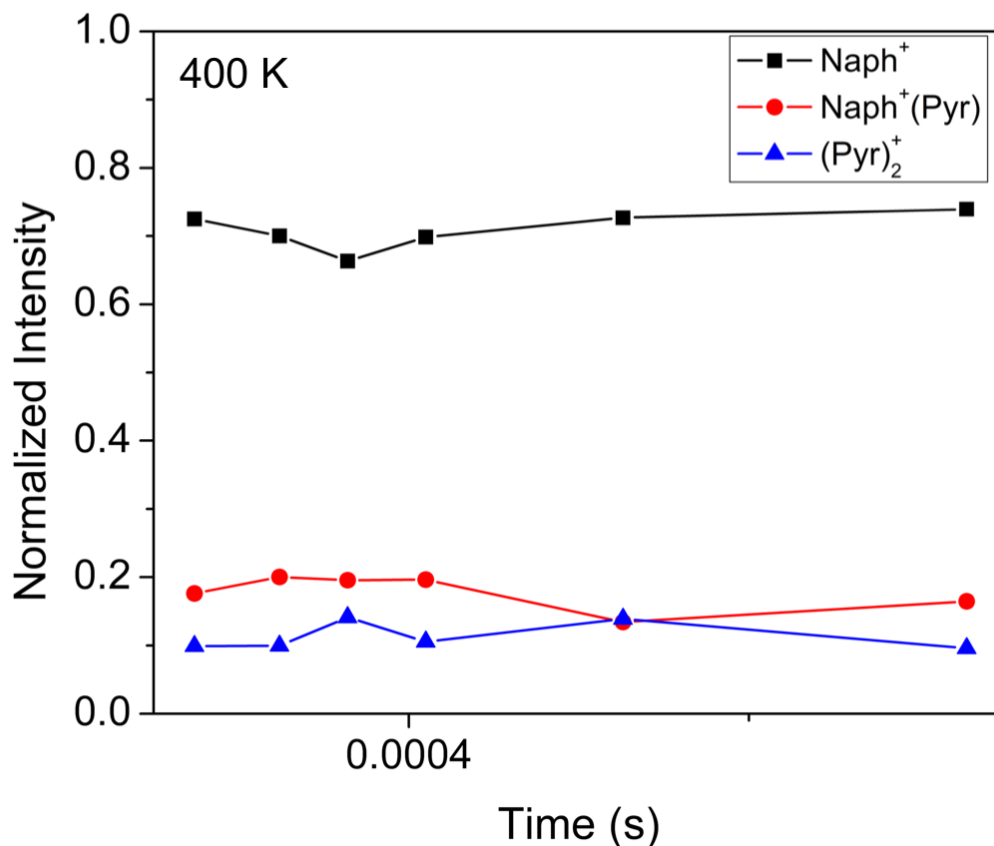


Figure 75. Time profile based on the arrival time distributions (ATDs) of the naphthalene radical cation (Naph⁺); the naphthalene⁺(pyridine) heterodimer, C₁₀H₈⁺⁺(C₅H₅N) (Naph⁺(Pyr)); and the protonated pyridine dimer, H⁺(C₅H₅N) (written as (Pyr)₂⁺) obtained following the injection of the mass-selected naphthalene radical cation into He/C₅H₅N vapor mixtures at 400 K.

Subsequent additions of pyridine to the naphthalene radical cation for C₁₀H₈⁺⁺(C₅H₅N)_n for *n* = 2-4 have decreasing measured $-\Delta H^\circ$ values of 11.0-9.5 ± 1 kcal mol⁻¹ as shown in Figure 74 and summarized in Table 11. This would suggest multiple binding sites around the naphthalene⁺(pyridine) heterodimer with increasing instability. The ATDs of C₁₀H₈⁺⁺(C₅H₅N)_n for *n* = 1 and 2 shown in Figure 76 overlap and have similar arrival times at 273-243 K. This suggests that the subsequent additions of pyridine to the covalent naphthalene⁺⁺•pyridine heterodimer are in equilibrium.

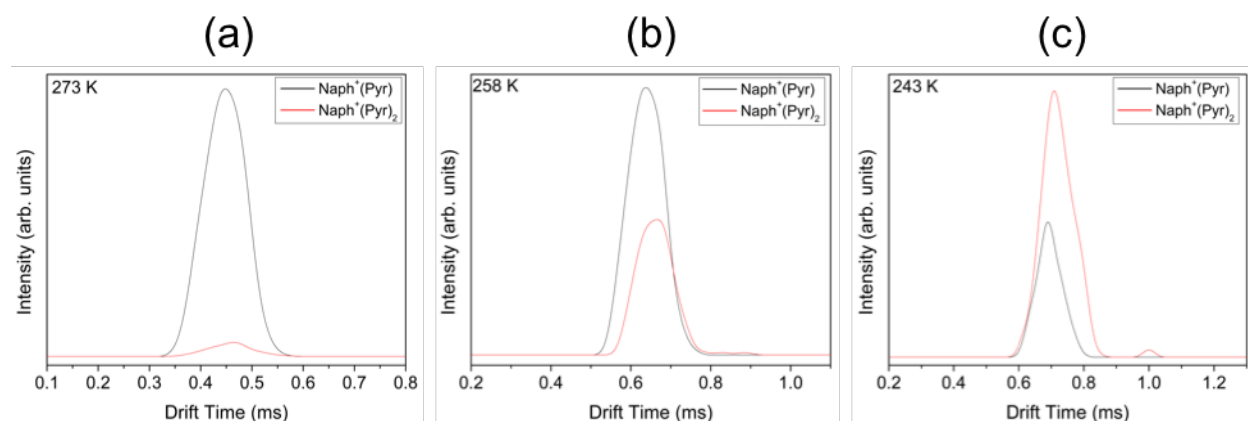


Figure 76. Arrival time distributions (ATDs) of the naphthalene⁺(pyridine) heterodimer, $\text{C}_{10}\text{H}_8^+(\text{C}_5\text{H}_5\text{N})$ ($\text{Naph}^+(\text{Pyr})$), and the second association product, $\text{C}_{10}\text{H}_8^+(\text{C}_5\text{H}_5\text{N})_2$ ($\text{Naph}^+(\text{Pyr})_2$), obtained following the injection of the mass-selected naphthalene radical cation into He/ $\text{C}_5\text{H}_5\text{N}$ vapor mixture at: (a) 273 K, (b) 258 K, and 243 K. Similar ATD overlap suggests the reaction is in equilibrium.

6.4.3.2. Ion Mobility Measurements for the (Naphthalene•Pyridine)⁺ Heterodimer

The mass spectra following the injection of the mass-selected (naphthalene•pyridine)⁺ generated from the coexpansion of naphthalene and pyridine into the drift cell containing helium are shown in Figure 77. At 300 K (Figure 77c) the peaks observed are the (naphthalene•pyridine)⁺ heterodimer [$(\text{Naph}\cdot\text{Pyr})^+$], the naphthalene radical cation monomer (Naph^+), the pyridine homodimer (Pyr_2^+), and the pyridine homotrimer (Pyr_3^+). If the (naphthalene•pyridine)⁺ heterodimer is injected into higher temperatures, such as 323 K (Figure 77b), the heterodimer begins to dissociate to the naphthalene radical cation and neutral pyridine monomers. At the highest measured temperature, 474 K (Figure 77a), the heterodimer has almost entirely dissociated to the naphthalene radical cation. When the drift cell is cooled (Figure 77d-e), the (naphthalene•pyridine)⁺ heterodimer is a major peak and at 223 K (Figure 77d), the (naphthalene•pyridine)⁺(pyridine) heterotrimer begins to appear. At the lowest temperature measured, 103 K (Figure 77e), the naphthalene₂⁺ is also present. The ATDs and t_d versus P/V plot for mobility experiments for the (naphthalene•pyridine)⁺ heterodimer are displayed in Figure 78a

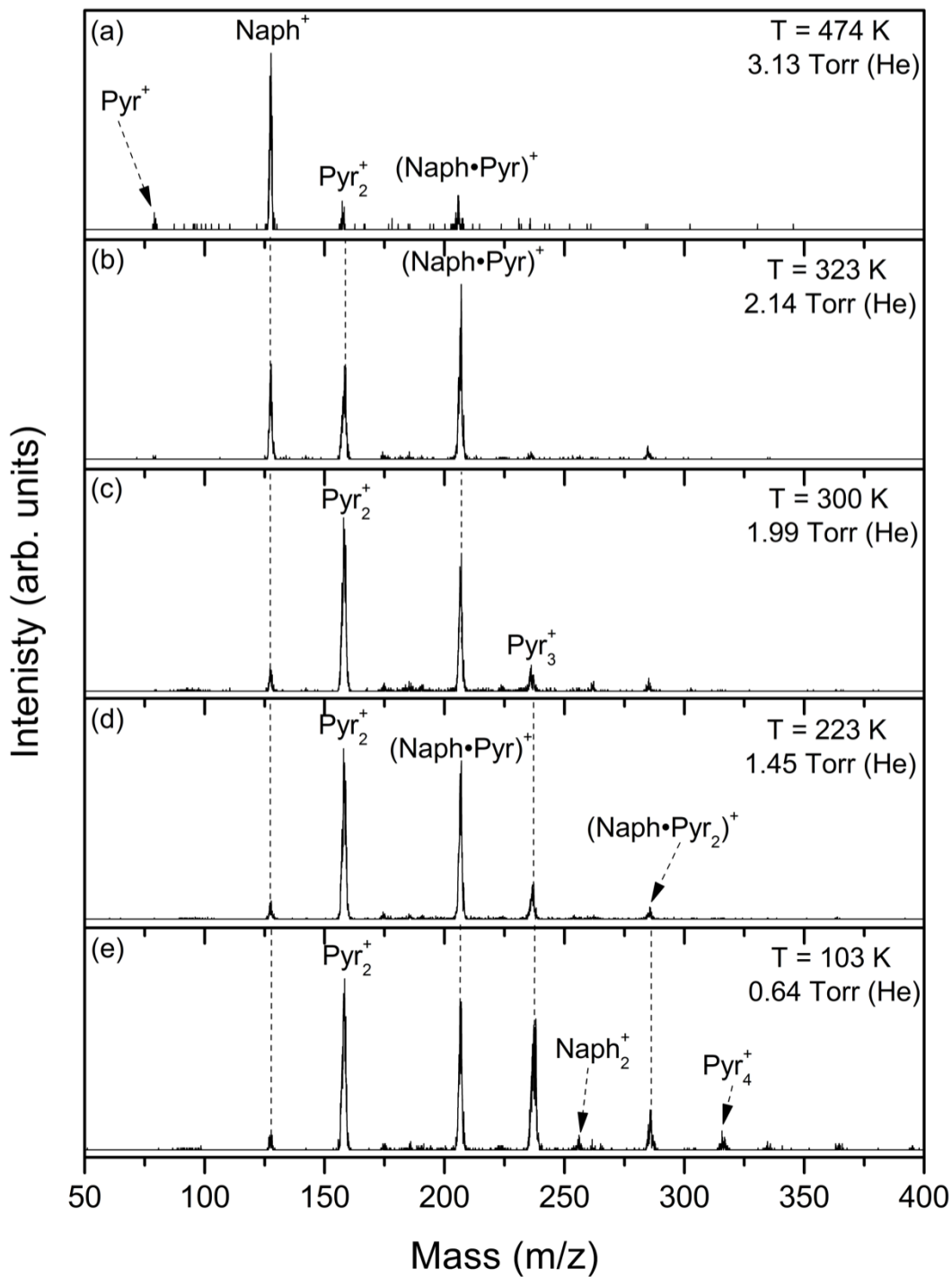


Figure 77. Mass spectra of the products of the coexpansion of a mixture of naphthalene and pyridine into the drift cell containing helium at the temperatures and pressures indicated. The ions are formed by 70 eV EI ionization and He was used as as carrier gas.

and Figure 78b respectively. The excellent linearity in the data shown Figure 78b indicates that under the low-field regime employed in the mobility experiments, the drift velocity of the (naphthalene•pyridine)^{•+} heterodimer is small compared to the thermal velocity and the ion mobility is independent of field strength.

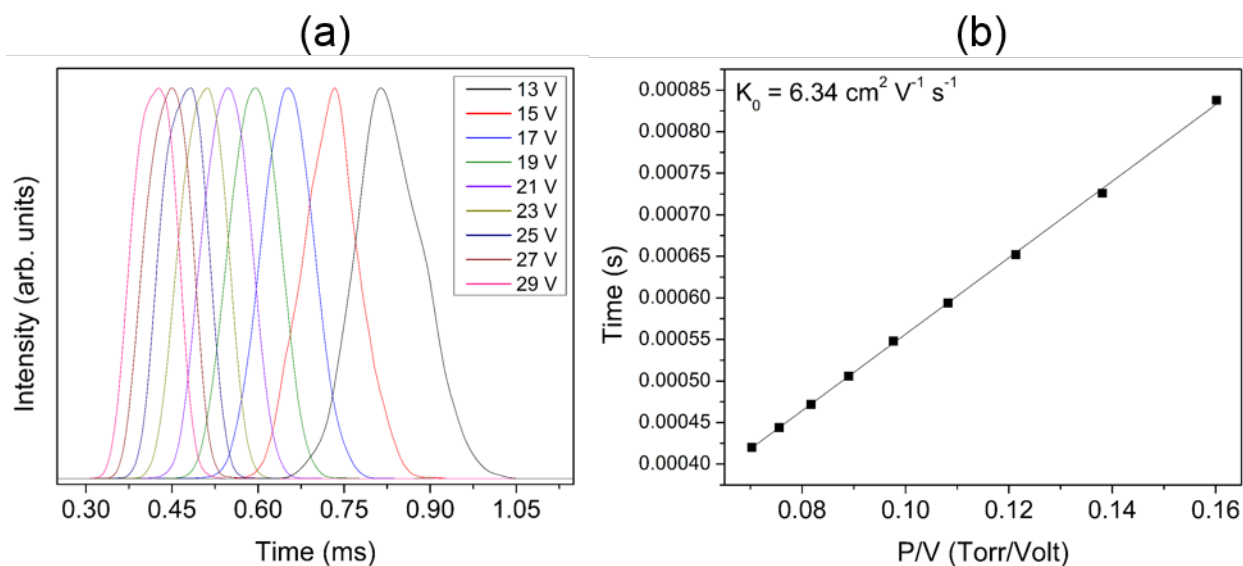
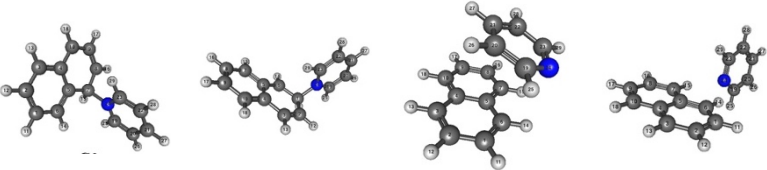


Figure 78. (a) ATDs and (b) t_d versus P/V plot for the naphthalene^{•+}(pyridine) heterodimer. All data are obtained in 2.2 Torr He at a temperature of 302 K.

The measured mobilities are used to calculate the average collision cross sections (Ω) for the (naphthalene•pyridine)^{•+} heterodimer in helium using Equation 3.21 and the resulting values are summarized in Table 12. The collision cross section of the (naphthalene•pyridine)^{•+} is 84.9 \AA^2 at 303 K and increases slightly to 87.5 \AA^2 at 222 K. The theoretical collision cross sections for four isomers calculated at the M06-2X/cc-pVTZ level of theory are also summarized in Table 12 and will be discussed in Section 6.4.3.3.

Table 12. Experimental-based collision cross sections of the naphthalene^{•+}(pyridine) heterodimer in helium at different temperatures as indicated. The calculated cross sections obtained from the trajectory method¹²⁵ for two covalent (C1 and C2), stacked parallel, and T-shaped structures optimized at M06-2X/cc-pVTZ level of theory. The bold face values represent the best agreement between the experimental and calculated cross sections.

Temp (K)	K_0 (cm V ⁻¹ s ⁻¹)	Ω (Å ²) Exp.				
			Ω (Å ²) Calc. C1	Ω (Å ²) Calc. C2	Ω (Å ²) Calc. Stacked Parallel	Ω (Å ²) Calc. T-Shaped
302	6.32	84.9	83.9	85.1	79.8	92.0
273	6.53	86.5	85.3	86.5	81.1	93.4
223	7.18	87.5	88.4	89.6	84.2	96.6

6.4.3.3. Calculated Structures of Naphthalene^{•+}(Pyridine)_n Clusters for $n = 1$ and 2

The calculated structures for the naphthalene^{•+}(pyridine) heterodimer are divided into three classes: covalent, stacked parallel, and T-shaped. The lowest energy isomers for each of these classes are shown in Figure 79. For the covalent class of isomers, two low energy isomers were calculated (Figure 79a and b) with the covalent bond forming between the N of the pyridine neutral and the α or β carbon of the naphthalene radical cation. The structure with the C-N covalent bond formed on the α carbon of the naphthalene (covalent structure 1, C1, Figure 79a) is a more stable complex compared to where the C-N bond is formed on the β carbon (covalent structure 2, C2, Figure 79b) by about 5 kcal mol⁻¹. These covalent isomers form distonic structures where the charge is delocalized on the pyridine between the three carbons in the *ortho*- and *para*-positions of the pyridine ring based on Mulliken population analysis. Based on the same Mulliken population analysis, the spin of the radical is delocalized between two carbons in the naphthalene ring (atoms 8 and 10 in C1 and atoms 6 and 9 in C2, Figure 79a and b). Although it is possible for the H at the site of the C-N covalent bond to be displaced around the heterodimer complex, as in the case of the (benzene•pyridine)^{•+} heterodimer forming (C₅H₅NH⁺•C₆H₅[•]), such structures are always lower in

energy than C1 and mostly smaller than C2 when the proton migrates to another site on the naphthalene rings.¹¹⁵ When the proton migrates around the pyridine ring (as it does in the benzene•pyridine heterodimer radical cation), the energy is only comparable to the energy of the C2 isomer when the H is at the *para*-position, but still comparable to when no migration occurs.

115

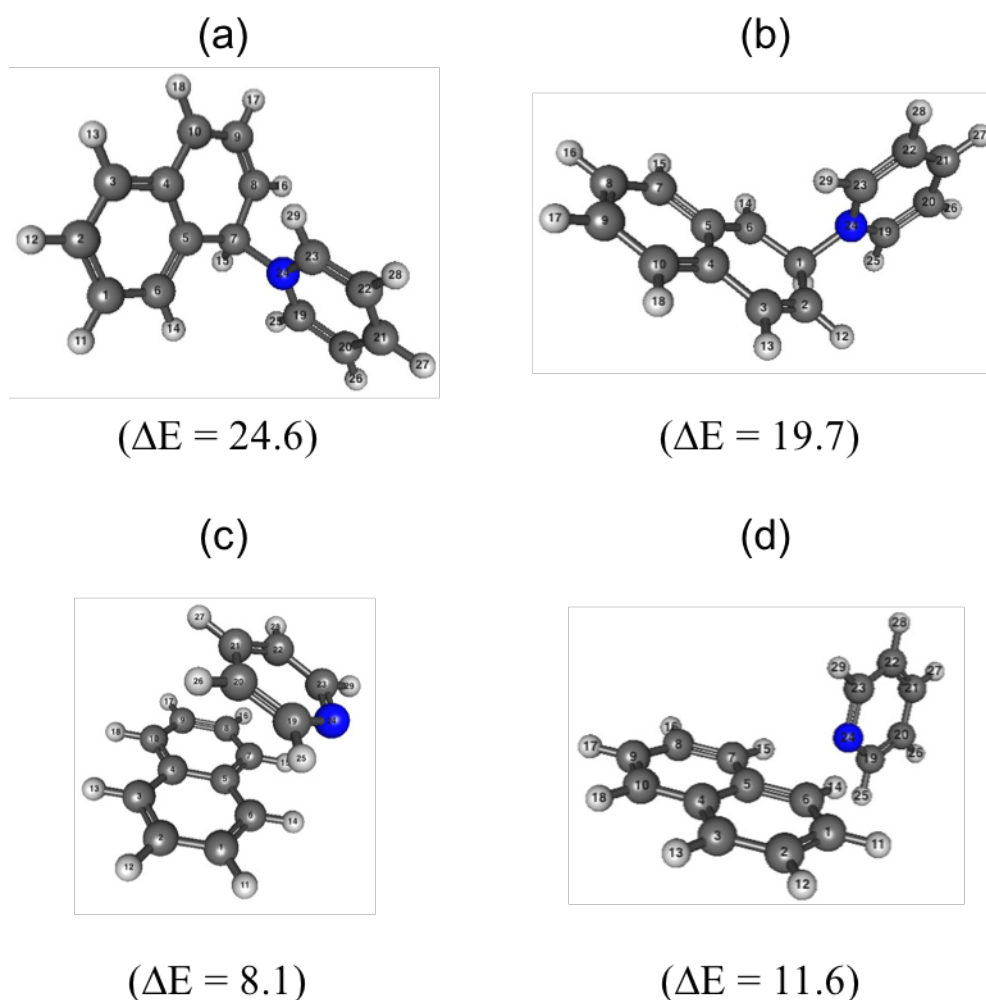


Figure 79. DFT structures and binding energies (ΔE , kcal mol⁻¹) of four isomers for the naphthalene^{•+}(pyridine) heterodimer: (a) covalent structure 1 (C1), (b) covalent structure 2 (C2), (c) stacked parallel, and (d) T-shaped calculated at the M06-2X/cc-pVTZ level of theory.

The stacked structure (Figure 79c) is a higher energy structure compared to covalent isomers and has a calculated binding energy, ΔE , of $8.1 \text{ kcal mol}^{-1}$ which is similar to that in the naphthalene^{•+}(benzene) heterodimer.¹²⁷ The structure of the two heterodimer isomers are also similar.¹²⁶ The T-shaped isomer (Figure 79d) is a lower energy isomer compared to the stacked structure, $11.6 \text{ kcal mol}^{-1}$ vs $8.1 \text{ kcal mol}^{-1}$ respectively, which differs from the naphthalene^{•+}(benzene) heterodimer where the T-shaped isomer is the highest-energy structure. The pyridine will bind to the naphthalene forming two $\text{CH}^{\delta+}\cdots\text{N}$ bonds at the α positions of the two naphthalene rings.

The experimental $-\Delta H^\circ$ value of $20.9 \pm 1 \text{ kcal mol}^{-1}$ for the naphthalene^{•+}(pyridine) heterodimer lies between the calculated binding energy of the two covalent isomers. This would suggest that the pyridine does form a covalent bond with the naphthalene radical cation, but a mixture of both C1 and C2 structures is present. The stacked parallel and T-shaped structure that are observed in the naphthalene^{•+}(benzene) heterodimer are unlikely to be observed for the naphthalene^{•+}(pyridine) heterodimer due to the electrostatic structures being higher in energy and binding energies that do not correlate with the experimentally observed results.

The C-N bond length between the naphthalene radical cation and neutral pyridine for the covalent structures are 1.53 \AA for the C1 structure and 1.54 \AA for the C2 structure. This bond length is relatively close to the normal C-N bond length of 1.47 \AA which supports the idea of a covalent bond formation.² The energy of formation of the C-N bond is interesting since both the experimental and calculated binding energies are well below the typical C-N binding energy of 73 kcal mol^{-1} .² This difference in energy is explained¹ by the distonic nature of the $\text{C}_{10}\text{H}_8^+(\text{C}_5\text{H}_5\text{N}^+)$ cluster. The bond formed is dative in character with the two electrons of the nitrogen creating the bond. This results on the charge localized on the pyridine as discussed earlier, which is

unfavorable. The bond also disrupts the aromaticity of the naphthyl radical and results in proton. Such interactions cause the normally strong covalent bond to become “frustrated” and thus a lower energy covalent bond is observed.

The measured collision cross sections for the (naphthalene•pyridine)⁺ heterodimer are in good agreement with the the calculated values of the covalent structures. At 302 and 273 K, the measured collision cross sections, 84.9 and 86.5 Å² respectively, are between the calculated values, 83.9 and 85.3 Å² for the C1 structure and 85.1 and 86.5 Å² for the C2 structure. At 223 K, the measured collision cross section is 87.5 Å², which is less than the calculated cross sections of 88.4 and 89.6 Å² for the C1 and C2 structures respectively. For the stacked parallel structures, the calculated collision cross sections were 79.8, 81.1, and 84.2 Å² for 302, 273, and 223 K respectively. At all temperatures, the calculated cross sections for the stacked parallel structure are less than the measured collision cross sections. Alternatively, the calculated collision cross sections for the T-shaped isomer of the (naphthalene•pyridine)⁺ (92.0, 93.4, and 96.6 Å² for 302, 273, and 223 K respectively), are about 10 % larger on average than the measured collision cross sections. These results are summarized in Table 12 and support the thermochemistry results that the naphthalene⁺(pyridine) heterodimer is a covalent structure where the pyridine forms a C-N covalent bond with the α or β carbon of the naphthalene radical cation. Based on the values, a mixture of the two structures is present, but there is likely a predominance of the structure where the C-N bond is formed at the β carbon of the naphthalene radical cation.

Using the two covalent structures of the naphthalene⁺(pyridine) heterodimer (Figure 79a and b) as starting points, the lowest energy structures for the addition of a second pyridine structure were calculated using *ab initio* molecular dynamics (AIMD) calculations with the resulting structures and binding energies, ΔE , shown in Figure 80. The second pyridine was added to either

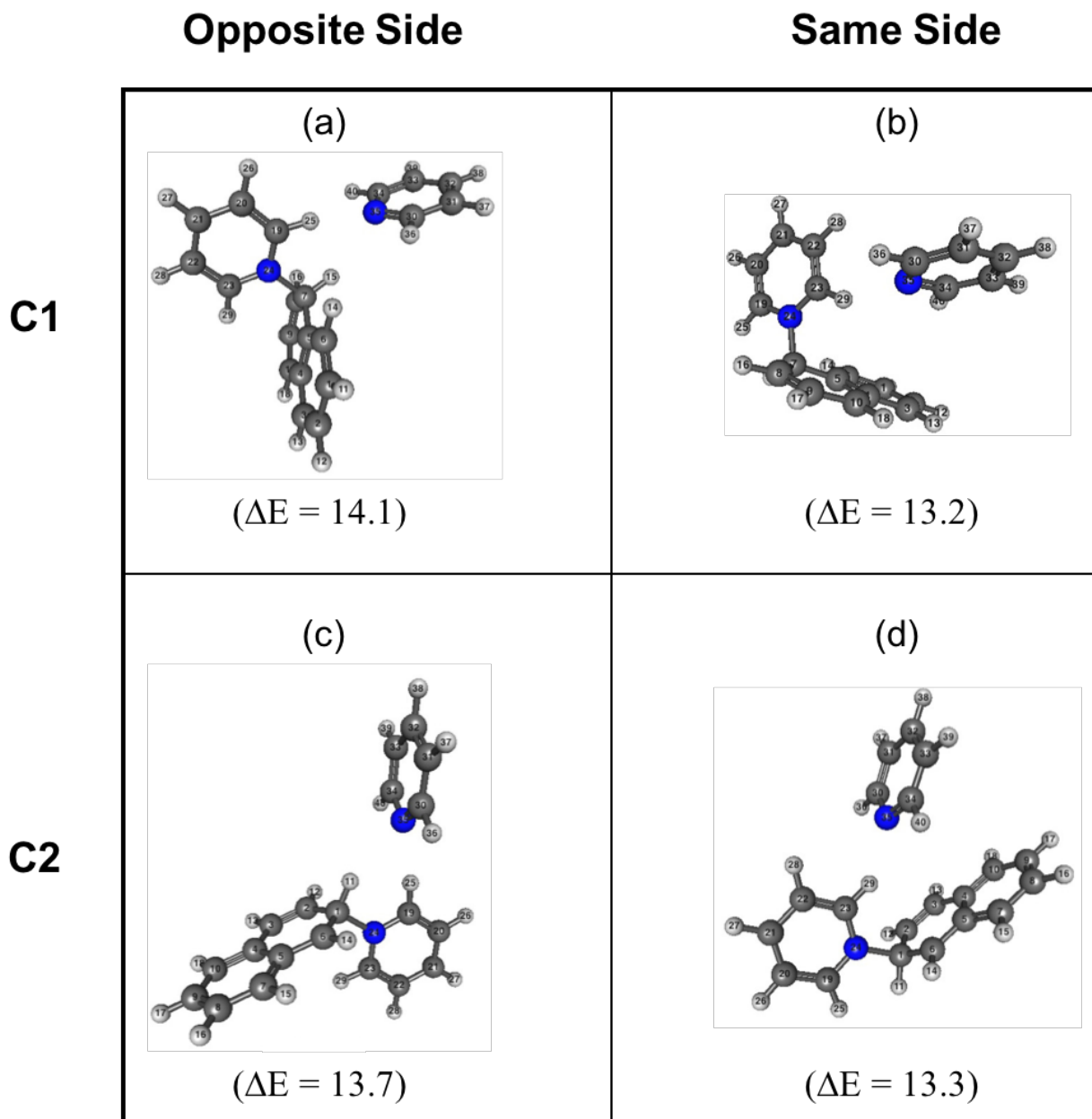


Figure 80. AIMD structures and binding energies (ΔE , kcal mol⁻¹) of four low energy isomers for the naphthalene⁺(pyridine)₂ heterotrimer using the two low energy covalent structures of the naphthalene⁺(pyridine) heterodimer (C1 or C2) as a starting point with the second pyridine molecule binding to the same side (SS) or opposite side (OS): (a) C1/OS, (b) C1/SS, (c) C2/OS, and (d) C2/SS

the opposite side (Figure 80a and c) or the the same side (Figure 80b and d) of the original pyridine that is attached to the naphthalene ring by a covalent bond for both the C1 and C2 isomers. The binding energy for all four isomers are relatively similar with a value of $13-14 \pm 1 \text{ kcal mol}^{-1}$. In all cases, the second pyridine molecule forms a network of H-bonds between all three molecules in the heterotrimer. The experimental $-\Delta H^\circ$ value of $11.0 \pm 1 \text{ kcal mol}^{-1}$ is less than the calculated structures, but given that there is an ensemble of structures predicted for the heterodimer, the heterotrimer should also contain an ensemble of structures. Calculations were also performed where the second pyridine bind covalently to the naphthalene ring, but the second pyridine is essentially unbound with only one structure containing a very small binding energy of 2 kcal mol^{-1} .

Unlike the $\text{naphthalene}^{*\text{+}}(\text{benzene})_2$ heterotrimer where the second benzene forms a sandwich structure, the second pyridine in the $\text{naphthalene}^{*\text{+}}(\text{pyridine})_2$ heterotrimer will move to maximize the H-bonding interactions with the dimer forming a slanted U-shaped structure. Further frequency calculations for the $\text{naphthalene}^{*\text{+}}(\text{pyridine})_2$ heterotrimer will allow better understanding into this hydrogen bonding behavior.

6.5. Summary and Conclusions

The equilibrium thermochemistry measurements for the $\text{naphthalene}^{*\text{+}}(\text{benzene})$ heterodimer and $\text{naphthalene}^{*\text{+}}(\text{pyridine})_n$ clusters for $n = 1-4$ were obtained using the ion mobility drift cell technique. The collision cross sections of the $(\text{naphthalene})_2^{*\text{+}}$ homodimer and $\text{naphthalene}^{*\text{+}}(\text{benzene})$ and $\text{naphthalene}^{*\text{+}}(\text{pyridine})$ heterodimers were calculated from the measured reduced mobility using the same technique. Using both sets of data, the structures of the measured dimers were determined from possible calculated isomers using DFT and *ab initio* molecular dynamic calculations.

The (naphthalene)₂^{•+} homodimer has a stacked parallel structure from 230-300 K with no presence of a T-shaped isomer observed. The charge resonance interaction between the two naphthalene molecules contributes to the binding energy, 17.8 kcal mol⁻¹, of the dimer.^{126,199} The naphthalene^{•+}(benzene) heterodimer, with a binding energy of 7.9-8.1 ±1 kcal mol⁻¹ (for C₆H₆ and C₆D₆), will appear as both a stacked parallel and T-shaped structures in the same 230-300 K. The stacked parallel structure is present at higher temperatures, while the T-shaped structure is predominant at lower temperatures. The -ΔH° for the naphthalene^{•+}(benzene)₂ heterotrimer was estimated by calculating the ΔG° at 219 K and resulted in a value of 8.4 kcal mol⁻¹. The resulting structure is a sandwich structure with the naphthalene radical cation between two benzene molecules.

The naphthalene^{•+}(pyridine) heterodimer has a measured binding energy of 20.9 kcal mol⁻¹ suggesting that the bond is formed with some covalent character. The heterodimer is a distonic structure of naphthalene[•](pyridine⁺) where the pyridine will form a C-N covalent bond on either the α or β carbon of the naphthalene ring. The second pyridine molecule forms a network of H-bonds with the covalent structure with a binding energy of 11.0 kcal mol⁻¹. Attempts to calculate a second covalent bond resulted in the C-N covalent bond breaking and forming the H-bond network. Subsequent additions have binding energies of 10.9 and 9.5 kcal mol⁻¹ suggesting that the pyridine will form H-bonding networks within the naphthalene^{•+}(pyridine)_n complex.

The unique structural motifs of the dimer radical cations could be useful for molecular design and recognition involving charged aromatic systems. Covalent additions of pyridine to the polycyclic aromatic hydrocarbon suggests the possibility of formation of complex heterocyclic species in ionizing environments in space.

Chapter 7: Stepwise Solvation of the Phenyl Cation by Small Polar Molecules with Comparisons to Naphthalene^{•+}

7.1. Introduction

The hydration of organic ions with small molecules such as water, methanol, hydrogen cyanide, and acetonitrile has a central role in many chemical, biological, and physical processes such as base pair stacking in DNA, conformation and folding of proteins, macromolecule assembly, biological membranes, drug design, clathrate hydrate formation, and micelles.^{7,35,70,132} Organic ions can form hydrogen bonds in nature; one example of this being observed in icy grains doped with polycyclic aromatic hydrocarbons (PAH) that are subjected to ionizing radiation in interstellar dust grains.^{205,206} Hydrogen bonding interactions involving ionized aromatics are important in radiation chemistry, electrochemistry, polymerization in aqueous solvents, and in astrochemical environments.^{66,69,205} These interactions include proton abstraction by solvent molecules such as water from ionized aromatics. These interactions are important for astrochemical processes and reaction mechanisms.^{54,69}

Ionic hydrogen bonding (IHB) interactions involving small polar molecules are important for ionized PAHs where unconventional carbon-based IHBs are formed. Here the hydrogen donors are the ionized aromatics containing CH groups and the hydrogen acceptors are electron lone pairs on heteroatoms such as O or N, olefin double bonds, or aromatic π systems.⁵ Water can cluster with PAH ions and condense to form large hydrogen-bonded networks around or on the surface of the PAH ion thus acting as nucleation centers for the formation of organic-doped icy grains. These organic-doped icy grains can form complex organics including membrane-forming components under interstellar UV radiation.^{52,54,55,89}

Understanding the reactions of the phenylium ion ($C_6H_5^+$) allows more insight into the chemistry of isolated gas-phase ions. This is because phenylium ions are produced upon electron and chemical ionization of many aromatic species.²⁰⁷ Due to the vacant sp^2 orbital of the phenylium ion, interactions with neutral molecules are strong ion-induced dipole in nature. The reactivity of the phenylium ion is both carbonium- and carbene-type and can thus interact with both σ - and π -type electron systems.^{207,208} Because of this, the energetics and structures of the products of ion-molecule reactions between phenyl cation and small molecules from in astrochemical environments is important.

The phenyl radical ($C_6H_5^{\cdot}$) has been investigated as a precursor to forming larger PAH molecules, such as indene, upon reacting with unsaturated hydrocarbons.²⁰⁹⁻²¹³ The phenylium ion has been shown to react much faster with unsaturated molecules such as acetylene when compared to benzene radical cation ($C_6H_5^{+\cdot}$) due to the barrier that originates from the absence of an available addition site.¹⁶⁸ The loss of a proton to allow this favorable reaction could occur in solar nebulae and interstellar environments by ionization processes by the abstraction of H by reactive radical species such as H and C_2H .³⁹

Despite this work on phenylium with unsaturated hydrocarbons, little work has focused on the gas phase interactions of the phenyl cation with small polar astrophysically relevant molecule such as water or hydrogen cyanide.²⁰⁷ Presented is the first study of the hydration the phenylium ion in the gas phase beyond a single water molecule. Using the information of the stepwise hydration of the phenyl cation in the gas phase can be used to extrapolate potential hydrophobic and hydrophilic hydration in macroscopic systems and larger PAH molecules.³⁵ The interactions between these ionized aromatics and water although common, are not experimentally characterized on a molecular level. Much of the information available relies upon chemical

intuition and theoretical models.^{69,70} To further investigate the H-bonding behavior of the phenyl cation, methanol was used as the solvation molecule. The astrochemically and biologically relevant molecule HCN and the similar acetonitrile are also used and can be used to form complex polycyclic aromatic nitrogen-containing molecules (PANHs).^{39,74,214-217}

In this chapter, the measured binding energies for the $(\text{C}_6\text{H}_5^+)(\text{H}_2\text{O})_n$ complexes for $n = 2-4$ and calculated structures and binding energies for 1-6 water molecules associated with the phenylium ion in $(\text{C}_6\text{H}_5^+)(\text{H}_2\text{O})_n$ clusters are shown. The results indicate that the first water molecule binds covalently to the phenylium ion to form a protonated phenol cation structure. Subsequent additions of water bind via IHBS to form a hydrogen bonding chain of water molecules with no indication of internal solvation. The resulting structures for these subsequent additions are similar to those of protonated phenol.²¹⁸ Thermochemistry results are also presented for the second and third step association steps of the phenyl cation to methanol, $\text{C}_6\text{H}_6^+(\text{CH}_3\text{OH})_n$ for $n = 2$ and 3 , as well as the second-forth association steps for HCN and acetonitrile, $\text{C}_6\text{H}_5^+(\text{HCN})_n$ and $\text{C}_6\text{H}_5^+(\text{CH}_3\text{CN})_n$ for $n = 2-4$ respectively. Experimental thermochemical results for the first association product could not be measured for these systems due to the formation of a covalent bond between the neutral molecule and the phenyl cation. This work aims to establish the structures and thermodynamics of solvated phenylium ion within clusters of polar molecules relevant to astrophysical environments.

7.2. Experimental Section

All experiments are performed with the VCU mass-selected ion mobility spectrometer with details of the system outlined in Chapter 2. During experiments, the C_6H_5^+ (Ph^+) ions are generated by electron impact ionization using an electron energy of 60-70 eV after supersonic expansion of 50-80 psi ($\approx 2500-3600$ Torr) ultra-high purity helium (AirGas) seeded with of bromobenzene

vapor, C_6H_5Br , through a pulsed supersonic nozzle (500 μm) into a source vacuum chamber maintained at a background pressure of 10^{-7} Torr. The $C_6H_5^+$ ions are mass-selected by a quadrupole mass-filter before being injected into a drift cell (in 25-50 μs pulses) containing helium (AirGas, Research Grade) or a He/neutral reagent vapor mixture. The neutral reagents used were: H_2O (deionized), MeOH (Fisher, laboratory grade), HCN (preparation discussed later), or CH_3CN (Sigma-Aldrich, $\geq 99.9\%$). Flow controllers (MKS #1479A) were used to maintain a constant pressure inside the drift cell within ± 1 mTorr. The temperature of the drift cell was controlled to ± 1 K using four temperature controllers. To cool the drift cell, liquid nitrogen was used by flowing it through solenoid valves. The reaction products leaving the drift cell were identified by scanning a second quadrupole mass-filter located after the drift cell and arrival time distributions (ATDs) were collected by monitoring the intensity of each ion as a function of time. The injection energies used in experiments (10-14 eV, laboratory frame) were only slightly higher than the minimum energies required to introduce the ions against the neutral reactant/He vapor mixture outflow at the drift cell entrance orifice. Most ion thermalization occurred outside of the drift cell by collisions with the gas mixture molecules escaping the drift cell entrance orifice.

The HCN gas used for experiments was prepared by sealing 5-8 g of NaCN (Sigma-Aldrich, 97 %) in a 500 mL stainless steel/glass bubbler. The solid was then pumped using an Edwards 30 mechanical pump (E2M, 250 V, $33.0\ m^3\ hr^{-1}$ pumping speed) to 20 Torr monitored by a Baratron pressure gauge (MKS-626A13TBD). Approximately 2.5-4 mL of pure sulfuric acid (H_2SO_4 , Sigma-Aldrich, 99.999%) was added to the bubbler via a stainless steel tube extension on the bubbler fitted with valves on each side to ensure vacuum of the NaCN. The sulfuric acid was dropped into the bubbler to react with the NaCN leading to the immediate production of HCN gas.

The equilibrium reaction for all experiments studied throughout this series chapter is represented by Equation 7.1:



where B is the neutral molecule: H₂O, MeOH, HCN, or MeCN respectively. This reaction is said to be in equilibrium when: (1) the ATDs of the product and reactant ions have equal arrival times and (2) there is a constant ratio of the integrated intensities of product and reactant ion over a range of drift cell field voltage thus changing the residence time of the ions at a constant temperature and pressure. Once equilibrium is established, the equilibrium constant, K_{eq} , is measured using the equation:

$$K_{\text{eq}} = \frac{[\text{C}_6\text{H}_5^+(\text{B})_n]}{[\text{C}_6\text{H}_5^+(\text{B})_{n-1}][\text{B}]} = \frac{I_{[\text{C}_6\text{H}_5^+(\text{B})_n]}}{I_{[\text{C}_6\text{H}_5^+(\text{B})_{n-1}]}} \quad (7.2)$$

where $I_{[\text{C}_6\text{H}_5^+(\text{B})_n]}$ and $I_{[\text{C}_6\text{H}_5^+(\text{B})_{n-1}]}$ are the integrated intensities of the ATDs of the reactant and product ions or the intensity of the ion peak on a mass spectrum and P_{B} is the partial pressure of the neutral vapor in atmospheres inside the drift cell. The equilibrium constant is measured at different temperatures to form a van't Hoff plot (using the van't Hoff equation as shown in Equation 3.5) where the ΔH° and ΔS° values are obtained from the slope and intercept respectively. All data was repeated at least three times with average values used in discussion.

7.3. Theoretical Calculations

Density functional theory calculations of the lowest energy structures for the various isomers of the cluster ions were performed using the Gaussian 03 program suite.¹²⁹ The calculations protonated phenol cation, $\text{C}_6\text{H}_5\text{OH}_2^+$, and first four additions of water to the phenyl cation, $(\text{C}_6\text{H}_5^+)(\text{H}_2\text{O})_n$ for $n = 1-4$ were performed at the B3LYP/6-311++G** level of theory. Vibrational frequency calculations were also performed for all the optimized geometries at the

same level of theory in order to obtain zero-point vibrational energy (ZPVE) and to verify the absence of imaginary frequencies.¹³⁰ For all calculations the binding energy (ΔE) was calculated at 0 K and was calculated using the equation:

$$\Delta E_{[(C_6H_5^+)(H_2O)_n]} = \left(E_{[(C_6H_5^+)(H_2O)_{n-1}] + E_{[B]}} \right) - E_{[(C_6H_5^+)(H_2O)_n]} \quad (7.3)$$

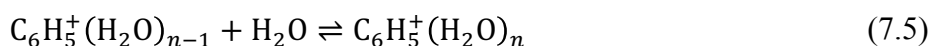
where $E_{[(C_6H_5^+)(H_2O)_{n-1}]}$, $E_{[B]}$, $E_{[(C_6H_5^+)(H_2O)_n]}$ and are the total electronic energies of the lowest energy isomers of the reactant ion, neutral molecule represented by B, and the product of the reaction shown in Equation 7.1.

7.4. Results and Discussion

7.4.1. Stepwise Hydration of the Phenyl Cation

7.4.1.1. Mass Spectra and Thermochemical Results for Phenyl⁺(H₂O)_n Clusters

The mass spectra obtained following the injection of the mass-selected phenyl cation into the drift cell containing He or a He/water vapor mixture are shown in Figure 81-Figure 83. When the drift cell contains only He the residual water in the drift cell binds to the C₆H₅⁺ resulting in the first hydration product (Ph⁺W) at $m/z = 95$ as shown in Figure 81a, Figure 82a, and Figure 83a. The presence of the Ph⁺W peak suggests strong binding of water to the phenyl cation at room temperature. Two pathways arise that illustrate this behavior and are shown by Equations 7.4 and 7.5:



In Equation 7.4, the water irreversibly binds to the phenyl cation resulting in the formation of the covalent product similar to the protonated phenol ion. Subsequent water additions would bind via reversible ionic hydrogen bonding. Equation 7.5 shows water forming reversible ionic hydrogen

bonds with the phenyl cation that are similar to those seen in other aromatic ions such as benzene and naphthalene.^{9,56,69,106}

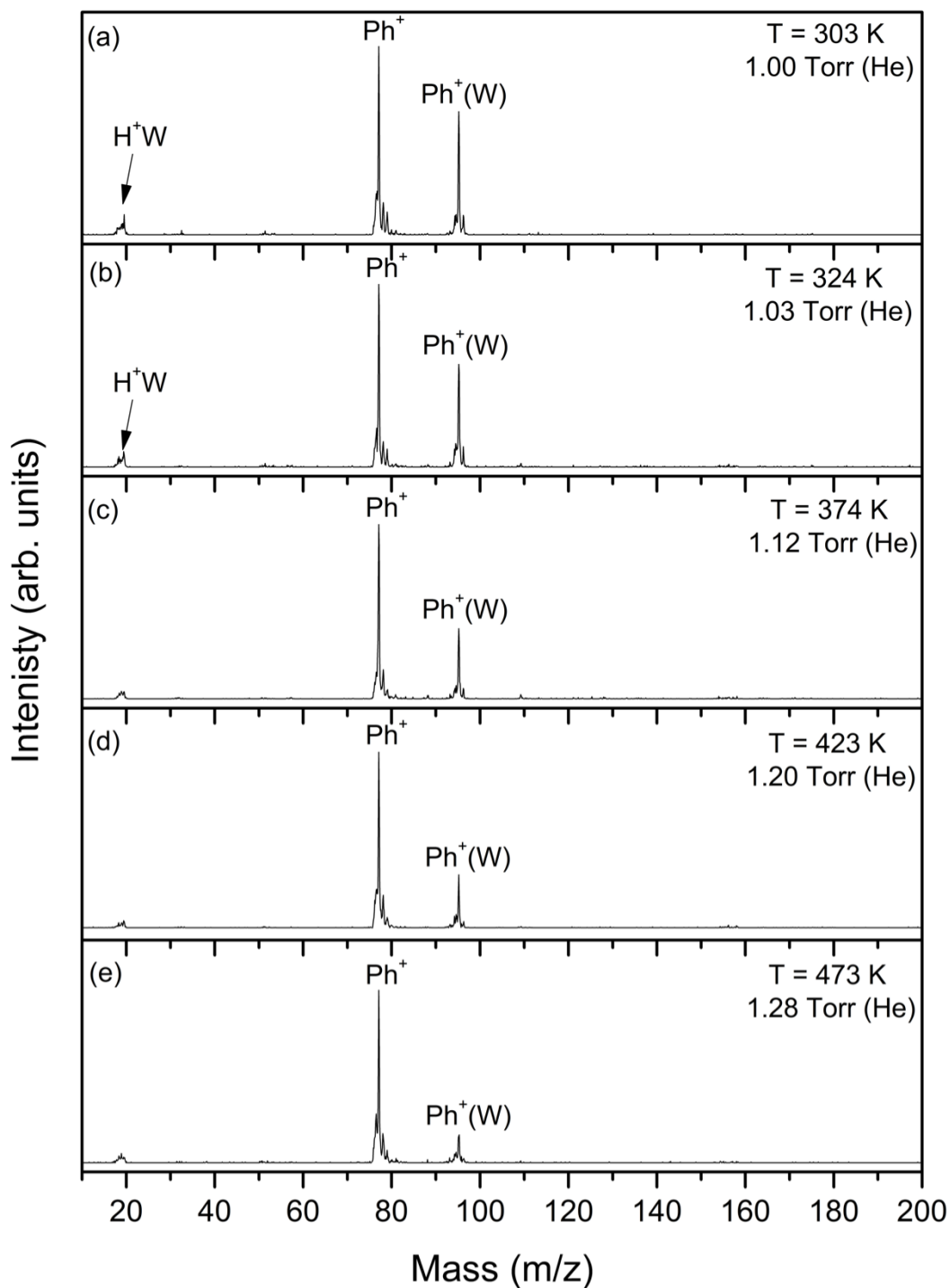


Figure 81. Mass spectra resulting from the injection of the mass-selected phenyl cation (C_6H_5^+ , Ph^+) into He gas at different pressures and temperatures as indicated.

The covalent protonated phenol cation (Ph^+W) shown in Equation 7.4 was shown to exist by observing the temperature dependence of the presence and intensity of the $\text{C}_6\text{H}_5\text{OH}_2^+$ peak ($m/z=95$) at high temperatures when the mass-selected phenyl cation is injected into the drift cell containing only He. The water present would be the residual water vapor in the drift cell as shown in Figure 81. The water should not come from the He since the concentration in the gas is only 0.2 ppb (99.9999 % pure). At 303 K (Figure 81a) both the Ph^+ and Ph^+W ions are the predominant species, but protonated water is also present. As the temperature increases, Ph^+ becomes the predominant species, but even at 473 K the Ph^+W is still present. The C_4H_3^+ peak observed at $m/z=51$ is a known fragment from the bromobenzene used to create the phenyl cation.²

Figure 82 and Figure 83 display the mass spectra obtained following the injection of the mass-selected phenyl cation (C_6H_5^+ , Ph^+) into the drift cell containing He or He-water vapor (W) gas mixture. In both Figure 82a and Figure 83a, the mass-selected phenyl cation is injected into the drift cell containing only He to act as a reference to the subsequent mass spectra where water vapor is present. Figure 82b-e shows the mass spectra obtained when the drift cell contains He-water vapor gas mixture at increasing temperatures between 303-553 K. In the presence of 0.07 Torr water vapor in the drift cell at 303 K, the association product Ph^+W_2 is the major product along with small intensities of Ph^+ , Ph^+W , and the protonated water cluster H^+W_4 as shown in Figure 82b. As the temperature of the drift cell increases, the dissociation of the Ph^+W_2 product to the Ph^+W product is observed along with protonated water and the C_4H_3^+ fragment ion peak. At 403 K the Ph^+W is the major product with complete dissociation of the second hydration product shown in Figure 82c. As the temperature is increased to 553 K, Figure 82e, the Ph^+W remains the major ion observed with little observation of the Ph^+ peak. This prevents the equilibrium to not be determined and thus the thermochemistry for the first hydration product was not measured. This

type of binding reinforces the notion of a strong covalent bond forming between the first water and the phenyl cation.

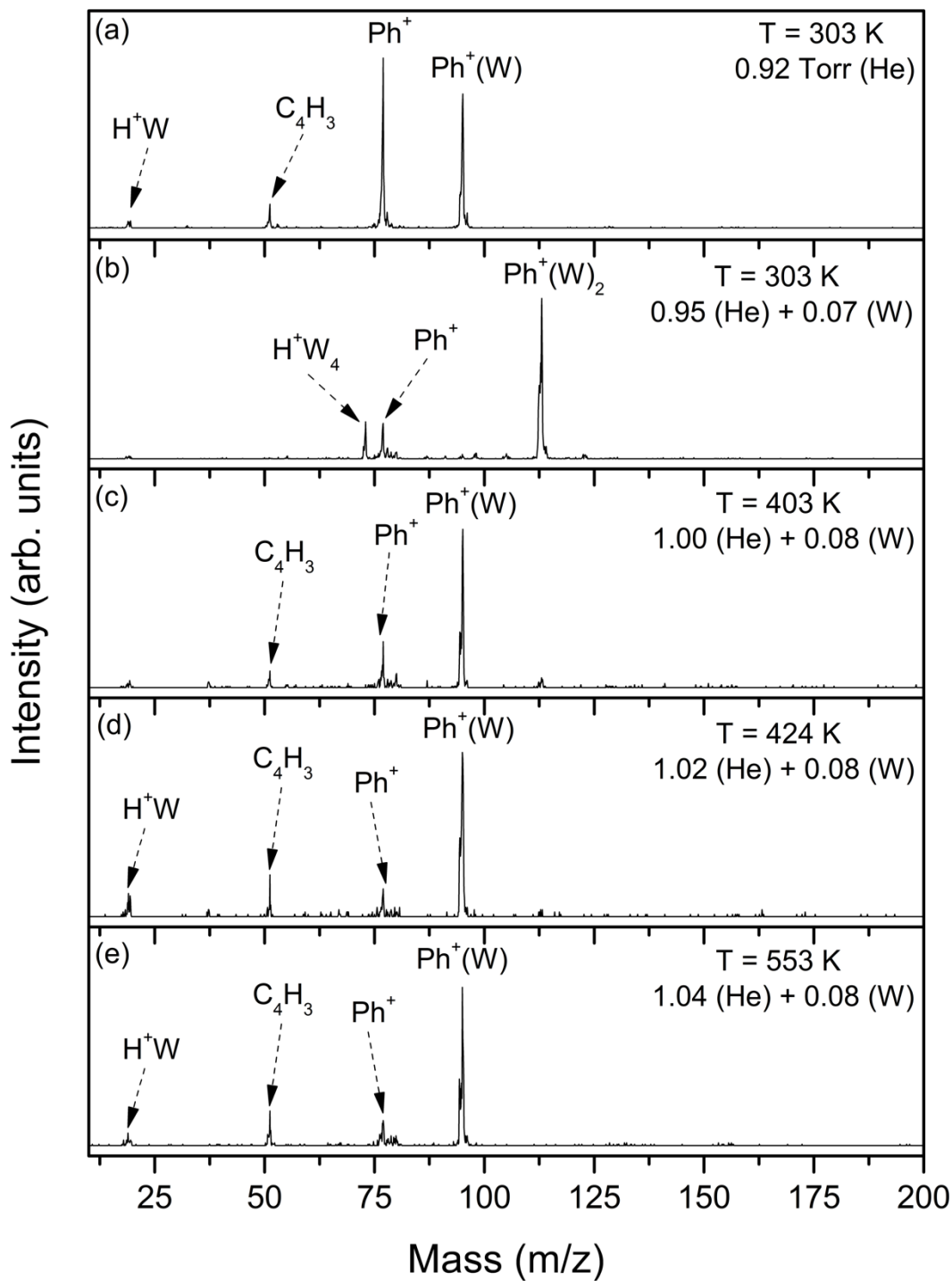


Figure 82. Mass spectra resulting from the injection of the mass-selected phenyl cation (C_6H_5^+ , Ph^+) into He gas (a) or He/water (W) vapor mixture (b-e) at different pressures (Torr) and increasing temperatures (K) as indicated.

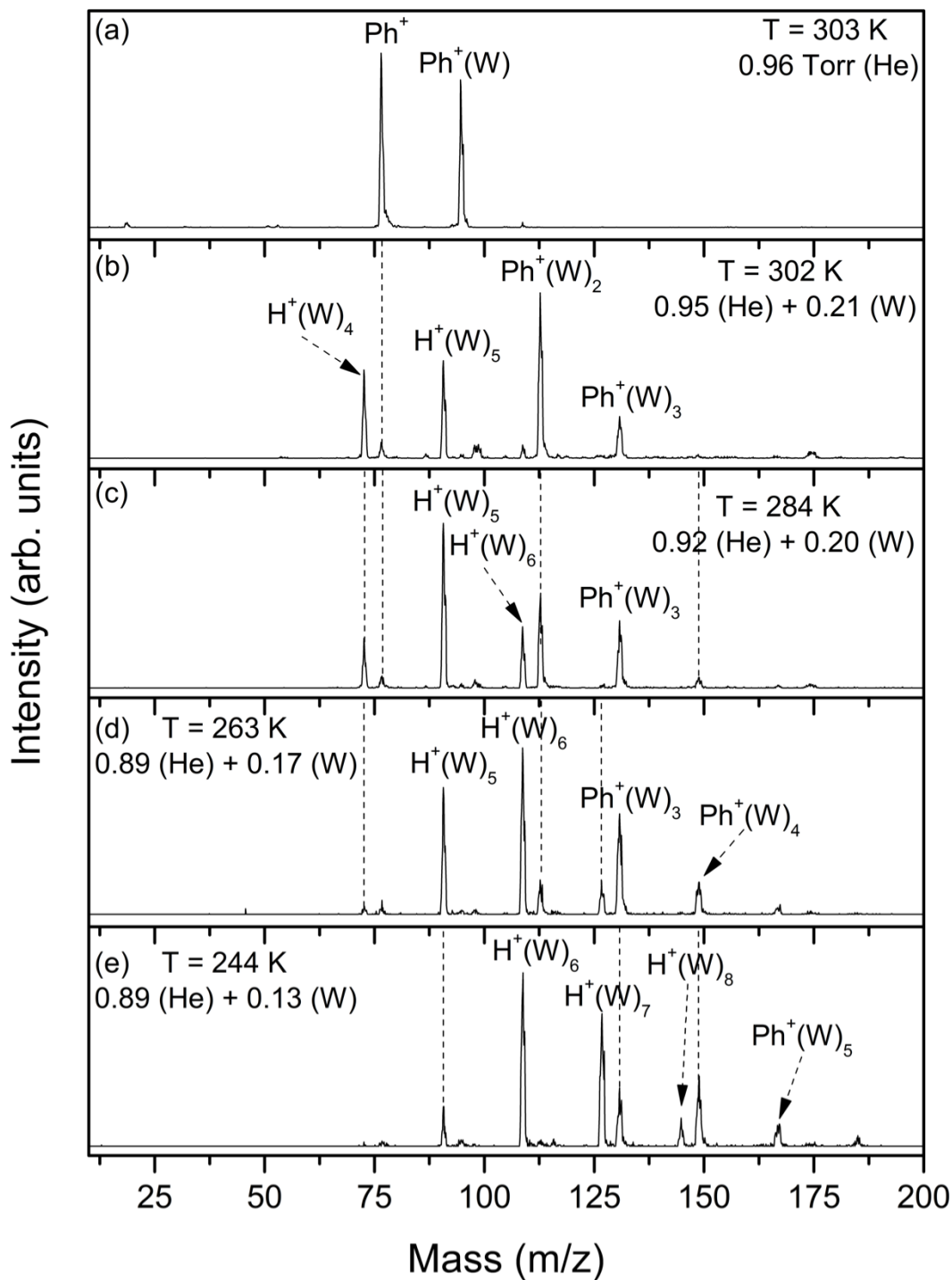


Figure 83. Mass spectra resulting from the injection of the mass-selected phenyl cation (C_6H_5^+ , Ph^+) into He gas (a) or He/water (W) vapor mixture (b-e) at different pressures (Torr) and decreasing temperatures (K) as indicated.

Figure 83b-e shows the mass spectra obtained when the drift cell containing He-water vapor gas mixture was cooled from 302 K to 244 K which is just above the point where water freezes in the drift cell. Unlike in Figure 82 where the lowest possible pressure of water is used to observe the first few hydration products, higher water pressure is used to observe higher hydration products prior to freezing the water vapor. In presence of 0.20 Torr water vapor at 302 K the hydration products $C_6H_5^+(H_2O)_n$, Ph^+W_n , for $n = 2-3$ along with small intensities of Ph^+ and protonated water clusters H^+W_n for $n = 4-5$ are observed as shown in Figure 83b. As the temperature decreases, higher association products Ph^+W_n for $n = 3-4$ are observed, but protonated water clusters become the predominant species present. At 244 K (just above the point where water freezes in the drift cell), the fifth hydration product begins to form as well as the protonated water clusters H^+W_n for $n = 5-9$ as shown in Figure 83e.

The equilibrium constants are measured for Equation 7.5 using Equation 7.2 by using the peak intensities of the stepwise hydration of $C_6H_5^+$ at different temperatures from Equation 3.5 with the resulting van't Hoff plots shown in Figure 84. The resulting $-\Delta H^\circ$ and $-\Delta S^\circ$ values are displayed in Table 13. A covalent structure is formed by the addition of H_2O to the $C_6H_5^+$ ion as well as a Noncovalent structure takes place. The covalent structure is lower in abundance, but due to its presence, the equilibrium for the first addition is disturbed and thus thermochemistry measurements could no be performed. The van't Hoff plot for the second hydration product of the phenyl cation has two distinct regions (Figure 84a), a low temperature region (288-373 K) and a high temperature region (373-423K). In the low temperature region, the $-\Delta H^\circ$ and $-\Delta S^\circ$ values for the formation of the second hydration product are $15.5 \pm 1 \text{ kcal mol}^{-1}$ and $25.7 \pm 2 \text{ cal mol}^{-1} \text{ K}^{-1}$. In the higher temperature region, the $-\Delta H^\circ$ and $-\Delta S^\circ$ values increase to $18.7 \pm 1 \text{ kcal mol}^{-1}$ and $33.2 \pm 2 \text{ cal mol}^{-1} \text{ K}^{-1}$. This increase can be explained by the fact that there is a mixture of the hydrated

covalent protonated phenol product of Equation 7.4 ($C_6H_5OH_2^+(H_2O)$) and the reversible IHB product of Equation 7.5 ($C_6H_5^+(H_2O)_2$). In both regions, the hydrated covalent protonated phenol product is present, but in the high temperature region, the IHB product is almost completely dissociated resulting in the increased $-\Delta H^\circ$ value. The measured $-\Delta H^\circ$ value for the first hydration product of protonated phenol, $17.3 \pm 1.6 \text{ kcal mol}^{-1}$, is similar to the values observed in the high temperature $-\Delta H^\circ$ for the second hydration product of the phenyl cation.²¹⁹ This supports the notion that water forms a covalent bond with the phenyl cation to form a protonated phenol cation.

Figure 84b displays the van't Hoff plots for the third and fourth hydration products of the phenyl cation with the values for $-\Delta H^\circ$ and $-\Delta S^\circ$ summarized in Table 13. The measured $-\Delta H^\circ$ and $-\Delta S^\circ$ for the formation of the third hydration product of the phenyl cation are $11.0 \pm 1 \text{ kcal mol}^{-1}$ and $22.9 \pm 2 \text{ cal mol}^{-1} \text{ K}^{-1}$ and $10.8 \pm 1 \text{ kcal mol}^{-1}$ and $26.4 \pm 2 \text{ cal mol}^{-1} \text{ K}^{-1}$ for the fourth hydration product. The lower binding energies using the $-\Delta H^\circ$ values and observation of these products at lower temperature suggest that subsequent water molecules do not bind covalently to the first hydration product and instead form IHBs. The similar $-\Delta H^\circ$ would suggest that water has multiple binding sites around the hydrated phenyl cation with relatively similar binding energies.

Table 13. Measured thermochemistry ($-\Delta H^\circ$ and $-\Delta S^\circ$)^a for the stepwise hydration of $C_6H_5^+(H_2O)_n$ clusters for $n = 2-4$.

$C_6H_5^+(H_2O)_n$	$-\Delta H^\circ$ (kcal mol ⁻¹)	$-\Delta S^\circ$ (cal mol ⁻¹ K ⁻¹)
2 (288-373 K)	15.5	25.7
2 (373-423 K)	18.7	33.3
3	11.0	22.9
4	10.8	26.4

^a Units, estimated error: $\Delta H^\circ \pm 1 \text{ kcal mol}^{-1}$ and $\Delta S^\circ \pm 2 \text{ cal mol}^{-1} \text{ K}^{-1}$

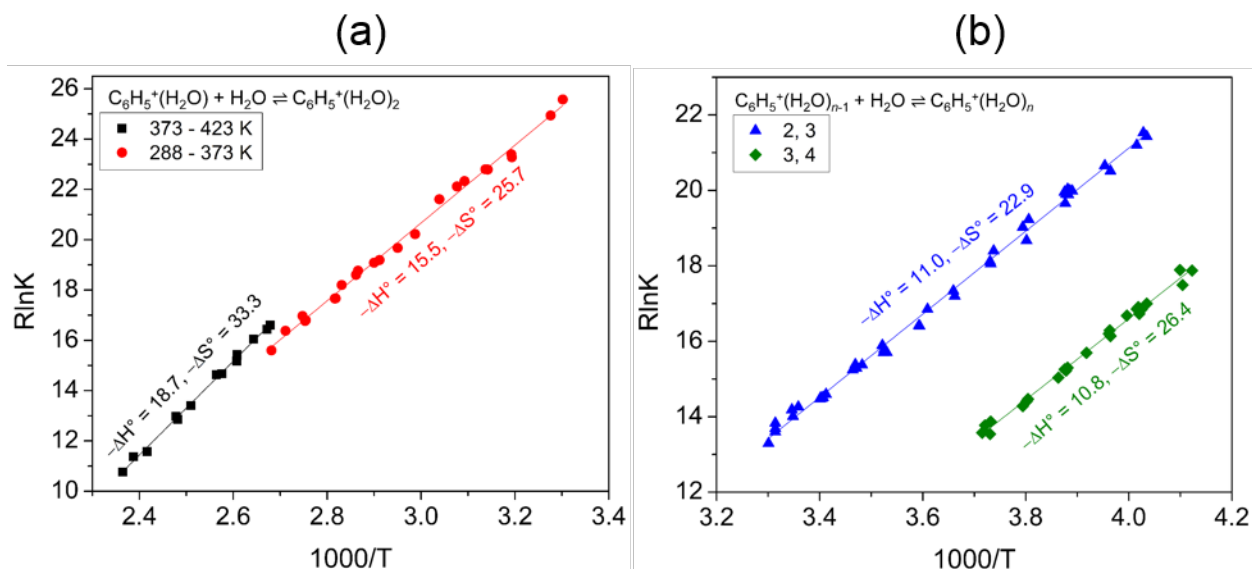


Figure 84 van't Hoff plots for the temperature dependence of the equilibrium constants of the association reaction of phenyl cation with water where (a) shows the first hydration product and the presence of two separate species and (b) shows the second and third hydration products. The resulting $-\Delta H^\circ$ and $-\Delta S^\circ$ are in (kcal mol^{-1}) and ($\text{cal mol}^{-1} \text{K}^{-1}$) respectively. The experimental error for these measurements are $\pm 1 \text{ kcal mol}^{-1}$ and $\pm 2 \text{ cal mol}^{-1} \text{K}^{-1}$.

7.4.1.2. Calculated Structures of the Hydrated Phenyl Cation with 1-5 Water Molecules

To help explain the thermochemistry results, structures for the first four hydration products for Equations 7.4 and 7.5 were calculated at the B3LYP/6-311++G**level. These reactions demonstrate the two possible pathways for the addition of the first water to the phenyl cation and the products of these reactions are shown in Figure 85. Figure 85a displays the covalent protonated phenol structure with a binding energy, ΔE , of $43.0 \text{ kcal mol}^{-1}$, which would explain the presence of the Ph^+W in the high temperature mass spectra of Figure 82. Structures where the water forms an ionic hydrogen bond (IHB) with the a CH hydrogen in the *ortho* or *para* positions are shown in Figure 85b and Figure 85c and have much lower binding energies of $\Delta E = 7.9\text{-}11.3 \text{ kcal mol}^{-1}$. Such structures would not be present at high temperatures, but could be present at lower temperatures resulting in the possibility of a mixture of different structures leading to products shown in Equation 7.5. The differences between the covalent and noncovalent structures are roughly 32 kcal mol^{-1} , which is explains the lack of equilibrium for thermochemistry measurements.

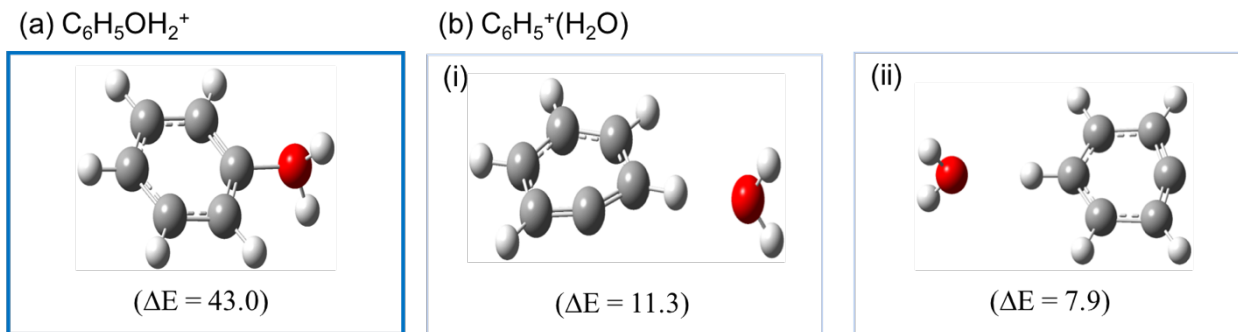


Figure 85. DFT Structures and binding energies (ΔE , kcal mol⁻¹) for (a) the formation of the covalent protonated phenol cation ($C_6H_5OH_2^+$) and (b) the addition of a water to the phenyl cation at the (i) *ortho* and (ii) *para* positions, represented as $C_6H_5^+(H_2O)$. Both sets are obtained at the B3LYP/6-311++G** level.

The structures of the second hydration product are shown in Figure 86 where the second water binds to the covalent protonated phenol cation structure (Figure 86a) or the structure where the second water forms an IHB with the hydrated phenyl cation (Figure 86b). When the second water binds to the hydrogen of the OH of the protonated phenol (Figure 86a) the calculated binding energy, ΔE , is 25.9 kcal mol⁻¹. When the water binds to the $C_6H_5OH_2^+$ at the *para*-CH hydrogen, the calculated binding energy, ΔE , drastically decreases to 5.4 kcal mol⁻¹. When the second water adds to the hydrated phenyl cation via “*internal solvation*” at the *ortho*-CH hydrogen opposite the initial IHB as in Figure 86a, the calculated binding energy is 10.1 kcal mol⁻¹. In the case where the second water adds to the hydrated phenyl cation via “*external solvation*” forming an H-bonded chain of water molecules similar to the structures of $C_{10}H_8^+(H_2O)_n$ clusters, the binding energy is 9.9 kcal mol⁻¹ as shown in Figure 86b which is nearly identical to the “*internally solvated*” structure.⁵⁶ Compared to the experimental $-\Delta H^\circ$ values of $15.5-18.7 \pm 1$ kcal mol⁻¹, no single structure appears to be present. Instead a mixture of the $C_6H_5OH_2^+(H_2O)$ and $C_6H_5^+(H_2O)_2$ appears to be present with the ratio of the two classes of structures changing at 373 K resulting in an increase in the experimental $-\Delta H^\circ$ value. It should be noted that the difference in the binding

energies between the two classes of molecules is 16 kcal mol⁻¹. This is a large decrease from the initial addition of water resulting in the formation of the protonated phenol product.

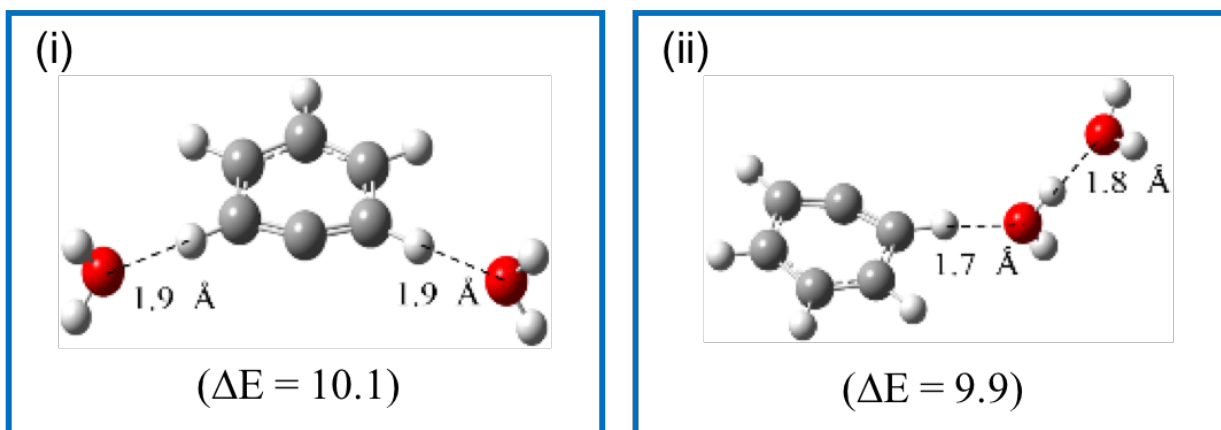
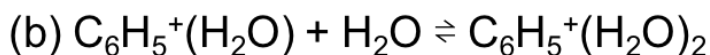
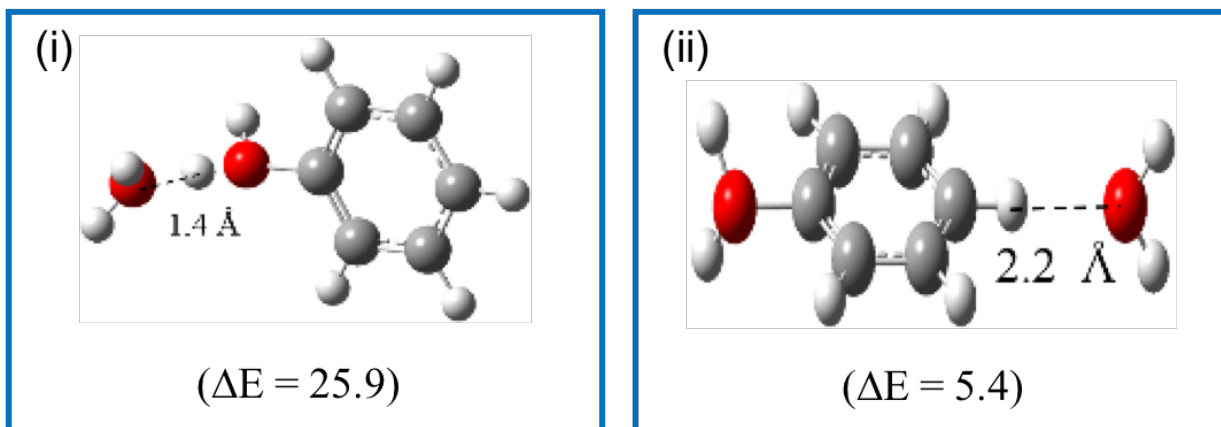


Figure 86. DFT Structures and binding energies (ΔE , kcal mol⁻¹) for (a) addition of a water molecule to the covalent protonated phenol and (b) the addition of a water to the hydrated phenyl cation. Both sets are obtained at the B3LYP/6-311++G** level.

The calculated structures for the third addition of water to the phenyl cation are shown in Figure 87 with the $\text{C}_6\text{H}_5\text{OH}_2^+(\text{H}_2\text{O})_2$ structures shown in Figure 87a and the $\text{C}_6\text{H}_5^+(\text{H}_2\text{O})_3$ structures shown in Figure 87b. Both low energy structures for the $\text{C}_6\text{H}_5\text{OH}_2^+(\text{H}_2\text{O})_2$ isomer have the third water add via “*external solvation*” where the third water adds to either the second OH hydrogen of the protonated phenol cation (Figure 87a) or forming a H-bonded chain of water

molecules similar to that seen in $C_{10}H_8^{*+}(H_2O)_3$ (Figure 87b).⁵⁶ The calculated ΔE values for these $C_6H_5OH_2^+(H_2O)_2$ structures are 19.6 and 17.8 kcal mol⁻¹ for Figure 87a and Figure 87b respectively. These calculated binding energies, ΔE , are higher than those for the $C_6H_5^+(H_2O)_3$ isomer where the structures are shown in Figure 87b. A mixed “*internally*” and “*externally solvated*” $C_6H_5^+(H_2O)_3$ structure is shown in Figure 87a and has a calculated ΔE of 9.2 kcal mol⁻¹ where the third water begins to form a H-bonded chain with one of the water molecules in the $C_6H_5^+(H_2O)_2$ structure. A completely “*internally solvated*” structure shown in Figure 87b where the third water forms an IHB with the *meta* CH hydrogen of the phenyl cation. This isomer has a lower binding energy of $\Delta E = 6.9$ kcal mol⁻¹ compared to the other structures shown for the third hydration product of the phenyl cation. With an experimental $-\Delta H^\circ$ value of 11.0 ± 1 kcal mol⁻¹, the structure of the third hydration product of phenyl appears to be a mixture of various $C_6H_5OH_2^+(H_2O)_2$ and $C_6H_5^+(H_2O)_3$ isomers with the noncovalent structure being the predominant species present. The differences in the binding energies between the covalent and noncovalent isomers for the third addition of water to the phenyl cation continues to decrease where for the third addition this addition is 10 kcal mol⁻¹.

The calculated structures for the fourth solvation product of the phenyl cation are shown in Figure 88. The structures for the $C_6H_5OH_2^+(H_2O)_3$ isomer are shown in Figure 88a where the low energy structure, shown in Figure 88a, appears to be “*externally solvated*.” Here the fourth water continues the H-bonded chain of the third hydration product with a binding energy, ΔE , of 13.7 kcal mol⁻¹. Higher energy structures, shown in Figure 88b and Figure 88c, have a mixed “*internally*” and “*externally solvated*” structure, with calculated binding energies much lower than the H-bonded chain. The values of these ΔE are 4.2 and 3.7 kcal mol⁻¹ for Figure 88b and Figure 88c respectively. The calculated ΔE values for the fourth IHB hydration product of

the phenyl cation, $C_6H_5^+(H_2O)_4$, range from 6.0-8.9 kcal mol⁻¹ for the various isomers (Figure 88b). The difference between the ΔE values for $C_6H_5OH_2^+(H_2O)_3$ and $C_6H_5^+(H_2O)_4$ structures is much lower (4.8 kcal mol⁻¹) than that observed in lower hydration products. This suggests that with further additions of water, the presence of a covalent bond for the initial hydration product becomes negligible. The binding of additional water molecules to the $C_6H_5OH_2^+(H_2O)_{n-1}$

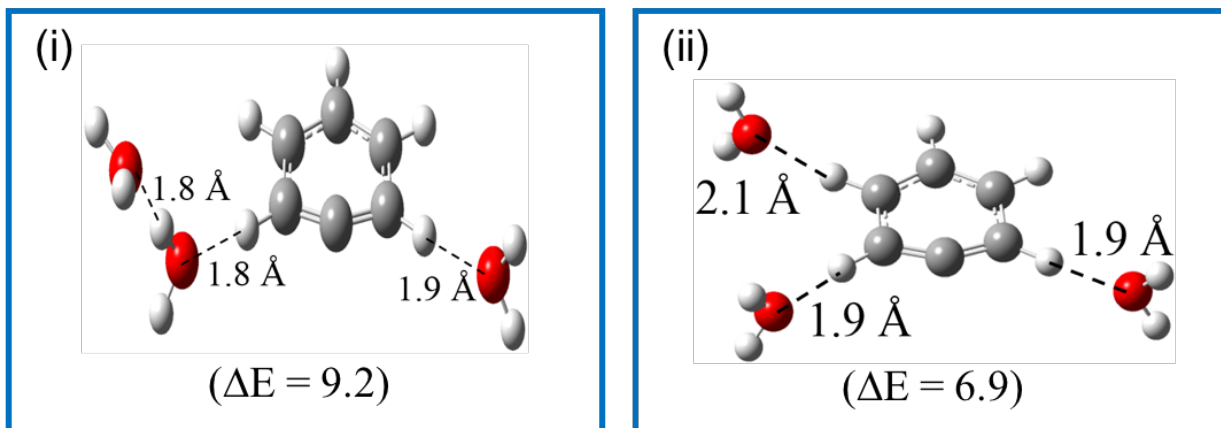
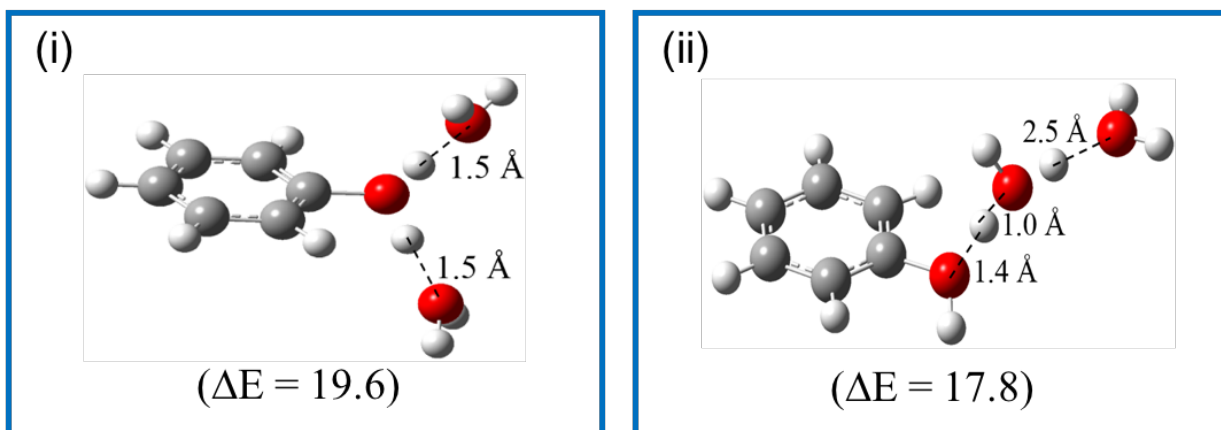
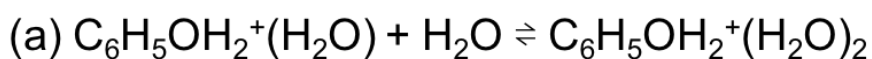


Figure 87. DFT Structures and binding energies (ΔE , kcal mol⁻¹) for (a) addition of a second water molecule to the covalent protonated phenol and (b) the addition of a third water to phenyl cation. Both sets are obtained at the B3LYP/6-311++G** level.

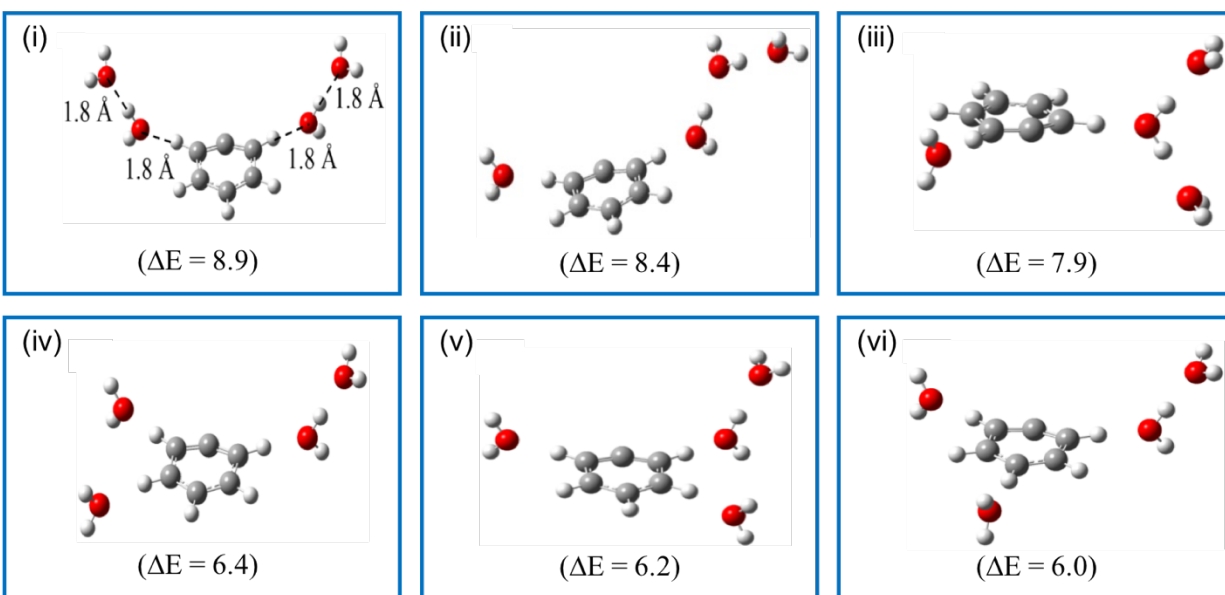
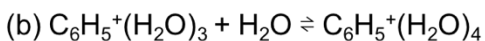
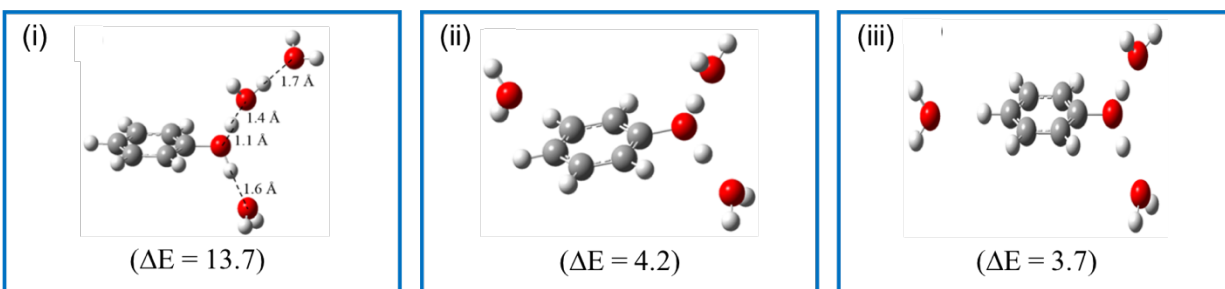
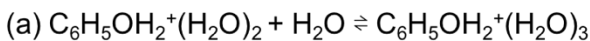


Figure 88. DFT Structures and binding energies (ΔE , kcal mol⁻¹) for (a) addition of a third water molecule to the covalent protonated phenol and (b) the addition of a fourth water to phenyl cation. Both sets are obtained at the B3LYP/6-311++G** level.

7.4.2. Thermochemistry Results for the Association of CH₃OH with the Phenyl Cation

The mass spectra obtained following the injection of the mass-selected phenyl cation (generated from the fragmentation of bromobenzene) ($C_6H_5^+$, Ph^+) into the drift cell containing He or a He/methanol (CH_3OH , M) vapor mixture are shown in Figure 89-Figure 90. When the mass-selected phenyl cation is injected into He, shown in Figure 89a and Figure 90a, the Ph^+ peak at $m/z = 77$ is the major peak along with protonated water and the first hydration product Ph^+W due to the residual water in the drift cell as observed in Figure 81. Upon injection the phenyl cation into the drift cell containing 0.09 Torr methanol (CH_3OH , M), the fourth protonated methanol

cluster at $m/z = 129$ is the major peak with the Ph^+ and first association product of phenyl cation with methanol (Ph^+M) at $m/z = 97$. A second series of peaks is also present in the mass spectra where the methanol appears to bind with the protonated phenol ion forming the first three association products, Ph^+MW , $\text{Ph}^+(\text{M})_2\text{W}$, and $\text{Ph}^+(\text{M})_3\text{W}$, at $m/z = 127$, 159, and 191 respectively. As the temperature of the drift cell increases, the higher association products dissociate and at 374K, the third protonated methanol cluster, H^+M_3 , and first association product of methanol to the protonated phenol, Ph^+MW at $m/z = 97$ and 127 respectively are nearly equal in intensity as shown in Figure 89c. At 525 K, shown in Figure 89e, the major peaks are the protonated methanol dimer and the protonated phenol cation with the phenyl cation and first association product of methanol to the phenyl cation are minor peaks.

When the phenyl cation is injected into the drift cell containing 0.15 Torr methanol at 299K, shown in Figure 90b, the first three association products of methanol to the phenyl cation, Ph^+M , Ph^+M_2 , and Ph^+M_3 ($m/z = 109$, 141, and 173 respectively), are present as well as the protonated methanol clusters and association products of methanol to the protonated phenol cation. Interestingly, at 273 K, the Ph^+M_3 disappears and the fifth protonated methanol cluster is the major ion. In addition, the major series containing the phenyl cation are methanol association products to the first hydration product of the phenyl cation. Subsequent cooling of the drift cell resulted in protonated methanol clusters as the major peak series for $\text{H}^+(\text{M})_n$ for $n = 5-7$ and at 243 K, Figure 90e, the first three association products of methanol to the phenyl cation are again present as minor peaks.

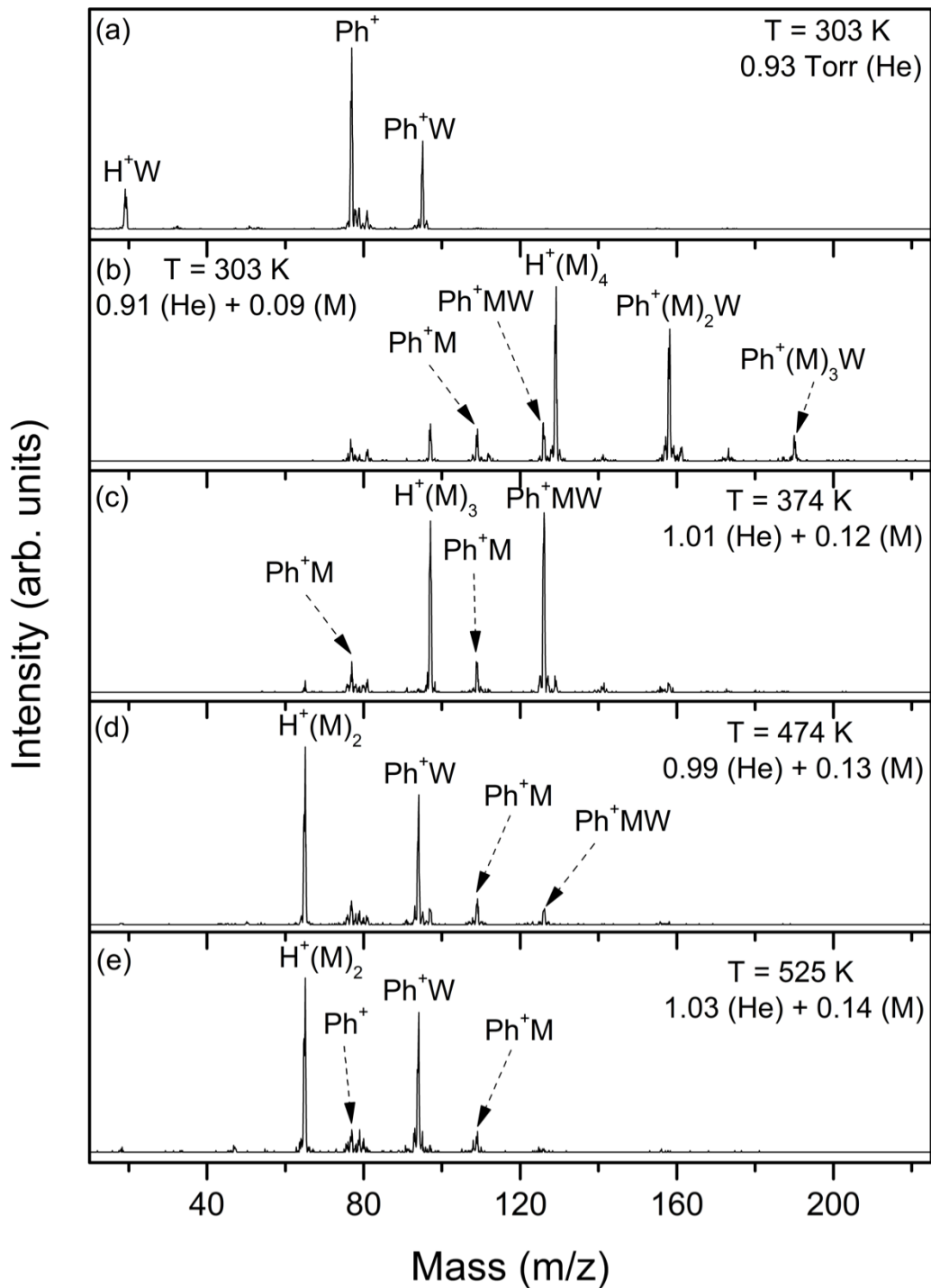


Figure 89. Mass spectra resulting from the injection of the mass-selected phenyl cation (C_6H_5^+ , Ph^+) into He gas (a) or He/methanol (M) vapor mixture (b-e) at different pressures (Torr) and increasing temperatures (K) as indicated.

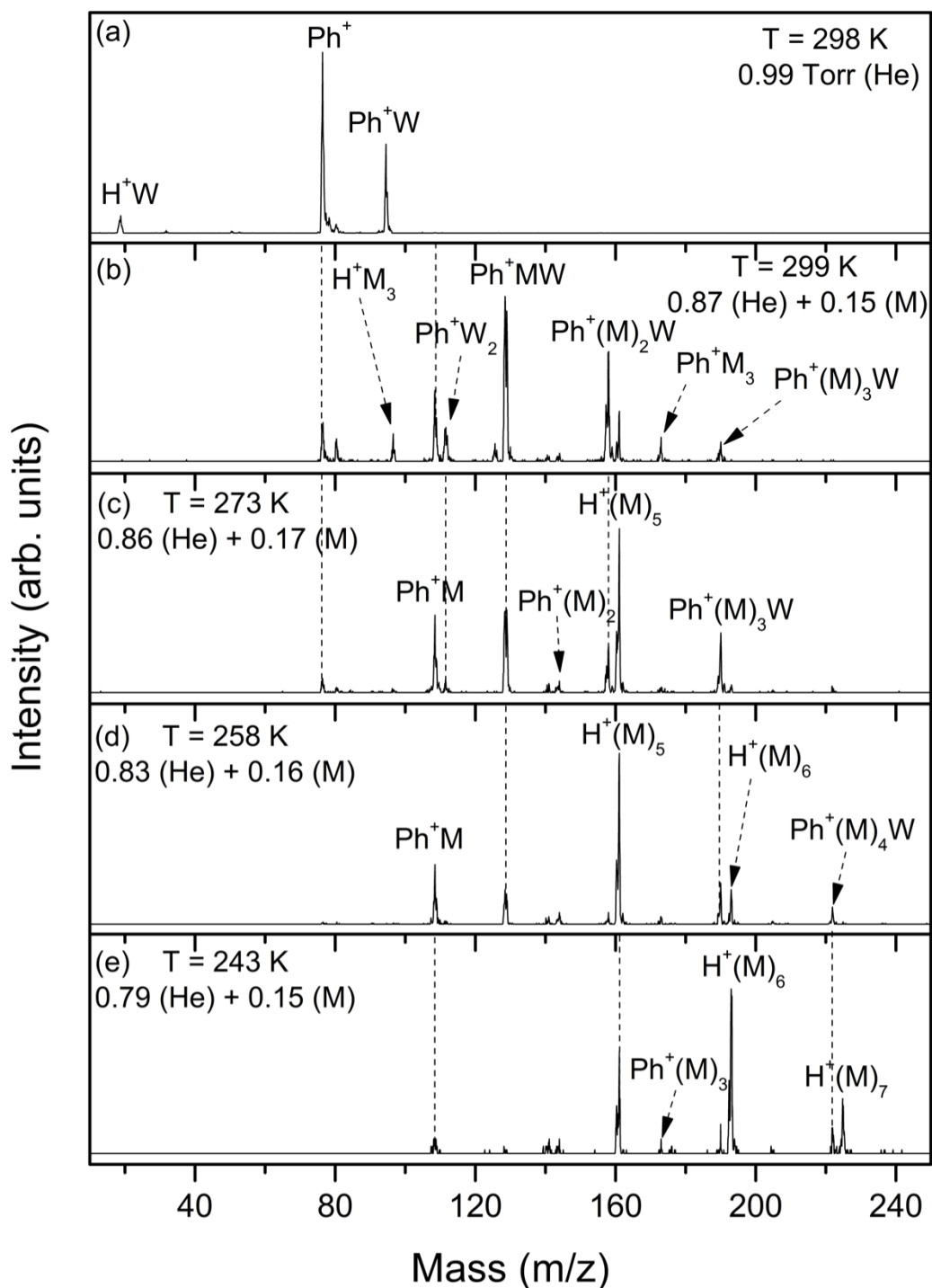
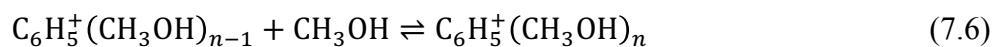


Figure 90. Mass spectra resulting from the injection of the mass-selected phenyl cation (C_6H_5^+ , Ph^+) into He gas (a) or He/methanol (M) vapor mixture (b-e) at different pressures (Torr) and decreasing temperatures (K) as indicated.

The equilibrium constant measurements for the association of methanol molecules with the phenyl cation is represented by Equation 7.6:



These measurements will be repeated and published together with the DFT calculations for the $\text{C}_6\text{H}_5^+(\text{CH}_3\text{OH})_n$ clusters. Comparisons will be made for the IHB $\text{C}_6\text{H}_5^+(\text{CH}_3\text{OH})_n$ clusters and the covalent $\text{C}_6\text{H}_5\text{OHCH}_3(\text{CH}_3\text{OH})_{n-1}$ clusters.

7.4.3. Thermochemistry Results for the Association of HCN with the Phenyl Cation

The mass spectra obtained following the injection of the mass-selected phenyl cation (generated from the fragmentation of bromobenzene) (C_6H_5^+ , Ph^+) into the drift cell containing He or a He/HCN gas mixture are shown in Figure 91-Figure 92. When the mass-selected phenyl cation is injected into He, shown in Figure 91a and Figure 92a, the Ph^+ peak at $m/z = 77$ is the major peak along with protonated water and the first hydration product Ph^+W due to the residual water in the drift cell as observed in Figure 81. Upon injection of the phenyl cation into 0.13 Torr HCN at 306K, the first and second association product of HCN to the phenyl cation, $\text{Ph}^+(\text{HCN})$ and $\text{Ph}^+(\text{HCN})_2$, at $m/z = 104$ and 131 respectively are present along with protonated HCN as a minor peak as shown in Figure 91b. At 411 K, $\text{Ph}^+(\text{HCN})_2$ completely dissociates to $\text{Ph}^+(\text{HCN})$, Figure 91c, but even at 573 K, Figure 91f, the first association product $\text{Ph}^+(\text{HCN})$ does not dissociate to Ph^+ . This suggests that the first HCN molecule binds to the phenyl cation via a covalent bond forming a structure that is similar to protonated phenyl isocyanide. These results are similar to what is observed in water and methanol.

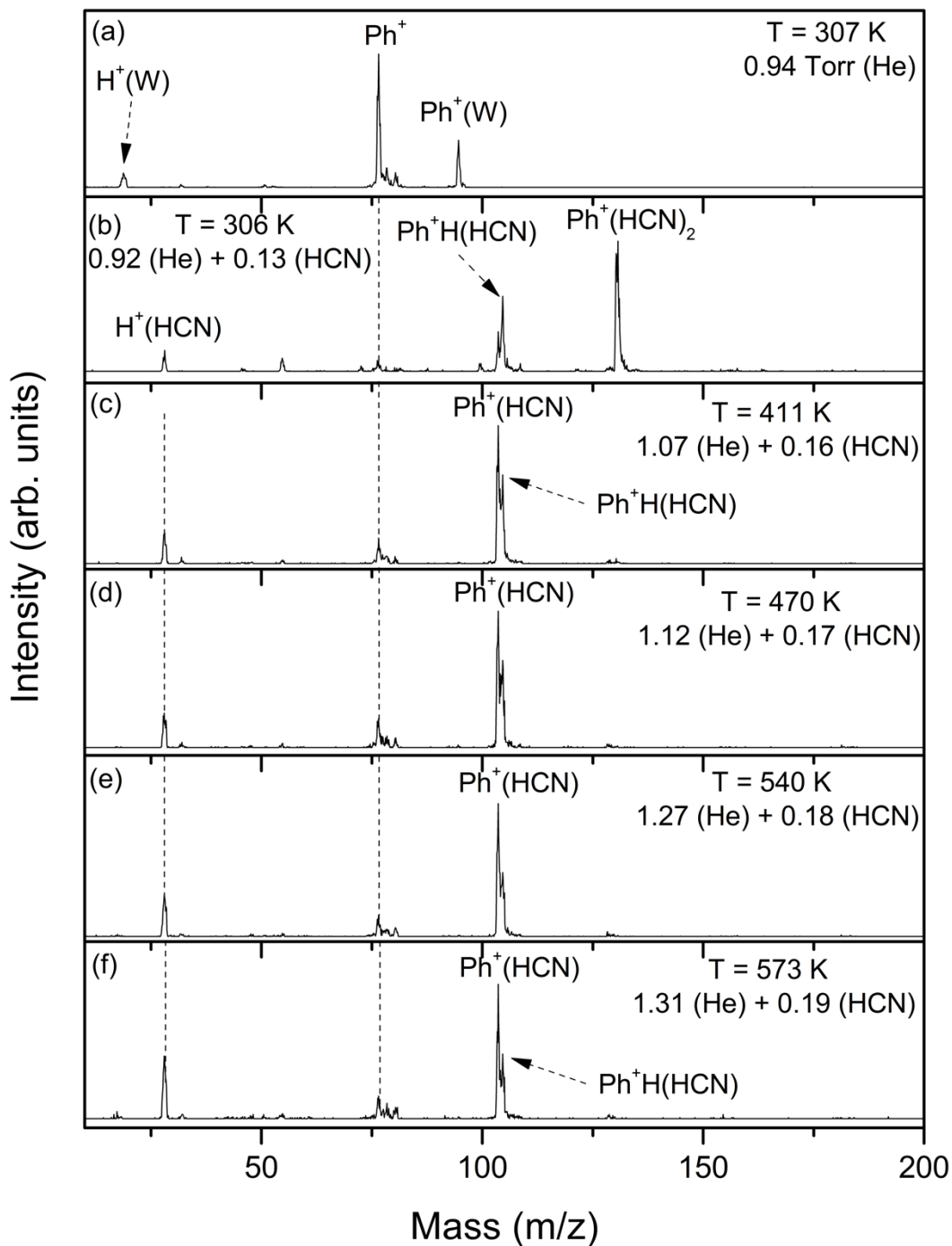


Figure 91. Mass spectra resulting from the injection of the mass-selected phenyl cations (C_6H_5^+ , Ph^+) into He gas (a) or He/HCN gas mixture (b-f) at different pressures (Torr) and increasing temperatures (K) as indicated.

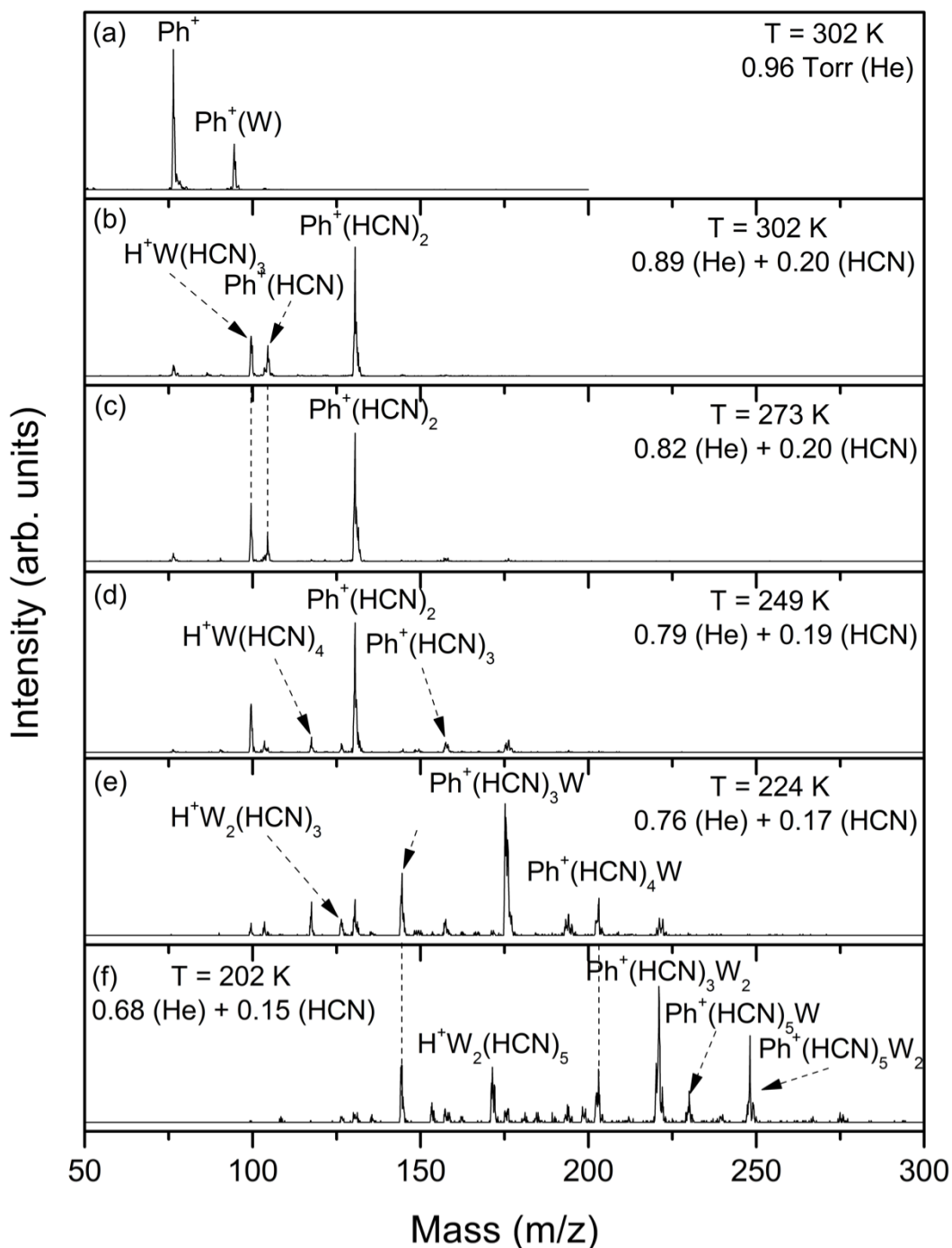


Figure 92. Mass spectra resulting from the injection of the mass-selected phenyl cations (C_6H_5^+ , Ph^+) into He gas (a) or He/HCN gas mixture (b-f) at different pressures (Torr) and decreasing temperatures (K) as indicated.

When the drift cell is cooled, the $\text{Ph}^+(\text{HCN})_n$ series is dominant with $n = 1-4$ appearing over the course of the study as shown in Figure 92. A second series of mixed water and HCN association products with the phenyl cation [$\text{Ph}^+(\text{HCN})_n\text{W}_m$] become the predominant series at 224K as shown in Figure 92e with the $\text{Ph}^+(\text{HCN})_3\text{W}$ being the major peak. After the $\text{Ph}^+(\text{HCN})_5\text{W}$ product forms, water begins to add a second addition, $\text{Ph}^+(\text{HCN})_5\text{W}_2$ at 202 K as shown in Figure 92f. This characterization would indicate that the complete first solvation layer of HCN to the protonated phenol cation forms after the fifth solvation step and for subsequent additions, water has preferential binding.

The association reaction of HCN to the phenyl cation is represented by Equation 7.7:



The equilibrium constants were measured for the reaction shown in Equation 7.7 using Equation 7.2 by obtaining the peak intensities of the $\text{Ph}^+(\text{HCN})$, $\text{Ph}^+(\text{HCN})_2$, $\text{Ph}^+(\text{HCN})_3$, and $\text{Ph}^+(\text{HCN})_4$ products and the pressure of HCN in the drift cell. The equilibrium constants at different temperatures were used to produce van't Hoff plots for the formation of $\text{Ph}^+(\text{HCN})_2$, $\text{Ph}^+(\text{HCN})_3$, and $\text{Ph}^+(\text{HCN})_4$ clusters using Equation 3.5 as shown in Figure 93. The resulting $-\Delta H^\circ$ and $-\Delta S^\circ$ values for Equation 7.7 obtained from the slope and intercept of the van't Hoff plots. Due to a lack of dissociation of the initial $\text{C}_6\text{H}_5^+(\text{HCN})$ product to C_6H_5 , the thermochemistry could not be measured. With each addition of HCN to the phenyl cation, the $-\Delta H^\circ$ value decreases indicating multiple binding sites with decreasing energy to create the first solvation layer. The second HCN molecule binds to the covalent $\text{Ph}^+(\text{HCN})$ forming $\text{Ph}^+(\text{HCN})_2$ with a $-\Delta H^\circ$ and $-\Delta S^\circ$ of 13.1 ± 1 kcal mol⁻¹ and 22.9 ± 2 cal mol⁻¹ K⁻¹ respectively. The binding energy greatly decreases for the third addition of HCN, $\text{Ph}^+(\text{HCN})_3$, where the $-\Delta H^\circ$ and $-\Delta S^\circ$ are 7.4 ± 1 kcal mol⁻¹ and 18.0 ± 2 cal mol⁻¹ K⁻¹. This large decrease in binding would suggest that by the third addition, there is little

difference in the binding energy of HCN solvation of the phenyl cation whether or not the initial addition is a covalent protonated phenyl isocyanide product or a noncovalent IHB structure. The fourth addition of HCN, $\text{Ph}^+(\text{HCN})_4$, binds with similar energies with a $-\Delta H^\circ$ of $6.0 \pm 1 \text{ kcal mol}^{-1}$ and a $-\Delta S^\circ$ of $13.8 \pm 2 \text{ cal mol}^{-1} \text{ K}^{-1}$. These results suggest that after the first two additions of HCN to the phenyl cation, the binding sites are relatively similar and results in the possibility of “external solvation” where the HCN can form a H-bonded chain of HCN molecules. DFT calculations can be used to determine the structures of the $\text{Ph}^+(\text{HCN})_n$ clusters as well as test the binding of water to the $\text{Ph}^+(\text{HCN})_n(\text{W})_m$ clusters for $n \geq 5$ and $m \geq 1$. In addition comparisons can be made between the covalent $\text{C}_6\text{H}_5\text{NCH}(\text{HCN})_{n-1}$ and noncovalent $\text{C}_6\text{H}_5(\text{HCN})_n$ clusters.

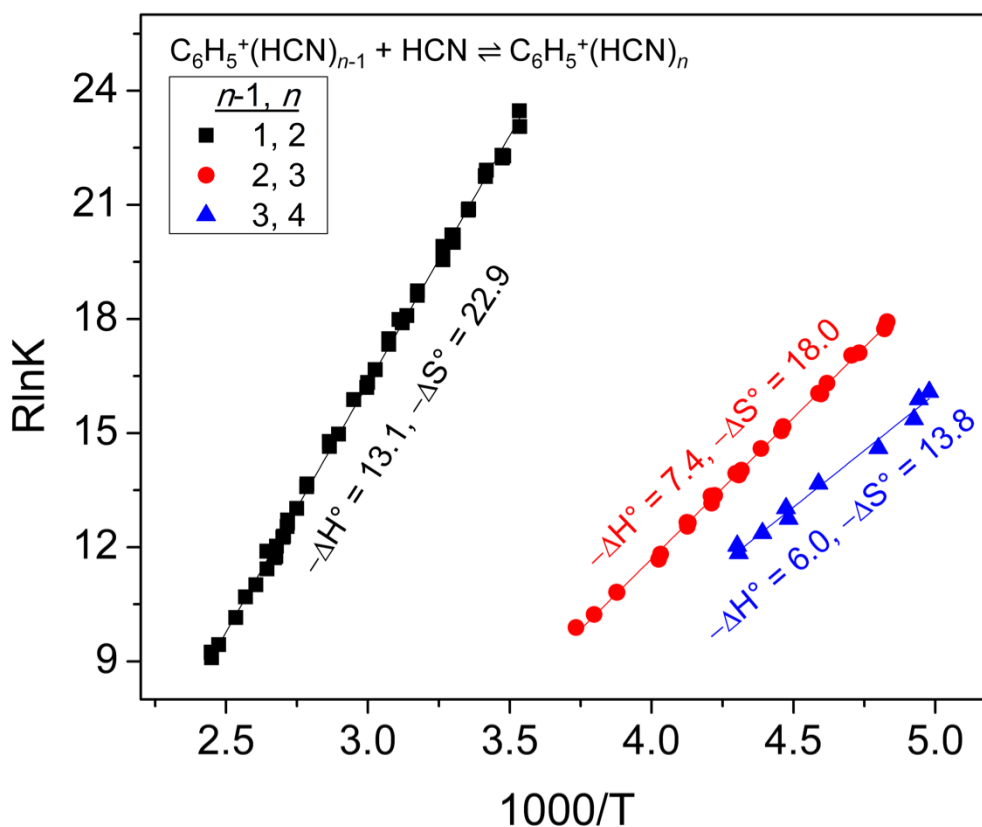


Figure 93. van't Hoff plot for the temperature dependence of the equilibrium constants of the association reaction of phenyl cation with HCN for the second, third, and fourth solvation products. The resulting $-\Delta H^\circ$ and $-\Delta S^\circ$ are in (kcal mol^{-1}) and ($\text{cal mol}^{-1} \text{ K}^{-1}$) respectively. The experimental error for these measurements are $\pm 1 \text{ kcal mol}^{-1}$ and $\pm 2 \text{ cal mol}^{-1} \text{ K}^{-1}$.

7.4.4. Thermochemistry Results for the Association of CH₃CN with the Phenyl Cation

The mass spectra obtained following the injection of the mass-selected phenyl cation (generated from the fragmentation of bromobenzene) ($C_6H_5^+$, Ph^+) into the drift cell containing He or a He/acetonitrile (CH_3CN , A) vapor mixture are shown in Figure 94-Figure 95. When the mass-selected phenylium ion is injected into He, shown in Figure 94a and Figure 95a, the Ph^+ peak at $m/z = 77$ is the major peak along with protonated water and the first hydration product Ph^+W due to the residual water in the drift cell as observed in Figure 81. Injecting the mass-selected phenyl cation into 0.61 Torr CH_3CN at 306 K resulted in the observation of the $Ph^+(A)$ and $Ph^+(A)_2$ products as shown in Figure 94b. Heating the drift cell resulted in the dissociation of the $Ph^+(A)_2$ cluster to $Ph^+(A)$ with complete dissociation by 379 K, Figure 94c. The $Ph^+(A)$ product did not dissociate into the parent ion, Ph^+ , even at 514 K, Figure 94f, indicating a strong covalent bond and a structure similar to *N*-phenylethanamine. Such results are similar to what was observed in other polar molecules studied.

When the drift cell is cooled, the ions of the $Ph^+(A)_n$ for $n = 1-4$ series are predominant along with protonated acetonitrile clusters. Mixed protonated water and acetonitrile clusters, $H^+W_mA_n$, were observed at 273 K as shown in Figure 95c. Unlike with methanol and HCN, acetonitrile appears to bind preferentially to the phenyl cation compared to the protonated phenol cation, but at 203 K, just above point at which the acetonitrile freezes as shown in Figure 95e, the $Ph^+W(A)_3$ product is present.

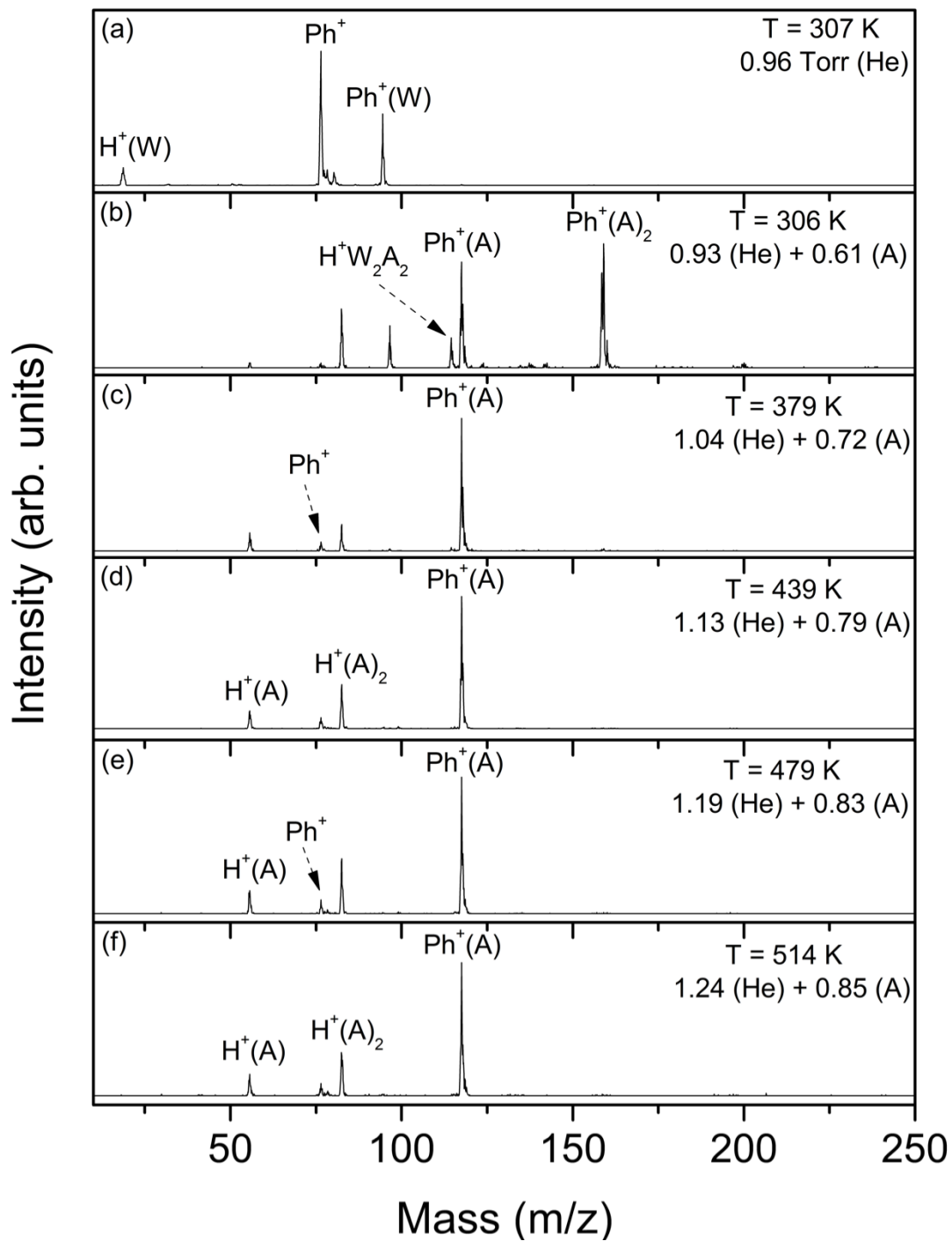


Figure 94. Mass spectra resulting from the injection of the mass-selected phenyl cation (C_6H_5^+ , Ph^+) into He gas (a) or He/acetone nitrile (CH_3CN , A) gas mixture (b-f) at different pressures (Torr) and increasing temperatures (K) as indicated.

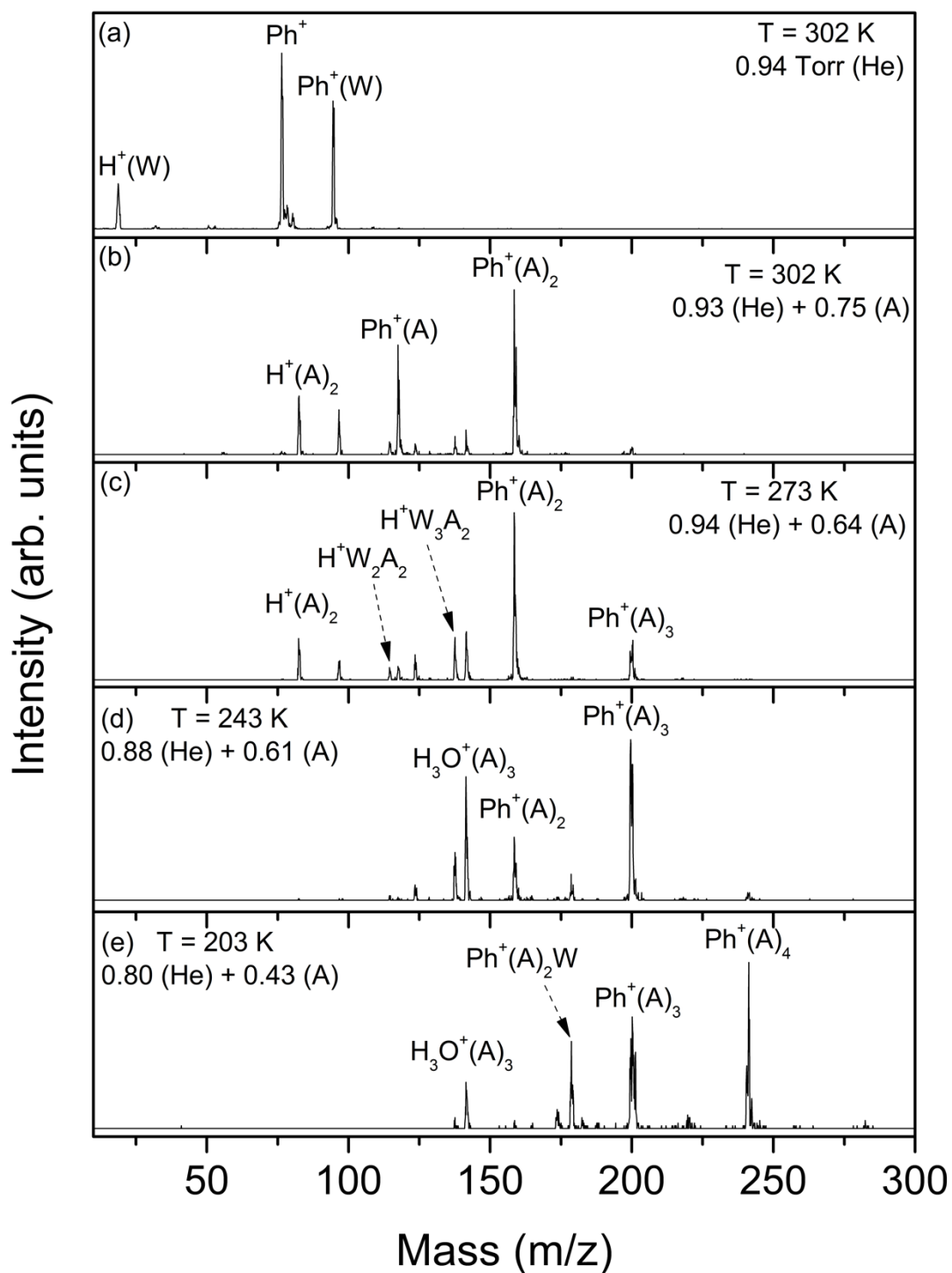
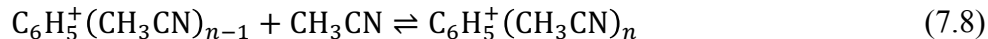


Figure 95. Mass spectra resulting from the injection of the mass-selected phenyl cation (C_6H_5^+ , Ph^+) into He gas (a) or He/acetone nitrile (CH_3CN , A) gas mixture (b-e) at different pressures (Torr) and decreasing temperatures (K) as indicated.

The association reaction of CH₃CN with the phenyl cation is represented by Equation 7.8:



The equilibrium constants were measured for Equation 7.8 using Equation 7.2 by obtaining the peak intensities of the Ph⁺(CH₃CN), Ph⁺(CH₃CN)₂, Ph⁺(CH₃CN)₃, and Ph⁺(CH₃CN)₄ products and the pressure of CH₃CN in the drift cell. The equilibrium constants at different temperatures were used to produce van't Hoff plots for the formation of Ph⁺(CH₃CN)₂, Ph⁺(CH₃CN)₃, and Ph⁺(CH₃CN)₄ clusters using Equation 3.5 as shown in Figure 96. The resulting -ΔH° and -ΔS° values for Equation 7.8 obtained from the slope and intercept of the van't Hoff plots. Similar to water, the second acetonitrile binding has binding that is dependent on the temperature of the drift cell. This would suggest that there is a difference in the ratio of the covalent vs. noncovalent structures present based on the temperature. At lower temperatures (253-324 K), the -ΔH° and -ΔS° are 9.2 ± 1 kcal mol⁻¹ and 11.1 ± 2 cal mol⁻¹ K⁻¹ respectively. At higher temperatures (340-390 K), the -ΔH° and -ΔS° values are 11.6 ± 1 kcal mol⁻¹ and 18.1 ± 2 cal mol⁻¹ K⁻¹. This would suggest that there is a mixture of structures for the Ph⁺(A) and Ph⁺(A)₂ products. Subsequent acetonitrile molecule binds with relatively similar energies as that measured at higher temperatures for Ph⁺(A)₂. The third acetonitrile binding with -ΔH° and -ΔS° values of -10.3 ± 1 kcal mol⁻¹ and 20.3 ± 2 cal mol⁻¹ K⁻¹ and the fourth acetonitrile binds with -ΔH° and -ΔS° values of 9.4 ± 1 kcal mol⁻¹ and 26.1 ± 2 cal mol⁻¹ K⁻¹. These similar binding energies would suggest multiple binding sites and the possibility of an H-bonded chain of acetonitrile with similar binding to form. In addition, the absence of a large drop in binding energy would suggest that the formation of a covalent bond in the first association step does not effect the binding of subsequent acetonitrile molecules to the phenyl cation. Just as observed with C₁₀H₈^{•+}(CH₃CN)_n clusters, the higher binding energies of acetonitrile compared to other polar molecules studied is due to the higher dipole moment of

acetonitrile compared to water, methanol, and hydrogen cyanide. The overlapping ATDs (Figure 97) for the first four association products of acetonitrile to the phenyl cation across several temperatures from 290 K to 233 K show that the reaction shown in Equation 7.7 is in equilibrium for the second-forth solvation steps.

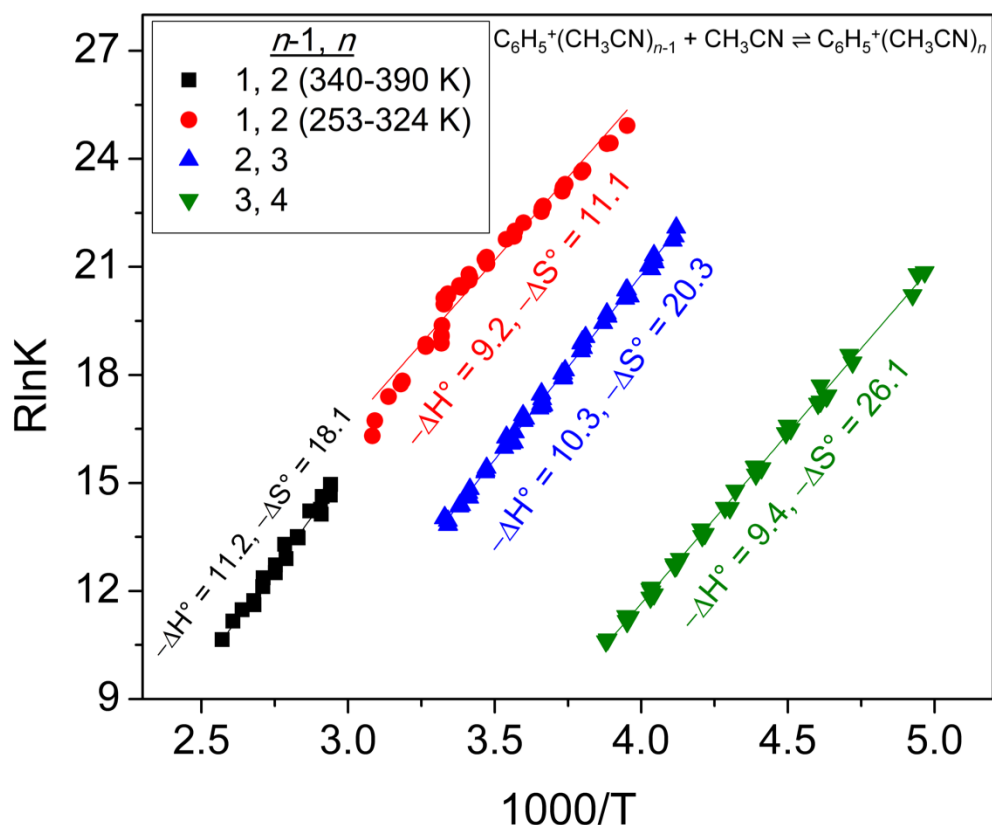


Figure 96. van't Hoff plot for the temperature dependence of the equilibrium constants of the association reaction of phenyl cation with acetonitrile for the second, third, and fourth solvation products. The resulting $-\Delta H^\circ$ and $-\Delta S^\circ$ are in (kcal mol^{-1}) and ($\text{cal mol}^{-1} \text{K}^{-1}$) respectively. The experimental error for these measurements are $\pm 1 \text{ kcal mol}^{-1}$ and $\pm 2 \text{ cal mol}^{-1} \text{K}^{-1}$.

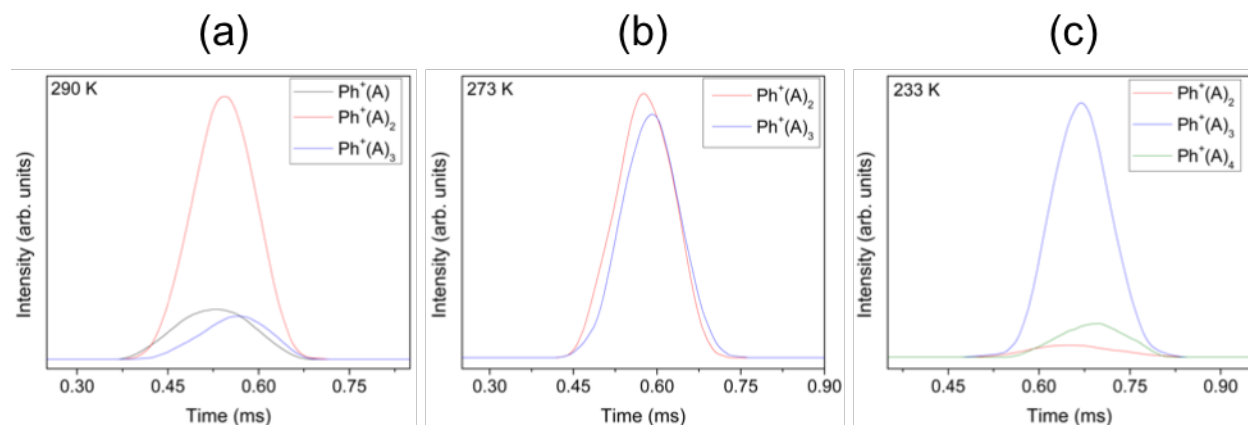


Figure 97. Arrival time distributions (ATDs) of the first four association products of the phenyl cation with acetonitrile (A), $C_6H_5^+(CH_3CN)_n$ for $n = 1-4$ ($Ph^+(A)_n$, $n = 1-4$), obtained following the injection of the mass-selected phenyl cation into He/ CH_3CN vapor mixtures at: (a) 290 K, (b) 273 K, and (c) 233 K. Similar ATD overlap suggests the reaction is in equilibrium.

7.4.5. Comparisons Between Interactions of Small Polar Molecules with the Phenyl Cation and Naphthalene Radical Cation

It is of interest to compare the association behaviors of small polar molecules such as water, methanol, hydrogen cyanide, and acetonitrile towards the phenyl cation with those of the naphthalene radical cation. One stark difference is that in the case of the naphthalene radical cation, the first polar molecule forms a bifurcated ionic hydrogen bond (IHB) with two $CH^{\delta+}$ hydrogens on the bicyclic naphthalene radical cation.^{56,57,67} The phenyl cation on the other hand appears to form a covalent bond with the small polar molecules due to the vacant sp^2 orbital on the aromatic ring. Subsequent steps in the solvation of the naphthalene radical cation with water and methanol tend to have similar binding energy due to the formation of a hydrogen bonded chain of water or methanol that is “*externally solvates*” the naphthalene radical cation.⁵⁶

For the association of HCN and acetonitrile with the naphthalene radical cation, the measured $-\Delta H^0$ decreases stepwise to 6-7 kcal mol⁻¹ by three HCN or CH_3CN molecules. This is of interest because this is the point where the $-\Delta H^0$ approaches the macroscopic enthalpy of vaporization, ΔH_{vap} , for liquid HCN and acetonitrile of 6.0 and 7.9 kcal mol⁻¹.^{2,57} For the phenyl cation, this occurs by four HCN molecules with the $Ph^+(HCN)_4$ cluster, but after four additions of

acetonitrile, the measured $-\Delta H^\circ$ is still $9.4 \text{ kcal mol}^{-1}$. This is still above the experimental error for the macroscopic ΔH_{vap} for acetonitrile.

The measured $-\Delta H^\circ$ for the association of water, methanol, and hydrogen cyanide to the phenyl cation also differs with that of the naphthalene radical cation in that the second polar molecule tends to bind at a higher $-\Delta H^\circ$ than the subsequent additions. This could be due to the second molecule forming an IHB with a hydrogen of the first molecule that is covalently bonded to the phenyl cation as observed in the water. Subsequent additions could form IHB with various hydrogens of CH groups in the phenyl cation which are weaker based on the DFT calculations for the Ph^+W_n clusters when $n \geq 2$.

7.5. Summary and Conclusions

Equilibrium thermochemical measurements by the mass-selected ion mobility drift cell technique have to utilized to investigate the binding energies and entropy changes associated with the step-wise solvation of the phenyl cation by a variety of small polar molecules that include: water, methanol, hydrogen cyanide, and acetonitrile. The mass scans for all molecules showed that the first association product forms a covalent bond with the phenyl cation. In the case of water, the first association product has a C-O covalent bond between the open sp^2 orbital of the phenyl cation and the oxygen of the water based on DFT calculations at the B3LYP/6-311++G** level for a protonated phenol structure of $\text{C}_6\text{H}_5\text{OH}_2^+$. The experimentally measured $-\Delta H^\circ$ for the formation of $\text{Ph}^+(\text{H}_2\text{O})_2$ and $\text{Ph}^+(\text{CH}_3\text{CN})_2$ is dependent on the temperature where the van't Hoff plot has two distinct regions. This would suggest that there is a mixture of isomers present in for formation of both of these association products. The stepwise solvation of the phenyl cation with acetonitrile to form $\text{Ph}^+(\text{CH}_3\text{CN})_n$ for $n = 2-4$ have experimentally measured $-\Delta H^\circ$ values that decrease gradually from $11.6 \pm 1 \text{ kcal mol}^{-1}$ to $9.4 \pm 1 \text{ kcal mol}^{-1}$. The second addition of the polar molecule to the

phenyl cation has as measured $-\Delta H^\circ$ much higher than subsequent additions for water, methanol, and hydrogen cyanide where there is nearly a 50 % loss of energy based on the $-\Delta H^\circ$ values. This unlike in previous studies with naphthalene where the step-wise solvation of the naphthalene radical cation with small polar molecules where the $-\Delta H^\circ$ is minimal.^{56,57,67} The structures of the $\text{Ph}^+(\text{H}_2\text{O})_n$ $n = 1-4$ appear to form a mixture of protonated phenol and IHB isomers. Subsequent water molecules form an ensemble of structures where they “*externally solvate*” the phenyl cation forming an H-bonded chain of water molecules for $n \geq 2$. To help explain the thermochemical results for the $\text{Ph}^+(\text{CH}_3\text{OH})_n$, $\text{Ph}^+(\text{HCN})_n$, and $\text{Ph}^+(\text{CH}_3\text{CN})_n$ step-wise solvation, DFT calculations for the $\text{Ph}^+(\text{CH}_3\text{OH})_n$, $\text{Ph}^+(\text{HCN})_n$, and $\text{Ph}^+(\text{CH}_3\text{CN})_n$ will be performed.

Chapter 8: Summary of Results and Future Outlooks

Characterizing the interactions of solvent molecules with ions is fundamental in understanding the thermodynamics of solution chemistry. These interactions are difficult to observe directly in solution because the number of solvent molecules far exceeds the number of ions present. It is because of this that the gas phase lends itself to be the ideal medium in the study of these interactions on a molecular level. When investigating an ion's energetics or reactivity with a neutral solvent or third body molecule, ion mobility mass spectrometry (IMMS) has been shown to be one of the most useful and accurate techniques available. IMMS has been used to study polycyclic aromatic hydrocarbon (PAH) molecules, which are a class of molecules of interest because they are considered the most abundant free interstellar organic molecules. Naphthalene ($C_{10}H_8$) is the simplest PAH and its solvation and thermochemistry with interstellar molecules are of interest. The research covered in this dissertation focuses on the stepwise solvation of the naphthalene radical cation ($C_{10}H_8^{*+}$) with a variety of neutral solvent molecules. The neutral solvent molecules can be divided into three major classes of molecules: (1) small polar molecules (discussed in Chapter 4:), (2) unsaturated nonpolar organic molecules (discussed in Chapter 5:), and (3) aromatic molecules (discussed in Chapter 6:). Experimental thermochemistry and mobility measurement using the VCU mass-selected ion mobility mass spectrometer (details discussed in Chapter 2:) have been used in conjunction with density functional theory (DFT) calculations to determine the binding energy and structure of the first neutral solvent molecule to the naphthalene radical cation. The thermochemistry results of these experiments are summarized in Table 14 with the structures of a selection of these association products from each class shown in Figure 98. The pattern of sequential additions is also of interest and therefore the binding energies and structures are also discussed.

Table 14. Summary of the measured thermochemistry ($-\Delta H^\circ$ and $-\Delta S^\circ$) for the formation of the first association product of the solvation of naphthalene radical cation ($C_{10}H_8^{\bullet+}$) with neutral molecules (B) as indicated the calculated binding energies (ΔE , corrected ZPVE) and calculated enthalpies at either the B3LYP/6-311++G**^a, M11/cc-pVTZ^b, or M06-2X/cc-pVTZ^c levels of theory for $C_{10}H_8^{\bullet+}$ (B) clusters. The experimental error for these measurements are ± 1 kcal mol⁻¹ and ± 2 cal mol⁻¹ K⁻¹ for $-\Delta H^\circ$ and $-\Delta S^\circ$ respectively.

	Neutral Molecule	$-\Delta H^\circ$ (kcal mol⁻¹)	$-\Delta S^\circ$ (cal mol⁻¹ K⁻¹)	ΔE° (kcal mol⁻¹)	$-\Delta H$ (calc) (kcal mol⁻¹)
Small Polar Molecules	H ₂ O	7.8	19.5	7.7 ^a	7.8 ^a
	D ₂ O	8.0	19.9	-	-
	CH ₃ OH	8.3	19.7	8.4 ^a	7.9 ^a
	EtOH	7.8	15.2	8.4 ^a	7.8 ^a
	1-PrOH	9.2	23.5	8.0 ^a	7.3 ^a
	2-PrOH	9.9	25.0	8.8 ^a	8.1 ^a
	1-BuOH	9.9	25.7	9.3 ^a	8.6 ^a
	2-BuOH	9.8	25.2	8.3 ^a	7.6 ^a
	HCN	7.1	16.4	7.8 ^a	7.4 ^a
	CH ₃ CN	11.3	20.9	10.8 ^a	10.0 ^a
Unsaturated Organic Molecules	C ₂ H ₂	3.3	10.9	-	-
	C ₂ H ₄	2.9	9.9	-	-
	C ₃ H ₆	4.4	15.4	-	-
	C ₄ H ₈	3.5	8.3	-	-
Aromatic Molecules	C ₆ H ₆	7.9	18.7	7.6-8.3 ^b	-
	C ₆ D ₆	8.2	18.9	-	-
	C ₅ H ₅ N	20.9	33.9	19.7-24.6 ^c	-

The small polar molecules found in this dissertation are: water (H₂O and D₂O), methanol, ethanol, 1-propanol, 2-propanol, 1-butanol, 2-butanol, hydrogen cyanide, and acetonitrile. The measured enthalpy values of 8 ± 1 kcal mol⁻¹ for water, methanol, ethanol, and HCN and 9 ± 1 kcal mol⁻¹ for the primary and secondary propanol and butanol molecules are lower than that of acetonitrile (11.3 ± 1 kcal mol⁻¹). This difference is explained by the stronger ion dipole interaction in the $C_{10}H_8^{\bullet+}$ (CH₃CN) cluster since the dipole moment is 3.92 Debye compared to the 1.55-2.98 Debye for the other polar molecules.² Despite these differences in binding energy, the calculated structure of the first association products at the B3LYP/6-311++G** level for all small polar molecules studied form a bifurcated ionic hydrogen bond (IHB) between two CH^{δ+} hydrogens of the naphthalene radical cation and the oxygen or nitrogen of the neutral polar molecule. The

differences in structures arise in the subsequent additions of the polar molecule to the naphthalene radical cation. In the case of acetonitrile, “*internally solvated*” structures are favored where additional acetonitrile molecules interact directly with the naphthalene radical cation and thus the naphthalene radical cation is isolated inside of the acetonitrile ice and not accessible for subsequent reactions. The other polar molecules studied form “*externally solvated*” structures where the neutral molecule forms a hydrogen bonded chain to which the naphthalene radical cation binds. Here the ionized polycyclic aromatic hydrocarbon sits on ice grains and is accessible for further reactions with incoming organic molecules.

The binding energies of unsaturated organic molecules to the naphthalene radical cation are much lower than those observed with small polar molecules. The experimental binding energies of acetylene and small olefin molecules (ethylene, propylene, and isobutene for this dissertation) are measured to be $3-4 \pm 1 \text{ kcal mol}^{-1}$. This decrease in binding energy compared is possibly due to weak charge-induced dipole interactions as well as $\text{CH}^{\delta+} \cdots \pi$ hydrogen bonding interactions between the naphthalene radical cation and nonpolar organic molecule. Such interactions would be similar to those observed with the benzene radical cation.¹⁰⁸ The similarity in binding energies for all nonpolar molecules suggests similar binding behavior and structures within this class. The formation of an ionic hydrogen bond is also not likely since there are no electrons available in this class to act as the hydrogen acceptor as is seen with the nitrogen and oxygen of the polar molecules. Future theoretical calculations would offer insight into these interactions as well whether the neutral organic molecule would condense on the naphthalene radical cation to produce larger polycyclic aromatic hydrocarbons such as anthracene, phenalene, and phenanthrene.

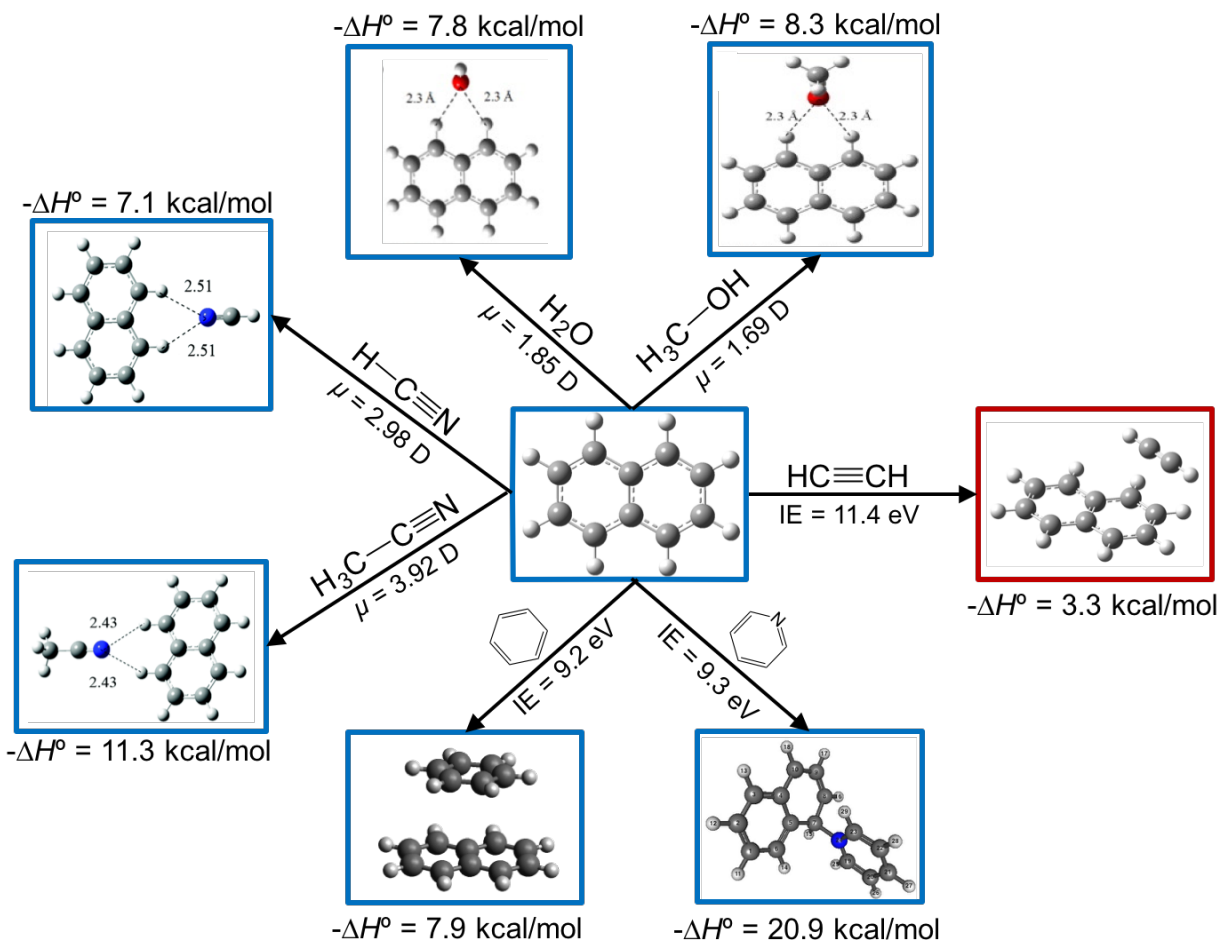


Figure 98. Summary of structures and binding energy (measured using $-\Delta H^\circ$ with an experimental error of $\pm 1 \text{ kcal mol}^{-1}$) for the first association product of the solvation of the naphthalene radical cation by various neutral molecules. Three classes are studied: (1) polar molecules (H_2O , CH_3OH , HCN , and CH_3CN are shown), (2) unsaturated organic molecules (an estimate for C_2H_2 is shown), and (3) aromatic molecules (C_6H_6 and $\text{C}_5\text{H}_5\text{N}$ are shown). The structures were calculated at B3LYP/6-311++G** level for the polar molecules, M11/cc-pVTZ level for C_6H_6 , and M06-2X/cc-pVTZ level for $\text{C}_5\text{H}_5\text{N}$.

The third class of neutral molecules discussed in this dissertation, aromatic molecules, interact with the naphthalene radical cation in a very different way compared to the other molecules mentioned. The binding energy of benzene (both C_6H_6 and C_6D_6) to the naphthalene radical cation is $8 \pm 1 \text{ kcal mol}^{-1}$. Although such binding energy is similar to that of polar molecules, the nature of the binding is quite different. Experimental mobility measurements and calculations at the M11/cc-pVTZ level show that the structure of the $(\text{naphthalene}\cdot\text{benzene})^{+\bullet}$ heterodimer ion is a

mixture of both a stacked parallel and T-shaped structure depending on the experimental conditions with the stacked parallel is the only structure present at higher temperatures and the T-shaped is the predominant structure at low temperatures. A second benzene molecule binds with a nearly identical binding energy on the opposite side of the naphthalene radical cation to form a sandwich structure. Pyridine is unique compared to the other molecules discussed because it is the only molecule that binds with some covalent character. The experimental binding energy is 20.9 kcal mol⁻¹ and results in the formation of a naphthalene C-pyridine N bond. The experimental mobility measurements as well as calculations at the M06-2X/cc-pVTZ level of the (naphthalene•pyridine)⁺⁺ heterodimer confirms this C-N covalent bond with a mixture of structures where the pyridine binds to either the α and β carbon of the naphthalene radical cation. The binding energy of the second pyridine molecule is significantly lower (11.0 ± 1 kcal mol⁻¹) than the first association products and binds by the formation of a hydrogen bonded network with the heterodimer.

The results of this dissertation show how the radical cation of the polycyclic aromatic hydrocarbon naphthalene interacts with various classes of neutral molecules. The binding energies and structures offer a starting point for the understand of how larger, more diffuse aromatic systems interact with molecules found in interstellar medium.¹⁷ Future research could involve two pathways. The first is to test further molecules such as tertiary alcohols, ethers, branched olefins, and pyrimidine to see if there are differences in the binding and structures compared to those molecules discussed here. The second path is the study of the interactions of larger PAH and PANH (polycyclic aromatic nitrogen containing hydrocarbons) radical ions with these same neutral molecules to show trends in binding and structure as the aromatic system increases in size.

List of References

- (1) Armentrout, P. B. In *Ion Mobility Mass-Spectrometry: Theory and Applications*; Wilkins, C. L., Trimpin, S., Eds.; CRC Press: Boca Raton, FL, 2011; pp 31-51.
- (2) *NIST Chemistry WebBook*.
- (3) Kebarle, P.; Searles, S. K.; Zolla, A.; Scarborough, J.; Arshadi, M. *J. Am. Chem. Soc.* **1967**, *89* (25), 6393–6399.
- (4) Kebarle, P.; Haynes, R. M.; Collins, J. G. *J. Am. Chem. Soc.* **1967**, *89* (23), 5753–5757.
- (5) Meot-Ner Mautner, M. *Chem. Rev.* **2005**, *105* (1), 213–284.
- (6) Kebarle, P. *Annu. Rev. Phys. Chem.* **1977**, *28*, 445–476.
- (7) Gao, B.; Wyttenbach, T.; Bowers, M. T. *J. Am. Chem. Soc.* **2009**, *131* (13), 4695–4701.
- (8) Ibrahim, Y.; Mabrouki, R.; Meot-Ner, M.; El-Shall, M. S. *J. Phys. Chem. A* **2007**, *111* (6), 1006–1014.
- (9) Ibrahim, Y.; Alsharaeh, E.; Dias, K.; Meot-Ner, M.; El-Shall, M. S. *J. Am. Chem. Soc.* **2004**, *126* (40), 12766–12767.
- (10) Momoh, P. O.; Hamid, A. M.; Abrash, S. A.; Samy El-Shall, M. *J. Chem. Phys.* **2011**, *134* (20), 204315.
- (11) Gao, B.; Wyttenbach, T.; Bowers, M. T. *J. Phys. Chem. B* **2009**, *113* (29), 9995–10000.
- (12) Liu, Z.; Fu, W.; Payzant, E. A.; Yu, X.; Wu, Z.; Dudney, N. J.; Kiggans, J.; Hong, K.; Rondinone, A. J.; Liang, C. *J. Am. Chem. Soc.* **2013**, *135* (3), 975–978.
- (13) Wyttenbach, T.; Gidden, J.; Bowers, M. T. In *Ion Mobility Mass-Spectrometry: Theory and Applications*; Wilkins, C. L., Trimpin, S., Eds.; CRC Press: Boca Raton, FL, 2011; pp 3–30.
- (14) Bowers, M. T.; Marshall, A. G. *J. Phys. Chem.* **1996**, *100* (31), 12897–12910.
- (15) Castleman, A. W., Jr; Keesee, R. G. *Annu. Rev. Phys. Chem.* **1986**, *37* (1), 525–550.
- (16) Castleman, A., Jr; Bowen, K. H., Jr. *J. Phys. Chem.* **1996**, *100* (31), 12911–12944.
- (17) Bowers, M. T. *Acc. Chem. Res.* **1994**, *27* (11), 324–332.
- (18) Meot-Ner (Mautner), M. *J. Phys. Chem.* **1987**, *91* (2), 417–426.
- (19) Ibrahim, Y.; Alsharaeh, E.; Mabrouki, R.; Momoh, P.; Xie, E.; El-Shall, M. S. *J. Phys. Chem. A* **2008**, *112* (6), 1112–1124.
- (20) Kim, S. K.; Lee, W.; Herschbach, D. R. *J. Phys. Chem.* **1996**, *100* (19), 7933–7937.
- (21) Dugourd, P.; Hudgins, R. R.; Clemmer, D. E.; Jarrold, M. F. *Rev. Sci. Instrum.* **1997**, *68* (2), 1122–1129.
- (22) Donald, W. A.; Leib, R. D.; Demireva, M.; Negru, B.; Neumark, D. M.; Williams, E. R. *J. Phys. Chem. A* **2011**, *115* (1), 2–12.
- (23) Zwier, T. S. *Annu. Rev. Phys. Chem.* **1996**, *47* (1), 205–241.
- (24) Belau, L.; Wilson, K. R.; Leone, S. R.; Ahmed, M. *J. Phys. Chem. A* **2007**, *111* (31), 7562–7568.
- (25) Belau, L.; Wilson, K. R.; Leone, S. R.; Ahmed, M. *J. Phys. Chem. A* **2007**, *111* (40), 10075–10083.
- (26) Enomoto, S.; Miyazaki, M.; Fujii, A.; Mikami, N. *J. Phys. Chem. A* **2005**, *109* (42), 9471–9480.
- (27) Miyazaki, M.; Fujii, A.; Ebata, T.; Mikami, N. *Chem. Phys. Lett.* **2004**, *399* (4-6), 412–416.
- (28) Mabrouki, R.; Ibrahim, Y.; Xie, E.; Meot-Ner, M.; El-Shall, M. S. *J. Phys. Chem. A*

- 2006**, *110* (23), 7334–7344.
- (29) Keesee, R. G.; Castleman, A. W., Jr. *J. Phys. Chem. Ref. Data* **1986**, *15* (3), 1011–1071.
- (30) Kemper, P. R.; Dupuis, N. F.; Bowers, M. T. *Int. J. Mass Spec.* **2009**, *287* (1-3), 46–57.
- (31) Han, F.; Du, Y.; Cheng, S.; Zhou, Q.; Chen, C.; KeyongHou; Wang, W.; Li, H. *Int. J. Mass Spec.* **2012**, *309*, 13–21.
- (32) Cooks, R. G.; Ouyang, Z.; Takats, Z.; Wiseman, J. M. *Science* **2006**, *311* (5767), 1566–1570.
- (33) Smith, J. N.; Keil, A.; Likens, J.; Noll, R. J.; Cooks, R. G. *Analyst* **2010**, *135* (5), 994–10.
- (34) Kanu, A. B.; Dwivedi, P.; Tam, M.; Matz, L.; Hill, H. H., Jr. *J. Mass Spectrom.* **2008**, *43* (1), 1–22.
- (35) Momoh, P. O.; El-Shall, M. S. *Phys. Chem. Chem. Phys.* **2008**, *10* (32), 4827–4834.
- (36) Tielens, A. G. G. M. *Annu. Rev. Astro. Astrophys.* **2008**, *46* (1), 289–337.
- (37) Szczepanski, J.; Vala, M. *Nature* **1993**, *363* (6431), 699–701.
- (38) Nagy, A.; Fulara, J.; Maier, J. P. *J. Am. Chem. Soc.* **2011**, *133* (49), 19796–19806.
- (39) Ricca, A.; Bauschlicher, C. W., Jr; Rosi, M. *Chem. Phys. Lett.* **2001**, *347* (4), 473–480.
- (40) Richter, H.; Howard, J. B. *Prog. Energy Combust. Sci.* **2000**, *26* (4), 565–608.
- (41) Fegley, B. *Space Sci. Rev.* **1999**, *90* (1-2), 239–252.
- (42) Sandford, S. A.; Aleon, J.; Alexander, C. M. O.; Araki, T.; Bajt, S.; Baratta, G. A.; Borg, J.; Bradley, J. P.; Brownlee, D. E.; Brucato, J. R.; Burchell, M. J.; Busemann, H.; Butterworth, A.; Clemett, S. J.; Cody, G.; Colangeli, L.; Cooper, G.; D'Hendecourt, L.; Djouadi, Z.; Dworkin, J. P.; Ferrini, G.; Fleckenstein, H.; Flynn, G. J.; Franchi, I. A.; Fries, M.; Gilles, M. K.; Glavin, D. P.; Gounelle, M.; Grossemy, F.; Jacobsen, C.; Keller, L. P.; Kilcoyne, A. L. D.; Leitner, J.; Matrajt, G.; Meibom, A.; Mennella, V.; Mostefaoui, S.; Nittler, L. R.; Palumbo, M. E.; Papanastassiou, D. A.; Robert, F.; Rotundi, A.; Snead, C. J.; Spencer, M. K.; Stadermann, F. J.; Steele, A.; Stephan, T.; Tsou, P.; Tyliszczak, T.; Westphal, A. J.; Wirick, S.; Wopenka, B.; Yabuta, H.; Zare, R. N.; Zolensky, M. E. *Science* **2006**, *314* (5806), 1720–1724.
- (43) Henning, T.; Semenov, D. *Chem. Rev.* **2013**, *113* (12), 9016–9042.
- (44) Micelotta, E. R.; Jones, A. P.; Tielens, A. G. G. M. *Astron. Astrophys.* **2010**, *526*, A52–17.
- (45) Ciesla, F. J.; Sandford, S. A. *Science* **2012**, *336* (6080), 452–454.
- (46) Reddy, S. N.; Mahapatra, S. *J. Phys. Chem. A* **2013**, *117* (36), 8737–8749.
- (47) CRAWFORD, M. K.; TIELENS, A.; Allamandola, L. J. *Astrophys. J.* **1985**, *293* (1), L45–L48.
- (48) Snow, T. P.; Le Page, V.; Keheyan, Y.; Bierbaum, V. M. *Nature* **1998**, *391* (6664), 259–260.
- (49) Sloan, G. C.; Hayward, T. L.; Allamandola, L. J.; Bregman, J. D.; DeVito, B.; Hudgins, D. M. *Astrophys. J.* **1999**, *513* (1), L65–L68.
- (50) Hudgins, D. M.; Bauschlicher, C. W.; Allamandola, L. J. *Spectrochim. Acta. A Mol. Biomol. Spectrosc.* **2001**, *57* (4), 907–930.
- (51) Pathak, A.; Sarre, P. J. *Mon. Not. R. Astron. Soc.* **2008**, *391*, L10–L14.
- (52) Bernstein, M. P.; Dworkin, J. P.; Sandford, S. A.; Cooper, G. W.; Allamandola, L. J. *Nature* **2002**, *416* (6879), 401–403.
- (53) Nuevo, M.; Milam, S. N.; Sandford, S. A.; Elsila, J. E.; Dworkin, J. P. *Astrobiol.* **2009**, *9* (7), 683–695.

- (54) Gudipati, M. S.; Allamandola, L. J. *Astrophys. J. Lett.* **2004**, *615* (2), L177–L180.
- (55) Gudipati, M. S.; Allamandola, L. J. *Astrophys. J.* **2006**, *638*, 286–292.
- (56) Attah, I. K.; Platt, S. P.; Mautner, M. M.-N.; El-Shall, M. S.; Aziz, S. G.; Alyoubi, A. O. *Chem. Phys. Lett.* **2014**, *613*, 45–53.
- (57) Platt, S. P.; Attah, I. K.; El-Shall, M. S.; Hilal, R.; Elroby, S. A.; Aziz, S. G. *Phys. Chem. Chem. Phys.* **2016**, *18* (4), 2580–2590.
- (58) Iglesias-Groth, S.; Manchado, A.; García-Hernández, D. A.; Hernández, J. I. G.; Lambert, D. L. *Astrophys. J. Lett.* **2008**, *685* (1), L55–L58.
- (59) Galazutdinov, G.; Lee, B. C.; Song, I. O. *Mon. Not. R. Astro. Soc.* **2011**, *412*, 1259–1264.
- (60) Rhee, Y. M.; Lee, T. J.; Gudipati, M. S.; Allamandola, L. J.; Head-Gordon, M. *Proc. Natl. Acad. Sci. U.S.A.* **2007**, *104* (13), 5274–5278.
- (61) Ricks, A. M.; Douberly, G. E.; Duncan, M. A. *Astrophys. J.* **2009**, *702* (1), 301–306.
- (62) Reddy, V. S.; Ghanta, S.; Mahapatra, S. *Phys. Rev. Lett.* **2010**, *104* (11), 111102–111104.
- (63) Ghanta, S.; Sivaranjana Reddy, V.; Mahapatra, S. *Phys. Chem. Chem. Phys.* **2011**, *13* (32), 14531–11.
- (64) Meot-Ner Mautner, M. *Chem. Rev.* **2005**, *105* (1), 213–284.
- (65) Tsuzuki, S.; Fujii, A. *Phys. Chem. Chem. Phys.* **2008**, *10* (19), 2584–13.
- (66) Conway, B. E. *Ionic Hydration in Chemistry and Biophysics*; Elsevier: Amsterdam, 1981.
- (67) El-Shall, M. S.; Attah, I. K.; Platt, S. P. In *Noncovalent Forces*; Springer International Publishing: Cham, 2015; pp 443–469.
- (68) Menor-Salván, C.; Marín-Yaseli, M. R. *Chem. Soc. Rev.* **2012**, *41* (16), 5404–5413.
- (69) Ibrahim, Y. M.; Meot-Ner, M.; Alshraeh, E. H.; El-Shall, M. S.; Scheiner, S. *J. Am. Chem. Soc.* **2005**, *127* (19), 7053–7064.
- (70) Ben-Naim, A. *Hydrophobic Interactions*; Plenum Press: New York, 1981.
- (71) Momoh, P. O.; Xie, E.; Abrash, S. A.; Meot-Ner Mautner, M.; El-Shall, M. S. *J. Phys. Chem. A* **2008**, *112* (27), 6066–6073.
- (72) Li, Q. *J. Geophys. Res.* **2003**, *108* (D21), 8827–16.
- (73) Herbst, E.; van Dishoeck, E. F. *Annu. Rev. Astro. Astrophys.* **2009**, *47* (1), 427–480.
- (74) Herbst, E. *Annu. Rev. Phys. Chem.* **1995**, *46* (1), 27–54.
- (75) Mumma, M. J.; DiSanti, M. A.; Magee-Sauer, K.; Bonev, B. P.; Villanueva, G. L.; Kawakita, H.; Russo, Dello, N.; Gibb, E. L.; Blake, G. A.; Lyke, J. E.; Campbell, R. D.; Aycock, J.; Conrad, Al; Hill, G. M. *Science* **2005**, *310* (5746), 270–274.
- (76) Lahuis, F.; Van Dishoeck, E. F.; Boogert, A. *Astrophys. J.* **2005**, *636*, L145–L148.
- (77) Matthews, C. N.; Minard, R. D. *Faraday Discuss.* **2006**, *133*, 393–399.
- (78) Pizzarello, S.; Holmes, W. *Geochimica et Cosmochimica Acta* **2009**, *73* (7), 2150–2162.
- (79) Zhao, Y.; Truhlar, D. G. *Acc. Chem. Res.* **2008**, *41* (2), 157–167.
- (80) Zhao, Y.; Truhlar, D. G. *Theor. Chem. Acc.* **2007**, *120* (1-3), 215–241.
- (81) Zhang, B.; Cai, Y.; Mu, X.; Lou, N.; Wang, X. *J. Chem. Phys.* **2002**, *117* (8), 3701–3711.
- (82) Zhang, C.; Wang, X.; Liu, L.; Wang, Y.; Peng, X. *J. Mol. Model.* **2008**, *14* (11), 1053–1064.
- (83) Dunning, T. H. *J. Phys. Chem. A* **2000**, *104* (40), 9062–9080.
- (84) Mohajeri, A.; Shakerin, N. *J. Mol. Struct.: Thermochem.* **2004**, *711* (1-3), 167–172.

- (85) Agarwal, J.; Turney, J. M.; Schaefer, H. F., III. *J. Phys. Chem. Lett.* **2011**, *2* (20), 2587–2592.
- (86) Yamabe, S.; Fukuda, T.; Yamazaki, S. *J. Phys. Chem. A* **2012**, *116* (4), 1289–1297.
- (87) Rusyniak, M.; Ibrahim, Y.; Alsharaeh, E.; Meot-Ner Mautne, M.; El-Shall, M. S. *J. Phys. Chem. A* **2003**, *107* (38), 7656–7666.
- (88) Stein, G. D. *Phys. Teach.* **1979**, *17* (8), 503–511.
- (89) Bernstein, E. R. *Atomic and Molecular Clusters*; Elsevier: New York, 1990; Vol. 68.
- (90) Momoh, P. O.; Hamid, A. M.; Soliman, A.-R.; Abrash, S. A.; El-Shall, M. S. *J. Phys. Chem. Lett.* **2011**, *2* (19), 2412–2419.
- (91) Smith, R. A.; Ditmire, T.; Tisch, J. W. G. *Rev. Sci. Instrum.* **1998**, *69* (11), 3798–3804.
- (92) Hagen, O. F. *J. Chem. Phys.* **1972**, *56* (5), 1793–11.
- (93) Fenn, J. B. *Int. J. Mass Spec.* **2000**, *200* (1), 459–478.
- (94) Vestal, M. L. *Chem. Rev.* **2001**, *101* (2), 361–376.
- (95) Evans, E. H.; Pretorius, W.; Ebdon, L.; Rowland, S. *Anal. Chem.* **1994**, *66* (20), 3400–3407.
- (96) Bush, M. F.; Forbes, M. W.; Jockusch, R. A.; Oomens, J.; Polfer, N. C.; Saykally, R. J.; Williams, E. R. *J. Phys. Chem. A* **2007**, *111* (32), 7753–7760.
- (97) Rejoub, R.; Morton, C. D.; Lindsay, B. G.; Stebbings, R. F. *J. Chem. Phys.* **2003**, *118* (4), 1756–1756.
- (98) Miller, P. E.; Denton, M. B. *J. Chem. Ed.* **1986**, *63* (7), 617.
- (99) Reuben, A. J.; Smith, G. B.; Moses, P.; Vagov, A. V.; Woods, M. D.; Gordon, D. B.; Munn, R. W. *Int. J. Mass Spectrom. Ion Processes.* **1996**, *154* (1-2), 43–59.
- (100) Campana, J. E. *Int. J. Mass Spectrom. Ion Processes.* **1980**, *33* (2), 101–117.
- (101) Campana, J. E.; Jurs, P. C. *Int. J. Mass Spectrom. Ion Processes.* **1980**, *33* (2), 119–137.
- (102) Tunstall, J. J.; Voo, A.; Taylor, S. *Rapid Commun. Mass Spectrom.* **1997**, *11* (2), 184–188.
- (103) Kemper, P. R.; Bowers, M. T. *J. Am. Soc. Mass Spectrom.* **1990**, *1* (3), 197–207.
- (104) Mabourki, R.; Ibrahim, Y.; Xie, E.; Meot-Ner Mautner, M.; Samy El-Shall, M. *Chem. Phys. Lett.* **2006**, *424* (4-6), 257–263.
- (105) Alsharaeh, E. H.; Ibrahim, Y. M.; El-Shall, M. S. *J. Am. Chem. Soc.* **2005**, *127* (17), 6164–6165.
- (106) Momoh, P. O.; El-Shall, M. S. *Chem Phys Lett.* **2007**, *436* (1-3), 25–29.
- (107) Armentrout, P. B. *J. Am. Soc. Mass Spectrom.* **2002**, *13* (5), 419–434.
- (108) Soliman, A.-R.; Hamid, A. M.; Abrash, S. A.; El-Shall, M. S. *Chem. Phys. Lett.* **2012**, *523* (C), 25–33.
- (109) Howdle, M. D.; Eckers, C.; Laues, A. M. F.; Creaser, C. S. *Int. J. Mass Spec.* **2010**, *298* (1-3), 72–77.
- (110) Rusyniak, M. J.; Ibrahim, Y. M.; Wright, D. L.; Khanna, S. N.; El-Shall, M. S. *J. Am. Chem. Soc.* **2003**, *125* (39), 12001–12013.
- (111) Helden, von, G.; Kemper, P. R.; Gotts, N. G.; Bowers, M. T. *Science* **1993**, *259* (5099), 1300–1302.
- (112) Helden, von, G.; Gotts, N. G.; Bowers, M. T. *Nature* **1993**, *363*, 60–63.
- (113) Helden, von, G.; Hsu, M. T.; Gotts, N.; Bowers, M. T. *J. Phys. Chem.* **1993**, *97* (31), 8182–8192.
- (114) Hunter, J. M.; Fye, J. L.; Jarrold, M. F. *J. Chem. Phys.* **1993**, *99* (3), 1785.
- (115) El-Shall, M. S.; Ibrahim, Y. M.; Alsharaeh, E. H.; Meot-Ner Mautner, M.; Watson, S.

- P. J. Am. Chem. Soc.* **2009**, *131* (29), 10066–10076.
- (116) Bleiholder, C.; Johnson, N. R.; Contreras, S.; Wytttenbach, T.; Bowers, M. T. *Anal. Chem.* **2015**, *87* (14), 7196–7203.
- (117) Krishnamurthy, M.; de Gouw, J. A.; Bierbaum, V. M.; Leone, S. R. *J. Phys. Chem.* **1996**, *100* (36), 14908–14913.
- (118) E A Mason, E. W. M. *Transport properties of ions in gases*; John Wiley & Sons, 1988.
- (119) Wytttenbach, T.; Gidden, J.; Bowers, M. T. *Ion Mobility Mass-Spectrometry: Theory and Applications*; Wilkins, C. L., Trimpin, S., Eds.; CRC Press: Boca Raton, FL, 2011; pp 3–30.
- (120) Hourdakakis, E.; Simonds, B. J.; Zimmerman, N. M. *Rev. Sci. Instrum.* **2006**, *77* (3), 034702–034705.
- (121) Revercomb, H. E.; Mason, E. A. *Anal. Chem.* **1975**, *47* (7), 970–983.
- (122) Baykut, G.; Halem, von, O.; Raether, J. F. A. O. In *Ion Mobility Mass-Spectrometry: Theory and Applications*; Wilkins, C. L., Trimpin, S., Eds.; CRC Press: Boca Raton, FL, 2011; pp 53-71.
- (123) Shvartsburg, A. A.; Smith, R. D. *Anal. Chem.* **2008**, *80* (24), 9689–9699.
- (124) Shvartsburg, A. A.; Jarrold, M. F. *Chem. Phys. Lett.* **1996**, *261* (1-2), 86–91.
- (125) Mesleh, M. F.; Hunter, J. M.; Shvartsburg, A. A.; Schatz, G. C.; Jarrold, M. F. *J. Phys. Chem.* **1996**, *100* (40), 16082–16086.
- (126) Platt, S. P.; Attah, I. K.; Aziz, S.; El-Shall, M. S. *J. Chem. Phys.* **2015**, *142* (19), 191102.
- (127) Attah, I. K.; Platt, S. P.; Meot-Ner Mautner, M.; El-Shall, M. S.; Peverati, R.; Head-Gordon, M. *J. Phys. Chem. Lett.* **2015**, *6* (7), 1111–1118.
- (128) Wytttenbach, T.; Helden, von, G.; Batka, J. J.; Carlat, D. *J. Am. Soc. Mass Spectrom.* **1997**, *8* (3), 275–282.
- (129) Frisch, M. J. T.; Schlegel, H. B.; Scuseria, G. E.; Robb, M. A.; Cheeseman, J. R.; Montgomery, J. A., Jr; Vreven, T.; Kudin, K. N.; Burant, J. C.; Millam, J. M.; Iyengar, S. S.; Tomasi, J.; Barone, V.; Mennucci, B.; Cossi, M.; Scalmani, G.; Rega, N.; Petersson, G. A.; Nakatsuki, H.; Hada, M.; Ehara, M.; Toyota, K.; Fukuuda, R.; Hasegawa, J.; Ishida, M.; Nakajima, T.; Honda, Y.; Kitao, O.; Nakai, H.; Klene, M.; Li, X.; Knox, J. E.; Hratchian, H. P.; Cross, J. B.; Bakken, V.; Adamo, C.; Jaramillo, K.; Gomperts, R.; Stratmann, R. E.; Yazyev, O.; Austin, A. J.; Cammi, R.; Pomelli, C.; Ochterski, J. W.; Ayala, P. Y.; Morokuma, K.; Voth, G. A.; Salvador, P.; Dannenberg, J. J.; Zakrzewski, V. G.; Dapprich, S.; Daniels, A. D.; Strain, M. C.; Farkas, O.; Malick, D. K.; Rabuck, A. D.; Raghavachari, K.; Foresman, J. B.; Ortiz, J. V.; Cui, Q.; Baboul, A. G.; Clifford, S.; Cioslowski, J.; Stefanov, B. B.; Liu, G.; Liashenko, A.; Piskorz, P.; Komaromi, I.; Martin, R. L.; Fox, D. J.; Keith, T.; Al-Laham, M. A.; Peng, C. Y.; Nanayakkara, A.; Challacombe, M.; Gill, P. M. W.; Johnson, B.; Chen, W. I.; Wong, M. W.; Gonzalez, C.; Pople, J. A. Gaussian Inc.: Wallingford, CT, 2003 v02.
- (130) Frisch, M. J.; Trucks, G. W.; Schlegel, H. B.; Scuseria, G. E.; Robb, M. A.; Cheeseman, J. R.; Scalmani, G.; Barone, V.; Mennucci, B.; Petersson, G. A.; Nakatsuji, H.; Caricato, M.; Li, X.; Hratchian, H. P.; Izmaylov, A. F.; Bloino, J.; Zheng, G.; Sonnenberg, J. L.; Hada, M.; Ehara, M.; Toyota, K.; Fukuda, R.; Hasegawa, J.; Ishida, M.; Nakajima, T.; Honda, Y.; Kitao, O.; Nakai, H.; Vreven, T.; Montgomery, J. A., Jr; Peralta, J. E.; Ogliaro, F.; Bearpark, M. J.; Heyd, J.; Brothers, E. N.; Kudin, K. N.; Staroverov, V. N.; Kobayashi, R.; Normand, J.; Raghavachari, K.; Rendell, A. P.; Burant, J. C.; Iyengar, S. S.; Tomasi, J.; Cossi, M.; Rega, N.; Millam, N. J.; Klene, M.; Knox, J. E.; Cross, J. B.;

- Bakken, V.; Adamo, C.; Jaramillo, J.; Gomperts, R.; Stratmann, R. E.; Yazyev, O.; Austin, A. J.; Cammi, R.; Pomelli, C.; Ochterski, J. W.; Martin, R. L.; Morokuma, K.; Zakrzewski, V. G.; Voth, G. A.; Salvador, P.; Dannenberg, J. J.; Dapprich, S.; Daniels, A. D.; Farkas, Ö.; Foresman, J. B.; Ortiz, J. V.; Cioslowski, J.; Fox, D. J. Gaussian, Inc.: Wallingford, CT, USA 2009.
- (131) Peverati, R.; Truhlar, D. G. *J. Phys. Chem. Lett.* **2011**, *2* (21), 2810–2817.
- (132) Jeffrey, G. A. *An Introduction to Hydrogen Bonding*; Oxford University Press: Oxford, UK, 1997.
- (133) Perrin, C. L.; Nielson, J. B. *Annu. Rev. Phys. Chem.* **1997**, *48* (1), 511–544.
- (134) Hamid, A. M.; Sharma, P.; Samy El-Shall, M.; Hilal, R.; Elroby, S.; Aziz, S. G.; Alyoubi, A. O. *J. Chem. Phys.* **2013**, *139* (8), 084304.
- (135) Chai, J.-D.; Head-Gordon, M. *Phys. Chem. Chem. Phys.* **2008**, *10* (44), 6615–6616.
- (136) McLean, A. D.; Chandler, G. S. *J. Chem. Phys.* **1980**, *72* (10), 5639–11.
- (137) Peterson, K. A.; Woon, D. E.; Dunning, T. H. *J. Chem. Phys.* **1994**, *100* (10), 7410–7417.
- (138) Solcà, N.; Dopfer, O. *J. Phys. Chem. A* **2003**, *107* (20), 4046–4055.
- (139) Feng, W. Y.; Lifshitz, C. *Int. J. Mass Spectrom. Ion Proc.* **1996**, *152* (2-3), 157–168.
- (140) Knochenmuss, R.; Cheshnovsky, O.; Leutwyler, S. *Chem. Phys. Lett.* **1988**, *144* (4), 317–323.
- (141) Provencal, R. A.; Casaes, R. N.; Roth, K.; Paul, J. B.; Chapo, C. N.; Saykally, R. J.; Tschumper, G. S.; Schaefer, H. F. *J. Phys. Chem. A* **2000**, *104* (7), 1423–1429.
- (142) Buck, U.; Ettischer, I. *J. Chem. Phys.* **1998**, *108* (1), 33–37.
- (143) Buck, U.; Siebers, J.-G.; Wheatley, R. J. *J. Chem. Phys.* **1998**, *108* (1), 20–14.
- (144) Tsuzuki, S.; Tokuda, H.; Hayamizu, K.; Watanabe, M. *J. Phys. Chem. B* **2005**, *109* (34), 16474–16481.
- (145) Hamid, A. M.; Soliman, A.-R.; El-Shall, M. S. *J. Phys. Chem. A* **2013**, *117* (6), 1069–1078.
- (146) Deakyne, C. A.; Meot-Ner Mautner, M.; Campbell, C. L.; Hughes, M. G.; Murphy, S. P. *J. Chem. Phys.* **1986**, *84* (9), 4958.
- (147) Daly, G. M.; Gao, J. L.; El-Shall, M. S. *Chem. Phys. Lett.* **1993**, *206* (5-6), 500–508.
- (148) Venables, D. S.; Schmuttenmaer, C. A. *J. Chem. Phys.* **1998**, *108* (12), 4935–11.
- (149) Brooke, T. Y.; Tokunaga, A. T.; Weaver, H. A.; Crovisier, J.; Bockelée-Morvan, D.; Crisp, D. *Nature* **1996**, *383* (6601), 606–608.
- (150) McKay, C. P.; Borucki, W. J. *Science* **1997**, *276* (5311), 390–392.
- (151) Cernicharo, J.; Heras, A. M.; Tielens, A. *Astrophys. J.* **2001**.
- (152) Woods, P. M.; Millar, T. J.; Zijlstra, A. A. *Astrophys. J.* **2002**.
- (153) Ehrenfreund, P.; Sephton, M. A. *Faraday Discuss.* **2006**, *133*, 277–12.
- (154) Waite, J. H.; Combi, M. R.; Ip, W.-H.; Cravens, T. E.; McNutt, R. L.; Kasprzak, W.; Yelle, R.; Luhmann, J.; Niemann, H.; Gell, D.; Magee, B.; Fletcher, G.; Lunine, J.; Tseng, W.-L. *Science* **2006**, *311* (5766), 1419–1422.
- (155) Pardo, J. R.; Cernicharo, J. *Astrophys. J.* **2007**, *654* (2), 978–987.
- (156) Pardo, J. R.; Cernicharo, J.; Goicoechea, J. R.; Guélin, M.; Ramos, A. A. *Astrophys. J.* **2007**, *661* (1), 250–261.
- (157) Waite, J. H.; Young, D. T.; Cravens, T. E.; Coates, A. J.; Crary, F. J.; Magee, B.; Westlake, J. *Science* **2007**, *316* (5826), 870–875.
- (158) Strazzulla, G.; Brucato, J. R.; Cimino, G.; Leto, G. *Adv. Space Res.* **1995**, *15* (10), 13–

- 17.
- (159) Strazzulla, G.; Arena, M.; Baratta, G. A.; Castorina, C. A.; Celi, G.; Leto, G.; Palumbo, M. E.; Spinella, F. *Adv. Space Res.* **1995**, *16* (2), 61–71.
- (160) Momoh, P. O.; Soliman, A.-R.; Meot-Ner, M.; Ricca, A.; El-Shall, M. S. *J. Am. Chem. Soc.* **2008**, *130* (39), 12848–12849.
- (161) Attah, I. K.; Hamid, A. M.; El-Shall, M. S. *Int. J. Mass Spec.* **2015**, *377*, 139–151.
- (162) Ono, Y.; Ng, C. Y. *J. Am. Chem. Soc.* **1982**, *104* (18), 4752–4758.
- (163) Booze, J. A.; Baer, T. *J. Chem. Phys.* **1993**, *98* (1), 186–16.
- (164) Coolbaugh, M. T.; Whitney, S. G. *J. Phys. Chem.* **1992**, *96*, 9139–9144.
- (165) Momoh, P. O.; Abrash, S. A.; Mabrouki, R.; El-Shall, M. S. *J. Am. Chem. Soc.* **2006**, *128* (38), 12408–12409.
- (166) Relph, R. A.; Bopp, J. C.; Roscioli, J. R.; Johnson, M. A. *J. Chem. Phys.* **2009**, *131* (11), 114305–114308.
- (167) Soliman, A.-R.; Hamid, A. M.; Attah, I.; Momoh, P.; El-Shall, M. S. *J. Am. Chem. Soc.* **2013**, *135* (1), 155–166.
- (168) Soliman, A.-R.; Hamid, A. M.; Momoh, P. O.; El-Shall, M. S.; Taylor, D.; Gallagher, L.; Abrash, S. A. *J. Phys. Chem. A* **2012**, *116* (36), 8925–8933.
- (169) Meot-Ner, M.; Sieck, L. W.; El-Shall, M. S.; Daly, G. M. *J. Am. Chem. Soc.* **1995**, *117* (29), 7737–7743.
- (170) El-Shall, M. S. *Acc. Chem. Res.* **2008**, *41* (7), 783–792.
- (171) El-Shall, M. S.; Daly, G. M.; Yu, Z.; Meot-Ner, M. *J. Am. Chem. Soc.* **1995**, *117* (29), 7744–7752.
- (172) Baldwin, K. G. H.; Watts, R. O. *J. Chem. Phys.* **1987**, *87* (2), 873–878.
- (173) Rezaei, M.; Michaelian, K. H.; McKellar, A. R. W.; Moazzen-Ahmadi, N. *Phys. Chem. Chem. Phys.* **2012**, *14* (23), 8415–4.
- (174) Takeuchi, H. *Comp. Theor. Chem.* **2011**, *970*, 48–53.
- (175) Meot-Ner Mautne, M.; Pithawalla, Y. B.; Gao, J.; El-Shall, M. S. *J. Am. Chem. Soc.* **1997**, *119* (35), 8332–8341.
- (176) Badger, B.; B, B. *Nature* **1968**, *219* (5151), 263.
- (177) Hübler, P.; Heinze, J. *Ber. Bunsen. Ges. Phys. Chem.* **1998**, *102* (10), 1506–1509.
- (178) Kochi, J. K.; Rathore, R.; Maguères, P. L. *J. Org. Chem.* **2000**, *65* (21), 6826–6836.
- (179) Kobayashi, H.; Tomita, H.; Naito, T.; Kobayashi, A.; Sakai, F.; Watanabe, T.; Cassoux, P. *J. Am. Chem. Soc.* **1996**, *118* (2), 368–377.
- (180) Rebek, J. *Chem. Soc. Rev.* **1996**, *25* (4), 255–10.
- (181) Fyfe, M.; Stoddart, J. F. *Acc. Chem. Res.* **1997**, *30* (10), 393–401.
- (182) Grimme, S. *Angew. Chem. Int. Ed.* **2008**, *47* (18), 3430–3434.
- (183) Headen, T. F.; Howard, C. A.; Skipper, N. T.; Wilkinson, M. A.; Bowron, D. T.; Soper, A. K. *J. Am. Chem. Soc.* **2010**, *132* (16), 5735–5742.
- (184) Searles, J. M.; Destree, J. D.; Snow, T. P.; Salama, F.; York, D. G.; Dahlstrom, J. *Astrophys. J.* **2011**, *732* (1), 50–56.
- (185) Small, D.; Zaitsev, V.; Jung, Y.; Rosokha, S. V.; Head-Gordon, M.; Kochi, J. K. *J. Am. Chem. Soc.* **2004**, *126* (42), 13850–13858.
- (186) Balucani, N. *Chem. Soc. Rev.* **2012**, *41* (16), 5473.
- (187) Burton, A. S.; Stern, J. C.; Elsila, J. E.; Glavin, D. P.; Dworkin, J. P. *Chem. Soc. Rev.* **2012**, *41* (16), 5459.
- (188) Jennings, W. B.; Farrell, B. M.; Malone, J. F. *Acc. Chem. Res.* **2001**, *34* (11), 885–894.

- (189) Hunter, C. A.; Lawson, K. R.; Perkins, J.; Urch, C. J. *J. Chem. Soc., Perkin Trans. 2* **2001**, 2 (5), 651–669.
- (190) Hunter, C. A.; Low, C. M. R.; Rotger, C.; Vinter, J. G.; Zonta, C. *Proc. Natl. Acad. Sci. U.S.A.* **2002**, 99 (8), 4873–4876.
- (191) Müller-Dethlefs, K.; Hobza, P. *Chem. Rev.* **2000**, 100 (1), 143–168.
- (192) Mecozzi, S.; West, A. P.; Dougherty, D. A. *J. Am. Chem. Soc.* **1996**, 118 (9), 2307–2308.
- (193) Dougherty, D. A. *Science* **1996**, 271 (5246), 163–168.
- (194) Gallivan, J. P.; Dougherty, D. A. *Proc. Natl. Acad. Sci. USA.* **1999**, 96, 9459–9464.
- (195) Ma, J. C.; Dougherty, D. A. *Chem. Rev.* **1997**, 97 (5), 1303–1324.
- (196) Mattioda, A. L.; Hudgins, D. M.; Bauschlicher, C. W.; Rosi, M.; Allamandola, L. J. *J. Phys. Chem. A* **2003**, 107 (10), 1486–1498.
- (197) Hudgins, D. M.; Charles W Bauschlicher, J.; Allamandola, L. J. *Astrophys. J.* **2005**, 632 (1), 316–332.
- (198) Mattioda, A. L.; Rutter, L.; Parkhill, J.; Head-Gordon, M.; Lee, T. J.; Allamandola, L. J. *Astrophys. J.* **2008**, 680 (2), 1243–1255.
- (199) Meot-Ner, M. *J. Phys. Chem.* **1980**, 84, 2724–2728.
- (200) Meot-Ner, M.; El-Shall, M. S. *J. Am. Chem. Soc.* **1986**, 108 (15), 4386–4390.
- (201) El-Shall, M. S.; Meot-Ner, M. *J. Phys. Chem.* **1987**, 91, 1088–1095.
- (202) Matsumoto, M.; Inokuchi, Y.; Ohashi, K. *J. Phys. Chem. A* **1997**, 101 (25), 4574–4578.
- (203) Peverati, R.; Truhlar, D. G. *J. Phys. Chem. Lett.* **2011**, 2 (21), 2810–2817.
- (204) Meot-Ner, M.; Hamlet, P.; Hunter, E. P.; Field, F. H. *J. Am. Chem. Soc.* **1978**, 100 (17), 5466–5471.
- (205) Woon, D. E.; Park, J.-Y. *Astrophys. J.* **2004**, 607 (1), 342–345.
- (206) Allamandola, L. J.; Sandford, S. A.; Wopenka, B. *Science* **1987**, 237 (4810), 56–59.
- (207) Ranasinghe, Y. A.; Glish, G. L. *J. Am. Soc. Mass Spectrom.* **1996**, 7 (5), 473–481.
- (208) Speranza, M.; Sefcik, M. D.; Henis, J.; Gaspar, P. P. *J. Am. Chem. Soc.* **1977**, 99 (17), 5583–5589.
- (209) Vereecken, L.; Peeters, J.; Bettinger, H. F.; Kaiser, R. I.; R Schleyer, von, P.; Henry F Schaefer, I. *J. Am. Chem. Soc.* **2002**, 124 (11), 2781–2789.
- (210) Chalyavi, N.; Dryza, V.; Sanelli, J. A.; Bieske, E. J. *J. Chem. Phys.* **2013**, 138 (22), 224307.
- (211) Landera, A.; Mebel, A. M. *Faraday Discuss.* **2010**, 147, 479–494.
- (212) Kaiser, R. I.; Asvany, O.; Lee, Y. T. *Planet. Space Sci.* **2000**, 48 (5), 483–492.
- (213) Le Page, V.; Keheyan, Y.; Snow, T. P.; Bierbaum, V. M. *Int. J. Mass Spec.* **1999**, 185, 949–959.
- (214) Ard, S.; Garrett, W. R.; Compton, R. N.; Adamowicz, L.; Stepanian, S. G. *Chem. Phys. Lett.* **2009**, 473 (4-6), 223–226.
- (215) Huntress, W. T.; Baldeschwieler, J. D.; Ponnampuruma, C. *Nature* **1969**, 223, 468–471.
- (216) Meot-Ner, M. *J. Am. Chem. Soc.* **1978**, 100 (15), 4694–4699.
- (217) Hamid, A. M. K. *Solvation of Organic Cations in the Gas Phase and within Molecular Clusters*, Virginia Commonwealth University: Richmond, 2012.
- (218) Solcà, N.; Dopfer, O. *Chem. Phys. Lett.* **2001**, 342 (1-2), 191–199.
- (219) Hauptert, L. J.; Wenthold, P. G. *J. Phys. Chem. A* **2013**, 117 (6), 1164–1170.

Vita

Sean Patrick Platt was born on August 19, 1986 in Grandview, Pennsylvania and is an American citizen. He graduated from Charleston Catholic High School in Charleston, West Virginia in 2005. He went on to receive a Bachelor of Science in Chemistry from Hampden-Sydney College in 2009 graduating *magna cum laude* with Departmental Honors in Chemistry. While there he was a member of Alpha Chi Sigma, professional fraternity in chemistry, and inducted into Chi Beta Phi, honorary society for the natural sciences. He later joined the Chemistry Department at Virginia Commonwealth University during the 2011 fall semester and has since worked in Dr. M. Samy El-Shall's research group. There he has been investigating gas phase interactions of aromatic ions with a variety of neutral solvent molecules using ion mobility mass spectrometry. He was awarded the Altria Fellowship in Chemistry during his fourth and fifth years at Virginia Commonwealth University.